Robotic Polarimetry of Blazars

Helen Elizabeth Jermak

A thesis submitted in partial fulfilment of the requirements of

Liverpool John Moores University

for the degree of Doctor of Philosophy.

June 2016.

Abstract

The motivation of this thesis was the study of radio-loud, active galaxies. These galaxies house relativistic jets at their centres, powered by accretion onto a super massive black hole. The focus was on the optical flux and polarised emission produced by these powerful jets. An automated pipeline was developed to reduce data from the Liverpool Telescope Ringo2 and Ringo3 polarimeters. As part of this work, the Ringo3 instrumental polarisation and depolarisation were characterised by repeated observations of standard stars. The Ringo2 and Ringo3 optical polarimetry and photometry of a sample of 20 γ-ray bright blazars were combined with Fermi γ-ray space telescope data and were used to explore possible correlations and thus probe the emission sites in the jet.

We found that optical and γ-ray fluxes had strong, positive correlations. This suggests that the dominant source of optical and γ-ray emission is from shared emission regions. If the Inverse Compton model is adopted to explain the γ-ray emission (i.e. upscattering of photons by relativistic electrons), this correlation suggests that synchrotron self-Compton emission processes are occurring in the jet, along with inverse Compton upscattering from nearby electrons (rather than those outside the jet).

The γ-ray flux and optical degree of polarisation were not significantly correlated. The optical flux and degree of polarisation were weakly positively correlated (with correlations that did not improve with an introduced lag). Both of these results imply that there is no large scale highly ordered magnetic field in the region where the γ-ray emission originates.

We found that the maximum degree of polarisation differs depending on the location of the source's synchrotron-peak. This may be a result of the viewing angle of the observer with respect to the jet. This suggests that the majority of optical polarisation is produced in shocked regions within the jet, downstream of the main emission region.

We found that the degree of polarisation was lower during a period of polarisation angle rotation compared with a period of non-rotation. This implies that the downstream magnetic field structure is either helical or compressed in a direction transverse to that of the jet.

Consistent with other work, our Ringo3 colour analysis showed that, with the exception of one source, flat spectrum radio quasars had a 'redder' when brighter property. This suggests that when the source is more luminous, the jet (i.e. non-thermal) emission dominates over the thermal emission from the accretion disk (which is powerful in FSRQs). We found that BL Lacs had a 'bluer' when brighter behaviour, suggesting that the brighter emission may come from more energetic photons within the jet.

We presented data from our long-term, multi-colour, blazar monitoring campaign. We found that all but one source had a 'redder' polarisation when the polarisation was higher. This implies that the highest polarisation is associated with higher densities of lower energy particles in the jet.

Well-sampled, regular cadence data is very important for the effective study and interpretation of blazars. This is particularly crucial for the interpretation of the position angle rotations, which can afford information about the electric vector angle (and hence the magnetic field angle). In this work, we presented the design of a new multicolour polarimeter, MOPTOP. The optical components in MOPTOP allow as much of the light from the source to be exploited as possible by replacing the rotating Polaroid (from the Ringo polarimeter design) with a rotating half-wave plate and beam splitter. MOPTOP's design minimises exposure times, allowing more frequent observations and a better sampling of data. A densely sampled monitoring program that is not interrupted by periods of sunlight would be highly desirable for the study of blazar jets.

Acknowledgements

When I look up at the night sky and think about the billions of stars out there, I think to myself: I'm amazing.

-Peter Serafinowicz

Contents

List of Tables

List of Figures

Chapter 1

Introduction

The centre of most, if not all luminous galaxies, contains at least one supermassive black hole (Kormendy & Richstone, 1995; Magorrian et al., 1998). The generally accepted model of an active galactic nucleus (AGN) is a supermassive black hole (SMBH) (M_{BH} = 10^5 - $10^9 M_\odot$) surrounded by an accretion disk (at radius $\sim$1-30 x 10^{14} cm) of material transported inwards by dissipative processes and outwards by angular momentum, which results in the material heating up through friction (Blandford & Znajek, 1977). The radiation from the heated accretion disk excites atoms close to the black hole, resulting in optical emission lines in an AGN spectrum (Urry & Padovani, 1995). Surrounding the accretion disk is a region of gas clouds (at radius $\sim$2-20 x 10^{16}cm) that are rapidly rotating around the SMBH. These regions produce broad emission lines ($\leq 10^4$ km s^{-1}) due to the velocity dispersion caused by their rapid movement and are therefore named the Broad Line Regions (BLRs). Further out (with an inner radius of $\sim 10^{17}$cm) there is a dusty torus that surrounds the accretion disk and obscures the central components of the AGN from some viewing angles. Still further out, at parsec to kiloparsec scales, are gas clouds with lower velocities which emit narrower emission lines ($\sim$500-1000 km s^{-1}): the Narrow Line Region (NLR). A small fraction ($\sim$15-20%) of AGN are radio-loud, where the definition for radio-loud

is the AGN having ratios of radio (5 GHz) to optical (B band) flux of ≥ 10 (Kellermann et al., 1989).

The viewing angle plays a vital role in the observed properties exhibited by an AGN. Figure 1.1 shows the AGN unification scheme, adapted from Urry & Padovani (1995). In type II AGN the dusty torus hides the light coming from the accretion disk from the observer, obscuring the galaxy's bright core and broad line region, resulting in spectra that show just the narrow line region. In type I AGN the disk is tilted with respect to the observer. This allows the broad- and narrow-line regions to be visible to the observer, along with the accretion disk. In type 0 AGN the disk is roughly perpendicular to the observer and the jet axis is aligned within $\lesssim 10°$ to the line of sight, resulting in the jet emission dominating the light output (Urry & Padovani, 1995).

Another classification of AGN depends on the optical spectral emission lines. The presence of emission features associated with forbidden transitions is indicative of low-density regions (where there is a lower probability of collisional de-excitation); such as the narrow-line region. If broad, permitted emission features are absent from the spectrum, the broad-line region is likely to be hidden from the observer (by the dusty torus, for example) due to viewing effects (Antonucci, 1993).

The variety of AGN subclasses which have been discovered over the last ~ 50 years can, in general, be reconciled according to their radio-loudness and their viewing angle (Antonucci, 1993). Radio sources have two classes according to Fanaroff & Riley (1974). Fanaroff and Riley type 1 (FR-1) sources have edge-darkened morphologies and Fanaroff and Riley type 2 (FR-II) sources have edge-brightened morphologies (Bridle & Perley, 1984). These structures can be explained by different interactions of low-powered (FR-I) or high-powered (FR-II) jets with the surrounding environment (Scheuer, 1974; Bicknell, 1986).

The radio dichotomy is a powerful factor in classifying these objects. Either radio-loud

and radio-quiet AGN are different sources, such that their magnetic field properties or black hole masses are different. Or the radio-loud and radio-quiet AGN are fundamentally the same, but differ in jet power and host galaxy properties which serve to quench the jet before it propagates far enough to be observed (Urry, 2004).

In this work, the focus was on blazars; radio-loud AGN with rapid variability, high and variable polarisation, high brightness temperatures and the absence of strong emission/absorption features (Urry & Padovani, 1995). These properties are attributed to a viewing angle (i.e. the angle of the jet relative to the line of sight) of $\lesssim 10°$ which results in Doppler boosting of the emission toward the observer.

1.1 Blazars

In many cases the viewing angle of an AGN determines its observational classification. The small viewing angle between the blazar jet and the line of sight results in the jetted emission being very strongly Doppler boosted towards the observer. This produces variable flux in all electromagnetic bands from radio to high energy TeV γ-rays (Punch et al., 1992). Blazars are defined by rapid flux variability with large amplitudes, high apparent luminosities, greater brightness temperatures than typical AGN, high polarisation and superluminal motion of ejected components in the jet.

The apparent superluminal properties and the rapid variability are caused by the beaming of the jet emission towards the observer, with resulting time dilation effects (Maraschi et al., 1992). The components in the jet are undergoing bulk motions with velocities close to the speed of light in a direction close to the line-of-sight of the observer. This means that radiation emitted at different times appears to have velocities $>c$, due to these time dilation effects.

---

[0]http://www.mssl.ucl.ac.uk/www_astro/guides/agn_unified.html - accessed December 2013
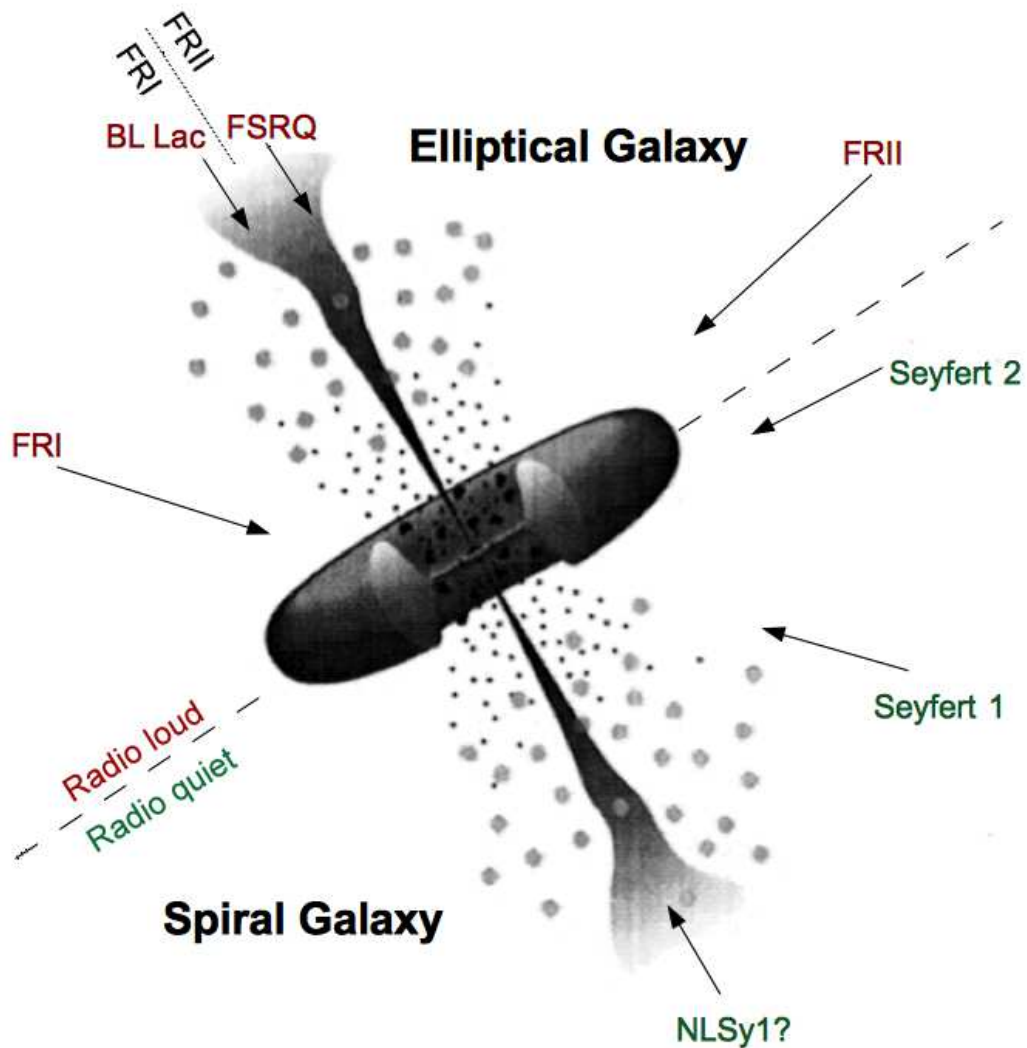
Figure 1.1: The proposed unification of AGN according to viewing angle, adapted from original image in Urry & Padovani (1995) from Holt et al. (1992). The Seyfert galaxies often have spiral hosts while the Fanaroff & Riley and blazar AGN are hosted in ellipticals. For the radio-quiet regime (shown in green), when viewed at an angle between ~45-60° and ~90° to the jet axis (depending on the thickness/uniformity of the torus), the torus can block the light from the central regions and observed emission is from the narrow-line region (NLR) and the torus itself (Seyfert 2 galaxy). At angles between 0 and ~45-60°, the broad- and narrow-line regions are visible (Seyfert 1). For the radio-loud regime (shown in red), the Fanaroff & Riley galaxies are shown from the same viewing angle but have different regions of highest intensity (the lobes/core).

The true velocity, ν, at an angle θ from the line of sight, with $\beta = \nu / c$, gives an apparent velocity (ν_a)

$$\nu_a = \frac{\nu \, \sin\theta}{1 - \beta \, \cos\theta} \qquad (1.1)$$

The observed flux density of the jet is increased by Doppler factor of δ^2 and a Doppler factor of δ^3 for distinct blobs in the jet. The Doppler factor is defined as $\delta = [\gamma \, (1\text{-}\beta \cos \theta)]^{-1}$, where γ is the Lorentz factor. The Lorentz factor is the change in time, length and relativistic mass of an object that is moving, and can be defined as $\gamma = \frac{1}{\sqrt{(1-\beta^2)}}$.

The Third Energetic Gamma Ray Experiment Telescope (EGRET) catalogue (Hartman et al., 1999; Thompson et al., 1993) identified many blazar sources (66 blazars from 271 sources), and these sources continue to be found with the Fermi gamma ray space telescope and its onboard Large Area Telescope (LAT) (Atwood et al., 2009).

One classification of blazars is to divide sources into two subclasses principally according to the equivalent widths of emission lines in their optical spectra. The equivalent width of an emission or absorption line is the wavelength integrated line flux divided by the continuum flux. These two classes are referred to as BL Lacs and Flat Spectrum Radio Quasars (FSRQs).

BL Lacertae was discovered in 1929, and was believed to be a variable star. It was given a stellar classification (Hoffmeister, 1929) which is now used to describe a subclass of blazars that share its properties. 39 years later the source was identified as a bright radio source with a faint host galaxy (Schmitt, 1968). The name BL Lac is used to describe all objects with similar features to the eponymous source : namely radioloudness, high luminosity, rapid variability, high optical polarisation and, in addition, spectral emission lines that are absent or have equivalent widths $<$5 Å (Burbidge & Hewitt, 1992). This definition is not a strict one owing to the variability of blazars which can result in some sources occasionally crossing into the opposite subclass (Vermeulen

et al., 1995; Sambruna et al., 2000; Perlman et al., 2001).

Like BL Lacs, FSRQs also have non-thermal continua but higher bolometric luminosities (Sambruna, 1997). They are classified as blazars that have emission lines with equivalent widths >5Å (Burbidge & Hewitt, 1992). They exhibit signs of thermal emission possibly related to an accretion disk in their optical and UV spectra (commonly referred to as the 'big blue bump': a feature of the blue optical/UV wavelength region of the blazar spectral energy distribution caused by accretion disk emission which rises above the non-thermal jet emission). BL Lacs, unlike FSRQs, have smooth continua (Sambruna, 1997). It has been suggested that the dichotomy of BL Lacs and FSRQs can be explained by different spins of the underlying black hole (Mukhopadhyay, 2013) or different accretion-powering processes.

Cavaliere & D'Elia (2002) discuss the possibility that both FSRQs and BL Lacs are centred on supermassive, Kerr black holes at close to maximal spin. Kerr black holes are an uncharged, rotating, spinning solution to the Einstein field equations (Kerr, 1963). In Cavaliere & D'Elia (2002), blazars are described to have different accretion rates (for FSRQ $\dot{m} \sim 1$ - 10 and for BL Lacs $\dot{m} \ll 1$), where $\dot{m} = \dot{M}c^2 / L_E$ (L_E is the Eddington luminosity $\sim 10^{47}$ $M_\odot^9$ ergs s^{-1}: the maximum luminosity an object can achieve when there is a balance between the radiation pressure and gravitational force). These values can be super-Eddington as they are not corrected for Doppler beaming. Xie et al. (2004) present Doppler-beaming-corrected accretion rates, consistent with those of Cavaliere & D'Elia (2002), of $\dot{m} = 0.02$-0.10 for BL Lac objects. For FSRQs they find $\dot{m} = 0.06$-0.17.

According to Cavaliere & D'Elia (2002), for a lower $\dot{m}$ the expected large-scale electric fields are less screened out than those posited by Fossati et al. (1998) (see Section 1.1.2) and accelerate fewer particles to high energies (i.e. higher frequencies). There are fewer particles due to the lower particle density in the acceleration region, however, the particles reach higher energies than those reached by higher accretion rates. The non-

thermal radiation (in BL Lacs) would peak at frequencies inversely correlated with the total output (i.e. higher spectral frequency peaks for BL Lac objects and lower spectral frequency peaks for FSRQ objects). The differing accretion rates result in typical bolometric luminosities of L$\sim 10^{44}$ ergs s^{-1} for BL Lacs and in excess of L$\sim 10^{46}$ ergs s^{-1} for FSRQ (constrained according to the energy directly extractable from a Kerr black hole).

BL Lacs and FSRQs are considered to be the beamed counterparts of the radio galaxies classed as Fanaroff & Riley (FR) I or II sources respectively (Fanaroff & Riley, 1974; Padovani & Urry, 1990, 1991; Urry et al., 1991). FR-Is have lower accretion rates which could be the cause of the non-existent or small ($<$5Å) optical emission lines seen in BL Lac spectra. A widely accepted view is that BL Lac-type blazars are moderately strong FR-I type radio galaxies orientated so that the jet is pointed toward the observer (Browne, 1983; Padovani & Urry, 1990, 1991). FSRQs have greater bolometric accretion disk luminosities (Sambruna, 1997) and so are associated with FR-II sources.

1.1.1   Spectral energy distribution

The broad band emission from blazars forms a characteristic 'double-humped' spectral energy distribution (SED) that spans the entire electromagnetic spectrum (see Figure 1.3). The first hump, peaking at lower frequencies (from the radio to UV or X-ray) is generally attributed to synchrotron emission from non-thermal, relativistic electrons spiralling in the jet magnetic field (Schwinger, 1949).

The higher frequency and energy peak (X-ray to γ-ray) is not fully understood, and can be modelled using leptons or hadrons. In leptonic models, the high energy emission is attributed to inverse Compton scattering. In the Thomson regime (where the energy of the scattering electron is low), the interaction between the electron and photon is con-

Figure 1.2: Figure taken from Böttcher (2012) (Fig. 8.5) of a blazar spectral energy distribution showing the distribution profiles of different contributory components of the system. The different line types aid the distinction of different components.

sidered elastic and the recoil of the electron is negligible. This means that in electron rest frame and laboratory frame, the energy is similar. When the electron is relativistic, the transfer of energy from the electron to the photon becomes more substantial. The difference between the rest and laboratory frame of the scattered relativistic photon is $\epsilon_s \sim \gamma^2 \epsilon$. Here ϵ_s is the scattered photon energy, γ is the Lorentz factor and ϵ is the pre-scattering photon energy. Any protons present are not accelerated to high enough energies to contribute to the dominant outflow.

The high energy peak can be explained by synchrotron self-Compton (SSC) emission, where the relativistic synchrotron electrons themselves upscatter the photons they produce (Marscher & Gear, 1985; Maraschi et al., 1992; Bloom & Marscher, 1996; Tavecchio et al., 1998), a combination of leptonic SSC and hadronic synchrotron emission (Mannheim & Biermann, 1992; Mücke & Protheroe, 2001; Böttcher et al., 2013b), or external Compton (EC) emission where the relativistic synchrotron electrons upscatter soft seed photons from a variety of sources such as: accretion disc radiation (Dermer et al., 1992; Dermer & Schlickeiser, 1993); optical and ultraviolet emission from the circumnuclear material (Sikora et al., 1994; Blandford & Levinson, 1995; Ghisellini & Madau, 1996; Dermer et al., 1997); infra-red emission from the dusty torus (Błażejowski et al., 2000); or synchrotron emission from other jet regions (Georganopoulos & Kazanas, 2003; Ghisellini & Tavecchio, 2008). It is still a highly debated issue, the answer may not be the same for all jets, and it is possible that emission processes may differ even for knots within the same jet (Böttcher, 2012).

In hadronic jet models both electrons and protons are accelerated to relativistic en-

ergies with protons exceeding the threshold for pγ photo-pion production (Böttcher et al., 2013b). Interactions between protons at relativistic energies result in the production of pions which decay to γ-rays, as such $\pi^0 \rightarrow 2\,\gamma$ (Mannheim, 1993). The high energy emission is dominated by proton-synchrotron emission, π^0 decay photons, synchrotron and Compton emission from secondary decay products of charged pions and the output from pair cascades initiated by these high-energy emissions intrinsically absorbed by $\gamma\gamma$ pair production (Mannheim & Biermann, 1992; Aharonian, 2000; Mücke & Protheroe, 2001; Mücke et al., 2003; Böttcher et al., 2013b). In these scenarios the lower frequency hump is caused by synchrotron radiation, as in leptonic models.

1.1.2 The blazar sequence

Blazars can be sub-divided according to the location of the synchrotron emission peak in their spectral energy distribution (SED). Flat spectrum radio quasars (those sources originally identified to have optical emission line equivalent widths $\geq$5Å) are included with BL Lac objects that have SED synchrotron peaks at low-frequencies (low-synchrotron-peaked LSP) ($\nu < 10^{14}$ Hz (IR), $\lambda \gtrsim$30000 Å). The intermediate synchrotron peaked sources (ISPs) and high synchrotron peaked sources (HSPs) are all BL Lac objects and have synchrotron peaks between 10^{14} Hz $\leq \nu \leq 10^{15}$ Hz (optical/IR, $\lambda \sim$3000-30000 Å) and $\nu > 10^{15}$Hz (UV, $\lambda \lesssim$3000 Å) respectively (Abdo et al., 2010b).

The shape and spectral properties of the first hump (that peaking at lower frequencies in the blazar SED) can probe the emitting components of the source. For example, FSRQs are posited to have more luminous accretion disks than BL Lacs, which means that when the jet is quiescent (and thus the synchrotron emission component, see Figure 1.2, is lower), it is possible to see contributory thermal emission from the hot accretion disk and a change to the shape of the SED. Simultaneous monitoring of blazars in IR, optical and UV would be the ideal solution to study the contributing components of
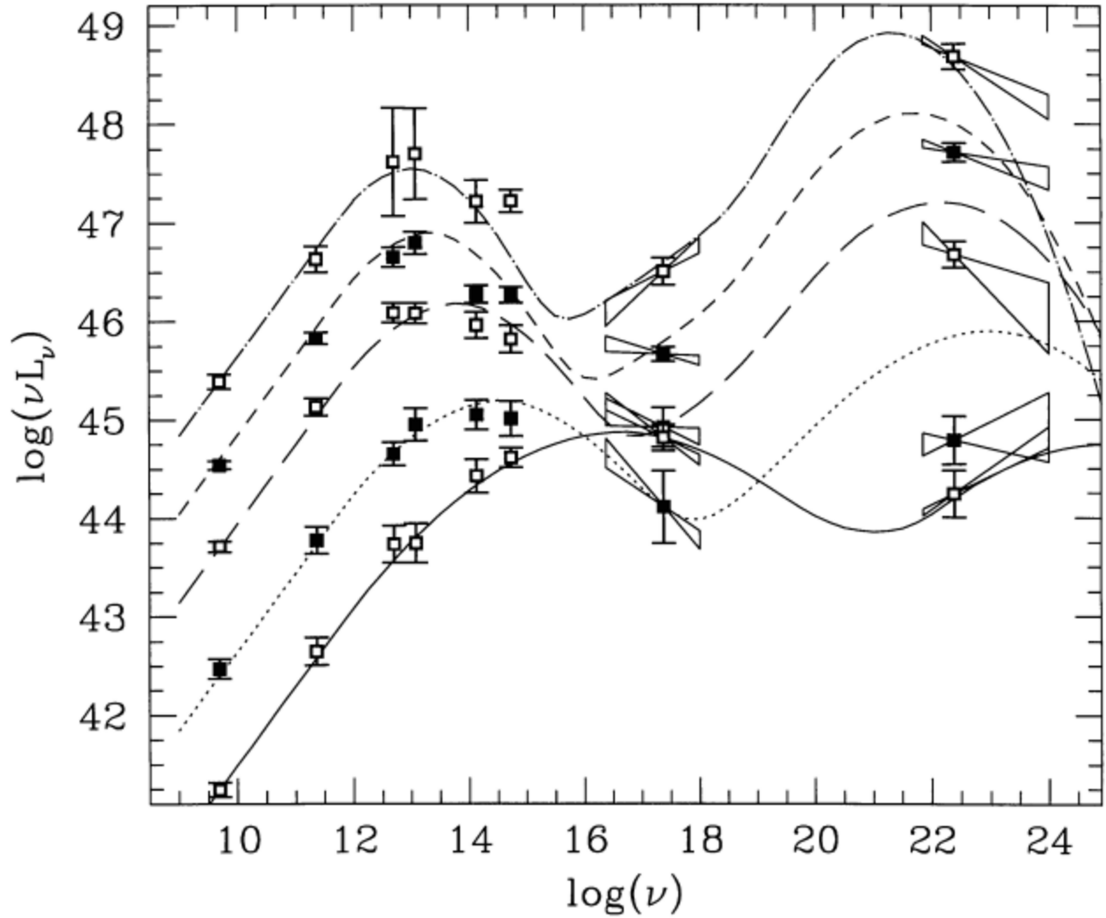
Figure 1.3: Figure taken from Fossati et al. (1998) (Figure 12) showing the average SEDs for blazars in five different luminosity bands (<42, 42-43, 43-44, 44-45, >45 log(L_{5GHz}). The curves are analytic approximations from Fossati et al. (1998) who find the frequency of the SED peaks to be correlated insomuch as the lower the synchrotron peak frequency, the lower the high energy peak frequency. The solid line corresponds to the <42 log(L_{5GHz} band, and the other line types represent the increasing frequency bands in order.

blazars during variability and thus explore the origin of the emission and constrain jet creation models according to accretion disk and jet power requirements.

Fossati et al. (1998) found that in blazar SEDs, the most luminous sources (i.e. FSRQs) peak at lower frequencies. They found that the frequency peak of the γ-ray component of the SED (i.e. the second hump) is correlated with the peak frequency of the synchrotron hump. They also reported that the high-low luminosity hump ratio increased with bolometric luminosity, suggesting that with a more luminous source, there are a greater number of external seed photons which are not the synchrotron photons themselves.

1.2 Jets

An on-going question in the area of blazar science is the formation, ejection and collimation of relativistic jets. The structure of the jet itself is generally agreed to be a 2-component configuration consisting of a spine (fast, magnetically-dominated jet) and a sheath (slower, matter-dominated outer layer of the jet) (Fragile, 2008). A schematic, simplified view of the inner regions of the jet is shown in Figure 1.4. The scale shows regions of the inner jet from the black hole itself to 10^5 R_S, where R_S is the Schwarzschild radius. The Schwarzschild radius is where the escape velocity from the surface of the compact object would equal the speed of light. Figure 1.4 shows the innermost regions, the acceleration and collimation zone, consisting of a helical magnetic field along which an emission feature moves (Marscher et al., 2008). This is the origin of the radio-resolvable emission features by facilities such as the very large baseline array (VLBA) (Marscher et al., 2010). High frequency radiation can be emitted close to the base of the jet where the electron energies are high enough to do so. As lower energy electrons can exist close to the base of the jet, or high energy electrons can be de-excited by scattering, lower frequency photons are also emitted there, as well as farther downstream (Georganopoulos & Marscher, 1998).

Although the jets exist out to megaparsec scales (as can be viewed in images of radio galaxies), in blazars, where the emission is relativistically beamed toward the observer, the area of interest is the inner jet. The emission features or shocks travelling along helical magnetic field lines are believed to create electric vector position angle (EVPA) rotations (Marscher et al., 2008, 2010; Zhang et al., 2014). Other explanations of EVPA rotations include a turbulent magnetic field resulting in the random walk of the polarisation vector (Jones et al., 1985; Marscher, 2014). It is also possible that visual, rather than physical, effects such as a bent jet and the trajectory of the polarisation angle on the sky can also cause polarisation angle rotations (Abdo et al., 2010a).
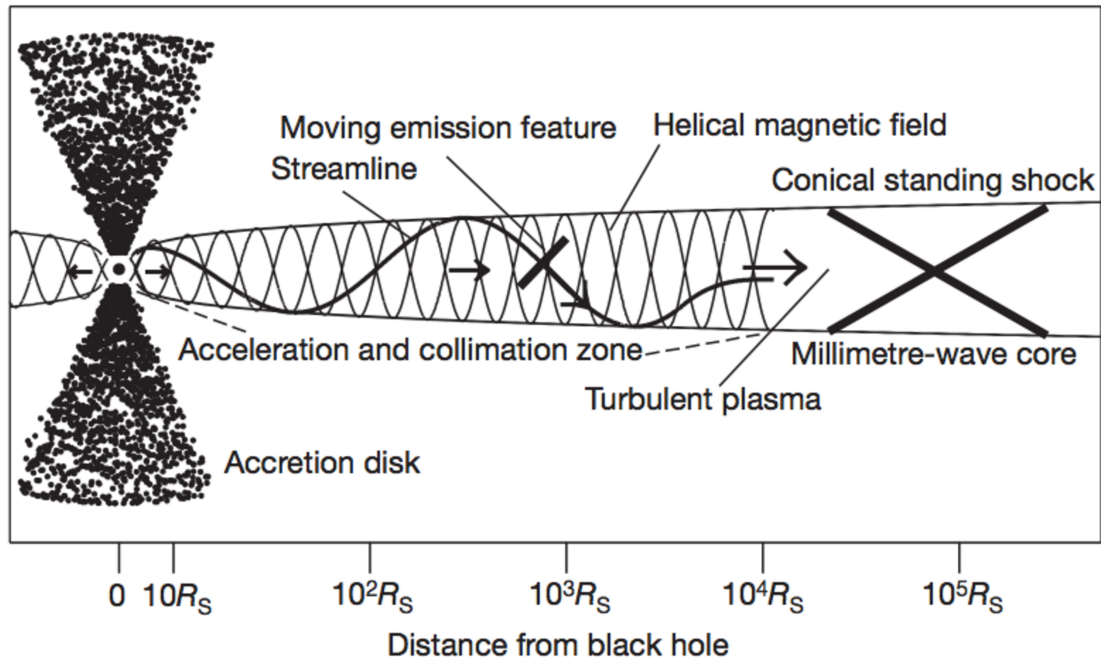
Figure 1.4: Schematic of the proposed inner jet (spine) model of the blazar BL Lac from Marscher et al. (2008). A logarithmic scale on the x axis (in units of Schwarzschild radii R_S) illustrates the phenomena on different scales. In BL Lac, the high apparent superluminal motion of the knots in the jet, and the variability at all wavelengths, suggests that the observed radiation is exclusively from the spine where the relativistic effects dominate (Marscher et al., 2008).

The conical standing shock component(s) (see Figure 1.4) are believed to be responsible for the acceleration of particles to γ-ray energies and the creation of high degrees of polarisation due to the compression within the shock, which causes the magnetic field to appear ordered in the direction of the line of sight (Laing, 1980).

There are various theories that address how relativistic jets can be formed from the vicinity of a black hole. One of the most popular models was presented by Blandford & Znajek (1977) in which the energy to create jets is released from a rotating (Kerr) black hole. This model requires an accretion disk and a strong poloidal magnetic field around the rotating black hole.

In the theory of jet formation, arguably the most important component is the magnetic field. The presence of a large-scale, ordered magnetic field in the jet is confirmed by the detection of synchrotron radiation. Synchrotron radiation is produced when a charged,

relativistic particle interacts with a magnetic field, causing it to spiral. Synchrotron radiation has a characteristic polarisation and the generated emission can cover the entire electromagnetic spectrum (Elder et al., 1947; Schwinger, 1949). In the context of relativistic jets, the electrons in the jet can produce synchrotron radiation up to γ-ray energies when the synchrotron-emitting electrons Compton up-scatter ambient synchrotron or thermal photons (Jones et al., 1974). Because synchrotron radiation is produced as a direct result of the presence of magnetic fields, it is used as a powerful probe of the structures of the magnetic field within a jet.

Using very long baseline interferometry (VLBI) it is possible to map the structure of the radio jet by determining the electric vectors/polarisation (Gabuzda et al., 1992). This can be used to define the projected orientation of the local magnetic field. For systems such as blazars and gamma-ray bursts, by exploring the temporal properties of the synchrotron radiation, the structure of the magnetic field can be probed indirectly. By comparing the change and values of the polarisation position angle and degree with those predicted by theoretical models, it is possible to constrain the structure of the magnetic field within these jet-axis sources and as such use this to explore methods of jet formation, collimation and ejection.

1.3 Polarisation

Light travels as an oscillating electromagnetic wave with the electric and magnetic fields perpendicular to the direction of travel. The wave can be defined by its amplitude (the height of the oscillation), frequency (the number of repeats per time interval) and wavelength (the distance between wave maxima). To describe the electric (and thus magnetic) field, it is necessary to measure the orientation of the electric field vector with respect to the direction of travel (which is transverse to the vibration of the electric field). The properties of 'polarisation' describe the orientation of the EVPA

with respect to a fixed plane, and the degree of polarisation (DOP) which describes the proportion of light with the predominant plane angle.

Using a clock-face as an example, a plane of polarisation could be identified according to one the numerals on the clock-face which respond to angles from 0 to 360°. In this sense a plane point at 12 or 6 would be identical, as would one points at 1 or 7, 2 or 8 etc. This means that the EVPA can have a measured value between 0 and 180° and these are ambiguous to these values ±180°. This introduces an observational complication as the data require interpretation in order to explore the behaviour of the EVPA rotation. More discussion continues in the following Chapters.

The electric field of circularly polarised light has two linear components perpendicular to each other, equal in amplitude but with a phase difference of $\pi/2$. The electric field rotates circularly around the direction of propagation and is either left- or right-handed depending on the rotation direction [1]. Marginally significant, low levels of circular polarisation ($\sim$1%) have been measured at optical wavelengths in blazars (Takalo & Sillanpaa, 1993; Valtaoja et al., 1993; Tommasi et al., 2001; Rieger & Mannheim, 2005). There are many proposed theories for the cause of circular polarisation in blazars and non-exclusively range from intrinsic (i.e. low levels of circular polarisation in synchrotron radiation) (Melrose, 1971), propagation-induced (i.e. travelling through a magnetised/relativistic plasma) (Wardle et al., 1998; Ruszkowski & Begelman, 2002), Inverse Compton scattering (Sciama & Rees, 1967), magnetic field configuration (Valtaoja, 1984), accretion disk radiation (Hartman et al., 2001) and dust scattering (Rieger & Mannheim, 2005). Detections of circular polarisation in blazars can help constrain these theories.

---

[1]http://www.edmundoptics.com/resources/application-notes/optics/introduction-to-polarization/
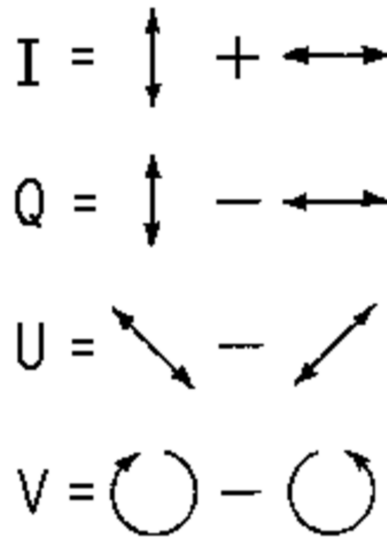
Figure 1.5: Diagram showing the angle of incident light used to calculate each of the Stoke Parameters. I is the intensity and has the sum of both vertical and horizontal components, Q is the difference between the vertical and horizontal components, U is the difference between the components at $\pm 45°$ and V is the circular polarisation component (not used in this work) which is the difference between the right and left circular components.

1.4 Stokes parameters

The Stokes parameters were named after George Gabrial Stokes and fully describe the polarisation of a beam of radiation. There are four parameters, I, Q, U and V, which represent the intensity (I), linear polarisation (Q & U) and circular polarisation (V) of light. These parameters can be defined by the combination of flux measurements through a polarising filter (i.e. one that only transmits light at a certain polarisation angle) at different angles in a 0-180° range and are shown in Figure 1.5.

$$I = S_0 = S_{0°} + S_{90°} \tag{1.2}$$

$$Q = S_1 = S_{0°} - S_{90°} \tag{1.3}$$

$$U = S_2 = S_{45°} - S_{135°} \tag{1.4}$$

$$V = S_3 = S_{RCP°} + S_{LCP°} \tag{1.5}$$

In this work the fluxes measured at each of eight rotor positions of a polaroid were combined to calculate the intensity and the linear normalised Stokes Parameters (i.e. q=Q/I, u=U/I) (the polarimeter does not have the capability to measure circular polarisation).

As shown in Equations 1.2-1.5, each normalised Stokes Parameter is calculated using the flux (S) at separations of 90°.

1.5   Polarisation signatures

The recurrent episodes of optical electric vector position angle (EVPA) rotations that are seen from AGN jets have been interpreted in a number of ways. Usually here we are referring to large-amplitude (>90°), smooth and long-lasting rotation events which seem to signal some coherent process developing within the jet. Although random walks in the Stokes plane, driven by turbulent magnetic fields, have been demonstrated to be able to explain rotations that gradually change over a long period of time (Jones et al., 1985; Marscher, 2014), they cannot, for example, explain preferred rotation directions within some specific sources (which goes against the stochastic nature of the random walk). Nor, as shown via Monte Carlo simulations by Blinov et al. (2015), can they answer for an entire population of rotations observed.

Other interpretations of the EVPA rotation link them to coherent jet features, such as (a) plasma following a helical path due to a large-scale helicoidal magnetic field configuration of the jet, resulting in long, slow rotations of the EVPA (Marscher et al., 2008, 2010; Zhang et al., 2014). They can also be described as (b) a bend or curvature in the jet which leads to a projection effect on the plane of the sky akin to a rotation, which can invert its rotation due to relativistic effects resulting from the collimated emission (Abdo et al., 2010a). Young (2010) graphically presents the idea discussed by Bjornsson (1982) that other kinematic effects causing variations of the viewing

angle in the co-moving frame could explain EVPA rotations up to 180°. Nalewajko (2010) continue with this idea and suggest that a symmetric emitting region on a bent jet could produce a gradual EVPA rotation.

Since the EVPA has a 180° ambiguity, long gaps in the polarisation light curves can lead to confusion when interpreting the EVPA rotations. To avoid introducing an incoherent view to the process with random 180° jumps being added to the EVPA dataset, in this thesis I chose to interpret the observed EVPA light curves following a continuity hypothesis. I have assumed that variations proceed in the smoothest way possible with no sudden jumps. Although there is no predefined limit to the length of gaps in the data, the interpretation is only applied when the difference between consecutive data points is <30 days. In this work we defined an EVPA rotation so that our results were consistent with those of the RoboPol group (Blinov et al., 2015), therefore an EVPA rotation is 'any continuous change of the EVPA curve with a total amplitude of $\Delta\theta_{max}$>90°, which is comprised of at least four measurements with significant swings between them'.

1.6 Overview of thesis

The aims of this thesis were to exploit polarisation data from the Liverpool Telescope to probe the conditions of a sample of γ-ray bright blazar sources. The sample was hand-picked, which means the results were not a reflection of the blazar class as a whole, but gave insight into the behaviour of individual sources through long term monitoring and intensive follow-up during periods of predicted or unprecedented flaring.

The sample was used to explore two main topics: the properties of blazar subclasses and how these particular sources contributed to the exploration of the fundamental physical differences between observationally classified blazars, and the individual properties of sources and how the photometric flaring and polarimetric variation behaviour

are linked, which can afford information about jet structure and emission conditions.

An additional component of this work was the instrumental and reduction calibration of the Ringo3 polarimeter and the development of an optimised successor which can provide more sensitive, multicolour polarimetric and photometric monitoring of blazars and other polarised sources on the same sized telescope.

The thesis is organised as follows; Chapter 2 details the telescopes, instrumentation and data reduction pipelines used in this work, Chapter 3 discusses the Ringo2 blazar sample, the photometric and polarimetric analysis using single wavelength data, and comparing this with simultaneous γ-ray observations, Chapter 4 details the multicolour polarimetric analysis of the Ringo3 data along with a description of the instrument calibration. Chapter 5 discusses the conclusions from Chapters 3 and 4, combining the long term analysis of the sources and concluding the findings of this project. Chapter 6 is the future work section, and details the design of the new MOPTOP polarimeter, along with other possible extensions and future plans for this project, and other blazar-like sources which can be explored by the techniques presented in this thesis.

Chapter 2

Instrumentation and Data Reduction

This chapter discusses the telescopes and instruments used in this work, and the methods used for data reduction. The observations were taken with the Liverpool Telescope, with additional data from the Kungliga Vetenskapakademien Telescope (KVA) and the Fermi gamma-ray space telescope. This chapter starts with a description of the telescopes used and then discusses the instruments and the separate data reduction techniques for each instrument (photometry and/or polarimetry).

2.1   Telescopes

The RINGO2 data used in this work were supplemented with KVA DIPOL data to provide better coverage. The RINGO3 data were more densely sampled and therefore do not have supplementary optical data (with the exception of SkyCamZ data where there were no secondary stars available in the frame for Mrk 421). Both the RINGO2 and RINGO3 data were compared with Fermi gamma-ray data, which is discussed in Chapters 3 and 4.

2.1.1   Liverpool Telescope

The Liverpool Telescope (LT) is the world's largest, fully autonomous, robotic optical telescope. The 2-metre telescope, located on the Canary Island of La Palma, was designed for the execution of quick, rapid follow-up of transient phenomena (Steele et al., 2004). Following the conceptualisation in the mid 1990s, the telescope was built locally in Merseyside and shipped in pieces to La Palma, with successful first light on 27th July 2003 and fully autonomous operation since 2004.

The LT utilises an intelligent dispatch scheduler to select observations according to a variety of conditions: weather, location of source on the sky, the priority of the proposal, for example. After each observation, the telescope runs an analysis of the possible observations to identify the highest ranked option (Steele & Carter, 1997). The telescope, designed to perform rapid follow-up observations on gamma-ray burst (GRB) objects, responds to Gamma-ray Coordination Network (GCN) triggers and slews efficiently to targets at a speed of 2°/sec.

The telescope has Ritchey-Chrétien optics and a f/10 focus at Cassegrain. The acquisition and guidance (A&G) box at the Cassegrain focus gives one straight-through port and eight science fold ports accessible by a deployable science fold mirror (Steele et al., 2004). There are currently seven instruments; five fed by the fold mirror, one at the straight through position (IO:O), and one spectrograph in the enclosure that is fed by fibres.

The all-sky camera, SkyCamZ, and the RINGO3 polarimeter were used as part of this project and are detailed in the following sections. The other instruments on the telescope are RISE, a fast-readout Wide Field Camera, which is used for the precise measurements of exoplanet transits (Steele et al., 2008) and FRODOSpec (Fibre-fed RObotic Dual-beam Optical Spectrograph), a multi-purpose integral-field input spectrograph, housed in its own enclosure within the telescope dome, that allows low- and

high- resolution spectroscopy on each arm (blue and red) (Morales-Rueda et al., 2004), LOTUS; a LOw-cosT Ultraviolet Spectrograph, SPRAT; a SPectrograph for the Rapid Acquisition of Transients and IO:I; a near-Infrared camera.

2.1.2 KVA

The Kungliga Vetenskapsakademien (KVA) telescope is located on the Canary Island of La Palma and is operated remotely from Finland. The KVA consists of two tele-scopes; a 35 cm Celestron and a 60 cm Schmidt reflector. The KVA 35 cm was used for the R-band photometric observations of the Tuorla blazar monitoring program[1]. The observations were coordinated with the MAGIC Imaging Air Cherenkov Telescope, and while the monitoring observations were typically performed two to three times a week (the weather allowing), during MAGIC observations the sources were observed every night. The KVA observations were taken by Finnish observers: A. Berdyugin, V. Kadenius, R. Reinthal, L. Takalo (all based at the Tuorla Observatory, University of Turku, Finland).

All the KVA data were analysed by Kari Nilsson, University of Tuorla, Finland, using the standard procedures with the semi-automatic pipeline developed in Tuorla (Nilsson et al. in prep.). The magnitudes were measured using the differential photometry and comparison star magnitudes found in the NASA/IPAC Extragalactic Database (NED) (Schmitz et al., 2011). The magnitudes were converted into Janskys using the standard formula $S = 3080 \times 10^{-(\mathrm{mag}/2.5)}$. For most of the sources in the sample, the contribution of the host galaxy to the measured flux was insignificant, the exceptions being Mrk 421 and Mrk 501. If the host galaxy was detected, its contribution was subtracted from the measured fluxes (Nilsson et al., 2008). Finally, the measured fluxes were corrected for Galactic extinction using the values from NED. While for many of the sources there were > 10 years of data, in this thesis only the data that were from

---

[1]http://users.utu.fi/kani/1m

the same observing periods as the DIPOL and RINGO2 polarisation measurements are used.

The KVA polarisation monitoring program began in December 2008 using the larger of the two telescopes: DIPOL. DIPOL, a 60 cm reflector, is equipped with a CCD polarimeter capable of polarimetric measurements in BVRI bands using a plane-parallel calcite plate and a super-achromatic $\lambda/2$ retarder (Piirola et al., 2005). The observations typically took place 1-2 times a week. The typical observation time per source was 960s and the observations were performed without a filter to improve the signal-to-noise. There were several gaps in the cadence when the source was too faint (R>15) and/or too weakly polarised (1-2%) to be detectable with KVA. In total, 10 to $\sim$100 polarisation measurements per source were collected. During some of the nights, polarised standard stars from Turnshek et al. (1990) were observed to determine the zero point of the position angle. The instrumental polarisation of the telescope was found to be negligible, with P_{inst}<0.01% (Berdyugin et al., 2016).

The sky-subtracted target counts were measured in the ordinary and extraordinary beams using aperture photometry. The normalised Stokes parameters and the degree of polarisation and position angle were calculated from the intensity ratios of two beams using standard formulae (e.g. Landi Degl'Innocenti et al., 2007).

2.1.3   Fermi gamma-ray telescope

The optical data in this project were combined with high energy γ-ray data to explore the connection between the emission at these two different energies. The high energy data were taken from the Fermi Gamma Ray Space Telescope spacecraft, which was launched on 11th June 2008. The principal scientific instrument on board the spacecraft is the Large Area Telescope (LAT), and the blazar data used in this project were taken using the LAT instrument. The LAT is an imaging telescope which covers high

γ-ray energy ranges from $\sim$20 MeV to >300 GeV. The telescope continually scans the sky and can observe the whole sky every three hours. It covers $\sim$20% of the sky at any one time (Atwood et al., 2009).

The Fermi-LAT light curve data were downloaded and analysed by Talvikki Hovatta, University of Turku, Finland. To produce the Fermi-LAT light curves the reprocessed Pass 7 data were downloaded and analysed using the ScienceTools version v9r32p5. In the event selection the LAT team recommendations for Pass 7 data[2] were followed. A 15 degree region was modelled around each source using the instrument response function P7REP_SOURCE_V15, Galactic diffuse model gll_iem_v05_rev1, and isotropic background model iso_source_v05.

The light curves were binned by T. Hovatta, using the adaptive binning method by Lott et al. (2012), with estimated 15% statistical flux uncertainty in each bin. The flux in each bin was then estimated using unbinned likelihood analysis with the tool gtlike (see http://fermi.gsfc.nasa.gov/ssc/data/analysis/scitools/). All sources within 15 degrees of the target that were listed in the 2FGL catalog (Nolan et al., 2012) were included in the likelihood model. The spectral indices of all sources were frozen to the values reported in 2FGL, and sources more than 10 degrees from the target fluxes were also frozen to the 2FGL values.

---

[2]http://fermi.gsfc.nasa.gov/ssc/data/analysis/documentation/Pass7REP_usage.html

<small>TABLE B : RINGO POLARIMETERS</small>

Name	Number of cameras	CCD Type	Instrument Type	Active Duration
RINGO	1	CCD	Ring	29-03-06 - 23-06-09
RINGO2	1	EMCCD	Image	02-08-09 - 26-10-12
RINGO3	3	EMCCD	Image	30-11-12 - present

Table 2.1: The three generations of RINGO polarimeter. The polarimeters evolved from RINGO, which transferred the polarisation signal from the rotor positions to a ring shape on a CCD, to RINGO3 which has three separate wavelength cameras which transferred images to an EMCCD (see Sections 2.2.1, 2.2.2 and 2.2.3).

2.2 Instruments and data reduction

2.2.1 RINGO

The RINGO polarimeter was commissioned in November 2005 and was on the Liverpool Telescope until it was decommissioned in June 2009 and replaced by its successor RINGO2. The RINGO instrument was based on a novel design polarimeter which consisted of a rapidly rotating Polaroid (550 rpm) that modulated the incoming beam of polarised light from a particular source into a time varying signal, if the source was polarised. The time varying signal would then be converted into a spatial signal (a ring) by a wedge shaped prism rotating with the Polaroid (Clarke & Neumayer, 2002). The time-varying polarisation signal would be mapped out in a $\sin(2\theta)$ pattern around each recorded ring onto a charged-coupled device (CCD) (Steele et al., 2006). The total intensity would then be calculated by integrating around the annulus.

The difficulty in reducing the ring data and the overlapping of sources in frames was resolved in 2009 with the introduction of the RINGO2 polarimeter (Table 2.1 shows a comparison of all three Ringo instruments).

2.2.2 RINGO2

RINGO2 was a fast-readout imaging polarimeter with a V+R hybrid filter (covering 460-720 nm) constructed from a 3mm Schott GG475 filter cemented to a 2mm KG3
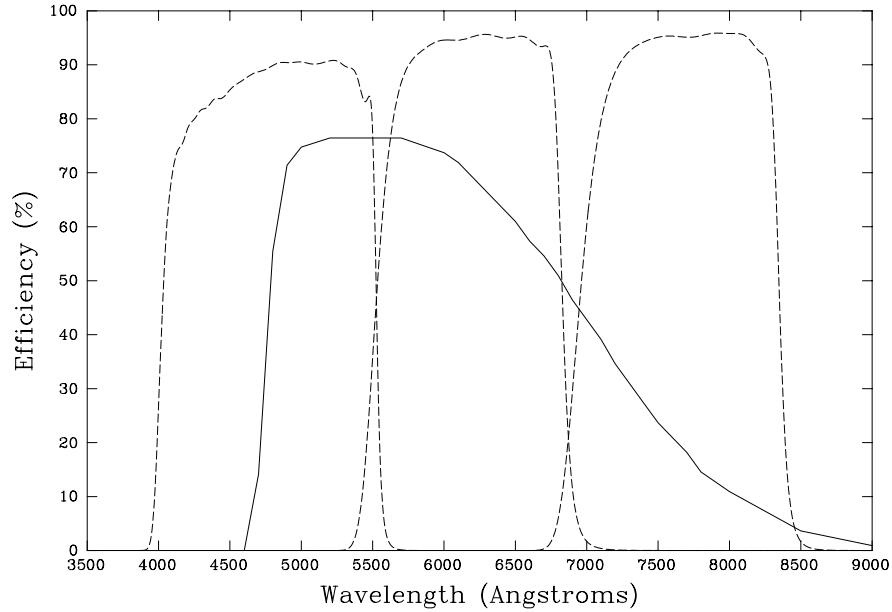
Figure 2.1: The throughput of the filter used in Ringo2 (solid line) compared with SDSS-g', r', i' filters (dashed lines from left to right) (Kopac et al. 2016 in prep.).

filter. RINGO2 used a rapidly rotating (∼1 revolution per second) Polaroid to modulate the incoming beam from the telescope (Steele et al., 2010).

RINGO2, which saw first light in June 2009, was designed to improve sensitivity of the polarimeter by replacing the CCD from the original design, with an electron multiplying charge coupled device (EMCCD) (Steele et al., 2010). Without the need to convert the data into a spatial signal (i.e. the ring) the EMCCD could rapidly read out an image of the source at a rate of 125 msec for each exposure. This reduced the excess sky signal and significantly improved the sensitivity of the instrument (Steele et al., 2010). The filter response was treated as R band in this work, as the RINGO2 filter is a good match to the R band. Figure 2.1 shows the throughput of the filter (solid line) compared with SDSS-g', r', i' filters (dashed lines from left to right) (Kopac et al. 2016 in prep.).

RINGO2 was operational from 2009 until late 2012 when it was succeeded by RINGO3; the most current generation of the RINGO polarimeters.

The rotating Polaroid in RINGO2 had 8 trigger points at 45° angles around the outside

RINGO2		
Field of view	4x4 arcmins	CCD size (pixels)
λ range	460-720 nm	512x 512

Table 2.2: Details about the Ringo2 instrument, field of view and wavelength range.

which triggered each observation and resulted in the production of 8 images per rotation, one for each of its Polaroid rotor positions. These rotor data were then stacked (for each rotor position) in the telescope pipeline to give 8 files made up of a number of individual images (the information stored under the 'NUMFRMS' FITS header).

Reduction

The method used to perform photometric and polarimetric reduction on RINGO2 data began with source identification and the extraction of measured counts of that source, as recorded by the charge-coupled device (CCD) pixels.

The automatic pipelines associated with the LT apply bias subtraction (the value applied to ensure the analogue-to-digital converter (ADC) receives positive counts), dark subtraction (to account for thermal behaviour of the detector), flat-field (to account for detector sensitivity) and supply the image with world-coordinate system (WCS) information, i.e. assigning the pixels a corresponding right ascension (RA) and declination (Dec) value to allow source identification.

The 8 rotor positions for each observation were stacked using the IMCOMBINE (average) command in IRAF (Tody, 1986) and the measuring of counts was performed on all frames using Source Extractor (Bertin & Arnouts, 1996). An aperture diameter of 9 pixels was used on all sources (4.1 arcsecs), independent of seeing. This was chosen as the minimum diameter that suitably encircles the point sources. The output of the source extraction was in the form of an American Standard Code for Information Interchange (ASCII) file which was read into the program using the read.table command in R. The object was identified by finding the nearest lying source in the field to the

literature right ascension (RA) and declination (dec) values of the source. The process was checked using a separate code which plots the field and highlights the object which the code has identified as the source of interest.

In cases where the source of interest lies close to another source in the frame, conditions of pixel location and ellipticity were utilised. For example, Mrk 421 lies in a field in which the world coordinate system (WCS) coordinates cannot be fitted due to the lack of field stars. The desired source is located close to the centre of the frame, along with a foreground galaxy. Using conditions of pixel location and, because Mrk 421 is a point-like source, using ellipticity constraints, the elliptical, background galaxy can be excluded.

To calculate the instrumental magnitude (m_{inst}) of a source, the flux (F) and exposure time (t_{exp}) are combined as:

$$m_{inst} = -2.5 \log_{10}(F/t_{exp}) - k \sec z \qquad (2.1)$$

where sec z is the airmass (i.e. the optical path length through the Earth's atmosphere) and k is a wavelength dependent constant.

To convert this airmass/extinction-corrected instrumental magnitude to a standard photometric system, a catalogue standard star's magnitude can be measured and compared to the literature value (m_{std}). The difference between the measured and literature values is the zeropoint; zpt = m_{std} - $m_{inststd}$[3]. Therefore the apparent magnitude of a source can be calculated as m = -2.5 $\log_{10}$(F/t_{exp}) - k sec z + zpt. This method was only used when there were no appropriate secondary sources available in the blazar field.

---

[3]http://www.vikdhillon.staff.shef.ac.uk/teaching/phy217/instruments/phy217_inst_photcal.html

For blazar frames where there are available secondary sources in the blazar field, the counts for each source were used, along with the counts for the secondary star and their R band magnitudes taken from the USNO-B1 catalogue (Monet et al., 2003), in the differential magnitude equation

$$m_1 = m_2 - 2.5.\log_{10} \frac{F_1}{F_2} \tag{2.2}$$

where m_1 and m_2 are the *apparent* magnitudes of the source and secondary star respectively, and F_1 and F_2 are their fluxes in standard flux units or in counts. This accounts for atmospheric extinction effects because the object and the secondary star both have roughly the same airmass.

For the calibration of blazars, which are highly variable, the stability of the secondary source in the frame was checked using a tertiary source to ensure no extrinsic variability contributed to the final measurement. To calculate the photometric errors, the error on the counts (i.e. F_1 and F_2) was propagated through Equation 2.2 as

$$B = F_1/F_2 \tag{2.3}$$

$$B_{err} = B * \sqrt{(F_{1err}/F_1)^2 + (F_{2err}/F_2)^2} \tag{2.4}$$

$$m_{1err} = \sqrt{2.5 * 0.434 * (B_{err}/B)^2 + (m_{2err})^2} \tag{2.5}$$

where m_{2err} is the quoted error associated with the literature magnitude of the secondary star.

Source Extractor calculates the error on the counts as FLUX_ERR = sqrt((A*sig^2) + F/g) where A is the object area, sig is the background RMS, F is the total flux, and g is the
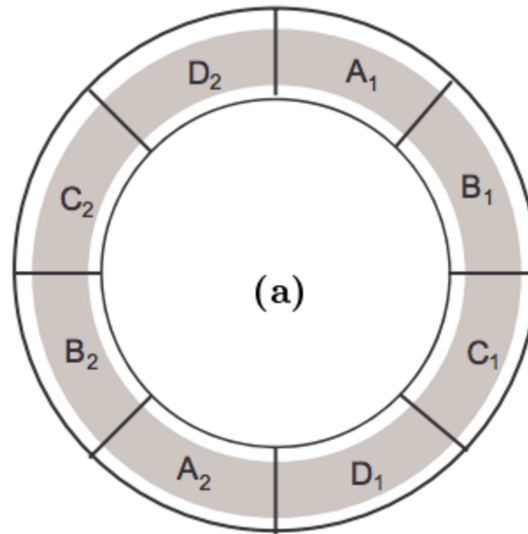
Figure 2.2: Diagram from Clarke & Neumayer (2002) showing the eight rotor positions of the Polaroid at which measurements were taken. These can then be combined to find the degree and angle of polarisation of the source according to the equations in Section 2.2.2.

gain[4].

Polarisation

In order to extract information about the degree and angle of polarisation, the data from the stacked and separate rotor frames (see Figure 2.2) were used in the equations from Clarke & Neumayer (2002) as follows :

The following combinations of the individual 8 rotor positions (see Figure 2.2)

$$S_1 = A_1 + A_2 + B_1 + B_2 + C_1 + C_2 + D_1 + D_2 \tag{2.6}$$

$$S_2 = A_1 + A_2 + B_1 + B_2 \tag{2.7}$$

$$S_3 = B_1 + B_2 + C_1 + C_2 \tag{2.8}$$

were used according to the equations in Clarke & Neumayer (2002) to calculate the

[4]http://www.ifa.hawaii.edu/ rgal/science/sextractor_notes.html

Linear Stokes parameters

$$q = \frac{Q}{I} = \pi \left(\frac{1}{2} - \frac{S_3}{S_1} \right) \qquad (2.9)$$

$$u = \frac{U}{I} = \pi \left(\frac{S_2}{S_1} - \frac{1}{2} \right) \qquad (2.10)$$

Fractional linear polarisation (degree of polarisation):

$$P = \sqrt{\frac{Q^2 + U^2}{I}} = \sqrt{q^2 + u^2} \qquad (2.11)$$

Position angle of plane of polarisation:

$$EVPA = \frac{1}{2} \tan^{-1} \frac{U}{Q} \qquad (2.12)$$

To account for the instrumental polarisation, observations of standard zero polarised stars from the Schmidt et al. (1992) catalogue were used. The mean q and u values for these sources (which should be equal to zero for an ideal instrument) were subtracted from the q and u values of the science sources.

With the instrumental polarisation and depolarisation defined, the degree of polarisation can be calculated as the radius of the q and u circle, where the x axis is the positive and negative q values, and the y axis is the positive and negative u values. The radius from the centre, according to the particular q and u value, is the degree of polarisation (equation 2.11).

To account for instrumental effects that cause depolarisation of the signal (such as the efficiency of the Polaroid's contrast ratio), comparison was made between q and u values found from measurements of standard polarised stars. The difference between the

measured and literature degree of polarisation was found to be a factor of 0.76±0.01 (D. Arnold, PhD thesis 2016) which was applied to all Ringo2 data.

Polarimetric Error Analysis

For both the DIPOL and RINGO2 polarimetric data, to correct P for the statistical bias associated with calculating errors from squares/square roots (where positive and negative q and u values are possible but only positive P values can result) we used the methodology presented by Simmons & Stewart (1985) to calculate 67% confidence limits and the most likely P value. As a check on this procedure we also ran a Monte Carlo simulation using Gaussian distributions of 1000 q and u values with standard deviations equal to their calculated errors and examined the resulting distribution of P. The results were identical. For those polarisation measurements where P/σ <2, the error bars are essentially upper limits. These values lie close to zero which means the lower error value was often negative. As it is not physically possible to measure negative values of polarisation, the point was still plotted in the figures, but is considered an upper limit.

The electric vector position angle (EVPA) in degrees was calculated as

$$EVPA = 0.5 * \mathrm{atan2(u, q)} + \mathrm{ROTSKYANGLE} + K \qquad (2.13)$$

where the function atan2() calculates the arctangent of u/q with a correct calculation of the sign and returns an angle between -180 and 180 degrees. ROTSKYANGLE is the angle of the telescope mount with respect to the sky when the image was taken and K is a calibration constant derived from repeated measurements of the EVPA of the polarised standard stars. Errors on EVPA were calculated according to the prescription in Naghizadeh-Khouei & Clarke (1993), and again confirmed by the Monte Carlo simulation.

RINGO3	red	green	blue
Field of view (diameter)	5.9 arcmin	4.1 arcmin	4.1 arcmin
λ range	770-1000 nm	650-760 nm	350-640 nm
Path	1 x transmission	2 reflections	1 reflection, 1 transmission

Table 2.3: Ringo3 specifics for each camera, field of view and wavelength range. The path describes whether the light travels through or is reflected by the dichroic mirrors.

As with any polarimeter, it is important to take into account any polarisation and de-polarisation introduced to the measurements by the instrument itself. The instrumental polarisation and depolarisation were constrained for RINGO2 using standard polarised and non-polarised stars and their literature values. For the RINGO instrument it was found that the instrument was most stable when observations were obtained at a constant Cassegrain mount rotator angle (represented in the FITS file header as ROTAN-GLE) and this was the same for RINGO2 also. For RINGO3 there were complications that made the initial analysis extremely difficult. This is discussed further in the following section.

2.2.3   RINGO3

The RINGO2 instrument was removed from the telescope in October 2012 and modi-fied to become the new RINGO3 polarimeter which was brought into service in early 2013. RINGO3 is a multicolour device fitted with dichroic mirrors (for dichroic mir-ror response see Figures 2.3 and 2.4) that split the polarised incoming beam of light into three optical wavebands: 'blue-visible'(350-640 nm), 'green'(650-760 nm) and 'red'(770-1000 nm) (see Figure 2.5 for a schematic diagram and Figure 2.6 for the instrument itself) (Arnold et al., 2012). This allows the measurement of polarisation degree and angle in three passbands simultaneously. Table 2.3 shows the wavelength ranges for each of the three cameras. The red camera has a different lens as opposed to the blue and green arms, which gives slightly different vignetting of the beam and the diameter of these vignetted fields of view are shown in Table 2.3.
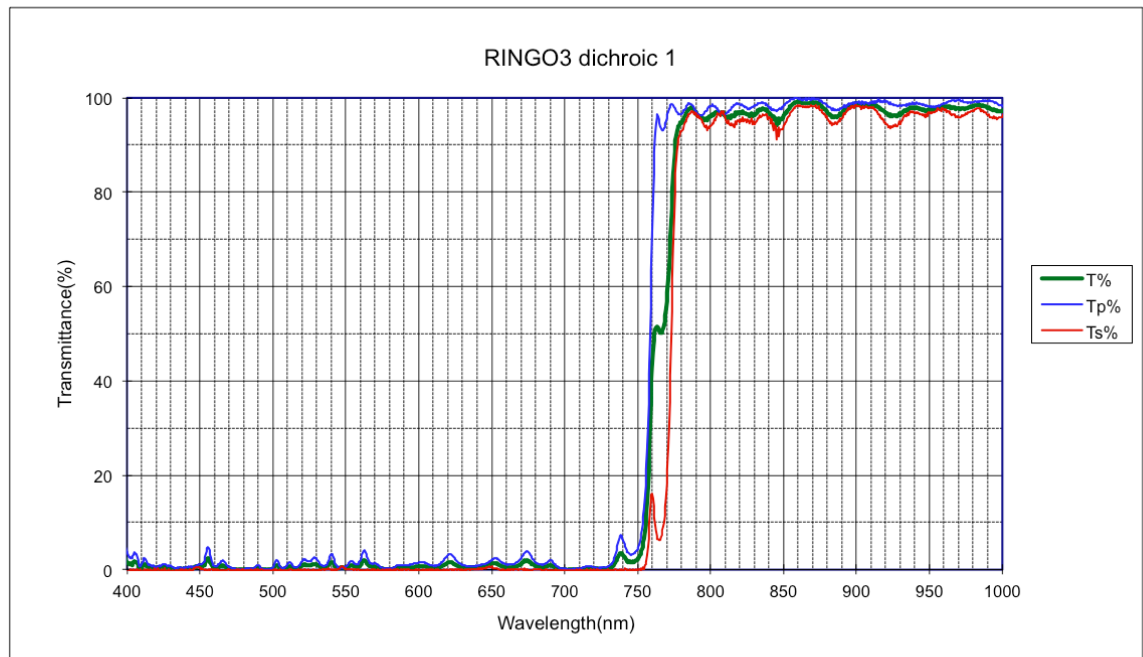
Figure 2.3: Transmittance the first of the two Ringo3 dichroic mirrors for the two polarisation planes, p (parallel, blue) and s (senkrecht, German for perpendicular, red). The overall transmittance is shown in green.
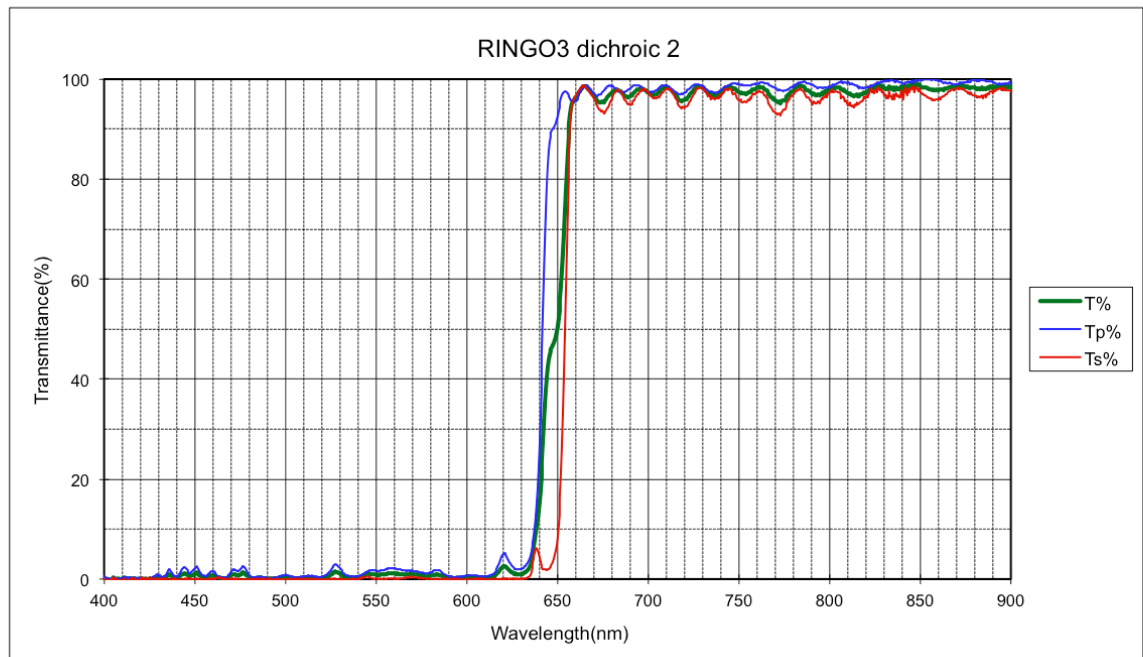
Figure 2.4: Transmittance for the second of the two Ringo3 dichroic mirrors for the two polarisation planes, p (parallel,blue) and s (senkrecht, German for perpendicular, red). The overall transmittance is shown in green.
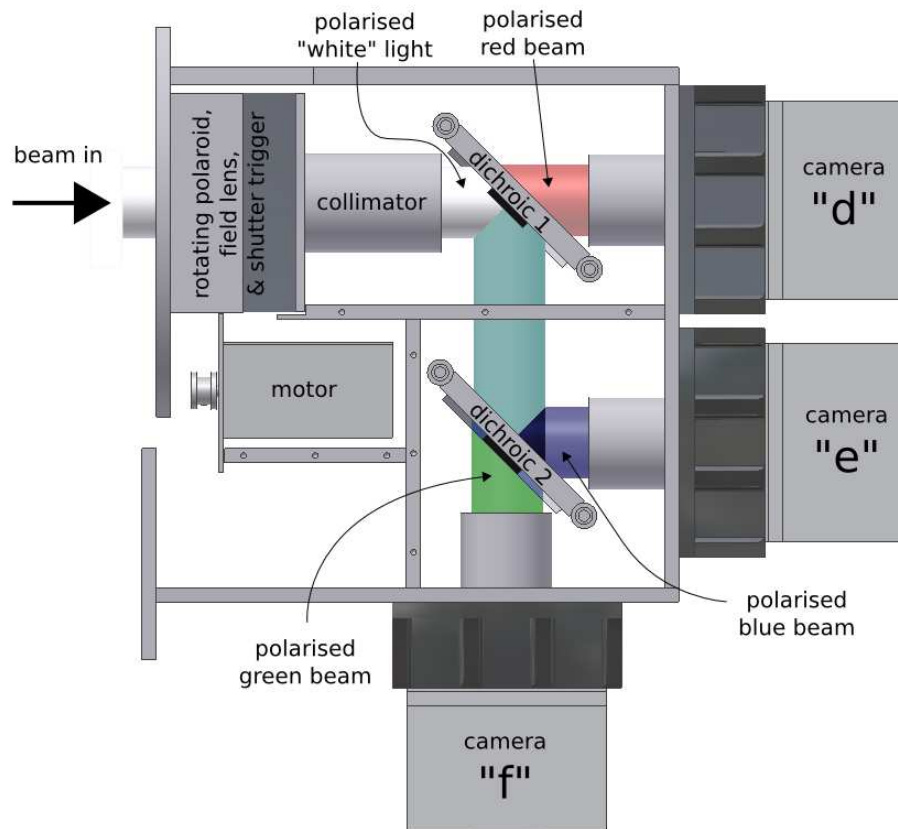
Figure 2.5: Schematic image of the Ringo3 instrument and the location of the three cameras. The light enters through the rotating Polaroid at the top left of the diagram. The light travels through the rotating Polaroid (powered by the motor) and the sensor triggers an observation in each camera. The light is collimated and depolarised in the same lens and is directed to the three cameras, being transmitted or reflected by two dichroic mirrors. The notations of 'polarised beam' refer to the original design without the depolarising optics (Arnold et al., 2012).
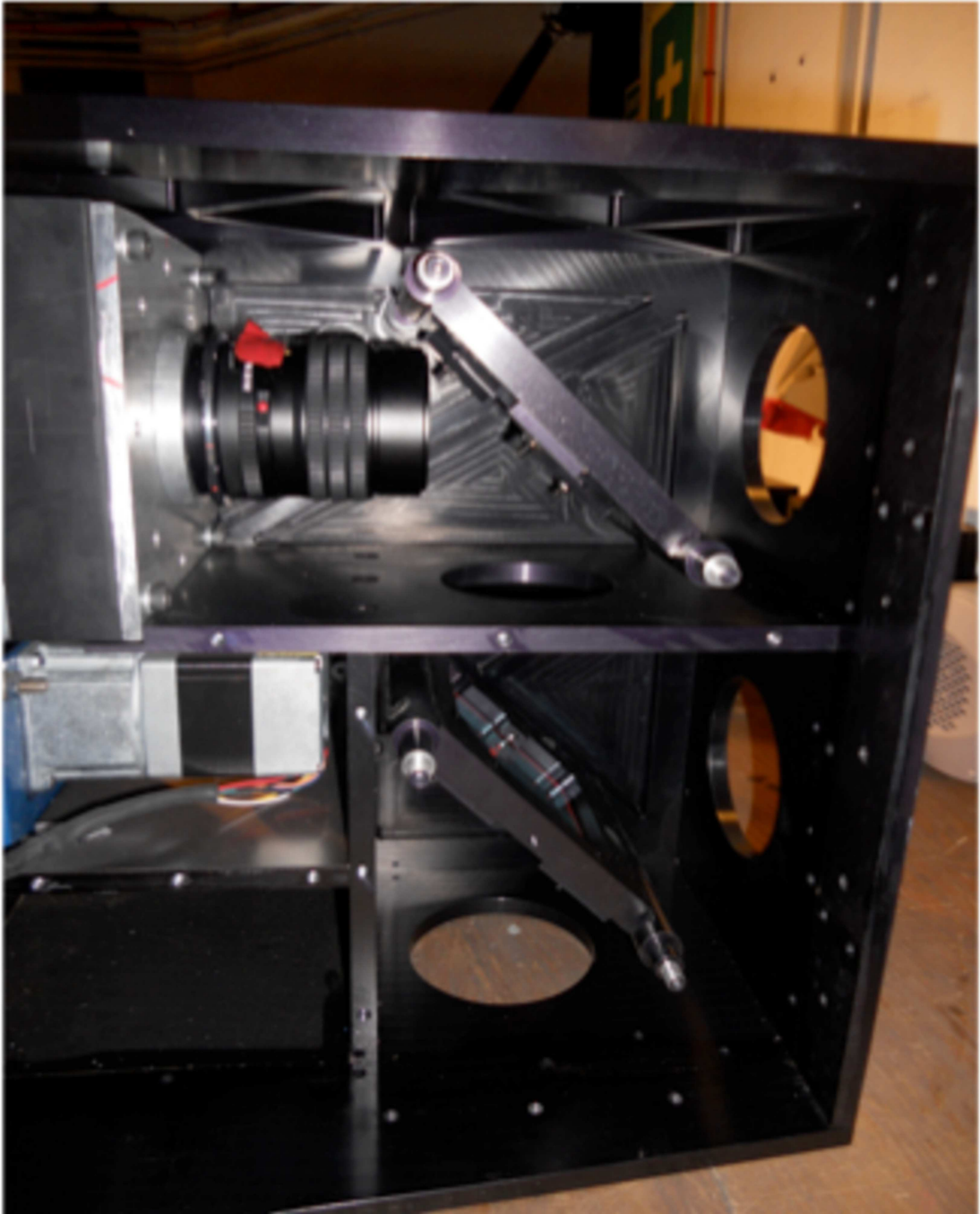
Figure 2.6: A photograph of the Ringo3 instrument with the side panel and cameras re-moved (during introduction of depolarising optic). The photo is of the same orientation as the schematic in Figure 2.5.

2.3 Pipeline

I wrote the semi-automated pipeline for the RINGO2 and RINGO3 data in the programming language R. The reduction procedure starts with a visual inspection of the data by the user, removing any frames that have cloud cover, tracking errors or very bad seeing. For each source an individual source file is created detailing the right ascension (RA) and declination (dec) of the secondary star (and where possible a tertiary star) which were identified by visual examination of the source frame. For RINGO2 their literature magnitudes (R band) were taken from the USNO-B1 catalogue (Monet et al., 2003). For RINGO3 the reference magnitudes were derived for each of the three wavelength bands (see Section 4.1.3).

The pipeline creates a .cl file that was used in IRAF software with the IMCOMBINE command to stack all 8 rotor positions to create a FITS file suitable for photometric analysis. There are cautionary checks in the pipeline in case the number of rotor positions !=8 (this is a rare occurrence when calibration frames are not removed from the data archive or rotor frames were missing). The pipeline then performs Source Extractor on every frame and automatically corrects the default.sex values for CAT-ALOG_NAME according to the name of the FITS file (in the standard LT format of IC_e_yyyymmdd_ON_0_RN_1.fits where e is an exposure, IC is the instrument camera (d, e, f for RINGO3, p for RINGO2), ON is the observation number and RN is the rotor position number (from 1-8). The pipeline also corrects the gain by multiplying the number of frames used to create the single rotor file (i.e. how many times the Polaroid rotates within the exposure time of the source) by the 0.32 electrons per count factor of gain for the EMCCD camera (the gain and number of frames values are taken from the FITS file). The gain is used in the calculation of the error on the counts measurement in Source Extractor (see Section 2.2.2).

The code reads in each FITS file and creates a variable that contains important FITS

header information (namely airmass, WCS fit error, rotor position, number of frames stacked to create the image, date of observation, time, exposure time and gain), along with the counts measured for the source and secondary star (according to the right ascension and declination co-ordinates specified in the individual source files). The pipeline then uses the counts for the source and secondary star and the literature magnitudes from the individual source files to calculate the apparent magnitude according to equation 2.2, and thus correcting for atmospheric extinction. Excluding the time taken to prepare the source input file and stack the rotor files, it takes ∼12 minutes for the code to extract information from 2500 frames.

After the photometric reduction there is the opportunity for visual/graphical inspection by the user, following which a second code performs the polarimetric reduction by identifying the 8 rotor positions according to the numbers in their filenames and calculating the degree and angle of polarisation according to equations 2.12 and 2.11. The polarimetric code was also used on standard polarimetric and non-polarimetric star frames to calculate the instrumental polarisation and depolarisation, and the zeropoint angle (K value; see Section 4.1.2).

2.4 SkyCamZ

SkyCamZ (zoomed field sky camera) is one of three piggy-back 'Small Telescopes Installed on the Liverpool Telescope'(STILT). It consists of a 1024x1024 pixel Andor camera inside an Orion Optics AG8 telescope and is fixed to the telescope top end ring. SkyCamZ parallel-points with the telescope and provides a 1 degree field of view (with 3 arcsec per pixel). When the enclosure is open, a 10 second exposure is taken once per minute by the SkyCam telescopes. The sensitivity limit for SkyCamZ is ∼18 mag (Mawson et al., 2013). In this project, SkyCamZ data were used as a replacement for Ringo2 and Ringo3 photometry in the case of sources where there was a lack of
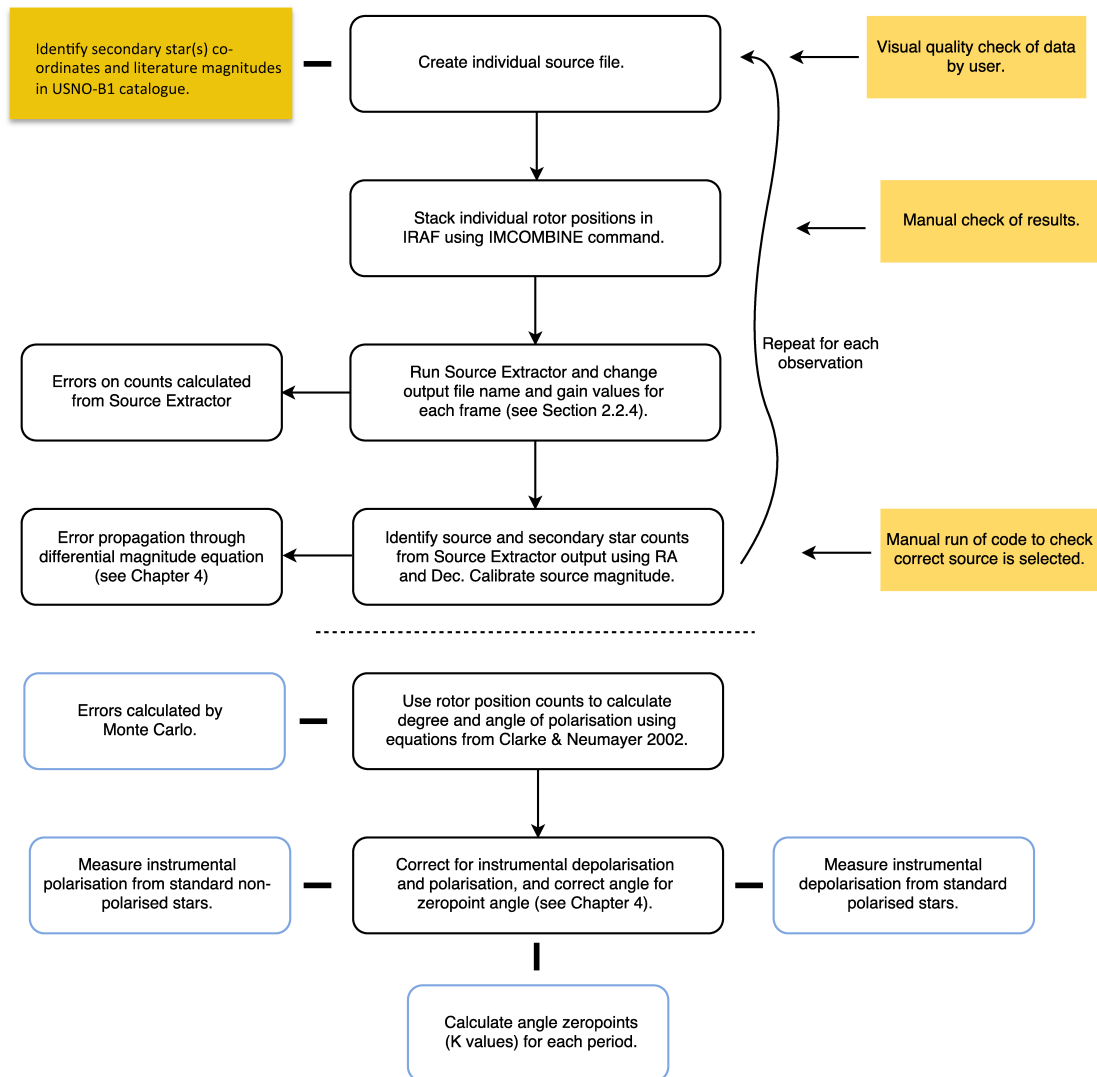
Figure 2.7: Pipeline flowchart showing the process of semi-automatically reducing the Ringo2 and Ringo3 data. Blue oblongs show processes performed using separate codes which were manually checked. The yellow shaded text shows manual operations by the user.

secondary stars in the field of view (polarimetry was still possible).

Photometry was calculated using the same pipeline as the Ringo data with a few conditions (due to the lack of rotor positions and different FITS headers). The data were manually quality checked and bad data, resulting from atmospheric and slewing effects, were rejected.

2.5   Chapter conclusions

In this chapter the telescopes and instruments used in this project were discussed, including the Fermi space telescope, KVA and the 2 metre, robotic, Liverpool Telescope (LT). The LT instruments used in this project were predominantly the Ringo2 & 3 polarimeters (from which photometry and polarimetry were taken) and the SkyCamZ piggy-back camera that sits on the telescope frame. Discussion about current and future LT instruments and their possible future applications with regards to this project are presented in Chapter 6.

Also presented were the data reduction procedures for photometric and polarimetric calibration (and error calculations), along with the pipeline created as part of the project. The next chapter will focus on the results and analysis of the blazars monitored using the RINGO2 polarimeter.

Chapter 3

The Ringo2 Catalogue of Blazars

This chapter presents results from a paper published in the Monthly Notices of the Royal Astronomical Society (MNRAS) journal (Jermak et al., 2016) and covers the analysis of the Ringo2 sample of blazars. Presented are $\sim$2000 polarimetric and $\sim$3000 photometric observations of 15 γ-ray bright blazars over a period of 936 days (11/10/2008 - 26/10/2012) using data from the Tuorla blazar monitoring program (KVA DIPOL) and Liverpool Telescope (LT) Ringo2 polarimeter (supplemented with data from SkyCamZ (LT) and Fermi-LAT γ-ray data). In 11 out of 15 sources we identified a total of 19 EVPA rotations and 95 γ-ray flaring episodes. The sources were grouped into subclasses based on their broad band spectral characteristics, and their observed optical and γ-ray properties were compared.

As described in chapter 1, due to the variability of blazars, the subclass of FSRQ/BL Lac is a loose one. The optical emission spectrum of a source has been shown to vary between the two classes depending on the activity state of the source (Ghisellini et al., 2011). For this reason, in this comparison we focused on studying the blazar subclasses according to the location of the synchrotron peak in the SED (plotted as ν f$_\nu$ against ν). With the peak being directly related to the energy distribution of the electrons within the jet, this classification allows the analysis of sources which may have different high

energy emission processes.

3.1 Observations

The polarisation monitoring program with Ringo2 was an extension of a program that ran at the Kungliga Vetenskapsakademien (KVA)-60 telescope in 2009-2011 (led by Kari Nilsson and Elina Lindfors). The KVA-60 telescope was used for optical support observations of the Major Atmospheric Gamma Imaging Cherenkov (MAGIC) telescopes (Lorenz & Martinez, 2005) and has a relatively small mirror diameter of 60 cm. The sample originally consisted of 8 γ-ray bright blazars that have optical magnitudes of R<16 and are known to show strong (>5%) polarisation: 3C 66A, S5 0716+714, OJ 287, ON 231, 3C 279, PKS 1510-089, PG 1553+113 and BL Lac. These sources have the longest polarisation light curves. When the monitoring with Ringo2 started in 2010, the sample was gradually expanded with sources with MAGIC telescope detections. See Table 3.1 for the full sample of fifteen sources, which includes Mrk 421 and Mrk 501 (long-term monitoring programs), and 1ES 1011+496, PKS 1222+216, Mrk 180 (short-term multi-wavelength campaigns and target of opportunity observations). In this work we have used the modified Julian date (MJD), which is equivalent to the Julian Date (JD) - 2400000.5.

3.2 Ringo2

Ringo2 observations of the blazar sources were obtained with a typical cadence of $\sim$3 nights whenever the source was observable from La Palma. Nightly observations of polarised and non-polarised standards from the catalogue of Schmidt et al. (1992) were also obtained. When a source was in a high γ-ray state, the schedule was adapted so that more intensive observations were made.

Name	z	Type	R Mag. range	Pol. range (%)	Fermi flux range ph cm^{-2} s^{-1}	Observation Period (MJD)	Absent data
3C 66A	≥0.3347	ISP	15.1-13.2	1.0-27.7	4.0×10^{-8}-1.1×10^{-6}	55413.17 - 56226.03	...
S5 0716+714	0.31	ISP	14.4-12.2	0.3-23.7	6.4×10^{-8}-1.3×10^{-6}	55651.86 - 56035.00	...
OJ 287	0.306	LSP	15.4-13.5	4.5-38.7	2.8×10^{-8}-1.4×10^{-6}	55641.91 - 56223.22	...
1ES 1011+496	0.212	HSP	15.6-14.7	0.8-6.8	4.2×10^{-8}- 9.7×10^{-8}	56006.93 - 56094.92	KVA (pol)
Mrk 421	0.031	HSP	13.0-12.0	0.2-8.8	1.0×10^{-7}-1.3×10^{-6}	55705.90 - 56096.89	Ringo2
Mrk 180	0.045	HSP	15.5-15.1	2.5-5.1	...	56006.89 - 56216.24	Fermi, KVA (pol)
1ES 1218+304	0.164	HSP	16.0-15.5	0.6-4.3	1.6×10^{-8}- 2.6×10^{-8}	56065.88 - 56136.90	KVA (pol)
ON 231	0.102	ISP	15.6-14.1	0.6-23.3	2.3×10^{-8}-8.6×10^{-8}	55573.26 - 56032.97	...
PKS 1222+216	0.432	LSP	15.8-14.7	0.5-9.7	8.6×10^{-8}-1.3×10^{-6}	55901.24 - 55935.16	...
3C 279	0.536	LSP	17.8-14.3	1.3-36.0	1.2×10^{-7}-2.7×10^{-6}	55575.29 - 56101.94	...
1ES 1426+428	0.129	HSP	16.3-15.7	0.4-5.2	...	56047.00 - 56171.87	Fermi, KVA(pol)
PKS 1510-089	0.36	LSP	16.6-13.1	0.5-16.5	2.6×10^{-7}-2.1×10^{-5}	55575.30 - 56062.09	...
PG 1553+113	<0.78	HSP	14.0-13.1	0.2-9.1	4.2×10^{-8}-1.0×10^{-7}	56007.13 - 56171.87	...
Mrk 501	0.034	HSP	13.3-12.5	0.8-6.6	3.9×10^{-8}-1.4×10^{-7}	55660.04 - 56136.89	KVA (pol)
BL Lac	0.069	ISP	15.0-12.7	1.2-27.3	10.0×10^{-8}-1.5×10^{-6}	55413.11 - 56225.94	...

Table 3.1: The full Ringo2 catalogue with redshift, source type, R-band magnitude range, Polarisation range, Fermi flux range, observation period information and details of absent/unavailable data (see Section 2.1.3). References for the redshift values can be found in Section 3.4.

The Ringo2 sky-subtracted target counts were measured in each image using aperture photometry. The associated error was computed by quadrature combination of the photon noise of the target, the sky noise in the aperture and error in sky determination. The photon noise was calculated according to an effective gain, that is, taking into consideration the multiple frames averaged to make a single image and the effect of multiplication noise in the electron multiplying charge coupled device (EMCCD) (Robbins & Hadwen, 2003). The sky noise takes into account the number of pixels in the aperture and the sigma-cleaned standard deviation of sky annulus pixels. The sky error was calculated according to the number of pixels in the sky annulus.

As described in chapter 2, Ringo2 produced 8 images, one for each of its Polaroid rotor positions. In order to obtain photometry measurements of these polarimetry data, the 8 rotor positions for a given observation were stacked using the IMCOMBINE (average) command in IRAF. Automated relative aperture photometry was then performed on these frames using Source Extractor (Bertin & Arnouts, 1996) and the source was identified by locating the closest lying source to the right ascension and declination values.

The reference magnitudes for the secondary stars were found in the USNO-B catalogue (Monet et al., 2003), and where they were not available, the magnitude values were

Period (MJD)	<55510	55510 - 55607	55607 - 56064	56045-56226
q	0.002357	-0.02346	-0.002434	-0.002998
u	-0.02507	-0.005321	0.030062	0.02657

Table 3.2: The mean instrumental polarisation values of Linear Stokes parameters q and u during different maintenance periods for Ringo2.

offset at overlapping time periods to match the KVA data (KVA has a larger field of view so more choice of secondary stars). The magnitude was also converted into Janskys using the standard formula shown in Section 2.1.2.

For Mrk 421 there were no usable secondary sources in the frame so magnitude calibration was not possible using the Ringo2 frames. SkyCamZ data were used instead.

To calculate the polarisation, the measured target counts in each rotor position were converted to linear Stokes parameters according to the equations in Clarke & Neumayer (2002) and then corrected for instrumental polarisation (see Table 3.2) by subtraction from the corresponding q and u value of the zero-polarised standard star (averaging over a period of time within which the polarimeter has not been removed from the telescope or altered). These corrected target counts and errors were then combined using the equations presented by Clarke & Neumayer (2002) to calculate q, u and their associated errors by standard error propagation. Analysis of the scatter in the q and u polarisation values derived from the zero-polarised standards allowed the estimation of the stability (0.25%) of the correction. This additional error was combined in quadrature to the final error estimate.

The measured value was then divided by the fractional instrumental depolarisation factor 0.76±0.01 (D. Arnold, priv. comm.) which was found by plotting the measured polarised standards against their catalogue values. The error on this value was found by comparison to an independent technique of measuring the polarised standards against catalogue values (by Kari Nilsson) which was within ±0.01.

For PKS 1510-089, we used averaged data to account for the large scatter in the data

points due to poor signal-to-noise ratio at low polarisation values. The data were averaged over 5-day bins. Within each bin, average q=Q/I and u=U/I values and corresponding root mean squared errors were computed.

3.2.1 KVA

The KVA 35 cm was used for the R-band photometric observations of the Tuorla blazar monitoring program[1]. The observations were coordinated with the MAGIC Telescope and while the monitoring observations were typically performed two to three times a week (the weather allowing), during MAGIC observations the sources were observed every night.

The polarimetric observations with DIPOL at KVA-60 were carried out by L. Takalo, A. Berdyugin, V. Kadenius, and R. Reinthal from Tuorla Observatory, University of Turku, Finland, and typically took place 1-2 times a week.

The data analysis was performed following the standard aperture photometry procedures with the semi-automatic software that was developed for monitoring purposes (software written and data reduced by K. Nilsson). See Section 2.1.2 for full details.

3.2.2 SkyCamZ

The SkyCamZ data used in this work (to populate the Mrk 421 light curve), were automatically dark subtracted, flat-fielded and fitted with a world co-ordinate system (WCS) by the STILT pipeline (Mawson et al., 2013). The data were then introduced to the same pipeline used to reduce the Ringo2 data (see Section 2.3). The pipeline runs Source Extractor on the data, and using a pre-identified secondary star (with its literature magnitude coming from the USNO-B1 catalogue), performs differential pho-

---

[1]http://users.utu.fi/kani/1m

tometry.

3.2.3 Fermi

To produce the Fermi-LAT light curves the reprocessed Pass 7 data were downloaded and analysed using the ScienceTools version v9r32p5 by T. Hovatta. In the event selection, the LAT team recommendations were followed for Pass 7 data[2]. T. Hovatta modelled a 15 degree region around each source using the instrument response function P7REP_SOURCE_V15, Galactic diffuse model gll_iem_v05_rev1, and isotropic background model iso_source_v05.

The Fermi light curves were binned by T. Hovatta using adaptive binning (Lott et al., 2012). For full details of the analysis see Section 2.1.3). The sources Mrk 180 and 1ES 1426+428 were too faint to produce adequate Fermi light curves for this analysis as the adaptive binning required for the 15% statistical flux would be too long.

3.3 Identification of Flares and Rotations

There are no exact definitions of a flare or flaring period in blazars. By eye it is possible to identify datapoints that appear to be flaring; however, producing a sample-wide condition that selects these points is difficult. Due to the varying baseline levels in blazar data, it is not possible to define a single level of quiescence above which the source is considered to be flaring. The detailed conditions of the code used to identify the peak of γ-ray flaring periods are discussed below.

It was also necessary to identify what was considered to be an EVPA rotation or swing. This is detailed in this section and follows on from definitions in other EVPA studies. A summary of the results of this analysis is presented in Table 3.3.

---

[2]http://fermi.gsfc.nasa.gov/ssc/data/analysis/documentation/Pass7REP_usage.html

3.3.1 Gamma-ray flares

A blazar flare may be associated with quasi-stationary, high density regions within the jet caused by magnetic field irregularities, or it may be associated with a knot or blob of emission moving along the jet (Bradt, 2014). The definition of a γ-ray flare is complicated due to it being relative to the (varying) baseline of the γ-ray emission at the time prior to the flare. The method used to identify flaring events was devised to be a quantitative description of the qualitative properties of the flares.

First an initial level of increased activity was established using a moving window (stepping through each datapoint individually), which defined 'active'points as those data points that were twice the standard deviation (or more) of the five preceding data points. Then for the data points that met this criterion, a further classification was made. The condition of a flare in this work was the 'active'points that were greater than five times the standard deviation of the preceding five active points. This allowed the differing sized flares to be distinguished from the baseline emission (which itself varied) in a consistent way.

In addition, due to the nature of the moving window, for the first five points in the light curve, if the flux was simply greater than the mean flux for the whole light curve then the points were classed as flaring.

Once the flare points were identified, a flare episode was defined by those flare points that were within 20 days of each other (this was an arbitrary number that suited the qualitative interpretation of the flares). These flaring episodes could often contain more than one peak; these were so close together that they were defined as one event. The flaring episodes are represented in the light curves by vertical blue lines covering all flares within the 20 day range. For the analysis in Section 3.5.2, the *centre* of this flaring episode was used.

3.3.2 Rotations of the polarisation angle

The recurrent episodes of optical electric vector position angle (EVPA) rotations that are seen from AGN jets have been interpreted in a number of ways. Usually, in this context, we are referring to large-amplitude (>90°), smooth and long-lasting rotation events which seem to signal some coherent process developing within the jet. Although random walks in the Stokes plane, driven by turbulent magnetic fields, have been demonstrated to be able to explain long rotations (Jones et al., 1985; Marscher, 2014), they cannot, for example, explain preferred rotation directions within some specific sources (which goes against the stochastic nature of the process). Nor, as shown via Monte Carlo simulations by Blinov et al. (2015), can they explain an entire population of rotations observed. Other interpretations of the EVPA rotation, which link them to coherent jet features, include (a) plasma following a helical path due to a large-scale helicoidal magnetic field configuration of the jet, resulting in long, slow rotations of the EVPA (Marscher et al., 2008, 2010; Zhang et al., 2014); (b) a bend or curvature in the jet which leads to a projection effect on the plane of the sky akin to a rotation, which can appear to invert a rotation due to relativistic effects resulting from the collimated emission (Abdo et al., 2010a).

Since the EVPA has an 180° ambiguity, long gaps in the polarisation light curves can lead to confusion when interpreting the EVPA rotations. To avoid introducing an incoherent view to the process with random 180° jumps being added to the EVPA dataset, we chose to interpret the observed EVPA light curves following a continuity hypothesis. We assumed that variations proceed in the smoothest way possible with no sudden jumps. Although there was no predefined limit to the length of gaps in the data, we used the interpretation only when the difference between consecutive data points was <30 days. In this work, an EVPA rotation is defined so that our results are consistent with those of the RoboPol group (Blinov et al., 2015). Therefore, an EVPA rotation is 'any continuous change of the EVPA curve with a total amplitude of $\Delta\theta_{max}$>90°,

which is comprised of at least four measurements with significant swings between them'.

3.4 Description of data

The flexibility of monitoring with a robotic telescope, such as the Liverpool Telescope, allows the user to increase monitoring of a particular source if its activity is deemed interesting. The main sample of blazars was added to over the period of the Ringo2 observations according to reported flaring, and thus some sources have more seasons and more data than others. The multi-wavelength light curves of the individual sources in this sample can be found at the end of this chapter.

3.4.1 3C 66A

3C 66A is a well-known BL Lac at redshift z$\geq$0.3347 (Furniss et al., 2013). The blazar is a bright source of HE (Acciari et al. 2009) and VHE γ-rays (E >100 GeV) (Aliu et al., 2009; Acciari et al., 2009a). There have been many polarimetric monitoring observations of this source (Takalo & Sillanpaa, 1993). In previous observations the polarisation degree was always high, typically between 10 - 20 % with a maximum measured value of 33 %. In the historical data, the EVPA was significantly variable but showed a preferred position angle around 20 - 40°, which is perpendicular to the direction of the VLBA jet. Ikejiri et al. (2011) and Itoh et al. (2013) also reported a rotation of EVPA of >180° (at MJD$\sim$54840, early January 2014) and a significant negative correlation of the flux and polarisation degree. Itoh et al. (2013) separated their $\sim$2 years worth of data into four sections according to the optical magnitude and polarisation degree. Our program did not cover their first and second periods.

During the first season, our polarisation data showed similar behaviour to that in Itoh

et al. (2013). In the period spanning August to November 2009 (MJD 55048-55150) we saw a ∼180° rotation of the EVPA. During November 2009 to January 2010 (MJD 55151 to 55220) our data appeared to show another 180° rotation (see Table 3.3 and Figure 3.12). The nature of the ±180° ambiguity and the smooth rotation selection of the EVPA data means that the absence of even one data point can be the difference between a rotation (our data) or a slight peak (Itoh et al., 2013). However, when we combined our data with that of Itoh (priv. comm.), the combined data suggested that there was a rotation. Itoh et al. (2013) described a polarisation degree which was systematically different among the four periods due to a long-term slow change. We see this behaviour in our data beyond their fourth period. The source entered a relatively quiescent phase after late July 2010 (MJD∼55400) and in the remaining three epochs the EVPA did not appear to rotate. The optical magnitude increased to ∼14.5 in the R-band and the γ-ray flux stayed low with the exception of a small flare at MJD∼56150 (August 2012).

3.4.2   S5 0716+714

The BL Lac object S5 0716+714 has been studied intensively at all frequencies. It has no spectroscopic redshift but constraints from intervening absorption systems gives a lower limit of z<0.2315 and an upper limit of z≥0.322 (95% confidence level). The upper limit was constrained from the truncation of a predicted Lyman α emitters distribution (Danforth et al., 2013). A host galaxy detection measurement gave z=0.31±0.08 (Nilsson et al., 2008). S5 0716+714 is a bright source of HE (Acciari et al., 2009a) and VHE (Anderhub et al., 2009) γ-rays. The source is thought to be observed very close to the line of sight of the jet, allowing an excellent view down the jet itself (Impey et al., 2000). There have been several dedicated studies of the optical polarisation behaviour of the source (Uemura et al., 2010). In the optical band the source showed extremely fast brightness and degree of polarisation variations. Intra-night variability

of the polarisation has been reported by Impey et al. (2000) and Villforth et al. (2009) with significant variations on timescales of 10-15 minutes. In our data we also saw fast brightness and degree of polarisation variations across the four seasons with a variation of $\sim$2 magnitudes in the optical and a range in degree of polarisation of 0-17%.

Typically the source has shown no correlation between optical brightness and polarisation degree (Ikejiri et al., 2011) and in this work we too found no evidence of a correlation with ρ= -0.0754 and p = 0.759 (see Table 3.6 on Page 98). S5 0716+714 also showed no apparent long-term trends and therefore it has been suggested that at all epochs there must be a number of polarisation components showing variations on a small timescale. The literature also reports rapid (6 days) (Larionov et al., 2008a) and slow (400 days) rotations of the EVPA of $>$300° (Ikejiri et al., 2011). In the historical data the range of the degree of polarisation is $\sim$0-25%. The interpretation of the $\pm$180° ambiguity in our data indicated that the EVPA may have undergone a rapid rotation of $\sim$180° in March 2009 (MJD$\sim$54900), a long slow rotation of $\gtrsim$200° in October 2010 (MJD$\sim$55550) and/or a rapid rotation of $\sim$200° in March 2012 (MJD$\sim$56000). A rotation which changes direction mid rotation, such as the rotation in March 2012 (MJD$\sim$56000), may be due to a knot of material crossing the observer's line of sight (Aleksić et al., 2014c). However, this behaviour may also be due to a random walk of the EVPA. The γ-ray and optical data showed correlations in late 2009 and early 2011 (see Section 3.5 for more details).

3.4.3 OJ 287

OJ 287 (z=0.305) is a BL Lac object and one of the most famous blazars as it hosts a supermassive *binary* black hole system at its centre (Sillanpaa et al., 1988). It is bright in HE γ-rays (Acciari et al., 2009a) but has not been detected in VHE γ-rays (Seta et al., 2009a). The dedicated studies of the optical polarisation behaviour (D'arcangelo et al., 2009; Villforth et al., 2010; Uemura et al., 2010) have shown that there is a

strong preferred position angle for the polarisation which is perpendicular to the flow of the jet. The observed polarisation is frequently high (maximum 35%). Occasionally the EVPA also shows rapid rotations with durations of 10-25 days. This behaviour has been interpreted as a signature of two components (Holmes et al., 1984; Villforth et al., 2010), stationary polarisation core and chaotic jet emission. Occasionally, flares with a negative correlation between flux and polarisation degree have been observed (Ikejiri et al., 2011).

Our data cover the period observed by Agudo et al. (2011) and we saw similar behaviour of the polarisation properties, particularly the rotation in April 2009 (MJD$\sim$54940) which displayed peculiar reverse-rotation behaviour which may be attributable to scatter.

With the exception of the rotation in April 2009, the EVPA remained relatively stable throughout the next three observing seasons. The degree of polarisation was high in the first and fourth seasons but dropped from $\sim$30% to <5% during the second season following a γ-ray flare. The optical magnitude was variable and ranged between 13.5 and 15.5 magnitudes.

3.4.4   1ES 1011+496

1ES 1011+496 has a redshift of z=0.212 (Albert et al., 2007b). It is a BL Lac object and until its discovery in VHE γ-rays (Albert et al., 2007a), was little studied. It is bright in HE γ-rays (Acciari et al., 2009a) and has little optical polarisation literature data. One archival polarisation observation from 1987 showed low polarisation $\sim$2% and an EVPA $\sim$86° (Wills et al., 2011). The KVA and Ringo2 data presented here were taken for multi-wavelength campaigns (Ahnen et al., 2016a,b), and showed similar results to the archival observations: low polarisation of <10% and an EVPA at $\sim$110°.

3.4.5 Mrk 421

Mrk 421 has a redshift of z=0.03 (de Vaucouleurs et al., 1991). It is a nearby BL Lac object that was the first extragalactic VHE γ-ray emitter to be discovered (Punch et al., 1992). Its optical polarisation behaviour has been studied extensively in the past (Hagen-Torn et al., 1983; Tosti et al., 1998b). In these data, for the majority of the time, the source showed rather low polarisation <5% and a rather stable EVPA of ~180°. Ikejiri et al. (2011) found an overall significant correlation between optical brightness and degree of polarisation and during a large optical flare in the winter of 1996-1997 (MJD~50350 onwards) the optical degree of polarisation rose to 12% (Tosti et al., 1998b). Tosti et al. (1998b) reported a rotation of the position angle of ~90° from May to October 1995 (MJD~49838-49991).

The data collected with the KVA and Ringo2 from 2008-2011 (MJD 55409-56226) agreed with this general behaviour, however from the beginning of 2012 (MJD~55900 onwards) the data showed a strong increase in polarisation degree and a 360° rotation of the position angle, along with a steady increase in the optical magnitude. This behaviour preceded an unprecedentedly large γ-ray flare which occurred after June 2012 (MJD~56100) and unfortunately was not accompanied by optical data due to the source's visibility.

3.4.6 Mrk 180

The BL Lac object, Mrk 180, has a redshift of z=0.045 (Falco et al., 1999). It was detected in VHE γ-rays in 2006 (MJD~53795) (Albert et al., 2006b). The source has a bright host galaxy and is little studied in optical polarimetry. Marcha et al. (1996) presented an optical degree of polarisation measurement of 2.4% which was consistent with the results we saw from early 2012 (MJD~56000) when our observations began. The Ringo2 data were taken as part of a multi-wavelength campaign which was started

in 2008 (MJD∼54500) (Rügamer et al., 2011). We have few data points for the Ringo2 period of observation, polarimetry from the KVA was unavailable, as were Fermi flux data. Our monitoring continues with the third generation polarimeter RINGO3 (Arnold et al., 2012). We found a stable EVPA of ∼40 ° and an R-band magnitude of ∼14.4.

3.4.7   1ES 1218+304

1ES 1218+304 is a BL Lac source at z=0.162 (Adelman-McCarthy & et al., 2009). It is a source of HE and VHE (Albert et al., 2006a) γ-rays. The optical magnitude has varied over the last ∼10 years from 15.2-16.4 magnitudes in the R-band (from Tuorla blazar monitoring campaign[1]). There are very few polarisation measurements in the literature, Jannuzi et al. (1994) reported a degree of polarisation of ∼5%. We present KVA (photometry only) and Ringo2 (polarimetry and photometry) data from March 2012 (MJD∼55987) until the end of the program. The source did not show any flares or rotations.

3.4.8   ON 231

ON 231, also commonly known as W Comae, has a redshift of z=0.102 (Weistrop et al., 1985). It is a HE and VHE γ-ray bright BL Lac object (Acciari et al., 2008, 2009a). Observations taken in 1981-1982 (MJD∼45000) and 1991-1992 (MJD∼48500) cover similar ranges, with a polarisation degree ranging from 5.2-19.2% and an EVPA of 50.0-93.3° (Wills et al., 2011). The source underwent three major outbursts in March 1995 (MJD∼49800), February 1996 (MJD∼50120) and January 1997 (MJD∼50450) (Tosti et al., 1998a) and a more energetic outburst in June 1998 (MJD∼50800-51000) which saw the brightness increase by ∼3 magnitudes in the R-band (Tosti et al., 1999). Ikejiri et al. (2011) observed this source from 2008-2010 and during this period the polarisation was 3.5-19.6% with an EVPA of 60-80°. They also found a significant

negative correlation between flux and polarisation degree. This can be seen in Figure 28 of Ikejiri et al. (2011). Sorcia et al. (2014) presented results from February 2008 to May 2013 and found a gradual decrease in mean flux over the ∼5 year period of ∼3 mJy. They found a maximum degree of polarisation of 33.8% ± 1.6% and a large rotation of the EVPA of ∼237° which coincided with a γ-ray flare in June 2008.

The KVA-60 and Ringo2 data in this work showed a degree of polarisation and EVPA consistent with the source in a low state. We saw slightly brighter optical and γ-ray fluxes in the first season (see Figure 3.19 in the Appendix) and the optical magnitude became less bright with the increase in degree of polarisation at the end of our last observing season.

3.4.9   PKS 1222+216

PKS 1222+216 has a redshift of z=0.435 (Veron-Cetty & Veron, 2006). It is a flat spectrum radio quasar (FSRQ), which has received a lot of attention since its discovery in VHE γ-rays (Aleksić et al., 2011a). Very few optical polarisation data are available in the literature. A single measurement from (Ikejiri et al., 2011) showed a degree of polarisation of 5.9%. The data presented here were taken in the 2011-2012 (MJD∼55600-56100) observing season when the source was in a quiescent state in optical magnitude and γ-rays. The EVPA showed very little variation and the degree of polarisation was low (<10%).

3.4.10   3C 279

3C 279, with a redshift of z=0.536 (Burbidge & Rosenberg, 1965), was one of the first extragalactic γ-ray sources discovered (Hartman et al., 1992) and was one of the first flat spectrum radio quasars to be detected in very high energy γ-rays (Albert et al., 2008). Over ∼10 years of observations its brightness has been in the range of 13-16

magnitudes in the R-band. In the space of ∼100 days, the source became fainter by 3 magnitudes and from MJD 54120-54200 showed a rotation which was intrinsic to the jet (Larionov et al., 2008b). This rotation was coincident with a low degree of polarisation which was higher before and after the rotation (at 23%). The low polarisation during the rotation was attributed by Larionov et al. (2008b) to the symmetry of the toroidal component of the helical magnetic field. In the period prior to the the start of the Ringo2 program, the source showed a rapid decline in brightness over the period of ∼1 month. This was synchronous with an increase in polarisation degree and a $180°$ rotation of the position angle (Abdo et al., 2010a). Kiehlmann et al. (2013), using data from Ringo2 and KVA-60 amongst other instruments, showed there was an increase in flux and degree of polarisation along with a ∼$150°$ rotation of the position angle in May 2011 (MJD∼55700). The addition of Fermi data showed that during this period of ∼2 months, the γ-ray flux decreased by ∼100 [10^{-8} ph cm^{-2} s^{-1}] (Aleksić et al., 2014c). This optical outburst with a rotation of the position angle and the increase in the degree of polarisation was interpreted as geometric and relativistic aberration effects. For example an emission knot's trajectory bending such that it crosses the observer's line of sight (Aleksić et al., 2014c).

We have three seasons of polarimetric data and four seasons of photometric data for this source. Having the same data as Kiehlmann et al. (2013), we saw the same behaviour. In the third and fourth seasons we saw rotations that rotate in one direction and then back on themselves. We saw an additional rotation which was followed by a lack of data. The source dropped in brightness at the start of the observing period and was at its highest in polarisation (∼40%). The source was brightest in the optical in the last two seasons of observations, with the degree of polarisation dropping to lower values.

3.4.11   1ES1426+428

1ES1426+428 is a lesser-studied BL Lac object at a redshift of z= 0.132 (Urry, 2000). It is classified as an extreme high-energy-peaked BL Lac object (HSP) (Costamante et al., 2001) and is a HE γ-ray source (Petry et al., 2000; Horan et al., 2002). Jannuzi et al. (1994) reported an optical degree of polarisation of <7 % over the period of 1988-1990 (MJD$\sim$47161 - 47892) and a non-constant EVPA which may show a slow rotation of $\sim$150°. The optical magnitude maintained a fairly constant value of $\sim$16-17 in the R-band. We found the degree of polarisation stayed below $\sim$6%, while the optical magnitude was constant with a median R-band magnitude of 15.6. The EVPA stayed relatively constant within the error bars. The source was too faint in γ-rays to be significantly detected within the analysed time window.

3.4.12   PKS 1510-089

PKS 1510-089 is a γ-ray bright (Acciari et al., 2009a) FSRQ/LSP at z=0.36 (Burbidge & Kinman, 1966). The source has shown bright flares in optical, radio, x-ray and HE γ-rays at the beginning of 2009 (MJD$\sim$54910-54920), along with the first detection of VHE γ-rays (Abramowski et al., 2013). During the γ-ray flaring from MJD 54950 - MJD 55000 (April 2009 onwards) the EVPA was reported to rotate by >720° and during the major optical flare the optical polarisation degree increased to <30% (Marscher et al., 2010). In early 2012 (MJD 55960 and onwards) it again showed high activity in HE γ-rays and was also detected in VHE γ-rays. Again there was a >180° rotation of the EVPA following this flare but the polarisation degree stayed low $\sim$2% (Aleksić et al., 2014b).

The polarimetric Ringo2 data we present for this source have been averaged over 5-day bins to account for the poor signal-to-noise in the data (see Section 3.2). Our data showed the above-mentioned γ-ray and optical flaring activity from the end of 2008
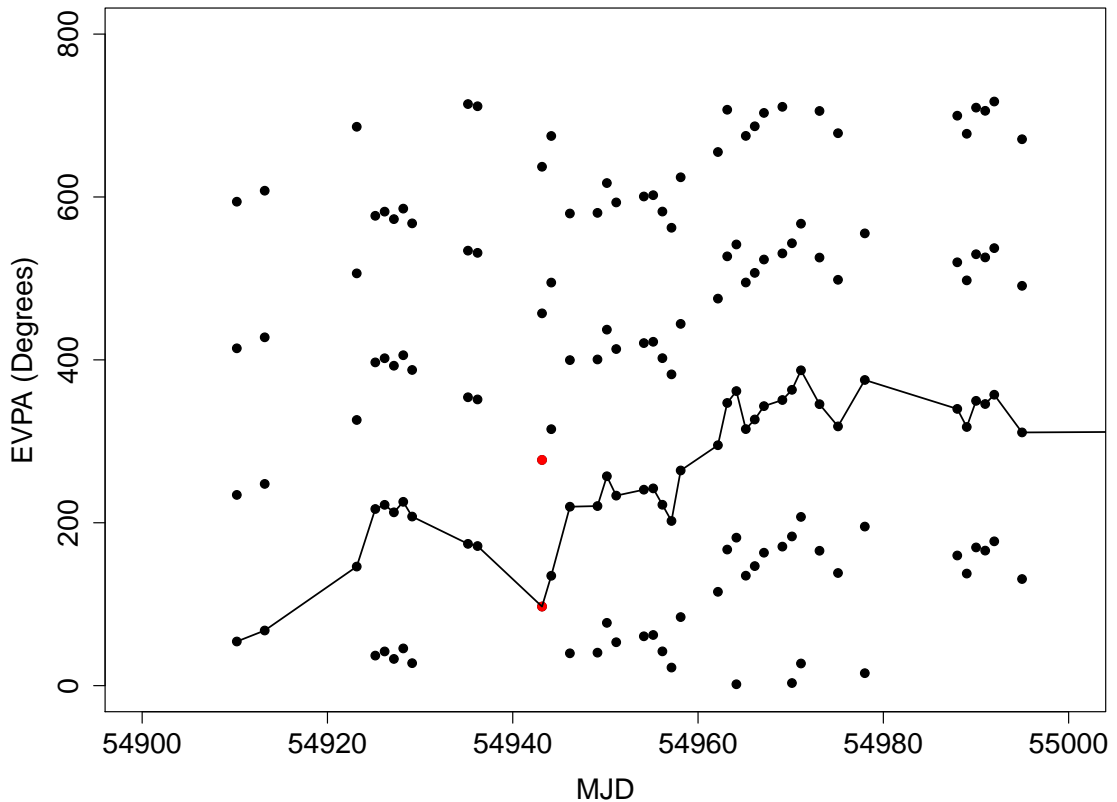
Figure 3.1: Zoomed view of PKS 1510-089 EVPA plotted against MJD (full data plot shown in Appendix, Figure 3.23). The EVPA data are plotted ±180 degrees from the measured value to show the ambiguity of the measurements. This plot can be compared with Figure 4 in Marscher et al. (2010) where the polarisation angle data were interpreted as showing a 720° rotation. Here we report a rotation of less than half that (333°) and this is due to the interpretation of this particular dataset by the EVPA trace code which, to account for the ±180, ambiguity identifies the next nearest lying point. The points in red highlight where the difference in identification originates.

into 2009. We saw a EVPA rotation at this time, but due to the interpretation of our data using the EVPA tracing code (see Section 3.3.2), our rotation (333°) is not as great as the 720° rotation reported by Marscher et al. (2010). The difference was due to the data sampling and as such highlights the need for intensive optical monitoring during γ-ray activity. For clarity we include a zoomed region of Figure 3.23 (see Figure 3.1) for comparison with the bottom panel of Figure 4 in Marscher et al. (2010). The red points show the EVPA data point as it was measured, and at the +180 position. The EVPA trace code in this work selected the lower of the two points, as it was closer to the previous point. Had there been intermediate points, the rotation might have shown to continue at a steeper gradient which would result in a ~600° rotation measurement.

Ikejiri et al. (2011) reported a correlation between V-band magnitude and degree of polarisation. We saw similar results in our analysis (see Table 3.6), however, because we lack data when the R-band magnitude was the brightest, we were unable to populate the brighter end of the magnitude-degree of polarisation plot.

3.4.13   PG 1553+113

PG 1553+113 is a γ-ray bright BL Lac object at z>0.395 (Danforth et al., 2010). It is a persistent source of VHE γ-rays (Albert et al., 2007a; Aharonian et al., 2006) which has triggered several multi-wavelength studies of the source (Aleksić et al., 2010). However, only few campaigns have included polarimetric observations. Polarisation observations were reported in Albert et al. (2007a), Andruchow et al. (2011) and Ikejiri et al. (2011) with the maximum value for polarisation degree of 8.2%. The observations of Ikejiri et al. (2011), which covered the longest period of time, did not show a clear preferred angle for the EVPA. In 2008 (MJD~54600 onwards) the EVPA was ~100-150°, while the later observations (in 2009 and 2010; MJD~55100 and 55200) only single data points show an EVPA ~50°. Ringo2 and KVA-60 data suffered from poor sampling but agreed with the literature showing an EVPA which was ~100-150° until March 2012 when there was a rotation over a period of a few months which coincided with a flare detected in HESS and MAGIC but not in Fermi (Abramowski et al., 2015a; Aleksić et al., 2015).

3.4.14   Mrk 501

Mrk 501 has a redshift of z=0.0337 (Ulrich et al., 1975). It is a BL Lac type source, which was discovered as a VHE γ-ray source in 1996 (Quinn et al., 1996) and above 1.5 TeV (Bradbury et al., 1997). The source was observed during a period of high activity in 1997 (MJD~50449) with a degree of polarisation of 1-3% (Joshi et al.,

2000) and R-band magnitude ∼13.5 (Petry et al., 2000). The source showed a VHE flare in 2009 (MJD∼54940) which was correlated with a 5% increase in the optical degree of polarisation, a significant increase compared to the typical polarisation level of 1-3% (Barres de Almeida, 2011). Along with the increase in degree of polarisation, the EVPA rotated by 15°. In our data we saw no rotations of the EVPA (see definition of EVPA rotation in Section 3.3.2) and a very stable optical magnitude, the degree of polarisation reached ∼6% which could be correlated with a small γ-ray flare, however, for the larger γ-ray flare the source was not visible from La Palma at night.

3.4.15   BL Lac

BL Lac has a redshift of z=0.069 (Vermeulen et al., 1995). It is a bright source of HE γ-rays and occasionally of VHE γ-rays (Albert et al., 2007b; Arlen et al., 2013). Its polarisation has been extensively studied with the two long-term studies presented in Hagen-Thorn et al. (2002b) and Hagen-Thorn et al. (2002a). In these publications observations from 1969 to 1991 (MJD∼40000-48500) were presented. It was found that the EVPA showed a preferred angle of ∼22° which is close to the direction of the jet in very long baseline interferometry (VLBI). In the second half of their data (1980-1991, MJD∼44239-48500) BL Lac showed significant periodicity of 308 days both in total flux and relative Stokes parameter q (Hagen-Thorn et al., 2002b). The polarisation degree for this 22 year period varied from <1% to ∼40%.

In October 2005 (MJD∼53660) the source underwent a double peaked optical outburst with rapid rotation of the EVPA during the first outburst, which led Marscher et al. (2008) to conclude that the rotation took place in the collimation and acceleration zone of the jet where a helical magnetic field would be present. In June 2011 (MJD∼55710) a rapid TeV flare was detected which coincided with a rapid change in optical polarisation angle (Arlen et al., 2013). This was concluded to support the model of Marscher et al. (2008). Raiteri et al. (2013) whose data coincided with that

of this work, reported an EVPA of $\sim15°$ which is nearly aligned with the radio core EVPA and mean jet direction.

Our EVPA tracing code (see Section 3.3.2) identified four polarisation angle rotations in the BL Lac data, however, only two of these could be classified as 'true' rotations according to the condition that the rotation must consist of 4 or more measurements with significant swings between them. The degree of polarisation varied between values of $\sim25\%$ and little or no polarisation signal at all. The drop to a degree of polarisation of ~0 coincided with a EVPA rotation and a γ-ray flare, along with brightening in optical magnitudes, and was consistent with previously reported behaviour.

3.5   Discussion

In this section comparisons are made between the polarisation properties, optical magnitude and γ-ray flux for those sources with reasonable sampling. This small sample is subject to selection biases (i.e. all the sources in this sample are γ-ray loud and have been observed by MAGIC exhibiting flaring periods) and therefore the results in this work cannot be generalised to the larger blazar population (which may not have undergone recent flaring, or are γ-ray quiet).

For those sources which have been observed only for a short period of time, which have sparse data sampling or lack sufficient multi-wavelength information (Mrk 180, 1ES 1011+496, 1ES 1426+496 and 1ES 1218+304), only optical-optical analysis and their light curves are presented and they are excluded from the γ-ray analysis. We will explore correlations between the optical data and the γ-ray flux, along with the frequency of flares in relation to optical polarisation rotations.

1. Source	2. Rot ↑ (anti-c-wise)	3. Rot ↓ (c-wise)	4. Flares	5. Type	6. Fermi mon. period (days)	7. Max. deg.	8. Flare rate flares/day (year)	9. Days between rot & flare	10. Flares during rot
3C 66A	1	0	10	ISP	1323	27.7	0.0076 (2.76)	20	0
S5 0716+714	2	2	16	ISP	1442	17.9	0.011 (4.05)	-14, 0 (x3)	3
OJ 287	1	0	3	LSP	1382	36.9	0.0022 (0.79)	...	...
Mrk 421	0	1	3	HSP	541	8.3	0.0055 (2.03)	1	0
ON231	0	0	5	ISP	1593	23.3	0.0031 (1.15)	...	...
PKS 1222+216	0	0	5	LSP (FSRQ)	530	5.4	0.0094 (3.45)	...	...
3C 279	3	1	11	LSP (FSRQ)	1464	29.7	0.0075(2.74)	8, -2, 0	1
PKS 1510-089	3	1	24	LSP (FSRQ)	1406	16.4	0.017 (6.23)	-4, 21, 39, -84, 0 (x10)	10
PG 1553+113	1	1	5	HSP	1241	9.1	0.0040 (1.47)	0	1
Mrk 501	0	0	4	HSP	594	6	0.0067 (2.46)	...	...
BL Lac	2	0	9	ISP	1431	27.3	0.0063 (2.30)	116, -21, 0, 98	1

Table 3.3: Tabulated data of the upward and downward EVPA rotations and γ-ray flares for different blazar subclasses for the 11 sources that have EVPA rotation/γ-ray flare events. Also included are the length of the Fermi monitoring period in days, the maximum degree of polarisation, the flare rate (and mean flare rate), days between rotations and flares (and mean of this value) and number of flares during a rotation.

3.5.1 Correlation analysis

Correlations between the optical photometric and polarimetric data and γ-ray data can be used to explore the emission regions within the different blazars and the magnetic field within the jet. For example, correlations between optical magnitude and γ-ray flux can show whether the emission is from similar or very nearby regions, or whether the emission comes from separate parts of the jet (or even outside the jet). It can probe the origin of inverse Compton seed photons and thus constrain emission models.

Correlations between the γ-ray flux or optical magnitude, and optical degree of polarisation, can explore the overall magnetic field structure of the jet. If there is a large-scale ordered magnetic field in the jet, there would be a correlation between the γ-ray or optical photometric data and the degree of polarisation. This is because, in Leptonic models, the synchrotron electrons upscatter seed photons to create γ-ray emission. If these seed photons are also highly polarised (from a large scale magnetic field) they would be correlated with the γ-ray (and optical) emission.

Due to observational constraints from ground-based telescopes, along with weather and observing priorities, we have imperfectly sampled optical data. While it was possible that the continuous Fermi γ-ray data could be binned to coincide with optical monitoring, this could not be done with the adaptive binning code used in this work as

it automatically sets the bin sizes according to the γ-ray brightness of the source (see Section 2.1.3). The binning of γ-ray data according to optical observations was likely to dilute flaring behaviour (which was displayed in more detail with the adaptive binning method) and also involved difficulties in establishing bin sizes because the optical observations only took $\sim$1-5 minutes.

In order to match the optical and γ-ray data points (which were of course not completely synchronous) we explored two methods. In method one we used each of the dates associated with optical observations and interpolated a value from the γ-ray light curve for this date by fitting a gradient to the nearest neighbouring γ-ray points and calculating the matched γ-ray flux using the equation for a straight line. The plots in Figure 3.2 were produced by such a method and show the overall behaviour of the sources according to their different subclasses.

It was also possible to match the optical and γ-ray data by using the same bins as the γ-ray data to bin the optical data. This method produced correlation plots (see Figure 3.3) which were less dense than those produced by leading with optical data sampling (compare with Figure 3.2). Binning of optical data in this way resulted in higher temporal frequency optical activity being averaged out. As the focus of this work was the optical data, we used the first method of matching the optical and γ-ray data points. The same method was applied using the optical polarisation degree data. When data on one axis did not vary over a period, and data on the other axis did, these periods appear on the correlation plots as straight horizontal or vertical lines.

We used the Spearman Rank Coefficient test to determine whether there were correlations between the data. The null hypothesis states that the two variables are not correlated and if $p < 0.05$ (i.e. $<2\sigma$), the null hypothesis can be rejected. For the analysis that involved magnitudes, the values of the correlation coefficient ρ were calculated so that the reverse nature of the parameter was appropriately used.

For exploring the distributions of Spearman Rank test results, we used the Kolmogorov Smirnoff (KS) test where the null hypothesis is that the two samples were drawn from the same population. The two-sample KS test quantifies the distance between the distribution functions of the two samples. If $p \leq 0.05$, then the null hypothesis can be rejected and the distributions are considered to be from different parent distributions. If $p > 0.05$ then there is no evidence for different distributions.

Optical and γ-ray flux correlations

To probe the possibility that photons of different wavelengths may be emitted from the same region of the jet, we explored the correlations between the optical magnitudes (apparent and absolute) and γ-ray flux. Figure 3.2 shows 6 plots of γ-ray flux against optical magnitude for all sources and 5 different subclasses; BL Lacs and FSRQs (identified according to the presence/strength of optical emission lines) and HSP, ISP and LSP sources (classified according to the location of the synchrotron peak in their SEDs). In the plot of all sources there appear to be two subclasses (see Figure 3.2), both with positive correlations but different ranges in optical and γ-ray fluxes. These two subclasses are shown to correspond to FSRQ and BL Lac sources in the next two panels. BL Lacs and FSRQs sources show differences in the strength of their optical emission lines, and *appear* to cover different ranges in γ-ray flux and optical magnitude.

The bottom 3 plots in Figure 3.2 show that when the sources are split by the location of their synchrotron peak, they also *appear* to cover different ranges in γ-ray and optical magnitude. LSP sources appear to have the brightest γ-ray fluxes and the maximum γ-ray flux appears to decrease as the spectral peak moves toward higher frequencies. The HSP sources in this sample have a much lower range in γ-ray fluxes than LSPs.

To further explore the different ranges in optical magnitude, Figure 3.5.1 shows the

	ρ	p	N
All	-0.153	$6.4\text{x}10^{-14}$	13
FSRQ	0.149	$7.3\text{x}10^{-4}$	3
BL Lac	0.395	$<2.2\text{x}10^{-16}$	10
LSP	-0.539	$<2.2\text{x}10^{-16}$	4
ISP	0.578	$<2.2\text{x}10^{-16}$	4
HSP	0.597	$<2.2\text{x}10^{-16}$	5

Table 3.4: Spearman rank correlation coefficient ρ, p value and number of sources for each blazar subclass for the γ-ray and optical magnitude correlations (See Figure 3.2 for plots).

same plot again but instead with *absolute* magnitude values. The absolute magnitude (M) was calculated from the apparent magnitude (m) and luminosity distance in parsecs (d_l)

$$M = m - 5(\log_{10} d_l - 1). \tag{3.1}$$

The luminosity distance was calculated using the comoving distance (d_m) as

$$d_l = (1 + z)d_m \tag{3.2}$$

where the comoving distance (d_m) was calculated using a cosmologial calculator[3], with the redshift of the source, Ω_0=0.3036 and H$_0$=68.14 km/s/Mpc. Since the redshifts are all fairly small ($\lesssim$1), the SEDs time-variable, and the wavelength ranges wide, we treated the fluxes as pseudo-bolometric and therefore did not apply any K-correction.

The γ-ray data in Figure 3.5.1 have been corrected for distance, according to the inverse square law, by dividing by the luminosity distance (d_l, as described above) squared. The different subclasses showed no clear trends in distance corrected γ-ray or optical absolute magnitude.

As the absolute magnitude and γ-ray distance corrections were simple logarithmic

---

[3]http://home.fnal.gov/g̃nedin/cc/

shifts applied to all the data, these do not change the correlation properties, so while the distance corrected properties are presented and explored for visual differences, correlation analysis was performed using the apparent magnitude and non-distance corrected γ-ray fluxes.

In Table 3.4 the results of the Spearman Rank analysis of these data are presented. We have considered the properties of each source (which are differently coloured in the figure) individually. In addition, in order to investigate the properties of the individual sources, the data were first separated into observing seasons to avoid false periods of apparently stable behaviour introduced by long periods of non-visibility (Itoh et al., 2013). The number of seasons for each sources depended on the availability of the optical data and vary from 1 to 4 seasons.

For each of the season datasets, a Spearman Rank Coefficient test was performed to identify and test the statistical relationship between one property (i.e. magnitude, γ-ray flux, degree of polarisation) against another. A summary of these results, along with those for other correlations, are presented in Table 3.5. The range of correlations for each of the sources within the different subclasses are presented for all probabilities, and for those that were considered significant (i.e. p$\leq$0.05).

Results for individual source seasons can be found in Table 3.6 in the Appendix. 68% of source seasons (25/37) showed a positive a correlation ($\bar{\rho} = 0.46$) with significant p values (i.e. p$\leq$0.05). Overall, 92% of source seasons (34/37) showed positive correlations ($\bar{\rho} = 0.36$) with significant and non-significant p values ranging between 0.000 - 0.988.

A KS test was performed on the HSP & ISP, ISP & LSP and HSP & LSP sources respectively to test whether the distribution of the Spearman Rank Coefficient ρ values for different blazar subclasses suggests that the subclasses originate from the same parent population. The mean of the distributions for each subclass were $\bar{\rho} = 0.30, 0.43$
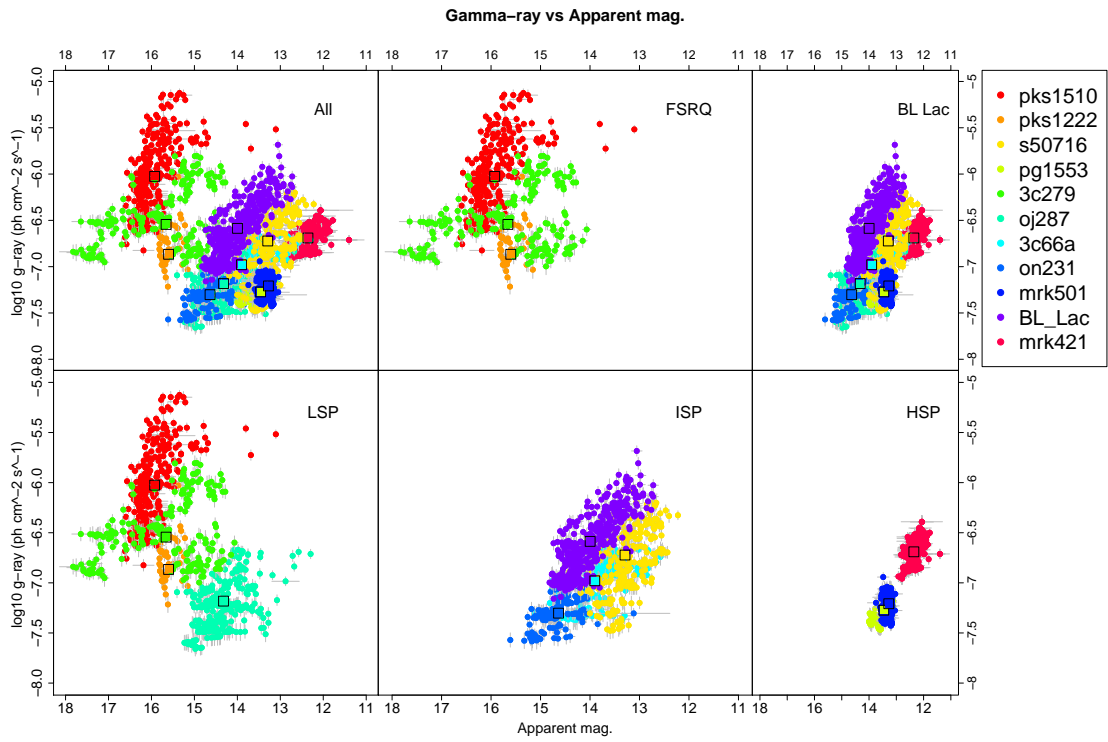
Figure 3.2: Fermi γ-ray data plotted against apparent magnitude for 11/15 sources (those which have >5 γ-ray datapoints) (each with a separate colour) and subsequent blazar subclasses: FSRQs, BL Lacs, LSPs, ISPs and HSPs. The γ-ray data points are interpolated to match the date of the optical data points (see Section 3.5.1). Black squares show the mean γ-ray and optical value for each source.
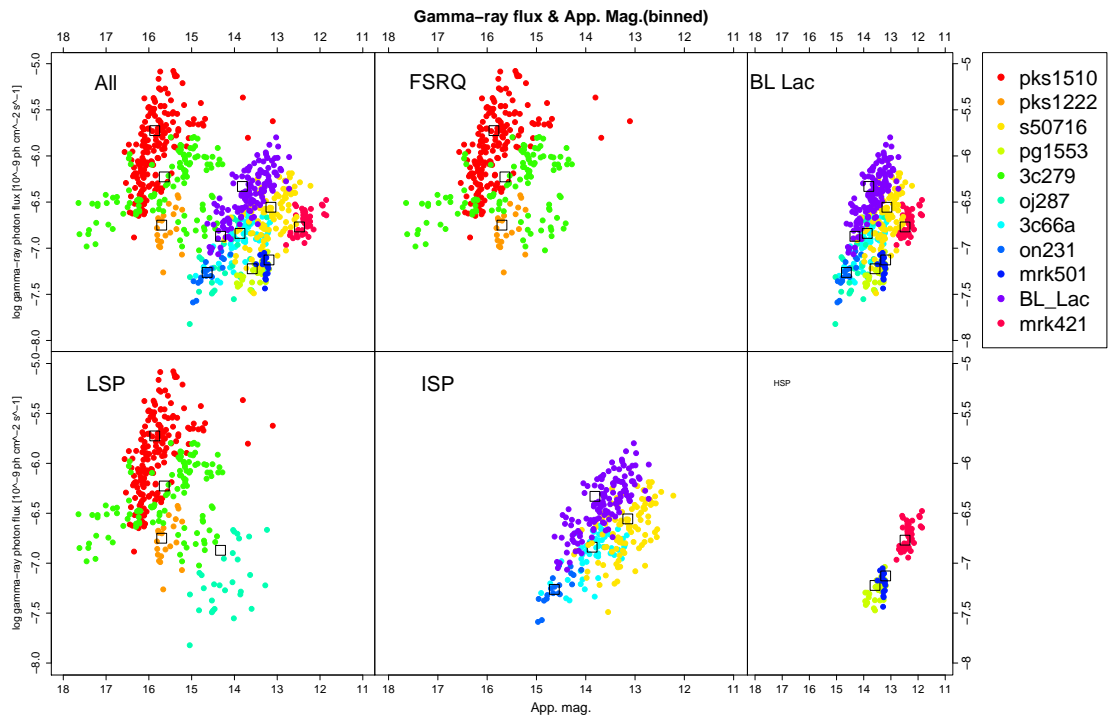
Figure 3.3: The same plots as Figure 3.2 with optical apparent magnitude data points binned according to the range of the Fermi bins. There are fewer data but the overall trends are similar.
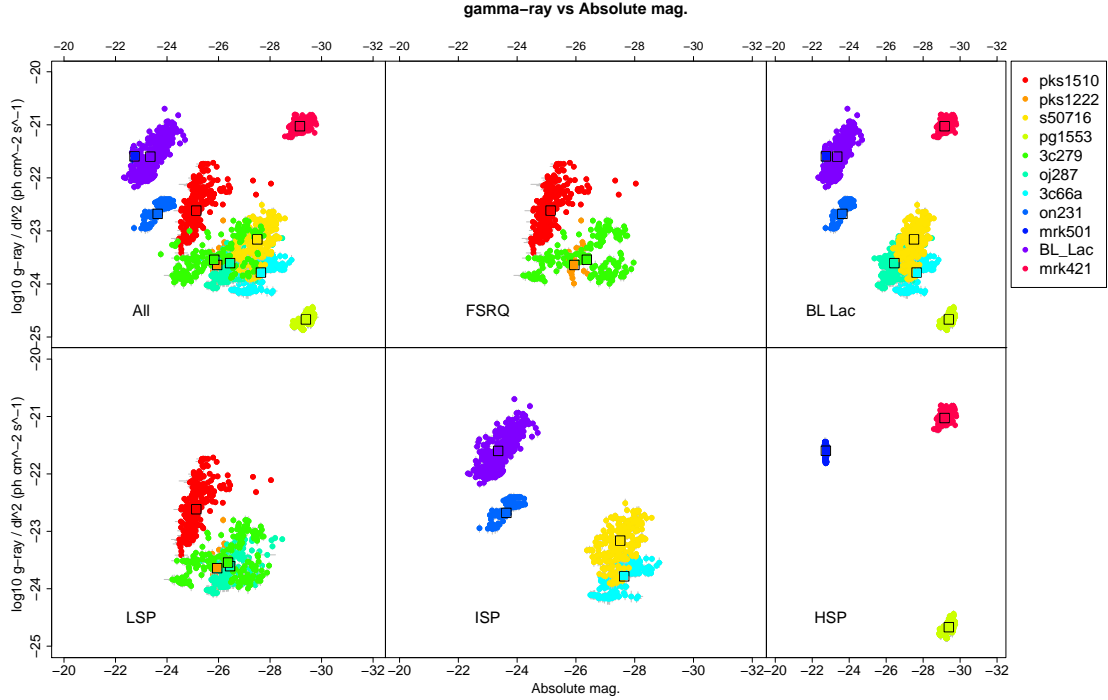
Figure 3.4: Distance-corrected Fermi γ-ray data plotted against absolute magnitude for 11/15 sources (those which have >5 γ-ray datapoints) (each with a separate colour) and subsequent blazar subclasses: FSRQs, BL Lacs, LSPs, ISPs and HSPs.

| | | All p | | | | | | p≤0.05 | | | |
	Type	Range p	Range ρ	Mean p	Mean ρ	Quantity -ρ,+ρ	Quantity	Range ρ	Mean ρ	Quantity -ρ,+ρ	Quantity
mag-gam	HSP	2.20×10^{-16} - 0.620	-0.0929 - 0.745	0.210	0.299	1,6	7	0.502 - 0.745	0.608	0,3	3
	ISP	4.97×10^{-11} - 0.524	-0.067 - 0.718	0.115	0.429	0,16	16	0.287 - 0.718	0.567	0,10	10
	LSP	0.000 - 0.988	-0.600 - 0.711	0.141	0.337	2,12	14	-0.600 - 0.711	0.390	2,10	12
	ALL	0.000 - 0.988	-0.600 - 0.745	0.142	0.369	3,34	37	-0.600 - 0.745	0.487	2,23	25
gam-deg	HSP	1.89×10^{-13} - 0.419	-0.121 - 0.633	0.196	0.231	1,4	5	0.160 - 0.633	0.397	0,2	2
	ISP	6.68×10^{-4} - 0.946	-0.560 - 0.411	0.370	-0.0382	8,8	16	-0.560 - 0.272	-0.229	2,1	3
	LSP	1.52×10^{-6} - 0.925	-0.249 - 0.556	0.340	0.0619	6,5	11	0.360 - 0.556	0.426	0,3	3
	ALL	1.89×10^{-13} - 0.946	-0.560 - 0.633	0.332	0.038	15,17	32	-0.560 - 0.633	0.173	2,6	8
deg-mag	HSP	1.98×10^{-5} - 0.695	0.0876 - 0.549	0.312	0.268	0,7	7	0.468 - 0.513	0.525	0,2	2
	ISP	1.53×10^{-11} - 0.0754	-0.485 - 0.395	0.0212	0.0334	2,2	4	-0.460 - 0.403	0.0697	1,2	3
	LSP	0.0607 - 0.999	5.47×10^{-4} - 0.270	0.472	0.154	0,4	4	NA	NA	NA	0
	ALL	1.53×10^{-11} - 0.999	-0.485 - 0.549	0.277	0.175	2,13	15	-0.460 - 0.513	0.252	1,4	5

Table 3.5: Summary of results from the Spearman Rank correlation test showing the p and ρ values for different sources within the subclasses for optical (apparent) magnitude vs γ-ray data, degree of polarisation vs γ-ray data and optical (apparent) magnitude vs optical degree of polarisation. The use of apparent magnitudes here does not affect the analysis as the correlations of all sources within a subclass are not studied (due to the biased nature of the sample). The full dataset is presented in Table 3.6 on Page 98.

and 0.34 for HSP, ISP and LSPs respectively.

The p values from the KS test indicated the probability of the HSP and ISP sources being from the same parent population was 56%, for ISP and LSP sources the probability was 58% and for the HSP and LSP sources the probability was 84%. The null hypothesis, that the samples were drawn from the same parent population, could not be rejected.

Optical degree of polarisation and γ-ray flux correlations

Figure 3.5 shows the γ-ray flux against optical degree of polarisation for all sources (each coloured individually) and the 5 subclasses. The γ-ray data are plotted on a logarithmic scale for visualisation purposes. The horizontal lines are caused by the polarisation varying during a wide γ-ray flare bin, usually in low γ-ray states. The vertical lines are caused by the γ-ray flux varying when the degree of polarisation was very low. For the γ-ray and degree of polarisation plots it was not possible to easily distinguish the FSRQ and BL Lac subclasses from each other by visual inspection. The FSRQs exhibited higher γ-ray fluxes than the BL Lacs. The spectral peak subclasses differed in their γ-ray flux value (as already shown in the previous section), however they also differed in their maximum degree of polarisation value. The LSP sources exhibited polarisation degrees up to $\sim$40%, ISPs $\sim$30% and the HSP sources had a maximum of $\sim$10%. The HSP sources also showed less variation than the LSP and ISP sources.

Figure 3.6 shows the distance corrected γ-ray flux against the degree of polarisation. There were no new visual trends seen in the data.

In order to investigate the correlations in more detail we split the data (because the sample itself was not representative of the blazar population) by individual source and by observing season and carried out a Spearman Rank analysis (see full summary of
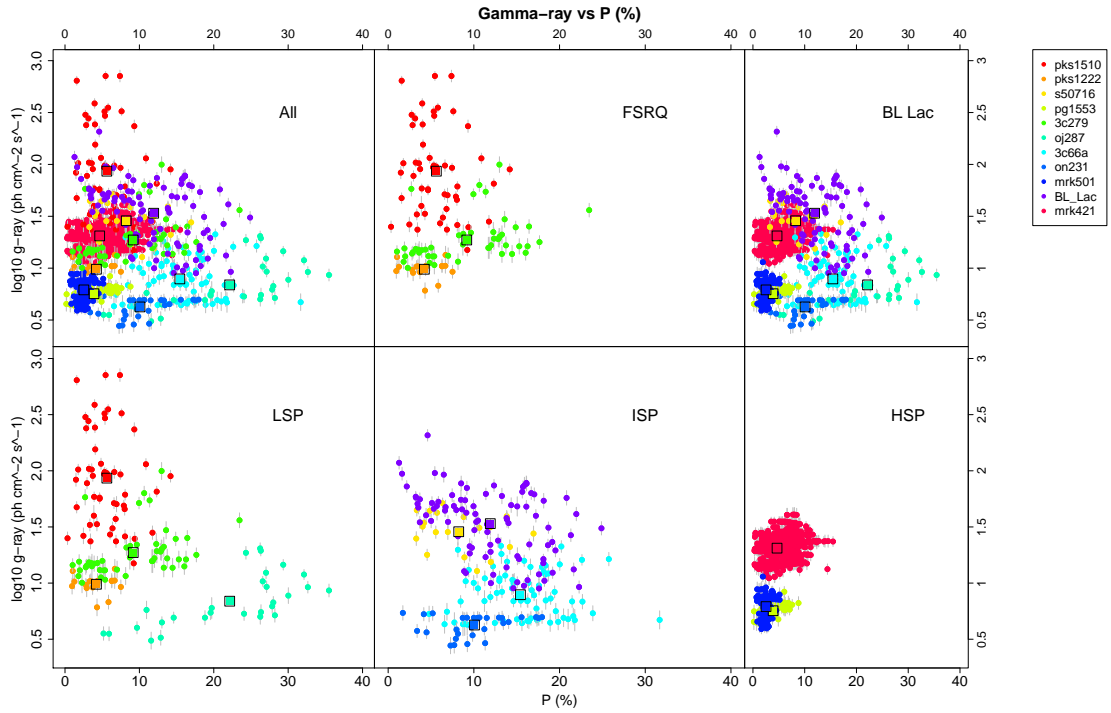
Figure 3.5: Fermi γ-ray flux against optical degree of polarisation for all sources and each blazar subclass, a different colour for each source separately. Black squares show where the mean of the source lies on the plot. Horizontal and vertical lines in the data show periods during which the γ-ray/optical data (respectively) are constant while the other continues to vary.
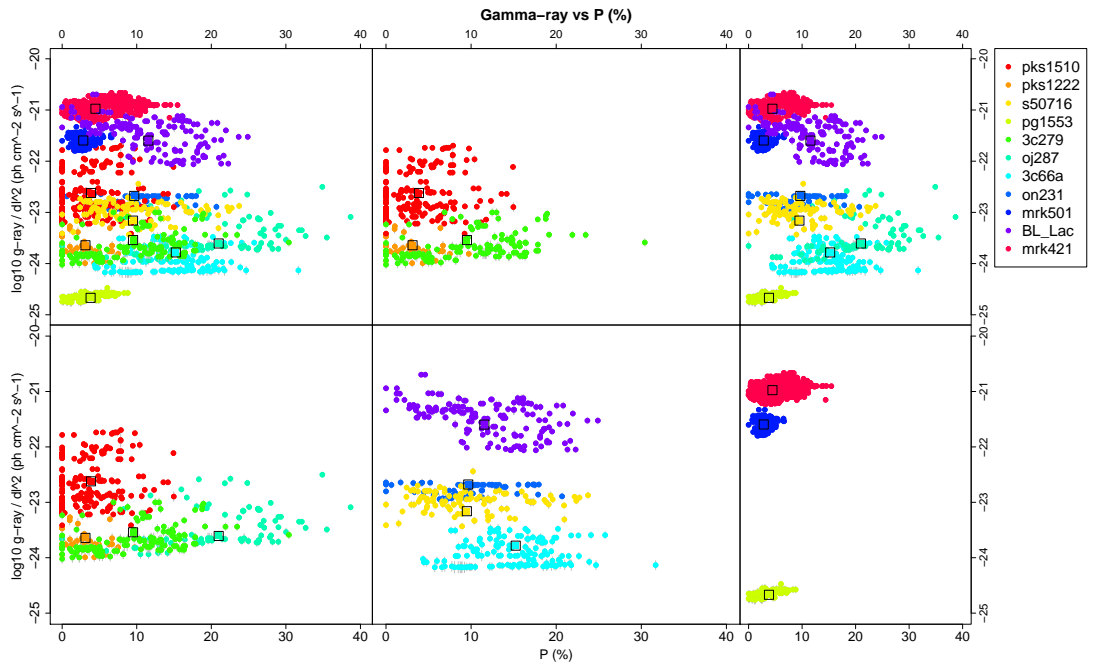
Figure 3.6: Distance corrected Fermi γ-ray flux against optical degree of polarisation for all sources and each blazar subclass, a different colour for each source separately. Black squares show where the mean of the source lies on the plot. Horizontal and vertical lines in the data show periods during which the γ-ray/optical data (respectively) are constant while the other continues to vary.
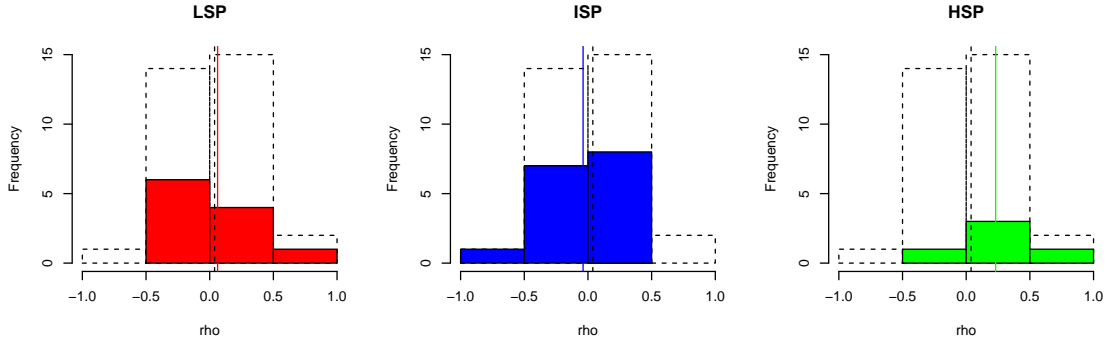
Figure 3.7: Histograms showing the distribution of ρ values from the Spearman Rank Coefficient test for the optical degree of polarisation and γ-ray flux. From left to right: LSPs (red), ISPs (blue) and HSPs (green). The dotted histograms are the distribution of the total sample and the black vertical lines show where the sample mean lies. The mean of the subclasses are shown as a vertical line in their respective colours.

results in Table 4). Figure 3.7 shows the distribution of the ρ coefficients as histograms. The peak of the overall distribution is close to zero (as shown in Table 3.5) and for the peak of the ρ value distributions, the LSP and HSP sources are positive and ISP sources are negative. Of the significant correlations, shown in Table 3.5, HSP and LSP source seasons showed positive correlations and ISP sources had a slight majority of positive correlations (despite the overall negative ρ value).

We carried out a KS test analysis on the distribution of ρ values. The HSP and ISP distributions had 0.44 probability of being from the same parent distribution and the HSP and LSP distribution had a 0.42 probability. The probability of the ISP and LSP sources being from the same distribution was 0.48. These probabilities were all >0.05 and therefore the null hypothesis (that the samples were drawn from the same distribution) could not be rejected.

Optical magnitude and degree of polarisation correlations

Figure 3.8 shows plots of the degree of polarisation against the optical apparent magnitude separated by object type. Here all 15 sources in our sample (i.e. including those without Fermi data) are plotted. Those sources that do not have synchronous
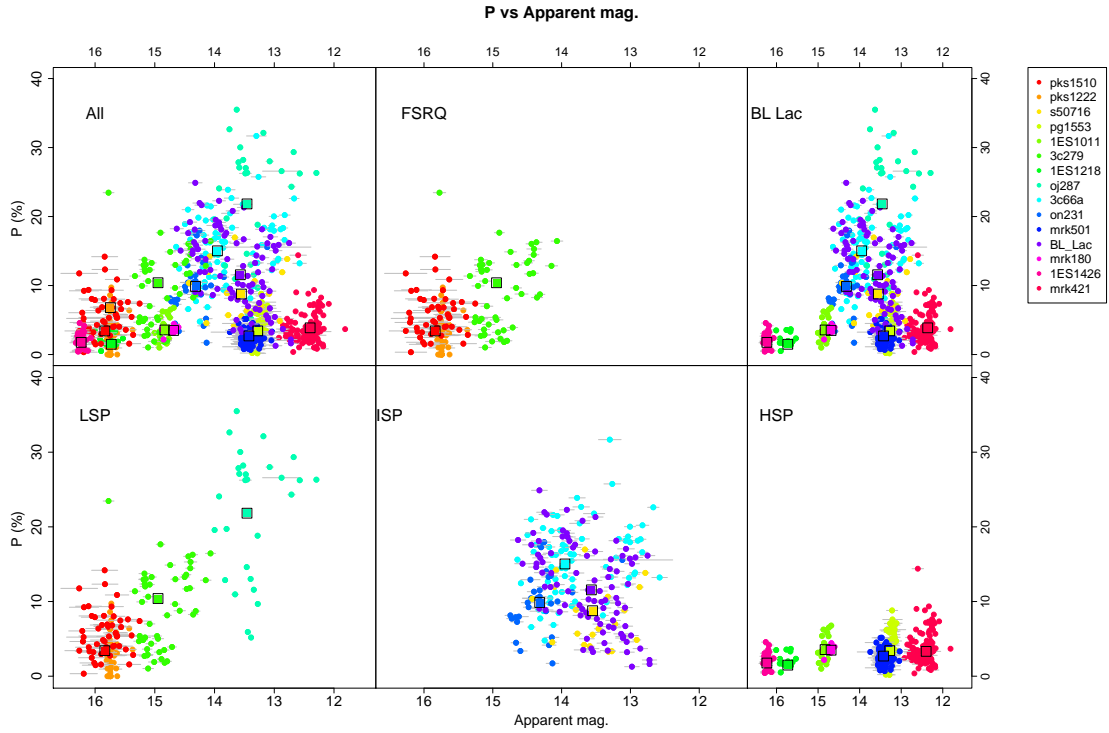
Figure 3.8: The optical degree of polarisation against optical apparent magnitude for all 15 sources. For those sources that do not have synchronous points (i.e. Mrk 421 and PKS 1222) we interpolate the nearest lying point from the neighbouring datapoints. Each source is coloured separately and black boxes show where the mean of that source lies on the plot.

magnitude and degree of polarisation (Mrk 180 and PKS 1222+216) had their points interpolated from neighbouring data, where available. In addition, as the data are synchronous, they were not split into seasons, but were compared across the whole available dataset. As already shown in the previous correlation plots, the HSP sources have degree of polarisation values <10%, while the LSP and ISP sources show greater variability, reaching a maximum polarisation of ~40% and ~30% respectively. The HSP sources showed tighter groupings than the LSP and ISP sources.

Figure 3.9 shows the degree of polarisation against the absolute magnitude. As with the other plots there were no new visual trends when the absolute rather than the apparent magnitude was used.

Table 3.5 shows the Spearman Rank Coefficient ρ and probability values for the optical magnitude and degree of polarisation data. 87% (13/15) of sources showed positive
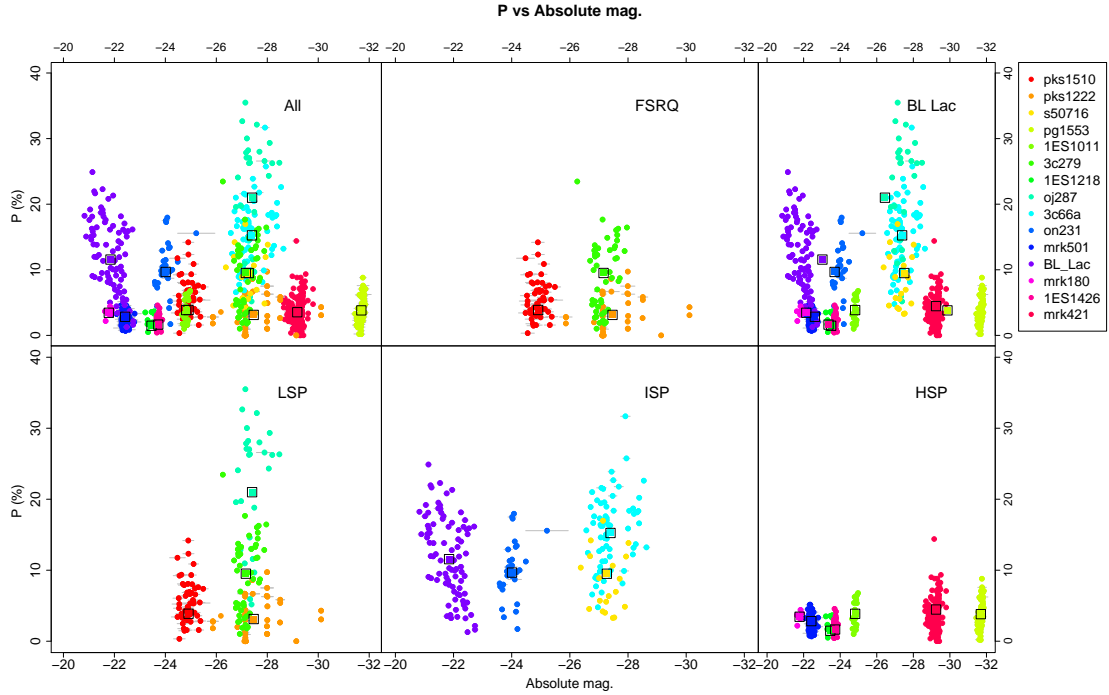
Figure 3.9: The optical degree of polarisation against optical absolute magnitude for all 15 sources. For those sources that do not have synchronous points (i.e. Mrk 421 and PKS 1222) we interpolate the nearest lying point from the neighbouring datapoints. Each source is coloured separately and black boxes show where the mean of that source lies on the plot.

weak correlations between the optical magnitude and the optical degree of polarisation with $\bar{\rho} = 0.18$ (with p values that range from 0-1). There were 4 sources that showed positive weak correlations with p≤0.05, however, the HSP sources lacked significant correlations.

The probability of the HSP, ISP and LSP distributions being from the same parent sample was tested using the KS test. For HSP and ISP sources p = 0.42, ISP and LSP p = 0.77 and HSP and LSP p = 0.66 also. None of these p values was ≤0.05 therefore the null hypothesis cannot be rejected and the samples may be drawn from the same distribution.

3.5. *Discussion*
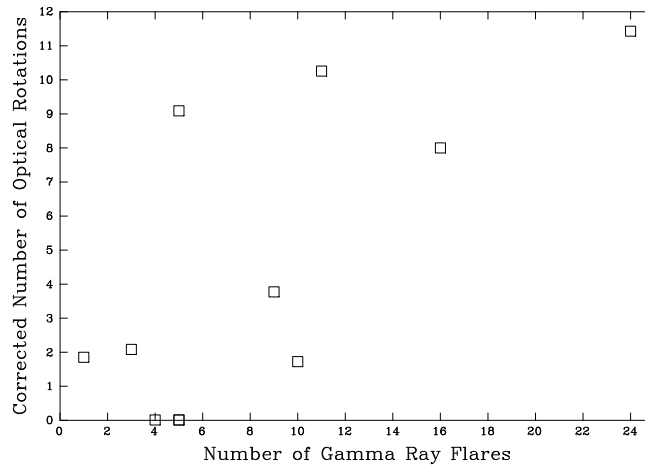
Figure 3.10: Number of observed optical rotations (corrected for the observing duty cycle) versus number of observed γ-ray flares for those sources which have sufficient γ-ray data (11/15 sources) - note there are two points at x=5, y=0.

3.5.2 Optical and γ-ray properties during EVPA rotations

A total of 95 γ-ray flare events (see Section 3.4 for the description of a flaring event) were identified in 11 sources. In the sample, the rate of flaring was between 0.0022 - 0.017 flares per day per source (0.8 - 6.2 per year, per source). The mean flare rates (and standard error on mean) for each subclass were HSP = 0.005 ± 0.0008 , ISP = 0.007 ± 0.003 and LSP = 0.009 ± 0.006 flares per day, per source, equivalent to HSP = 1.9$\pm$0.3, ISP = 2.5$\pm$0.6, LSP = 3.2$\pm$1.1 flares per year per source. These results indicated that there were no significant differences between the rate of flaring in the different subclasses.

In order to make a simple assessment of whether flaring and rotation activity are associated, we compared the number of flares per source with the number of rotations. Since there were missing optical data due to seasonal effects, we corrected the number of rotations of a given source by dividing by its optical duty cycle (defined as the fraction of time when optical coverage overlapped with the Fermi data). The results of this analysis are presented in Figure 3.10. There was a significant correlation ($\rho = 0.59, p = 0.05$). It therefore appeared that there may be some link between a propensity for γ-ray flaring and that for optical polarisation rotations.

Due to the visibility of the sources, 67 of the γ-ray flaring events occurred during periods where coincident optical data were unavailable, or there were no data between the data point and the nearest flare. Of the remaining 28 γ-ray flares that had optical photometry and polarimetry in coincident periods with the γ-ray data, there were 17 flares that occurred during periods of rotation of the EVPA (see Table 2, Column 10). However, we note that this statistic was dominated by one source (PKS 1510-089) which had the highest mean flare rate and multiple flares within a single long EVPA rotation. In addition, we could associate 11 flares that occurred outside an EVPA rotation with the closest in time EVPA rotation (i.e. the nearest lying rotation to a flare where there were no missing data in between). There were 5 flares that occurred <84 days after the rotation and 6 flares that occurred <116 days before the rotation (see Table 2, Column 9). Even though we did not analyse flares that occurred during periods when we lacked optical data, we must be cautious; the average observing season was $\sim$180 days which meant that it may be possible that flares were associated with closer lying rotations that occurred when we were unable to observe them.

In order to investigate the γ-ray and optical properties during and outside of rotations we separated the data for each source into two periods: (a) rotation and (b) non-rotation. The first two histograms in the top panel of Figure 3.11 show the degree of polarisation for all sources during those periods. The data are presented as a fraction of the full range of the degree of polarisation for a particular source and the whole histogram has been divided by the ratio of the number of points in the larger dataset (outside of EVPA rotations) over the number of points in the smaller dataset (during EVPA rotations), this removes rare events from the analysis and takes into account any selection effects. After this normalising, we found that the distributions did not change and each bin still has $\geq$1 occurrence.

The top panel shows the distribution of the degree of polarisation during a rotation was generally shifted toward lower values and the high polarisation tail was suppressed.

Outside of the rotations the data appear to have a more Gaussian distribution. The mean of the distributions of degree of polarisation ($\bar{DoP}$) during a rotation was 0.34 and outside of a rotation $\bar{DoP}$ = 0.46. On average the degree of polarisation was therefore 26% lower during a rotation.

A KS test was performed on the data to establish the probability that the degree of polarisation during rotation and non-rotation events were from the same parent distribution. There was a very low probability (p<0.01) that the degree of polarisation during rotations comes from the same distribution as the degree of polarisation during non-rotations. The null hypothesis was rejected; the distribution of the degree of polarisation was different during rotations to outside of rotations.

In the middle panel of Figure 3.11 the first two histograms show the R magnitude, during EVPA rotations and outside EVPA rotations, as a fraction of the normalised range of the total magnitude. Similar to the degree of polarisation, in very relatively few points does the magnitude reach >90% of the total flux during a rotation whereas outside of rotations there were ~300 points that have polarisation values >90% of the total flux. The mean of the distribution during a rotation was $\bar{R}$ = 52% and outside of rotation periods the magnitude was $\bar{R}$ = 59%. On average the optical flux was therefore 17% lower during a rotation. The results from the KS test showed, as for the degree of polarisation, the two distributions of magnitude during and outside of rotation periods had a very low (p<0.01) probability of being from the same parent sample. The null hypothesis was again rejected; during a rotation the optical magnitude was lower compared to outside of a rotation and their distributions were not from the same initial sample.

The first two histograms in the bottom panel of Figure 3.11 show the relative strength of the γ-ray flux during- and outside of- EVPA rotations. During the rotations the γ-ray flux never rises above 59% of the peak γ-ray flux. Outside of the rotations the γ-ray flux had a longer high-γ flux tail, with the maximum brightness occurring outside
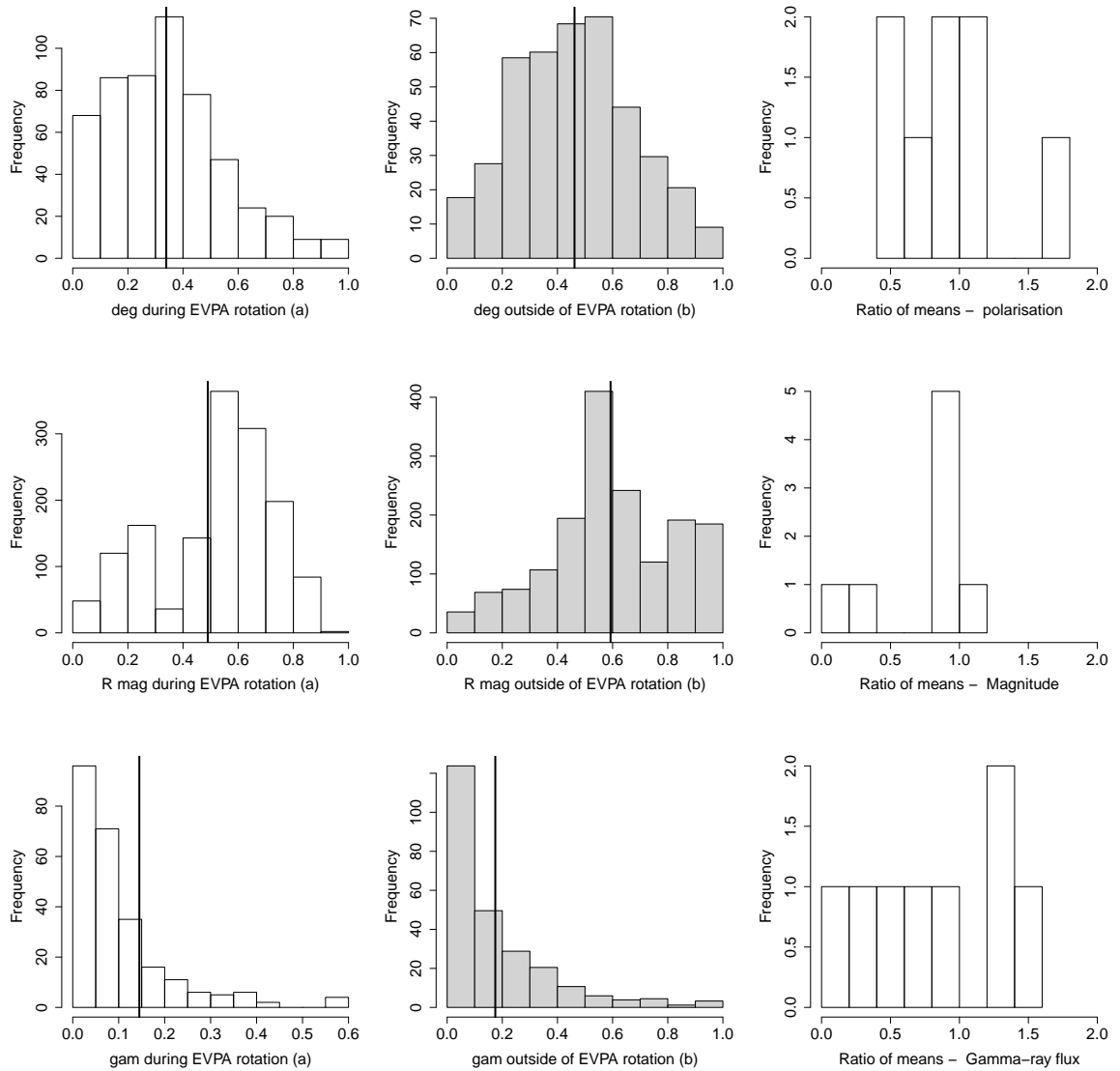
Figure 3.11: The degree of polarisation (top), optical magnitude (middle) and γ-ray flux (bottom) displayed as a fraction of the normalised range for a) during EVPA rotations (white) and b) outside of EVPA rotations (grey) and, in the final column, as a ratio of the mean of each property during a rotation over the mean of each property outside of a rotation for each individual source (see Section 3.5.2 for more details). The black vertical lines in the first two columns show the mean of the histograms.

of a rotation event. The KS test results showed that the likelihood of the rotation and non-rotation γ-ray flux to be from the same parent population was 0.24. This meant that the null hypothesis; the samples were from the same distribution, cannot be formally rejected. However we noted that during rotations, the mean of the γ-ray flux distribution ($\bar{\gamma} = 10\%$) was 42% lower compared to that outside of a rotation ($\bar{\gamma} = 17\%$).

The third column in Figure 8 shows, for each individual source, the mean ratio of degree of polarisation (top), R magnitude (middle) and γ-ray flux (bottom) during and outside of a rotation. For the degree of polarisation, 5/8 sources had lower values (i.e. ratios <1) during rotations. For the R magnitude there were 7/8 sources that have lower values during a rotation. For the γ-rays there were 5/8 sources which were less bright in γ-rays during a rotation.

3.6 Conclusions

There are important caveats to consider before making concluding remarks about the results presented in this chapter. Firstly, the Ringo2 blazar monitoring survey was designed to follow-up sources detected by MAGIC so the essence of the sample is that the sources are all γ-ray bright and have exhibited some kind of flaring activity (hence the reason they were added to the sample). Thus, due to this selection bias, the presented sample-averaged results could not be generalised to the larger blazar population, however, the correlations for individual sources are robust.

In this chapter a detailed discussion of the behaviour of the individual sources has been presented. The direction of the EVPA rotation for each source (i.e. whether it was upward or downward) does not give any information about the nature of jet. This is because the rotation direction is subject to the arbitrary nature of the magnetic field and its properties, which vary from blazar to blazar.

In four sources 3C279, PKS 1510-089, PG 1553+113 and S5 0716+714 we observed upward then downward rotations and in the case of S5 0716+714 we saw the EVPA rotate upward, downward and then upward again (see plots for these sources in the Appendix). We also had cases in four sources PKS 1510-089, S5 0716+714, PG 1553+113 and Mrk 421 in which there was a γ-ray flare during, or temporally close to, a rotation. Such behaviour of the EVPA was potentially important in studying the magnetic field and/or the orientation of the jet/emission blob within the jet with respect to the observer. Monte Carlo analysis by Blinov et al. (2015) suggested that a single EVPA rotation event could be caused by a random walk of the EVPA, but it was unlikely that *all* rotations were due to random walk.

A statistical study of the general properties of these sources was performed without considering their individual behaviour. We found the following principal results:

1. The maximum observed degree of optical polarisation for the LSP sources was $\sim 40\%$. For ISP sources it was $\sim 30\%$ and for HSP sources $\sim 10\%$. It is natural to attribute the low maximum polarisation degree in HSP sources to their optical light being dominated by non-synchrotron emission which can originate from the accretion disk or emitting regions outside of the jet. This explanation also accords with the low optical variability in these sources, however it could also be a signature of low-ordered or disordered magnetic fields in the jet. It must also be reiterated that these results cannot be applied to the larger blazar population.

2. On average the optical degree of polarisation and γ-ray flux were not strongly correlated. ISP and LSP sources showed no strong preference for either positive or negative correlations. HSP sources showed a stronger (yet still weak) positive correlation.

3. In 92% (34/37) of source seasons we found a positive correlation ($\bar{\rho} = 0.37$) between optical and γ-ray flux. In over half of the seasons (25/37 = 68%) the prob-

ability of correlation was significant (i.e. p≤0.05). Similar findings have also been reported by Hovatta et al. (2014) and Cohen et al. (2014). Such behaviour may provide evidence of a close physical association between the optical and γ-ray emitting regions in blazars. We found no significant differences between the distributions of the correlation coefficients for HSP, ISP and LSP sources. This suggested that, on average, a common emission site connects γ-ray flaring and optical polarisation in these different blazar subclasses.

4. There was a weak positive ($\bar{\rho} = 0.18$) correlation between optical magnitude and degree of polarisation in 13/15 source seasons. In 5/15 cases the the probability of correlation was significant (i.e. p≤0.05) and $\bar{\rho} = 0.25$.

5. All blazar subclasses showed γ-ray flaring and EVPA rotations. There was a significant correlation ($\rho = 0.59$, p = 0.05) between the number of flares and the number of EVPA rotations in a given object. We do not, however, find any systematic difference by class in γ-ray flaring rate or number of EVPA rotations.

6. γ-ray flaring episodes occurred during and outside of rotation events. The distribution of lead and lag values between flares and rotations showed that there was no preference for either behaviour. The association of the γ-ray flare and the EVPA rotation could provide evidence for the cause of the rotation and the flare originating from the same shock region, with the shock providing electrons for up-scattering photons via Inverse-Compton processes and the tangled magnetic field providing the structure for the EVPA rotation. However, optical and gamma-ray flaring was not always synchronous with an observed rotation, suggesting that other mechanisms were involved in some instances.

7. The mean degree of polarisation as a fraction of the total range of polarisation was 26% lower during periods of rotation compared to periods of non-rotation, Blinov et al. (2016) also report a decrease in polarisation during rotations. The

mean optical magnitude was 17% lower during a rotation compared with outside rotations and the mean γ-ray flux was 41% lower during a rotation compared with outside a rotation. The lower degree of polarisation during a rotation could be interpreted as a difference in the degree of ordering of the magnetic field during a rotation compared with non-rotation. Alternatively it could be evidence for their association with emission features or shocks travelling along helical magnetic field lines (Marscher et al., 2008; Zhang et al., 2015c).

3.7 Polarisation and Photometry Plots

We present here the fifteen light curves and polarisation plots covering the Ringo2 period of monitoring. The four windows show (from top to bottom) Fermi γ-ray data, optical EVPA, optical degree of polarisation and optical magnitude. In the Fermi window the areas of rotations are shown (pink for upwards rotation, green for downwards rotation), along with the areas that lack corresponding optical polarisation data (grey) and the Fermi flares (blue) identified using the automated code (see Section 3.3.1 for definition of a flare). The errors on the x axis represent the bins used for the Fermi data.

The second panel shows the optical polarisation angle or electric vector position angle (EVPA), the grey points are Ringo2 data and the black points KVA-DIPOL data. The black line traces the temporally closest EVPA points, showing the most likely behaviour of the EVPA. The EVPA are presented four times with a $\pm 180°$ shift. This is because there is an 180° ambiguity in the data.

The third panel shows the optical degree of polarisation. The points close to zero that have single upward error bars, while presented as points, can be interpreted as upper limits. The fourth panel the optical magnitude and all point colours are the same as those for panel 2. The error bars are generally smaller than the point size.
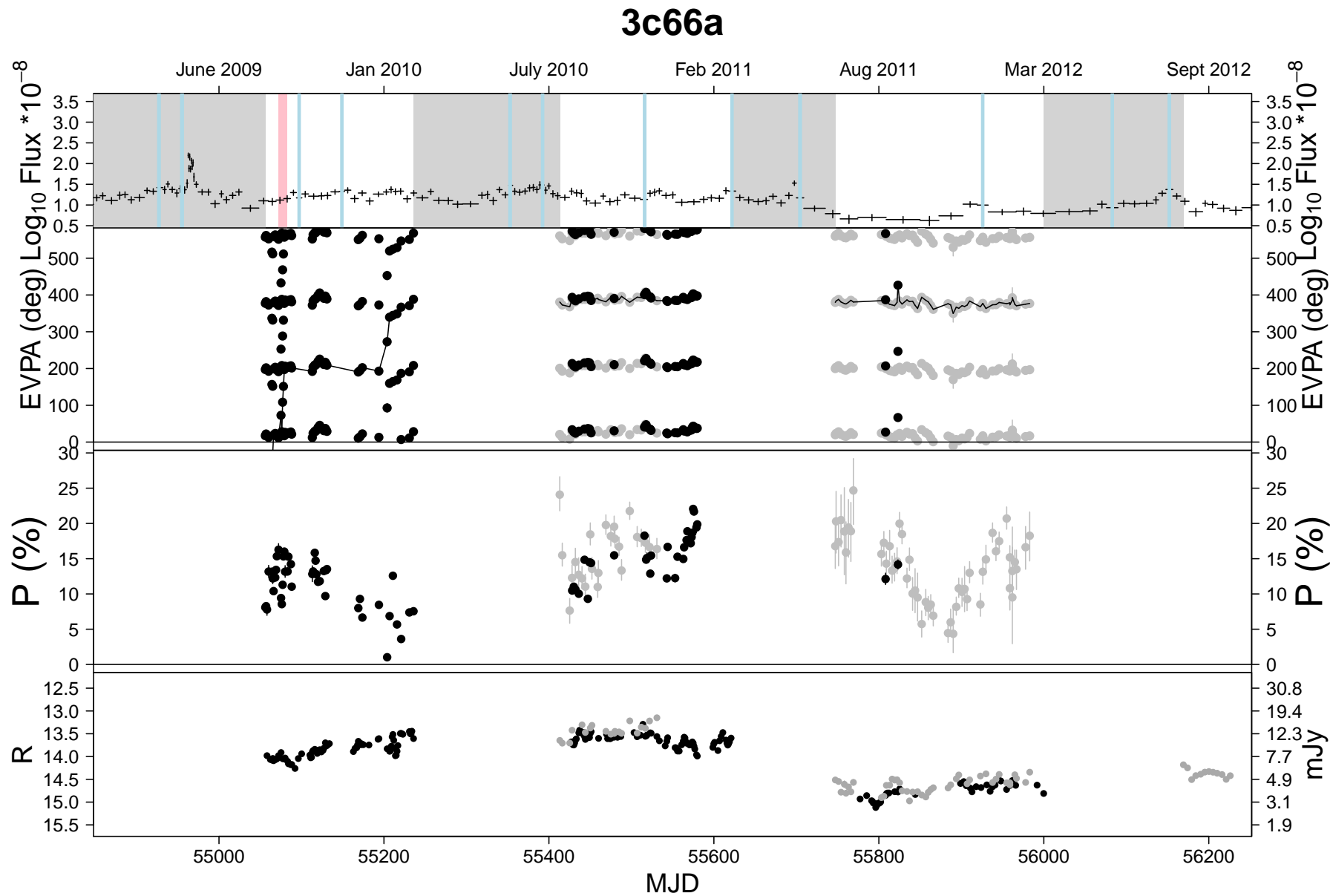
Figure 3.12

s50716
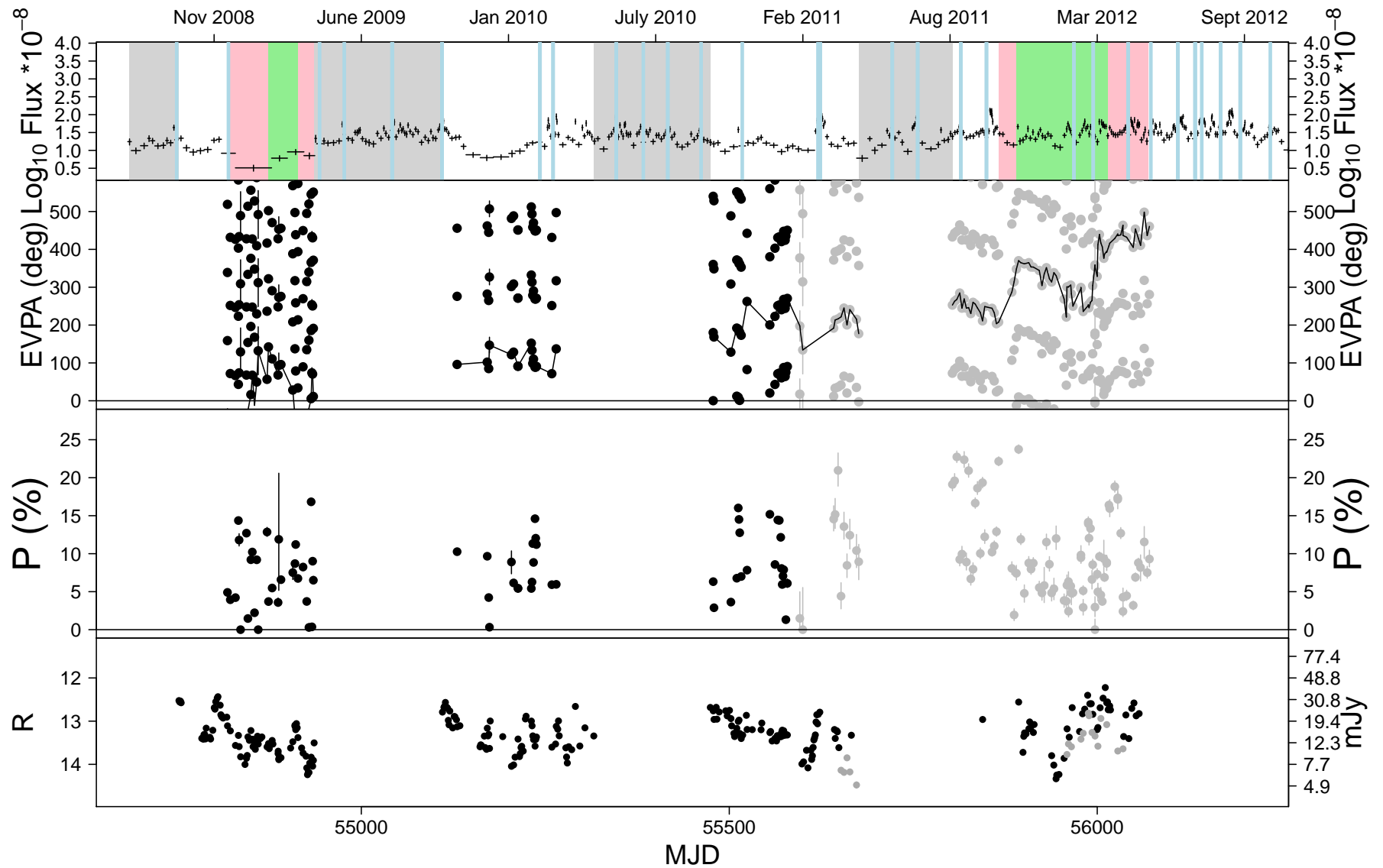
Figure 3.13
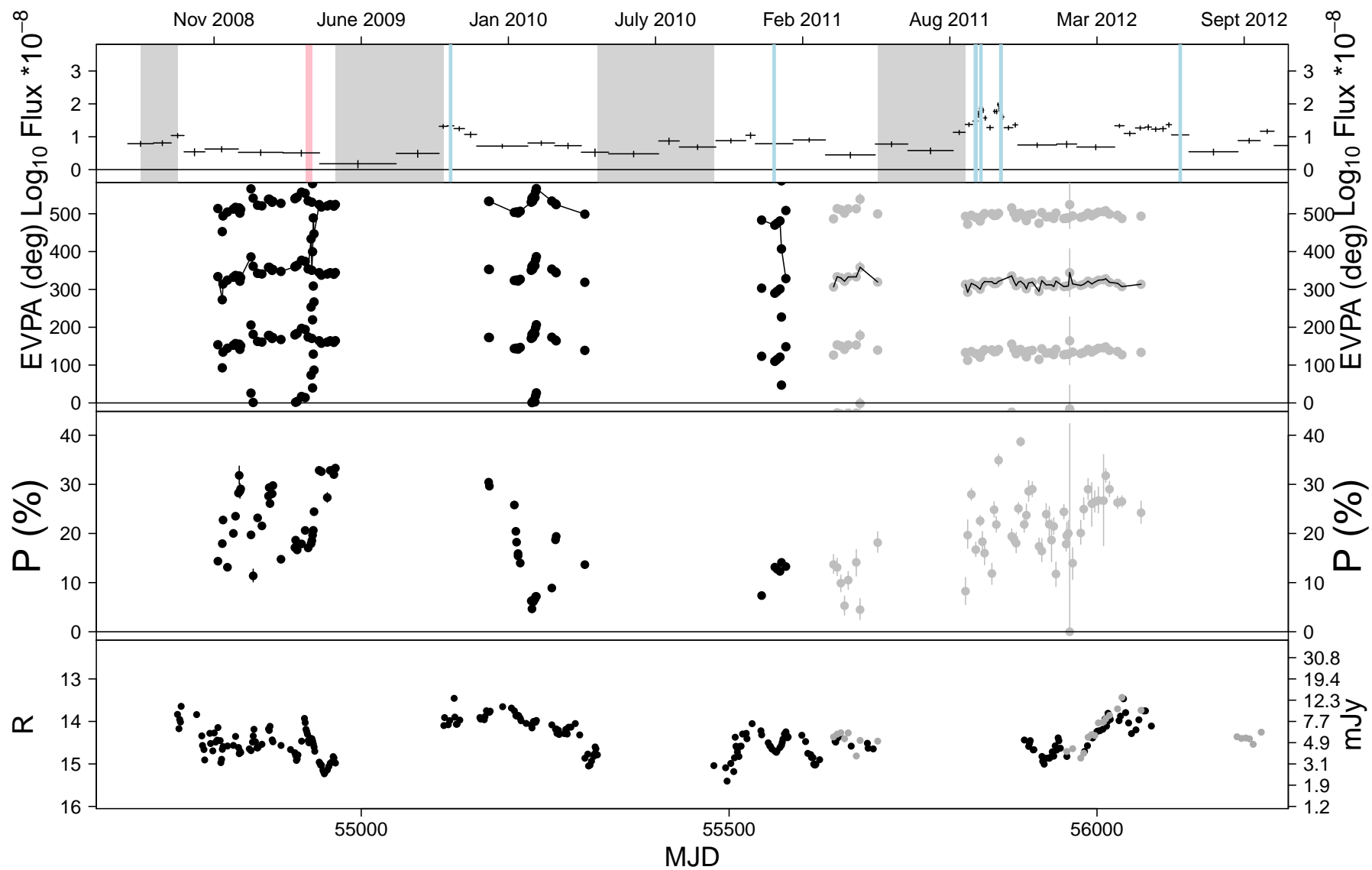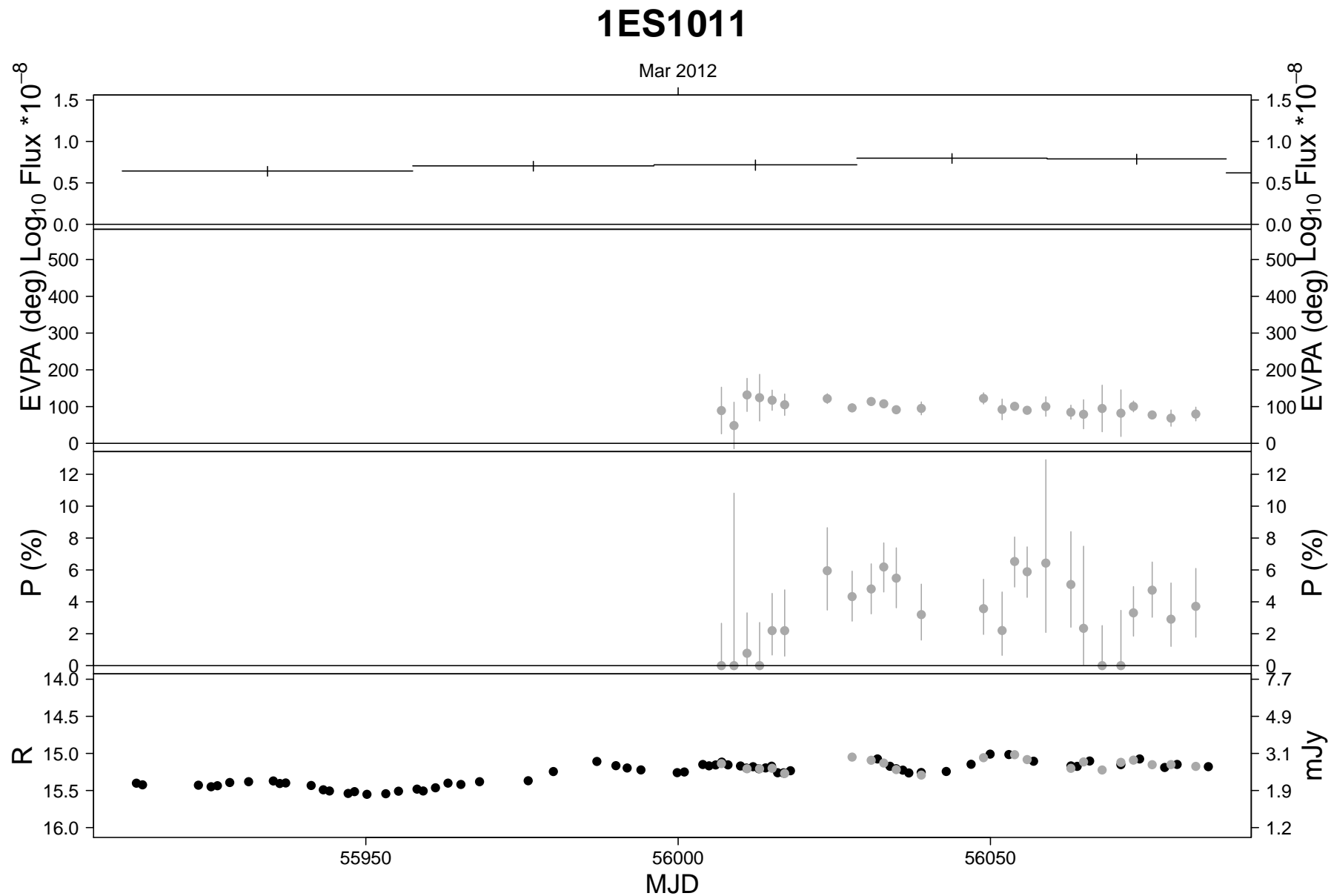
Figure 3.14

Figure 3.15
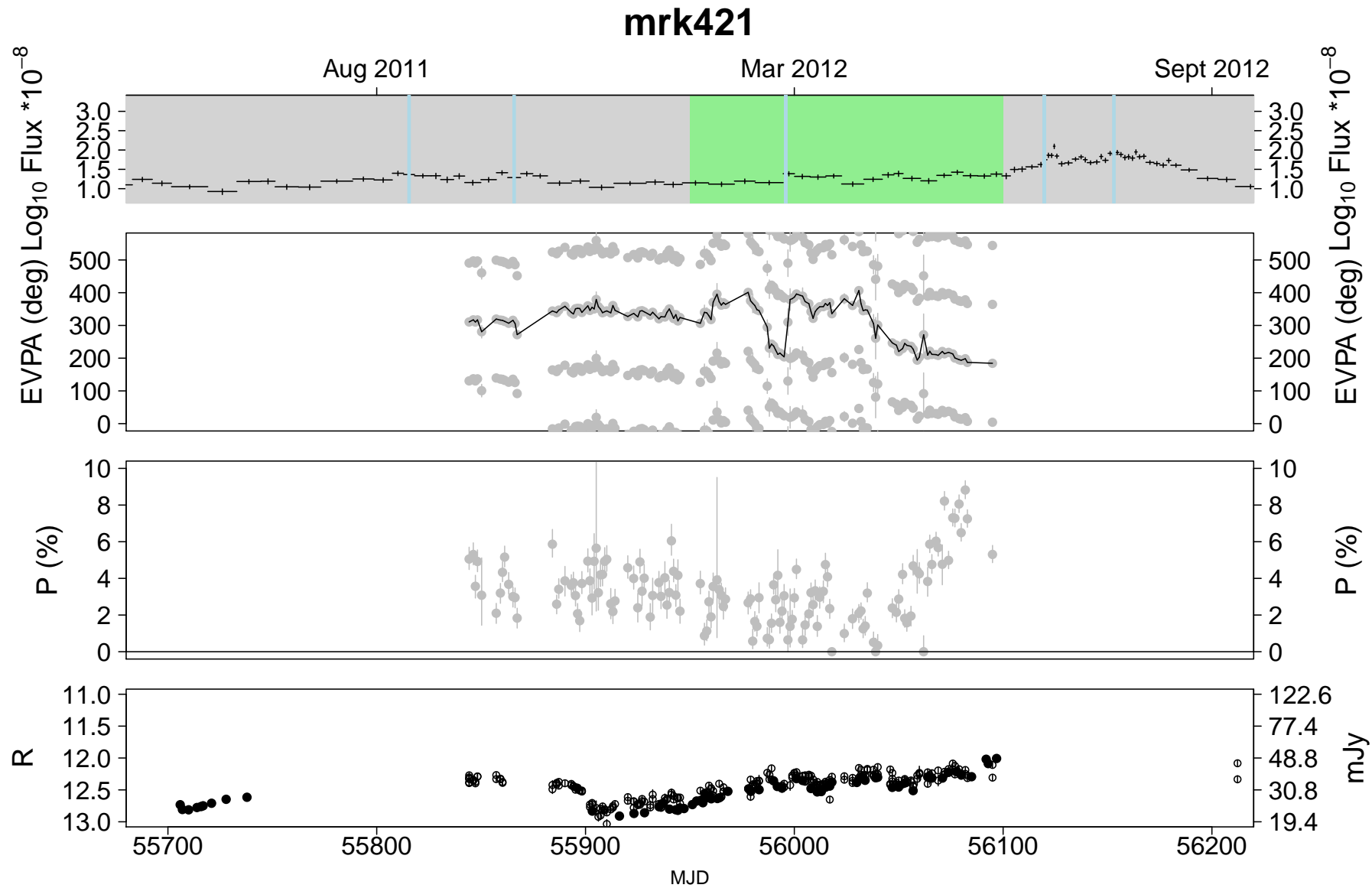
Figure 3.16

Figure 3.17

1ES1218
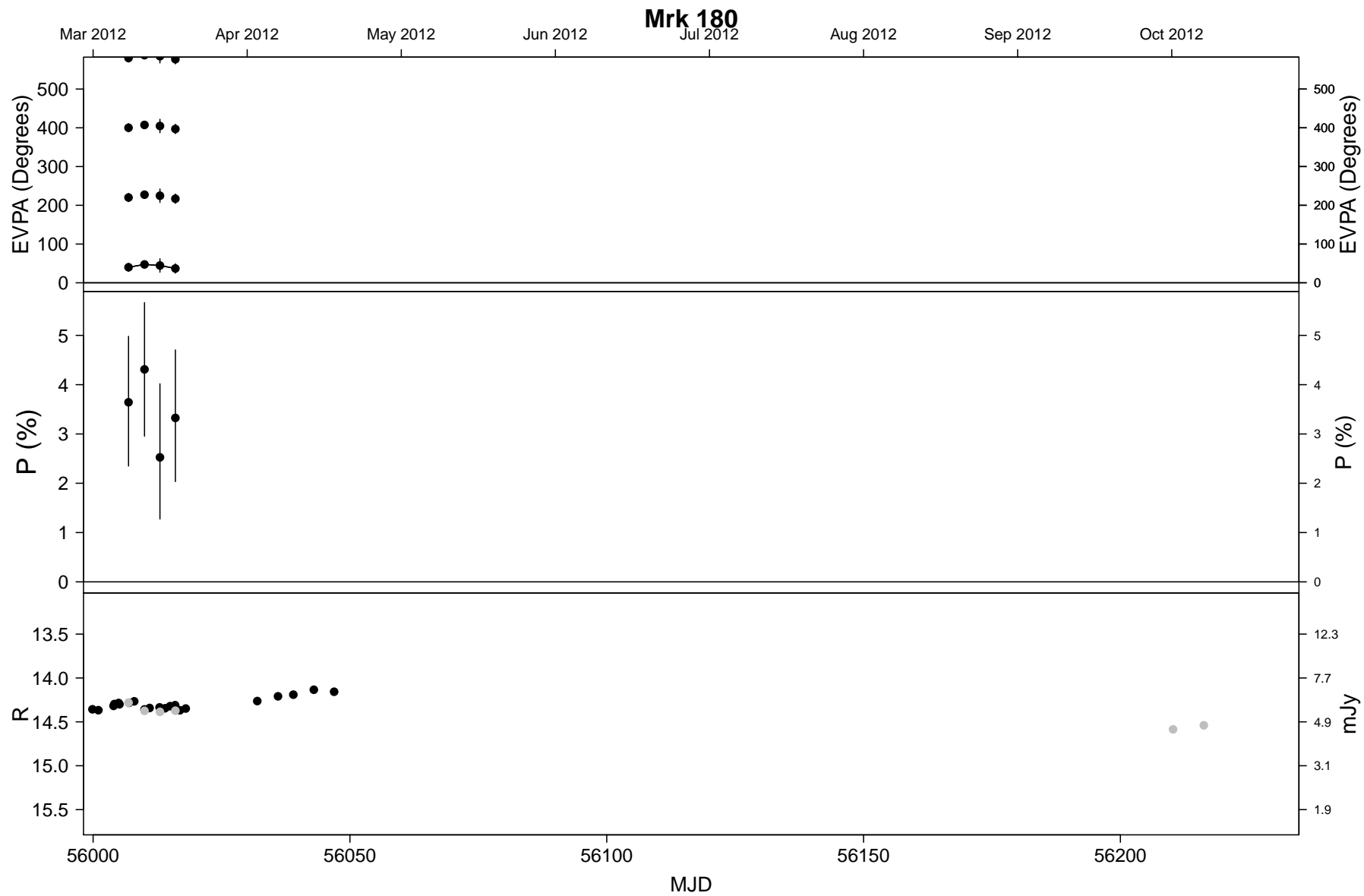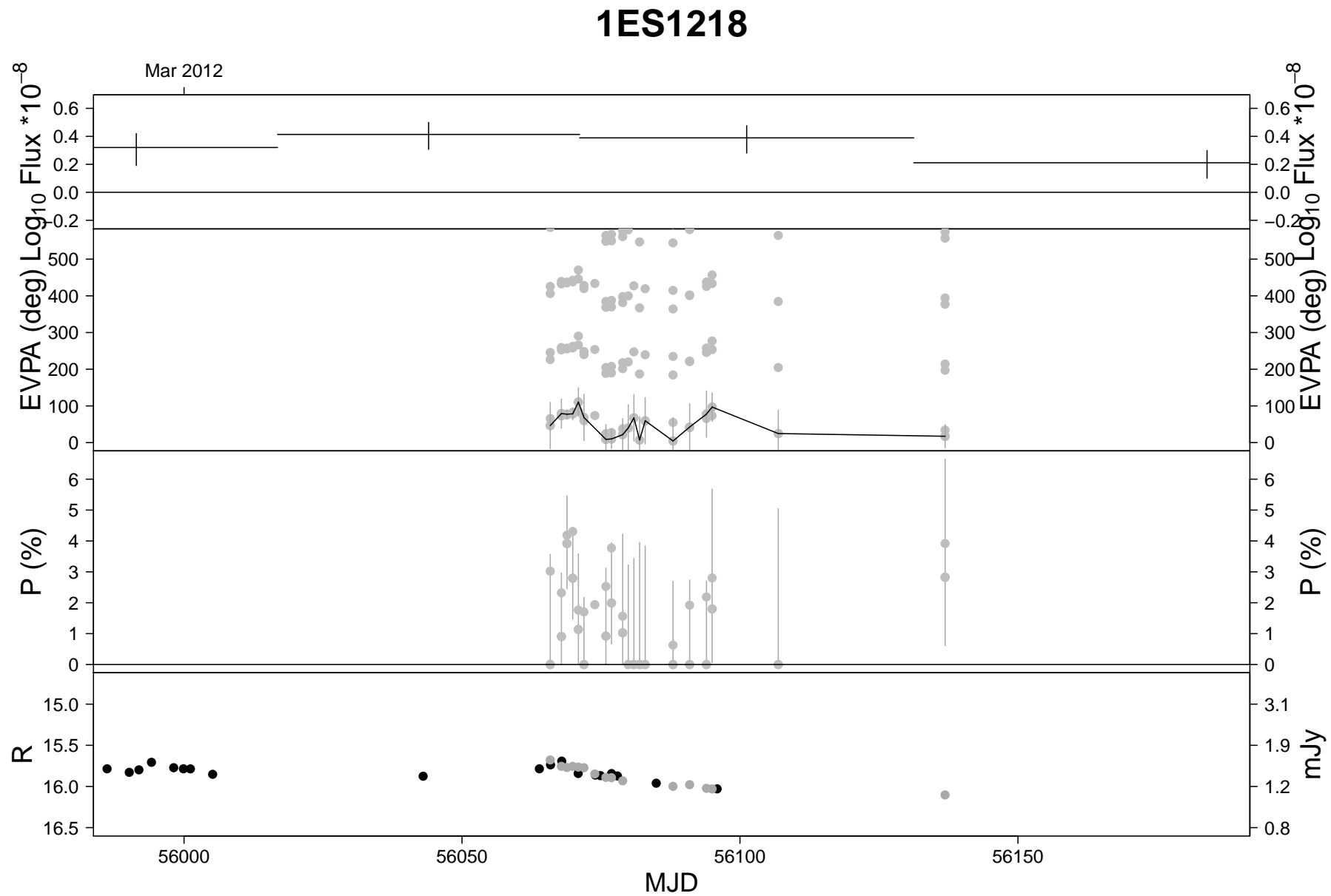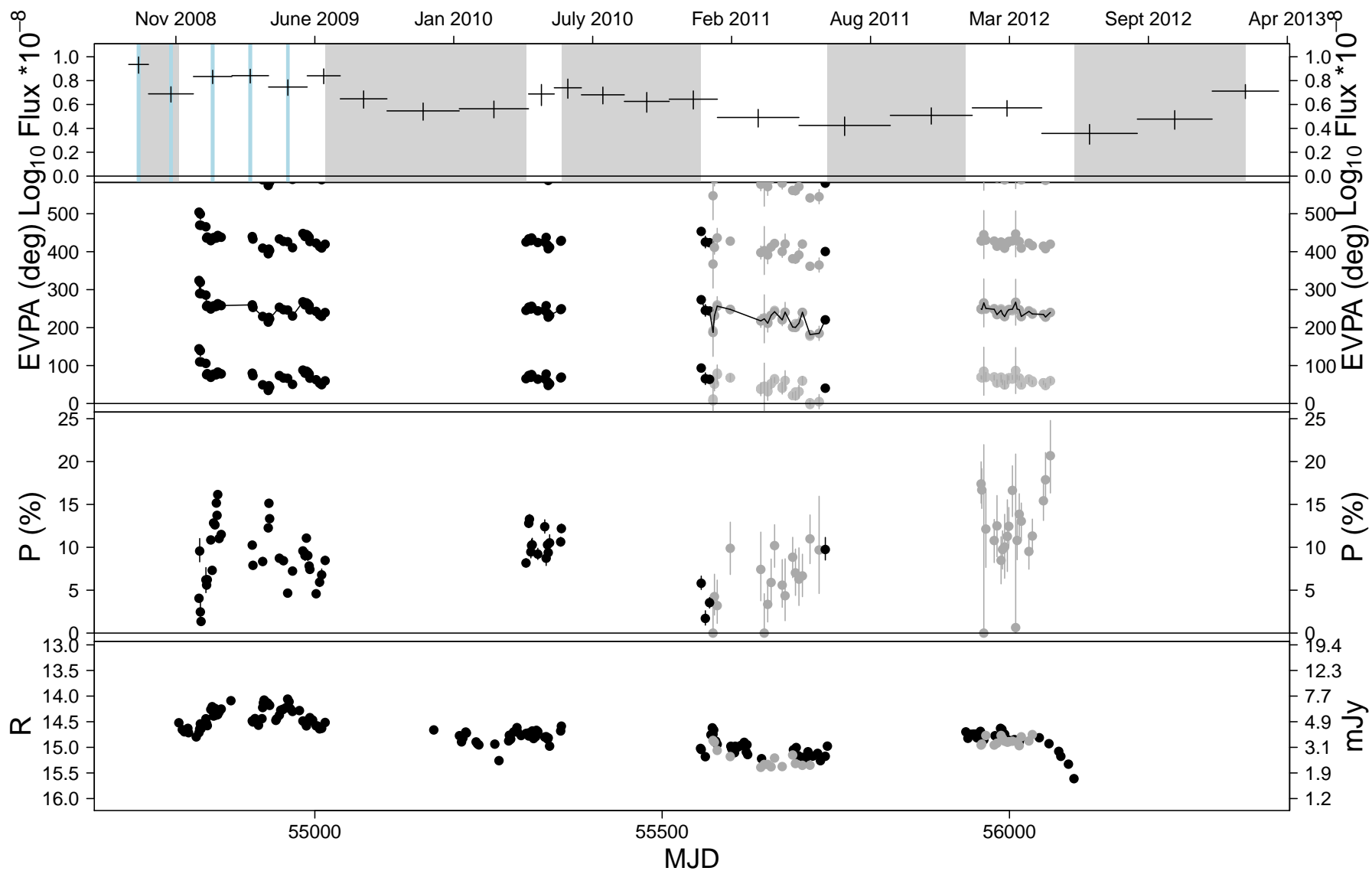
Figure 3.18
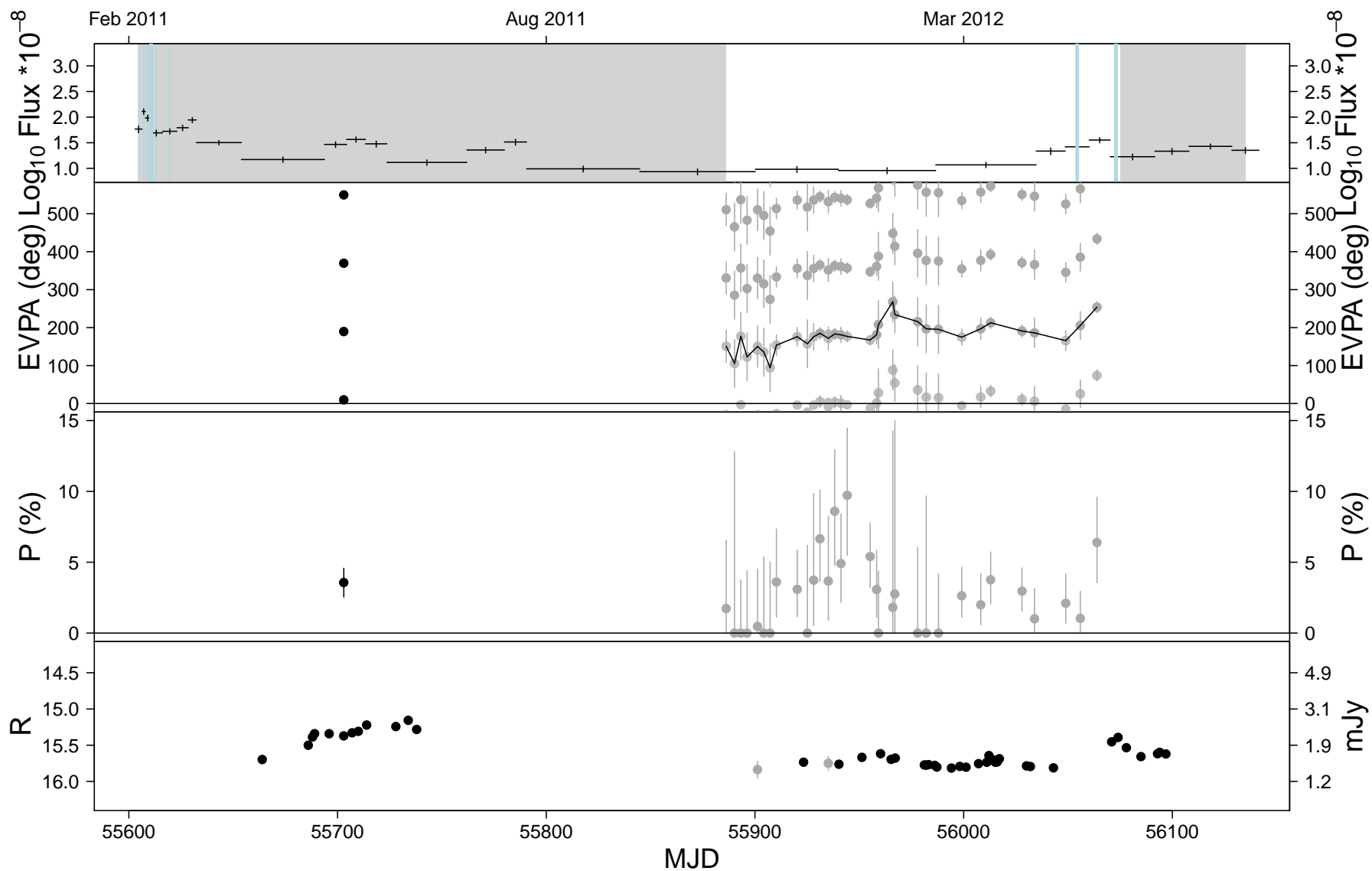
Figure 3.19

Figure 3.20

3c279
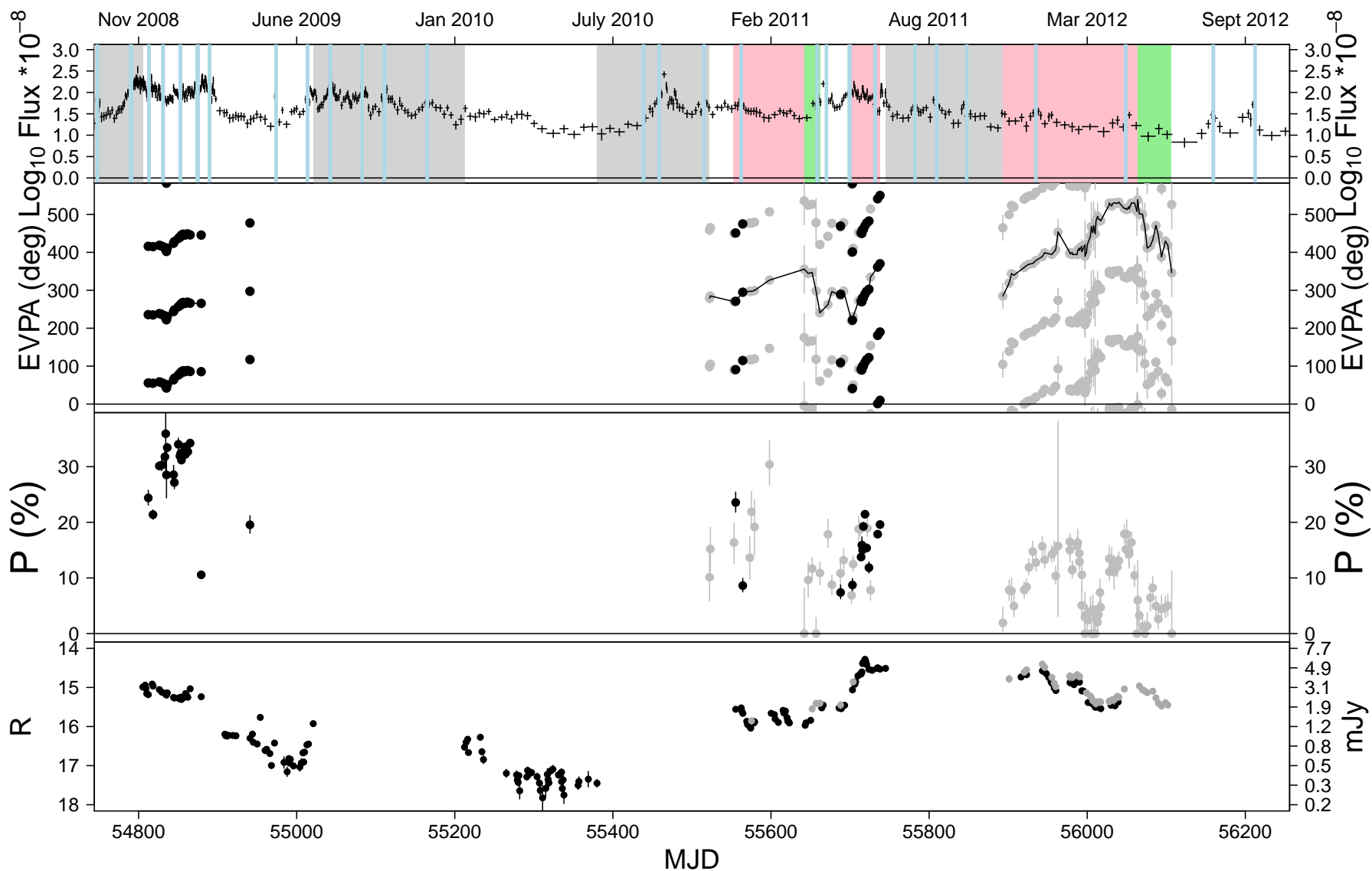
Figure 3.21
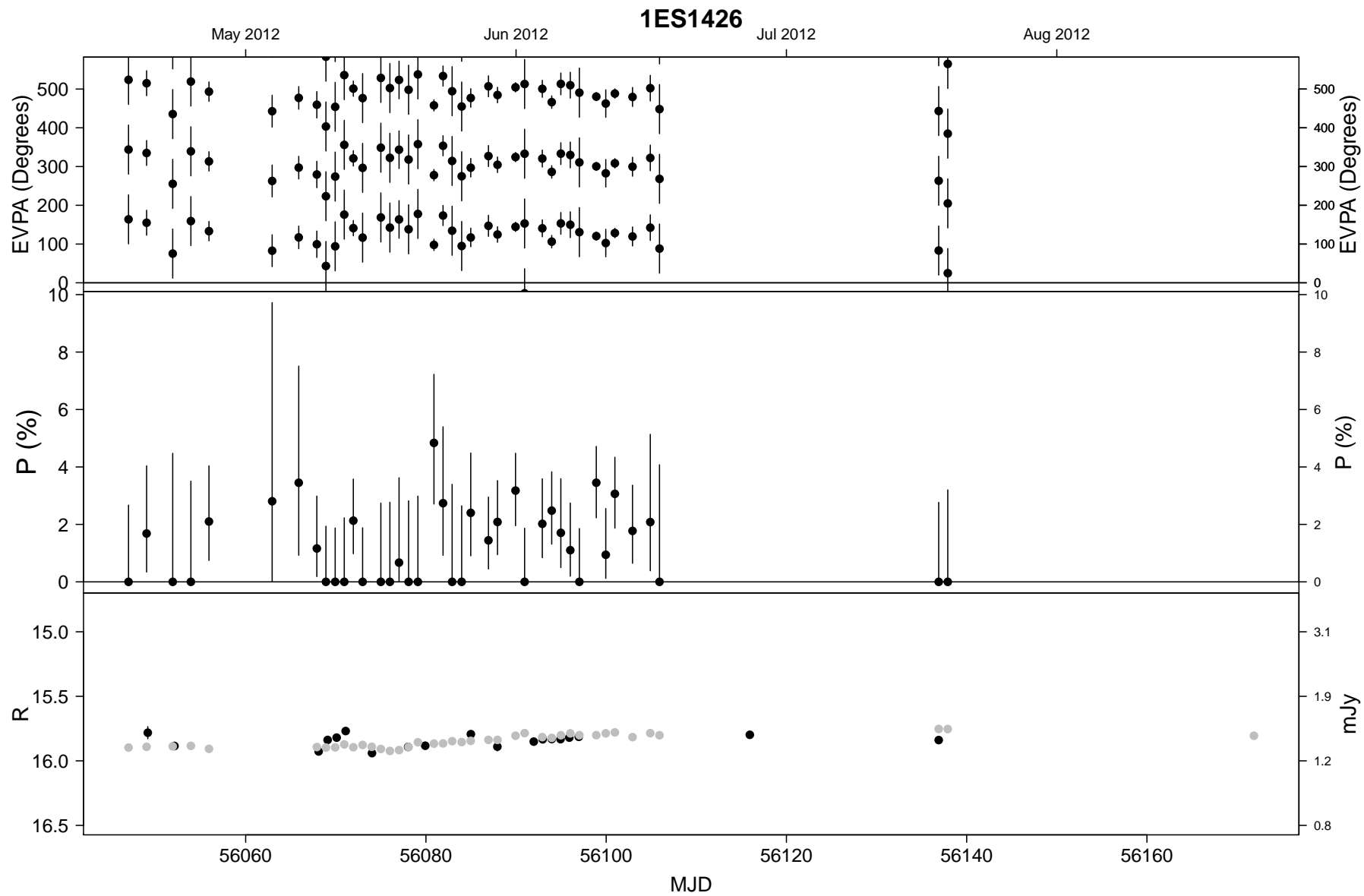
Figure 3.22
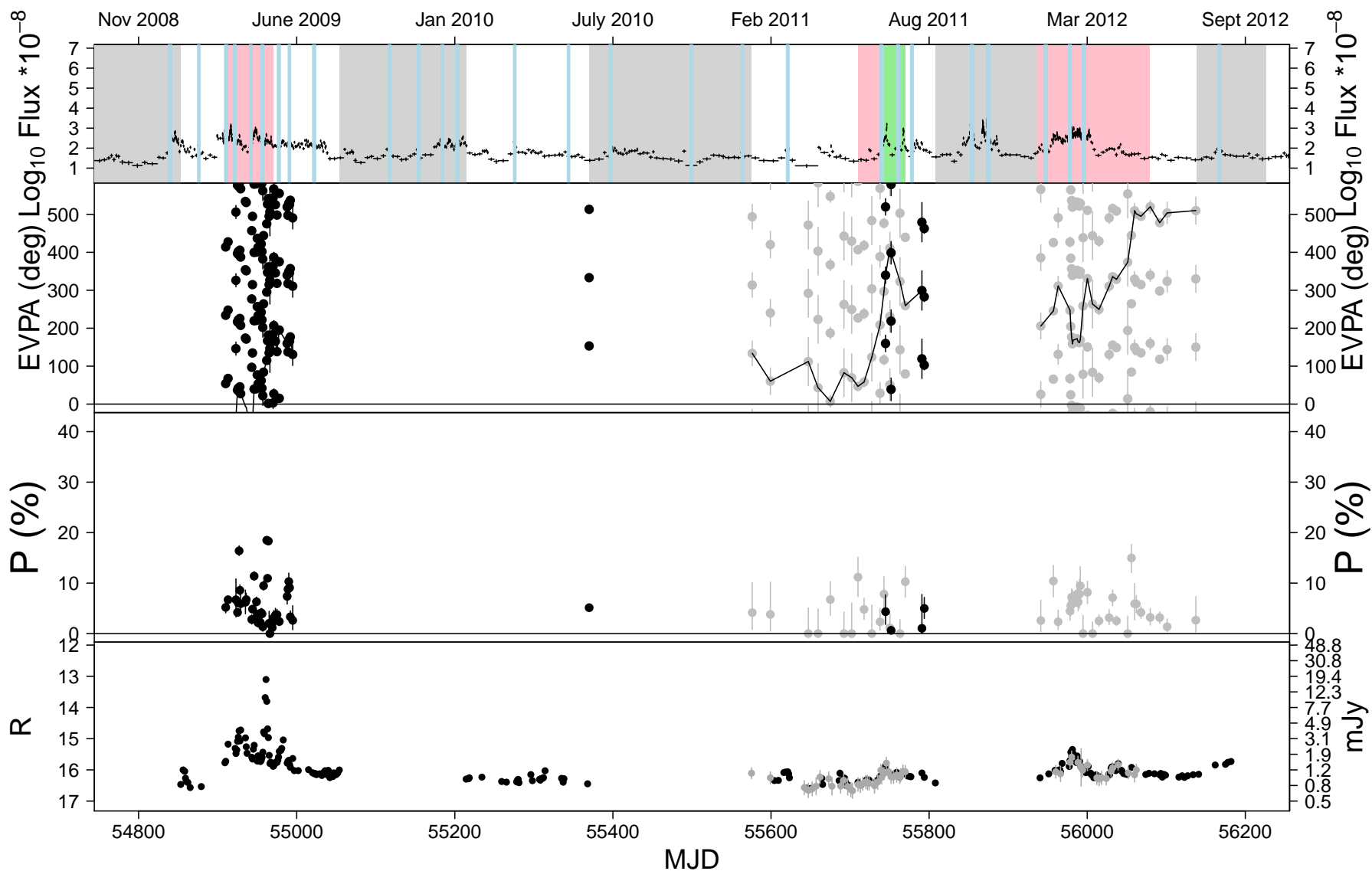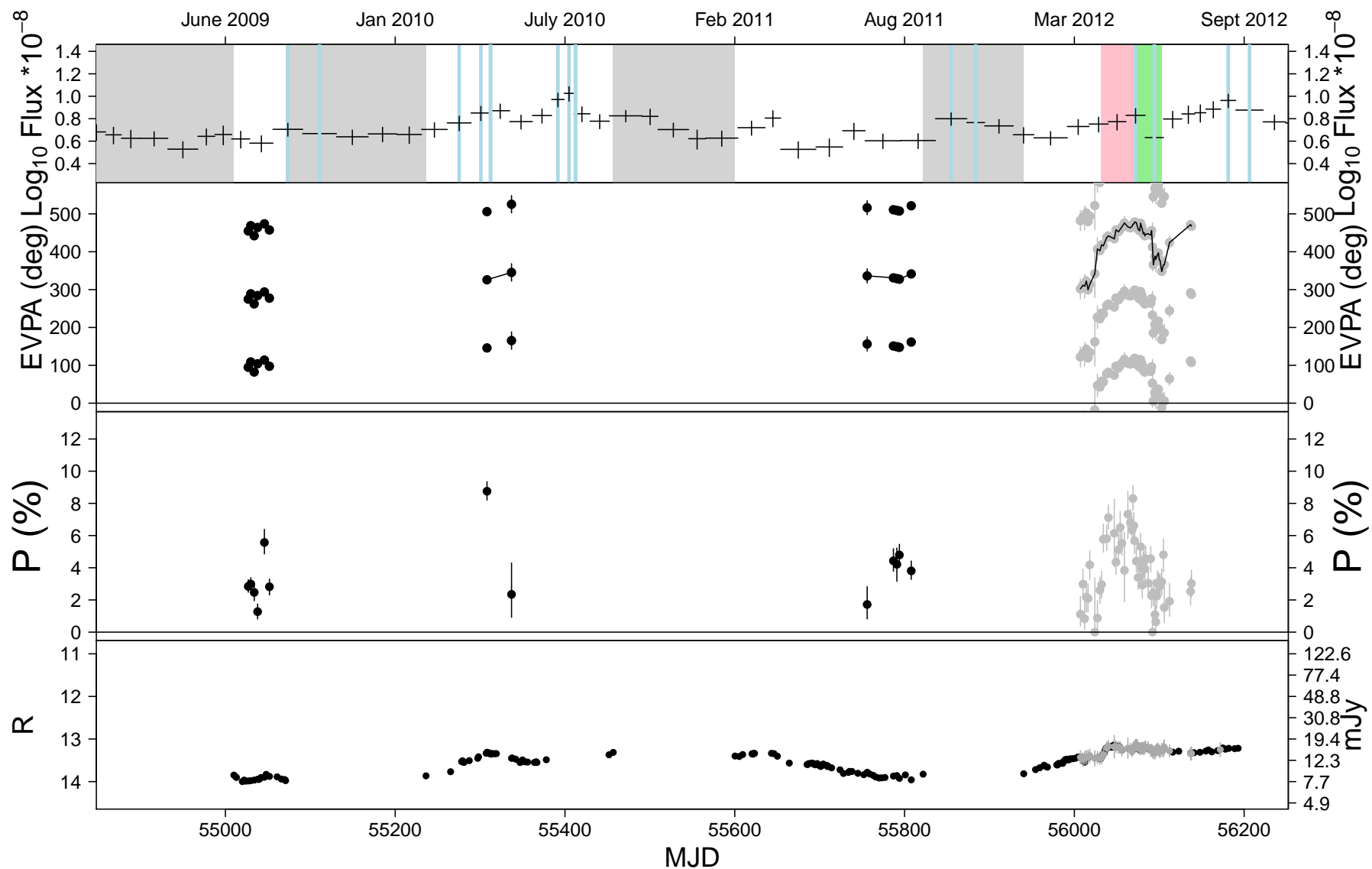
Figure 3.23
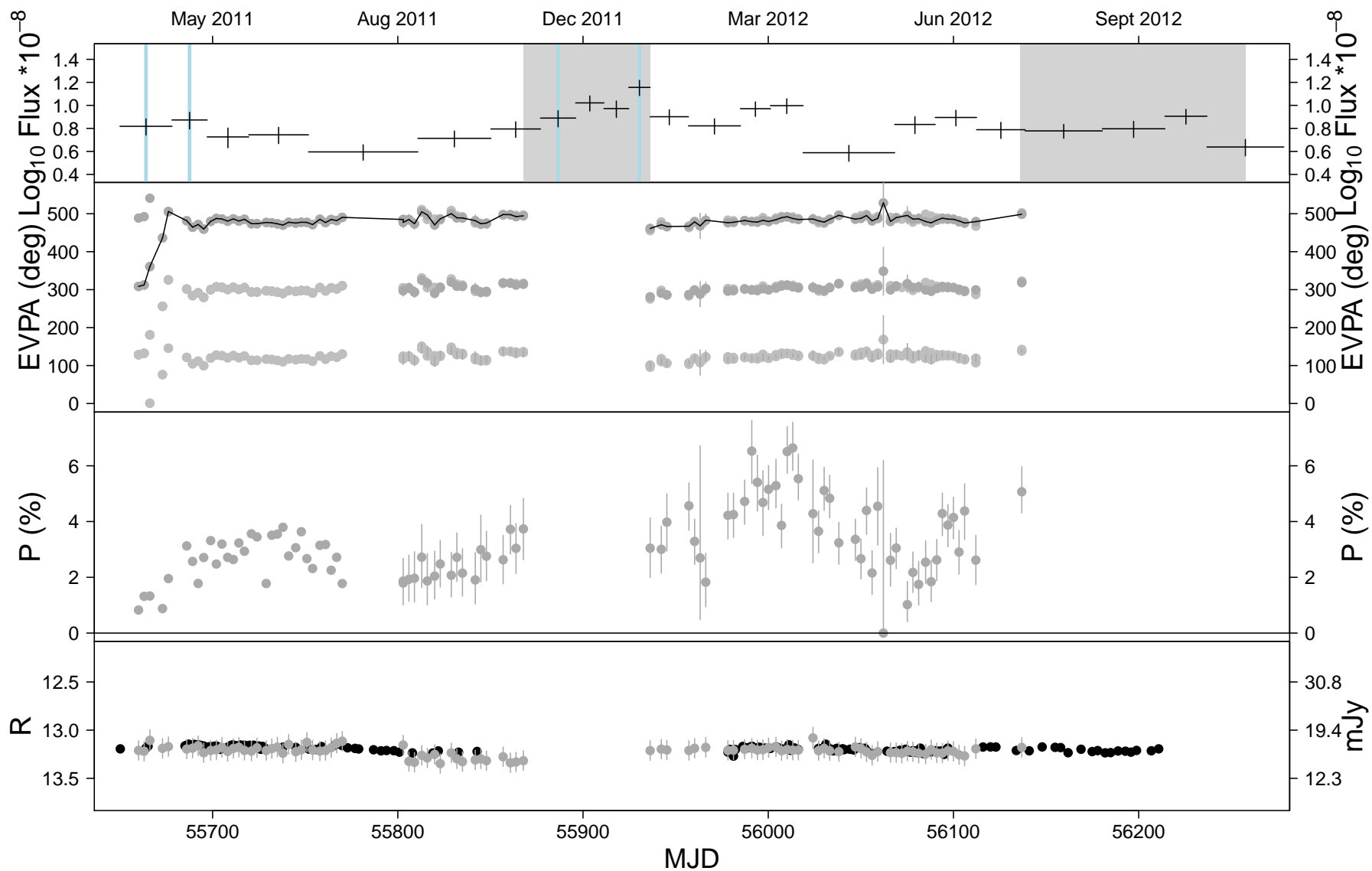
Figure 3.24

Figure 3.25

BL Lac.
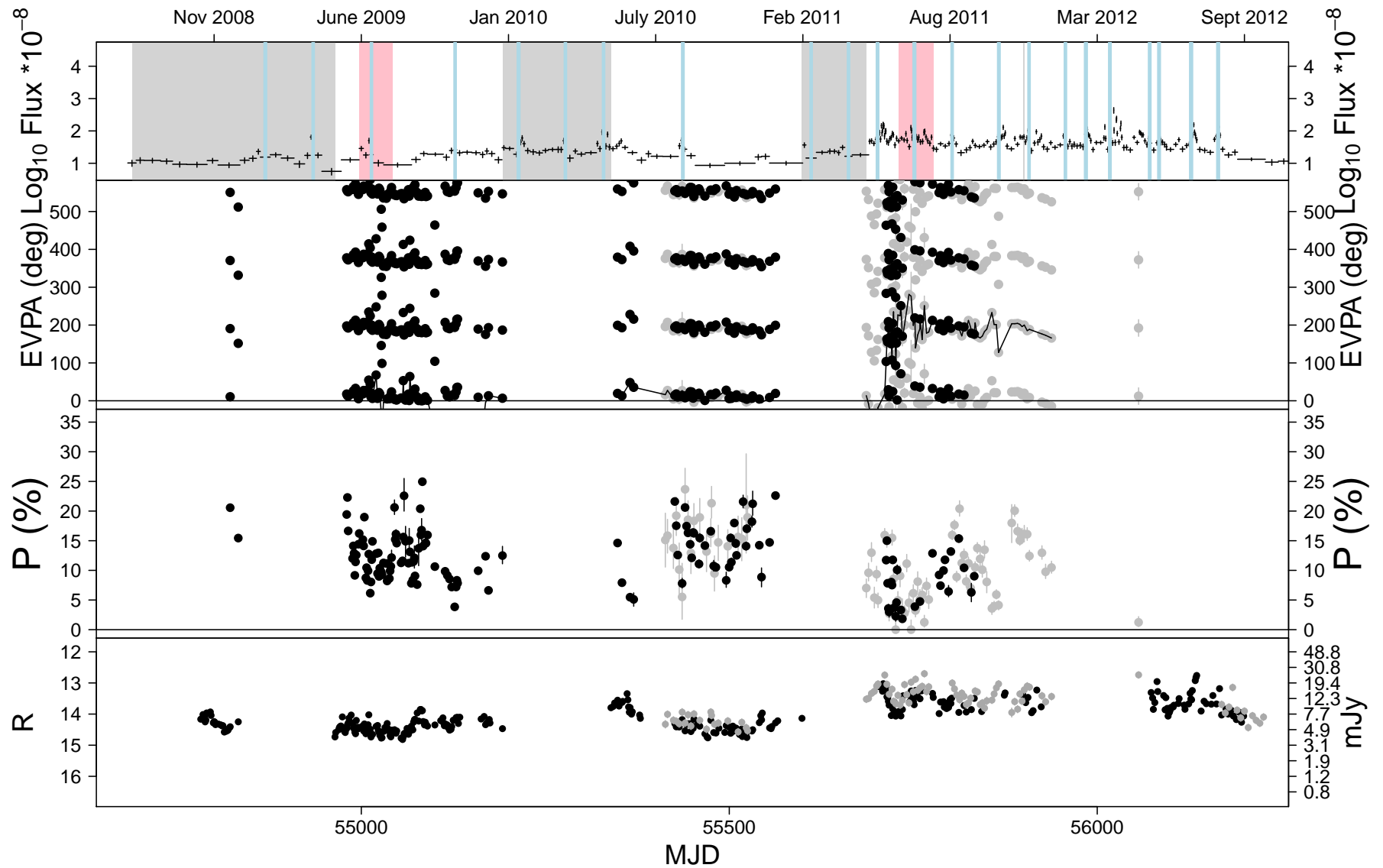
Figure 3.26

3.8 Chapter conclusions

The results from the Ringo2 analysis were presented in this chapter with a discussion of the sources, their properties and historical behaviour. We have found that the γ-ray and optical fluxes were significantly correlated which supports a single-site emission model for these two properties. The γ-ray/optical flux vs degree of polarisation were not strongly correlated, which suggests that at the emission site of the optical and γ-ray photons, the magnetic field is not strongly ordered.

We have shown that, for each source, when the number of optical rotations were corrected for their duty cycle, they were correlated with the number of γ-ray flares occurring during the same period. This can be explained by the model presented by Zhang et al. (2015b) in which they predict the features of a optical/γ-ray flaring event that coincides with a drastic change in polarisation signatures in 3C279 and interpret it as magnetic energy dissipation driving the flaring event. We have also found that all blazar subclasses show γ-ray flaring and EVPA rotations, but there are no systematic differences by class in γ-ray flaring rate or number of EVPA rotations. This is consistent with other studies.

Further discussions of the implications of these results (combined with the Ringo3 data) are presented in Section 5.1.

Source/Season	MJD range	ρ (gam-mag)	ρ (gam-deg)	ρ (deg-mag)	p (gam-mag)	p (gam-deg)	p (deg-mag)
3C66A							
a	<55300	0.508	-0.287	0.299	7.30×10^{-6}	0.0659	0.00941
b	>55300 & <55700	0.0670	-0.400	...	0.524	0.000668	...
c	>55700 & <56100	0.119	0.114	...	0.287	0.261	...
d	>56100	0.491	0.188	...	0.154	0.608	...
S50716+714							
a	<55000	0.480	-0.0129	-0.0754	9.94×10^{-6}	0.946	0.759
b	>55000 & <55400	0.523	0.411	...	2.54×10^{-5}	0.101	...
c	>55400 & <55800	0.127	0.272	...	0.302	0.0108	...
d	>55800	0.586	-0.0324	...	1.83×10^{-6}	0.758	...
OJ287							
a	<55000	0.493	-0.230	0.000547	3.41×10^{-6}	0.177	0.999
b	>55000 & <55400	0.565	-0.235	...	3.75×10^{-6}	0.331	...
c	>55400 & <55800	-0.304	0.351	...	0.0153	0.120	...
d	>55800	0.470	0.0126	...	1.54×10^{-4}	0.925	...
1ES1011+496							
a	>56000	...	...	0.500	...	...	0.0191
Mrk421							
a	>55800 & <55150	0.577	0.0649	0.0933	2.2×10^{-16}	0.296	0.133
Mrk180							
a	<56025	...	...	0.429	...	...	0.419
1ES1218+304							
a	>56050	...	...	0.111	...	...	0.695
ON231							
a	<55100	0.0860	0.130	0.395	0.506	0.455	1.53×10^{-11}
b	>55100 & <55500	0.297	0.126	...	0.0660	0.683	...
c	>55500 & <55800	0.635	-0.560	...	1.64×10^{-4}	0.00830	...
d	>55800	0.708	-0.305	...	7.43×10^{-5}	0.178	...
PKS1222+216							
a	<55800	0.0303	...	0.245	0.946	...	0.342
b	>55800	-0.600	-0.199	...	8.23×10^{-6}	0.174	...
3C279							
a	<55100	0.711	-0.249	0.270	0.000	0.263	0.0607
b	>55100 & <55500	0.376	...	...	0.0238	...	...
c	>55500 & 55800	0.697	-0.0197	...	6.54×10^{-9}	0.912	...
d	>55800	0.489	0.556	...	0.00525	1.52×10^{-6}	...
1ES1426							
a	<56120	...	...	0.105	...	...	0.518
PKS1510-089							
a	<55100	0.669	0.360	0.0986	3.67×10^{-12}	0.0248	0.486
b	>55100 & <55500	0.00339	...	...	0.988	...	...
c	>55500 & <55900	0.554	-0.0277	...	4.51×10^{-7}	0.817	...
d	>55900	0.565	0.362	...	1.17×10^{-8}	3.91×10^{-5}	...
PG1553+113							
a	<55100	0.180	0.419	0.549	0.435	0.419	1.98×10^{-5}
b	>55100 & <55500	0.745	...	...	2.34×10^{-6}	...	...
c	>55500 & <55900	0.0718	...	...	0.620	...	...
d	>55900	0.502	0.633	...	5.60×10^{-16}	1.89×10^{-13}	...
Mrk501							
a	<55900	0.109	-0.121	0.0876	0.262	0.235	0.403
b	>55900	-0.0929	0.160	...	0.152	0.0288	...
BL Lac							
a	<55300	0.287	-0.210	-0.485	0.000493	0.0627	1.50×10^{-6}
b	>55300 & <55650	0.680	0.0168	...	4.97×10^{-11}	0.900	...
c	>55650 & <55990	0.548	-0.205	...	1.71×10^{-5}	0.0719	...
d	>55990	0.718	0.143	...	3.66×10^{-8}	0.803	...

Table 3.6: Full table of Spearman Rank Correlation results (ρ and p value) for all sources and all seasons. Empty fields represent sources that were not observed in that season or lack one of the datasets required for that analysis. For the optical magnitude and degree of polarisation values there is only one for each source as the data were not split into seasons (see Section 3.5.1 for more details).

Chapter 4

Ringo3 analysis

The Ringo2 sample of blazars detailed in the previous Chapter continued to be monitored using the Ringo3 polarimeter (Ringo2's successor). There are an additional 5 sources in the sample (S4 0954+658, IC310, 3C120, PKS 0502+049 and PKS 0736+017). These were added as they were reported as being γ-ray active. The same analysis used to explore the Ringo2 sample was extended to the Ringo3 data, with the addition of a colour analysis made possible by the three wavebands on the Ringo3 instrument.

The Ringo3 data reduction and calibration procedures were a significant part of this project and are detailed in this chapter along with the analysis, results and conclusions for this data set.

4.1 Data reduction

The principal hardware components of Ringo3 were taken from Ringo2 and therefore the data extraction procedure was the same (see Section 2.3). However, with the introduction of the dichroic mirrors and a higher quality Polaroid, there were changes in the polarimetric reduction process. The specific Ringo3 improvements and reduction

requirements are detailed below.

4.1.1 Instrumental Polarisation

The nature of the observations using the Liverpool Telescope (at different sky position angles) results in the measured Stokes parameters being presented as a circle, the radius of which is the degree of polarisation (see Section 2.2.2). To correct for instrumental polarisation it was necessary to constrain the amount by which this circle was offset from the origin of the plot. For Ringo2 this was a constant, however, initially for Ringo3 the circle was imperfect and the origin-offset varied (see Figure 4.2). The cause of this was traced back to the interaction between the polarised light output from the Polaroid and the dichroic mirrors: it was introducing an additional polarisation to the measured value. The origin of the circle/ellipse varied as a function of the polarisation of the source, so unless one had prior knowledge of the location of the origin (note that repeated measurements of variable polarisation sources do not produce a circle like the observations of the standard stars) the degree or angle of polarisation could not be calculated correctly.

Between 3rd - 6th December 2013 there was a maintenance trip to Roque de los Muchachos, La Palma, Canary Islands. During this visit I fitted a quartz-wedge achromatic depolariser (DPU-25 from Thor Labs[1]) to the collimator lens input in order to reduce the polarised light interacting with the dichroic mirrors (which produced an instrumental polarisation). The depolariser pseudo-randomises the polarised beam of light (i.e. it does not become truly unpolarised) using two crystal quartz wedges, one which is half as thick as the other. The light is polarised in the same direction as the optic axis of the thick wedge, at varying degrees due to the difference in width from the top to the bottom of the wedge. The light then travels through the optic axis of the thin wedge which is at a $45°$ angle to the thick wedge and the width differences in this

---

[1] www.thorlabs.de
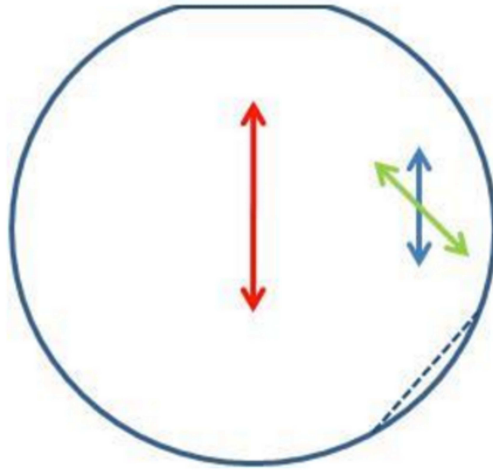
Figure 1. Input polarization in a parallel arrangement with the optic axis of the thick wedge.

Figure 4.1: Schematic of the depolariser used in the collimator lens to randomise the polarised beam of light. The red arrow shows the direction of the input polarisation and the blue and green arrows show the orientation of the thick and thin wedges within the depolariser. Taken from http://www.thorlabs.de/newgrouppage9.cfm?objectgroup_id=870

wedge cause further randomising of the polarisation of the light beam.

The following description was taken from a site report written, by myself, during the Ringo3 maintenance.

The first step was to remove Ringo3 from the telescope. This involved removing the appropriate cables and switching off the controlling computers. The individual cameras were then removed, one by one, carefully, as their lenses protruded into the main polarimeter body. The main body of the polarimeter was then removed from the telescope. Each camera requires a different length in order to focus the light correctly which means that some of the cameras have 'spacers' with them which are either panels or washers to align them correctly. These were all removed from the body of polarimeter including the front panels of the instrument. Then the appropriate screws were located and removed in order to delicately remove the side panel from the instrument (the side that has the junction box on it). Once the side was removed the dichroic mirrors were visible. The top dichroic mirror was removed carefully and placed to one side. The collimator lens was then replaced with a similar one, previously constructed
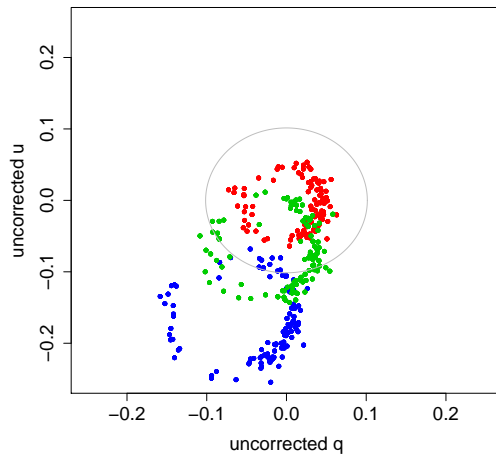
Figure 4.2: Linear Stokes parameters q and u for polarised standard star VI Cyg 12, prior to introduction of the depolariser to the collimator lens. The points create a circle due to the angle of the instrument changing with respect to the source. The grey circle shows the R band literature polarisation for the source, the red, green and blue points are from the red, green and blue cameras respectively.
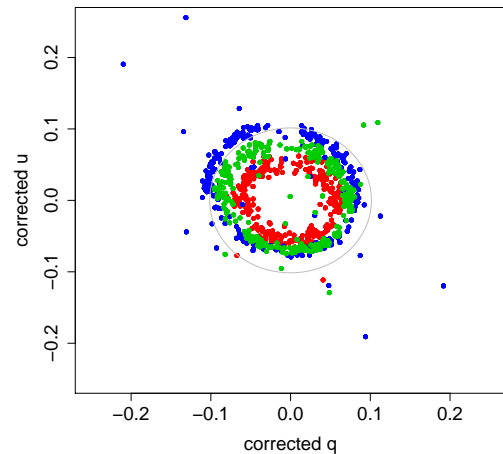
Figure 4.3: Linear Stokes parameters q and u for polarised standard star VI Cyg 12, post introduction of the depolariser to the collimator lens. The points create a circle due to the angle of the instrument changing with respect to the source. The grey circle shows the R band literature polarisation for the source, the red, green and blue points are from the red, green and blue cameras respectively.

with the Lyot depolarising prism inside the body. Care was taken to insure the replacement lens was the same as the previous one, and the focus and f/ratio settings were identical. Once this was done the lens was returned to its place and the settings were sticky-taped into place. The pieces were all then replaced in the correct order onto the polarimeter and it was carefully returned to the LT along with all three of its cameras.

The introduction of a depolariser to an instrument designed to measure polarisation seems counterintuitive. However, because the Ringo3 polarimeter measures the polarisation properties of a source according to the intensity of the light through different Polaroid positions, once the light is through the Polaroid, the polarisation is no longer important. The depolariser greatly improved the repeatability of standard star measurements (see Figures 4.2 and 4.3 for comparison). For even greater improvement, on 08-06-2014 the depolariser was moved from the lens input to the collimated beam where it intercepted a wider beam leading to greater depolarising efficiency.

Period (MJD)	56226 - 56392	56392 - 56638	56638 - 56816	56816 - 57202	>57202
q (red)	NA	NA	-0.0119	-0.0154	-0.0131
u (red)	NA	NA	-0.0410	0.0295	-0.0336
q (green)	NA	NA	-0.0163	-0.0157	-0.0105
u (green)	NA	NA	-0.0371	0.0333	-0.0356
q (blue)	NA	NA	-0.00968	-0.00775	-0.00476
u (blue)	NA	NA	-0.0177	0.0215	-0.0218

Table 4.1: The mean values of Linear Stokes parameters, q and u, of zero polarised standards during different maintenance periods for each Ringo3 camera. The NA values represent periods when the instrumental polarisation was not constrainable.

The procedure of calculating the residual instrumental polarisation was the same as that for Ringo2. The linear Stokes Parameters, q and u, were calculated for zero-polarised standards (which effectively should have q=u=0). The deviation from zero was recorded for different periods of stability (i.e. in between maintenance or removal of the instrument), and the median of the Stokes Parameters (q and u) over the period was then subtracted from the Stokes Parameters measured for the science target (see Figure 4.4 for an example of q and u offsets for two periods of stability). The full lists of instrumental polarisation offsets are shown in Table 3.2 for Ringo2 and Table 4.1 for Ringo3.

4.1.2 Instrumental Depolarisation

Instrumental depolarisation is related to the efficiency of the Polaroid's contrast ratio. The instrumental depolarisation for Ringo3 was characterised by comparing the measured degree of polarisation (from the radius of the q and u circle) to that in the literature for standard polarised sources. The presence of dichroic mirrors causes the Stokes circle to be elongated (with the semi-major axis parallel to the q values on the x axis) and shifted from the origin. A multiplicative factor of 1.14 applied to the q values corrects for the ellipticity (priv. comm. D. Arnold).

The degree of polarisation (DOP) was measured as the radius of the standard star q and u ring (i.e. DOP = $\sqrt{q^2 + u^2}$). The introduction of the depolarising optic meant that
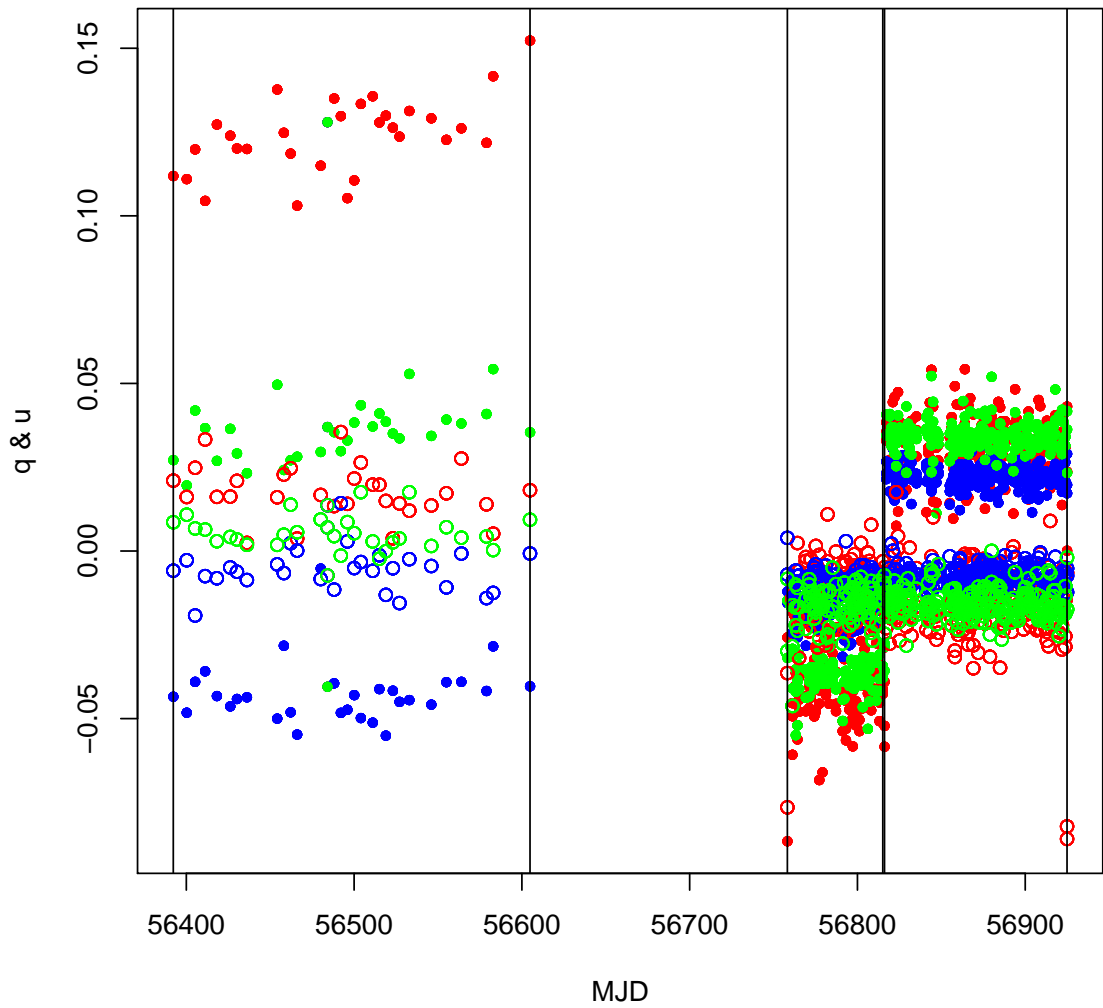
Figure 4.4: Linear Stokes parameters for BD+28 4211 which are used for instrumental polarisation calibration for Ringo3. Open circles are q values and closed circles are u values, for each camera (red, green and blue points).
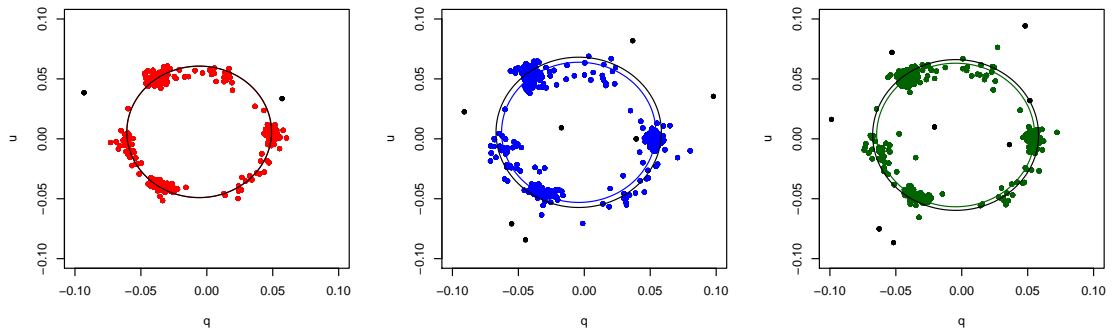
Figure 4.5: q and u plots for standard polarised star BD+25 727 for red, blue and green cameras. The black circle shows the literature polarisation value in each band. The coloured points are the q and u values for each camera and the coloured circle has a radius equal to the mean of the points.

the ring had a standard offset from the origin which was calculated by measuring the mean difference between the q and u values for non-polarised standard stars and zero (making the assumption that these standards were 100% non-polarised).

For visual comparison of literature to measured degree of polarisation (DOP) for standard stars, a circle was fitted to the datapoints for the measured (mean) DOP and the literature DOP. Figures 4.5, 4.6, 4.7 and 4.8 show the mean (blue circle) and literature (black circle) degree of polarisation. The q and u values associated with measurements of 110 counts or less were not included in the fit due to the low number of counts causing them to skew the analysis (see black points in Figures 4.5, 4.6, 4.7 and 4.8). In the red band the measured DOP was slightly larger than the literature value. This may be due to non-standard (e.g. not Johnson Cousin) filters used in Ringo3, however, for uniformity we applied the depolarisation correction to correspond with the literature values.

Figure 4.10 shows the comparison between the literature and measured degree of polarisation values. The mean of each gradient; red = 1.15, blue = 0.89 and green = 0.82 (shown in Table 4.3) was taken (0.96), and this factor was applied to the all science measurements of the degree of polarisation with Ringo3 (this factor was included in the R pipeline written for this project).
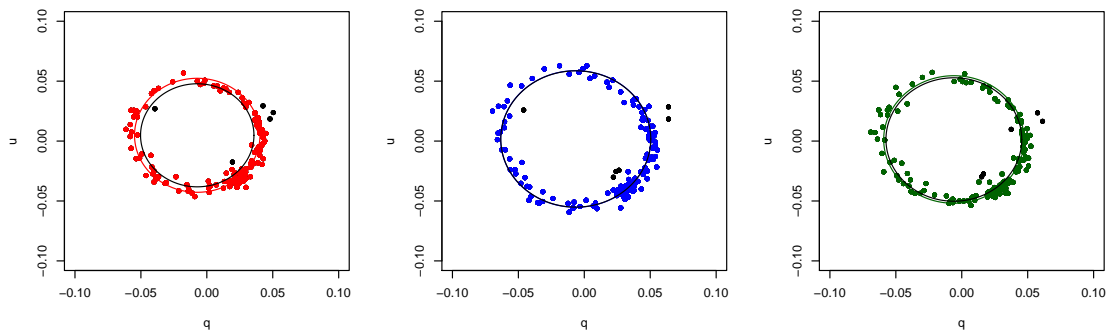
Figure 4.6: q and u plots for standard polarised star BD+64 for red, blue and green cameras. The black circle shows the literature polarisation value in each band. The coloured points are the q and u values for each camera and the coloured circle has a radius equal to the mean of the points.
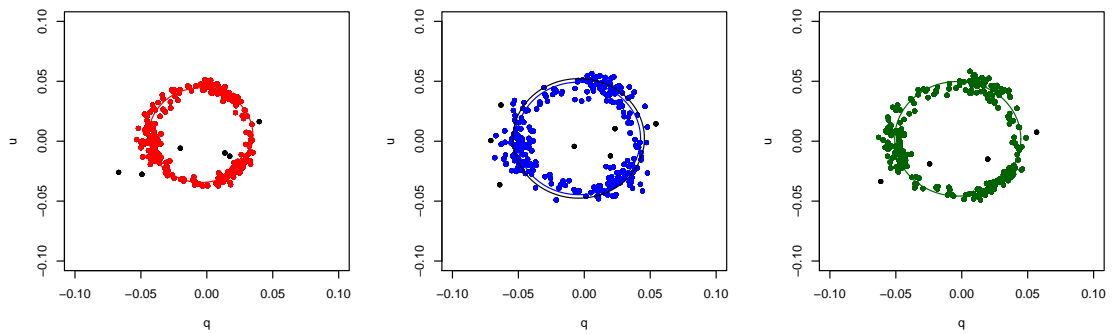
Figure 4.7: q and u plots for standard polarised star HD155528 for red, blue and green cameras. The black circle shows the literature polarisation value in each band. The coloured points are the q and u values for each camera and the coloured circle has a radius equal to the mean of the points.
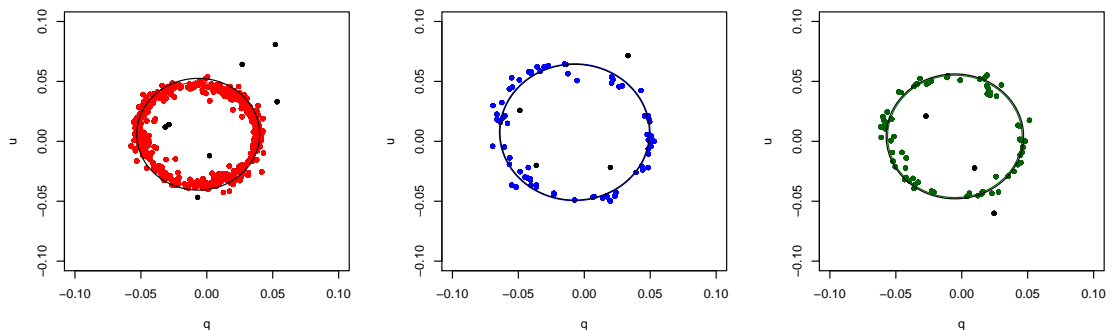
Figure 4.8: Linear Stokes Parameters (q and u) plots for the three Ringo3 cameras, red, blue and green for the standard polarised star Hiltner 960. The coloured points show the q and u values measured by the instrument, the black points show those data that were not included due to them being outliers and having counts <110. The coloured circle is the mean of the coloured points and the black circle is the literature polarisation value for the nearest lying band.

A study by other Ringo3 users reported degree of polarisation correction values of blue = 0.78 green = 0.84 and red = 0.75 (Słowikowska et al., 2016). Our methods of calculating the Stokes Parameters were slightly different. Słowikowska et al. (2016) used the n-polarizer method which assumes the eight Ringo exposures are through eight different fixed Polaroids (Sparks & Axon, 1999), whereas the Clarke & Neumayer (2002) method used in this work assumes the same Polaroid is used at eight different angles. We also corrected our Ringo3 data for ellipticity of the q-u ring (a multiplicative factor of 1.14 applied to the q values). This required the adjustment factor to be slightly larger than that used by Słowikowska et al. (2016). Different literature polarisation values were used in the Słowikowska et al. (2016) work to this project. We used the value of 0.96 for this analysis. Our values yielded final measurements that were comparable with polarisation values from the Steward Observatory[2] (see Figure 4.9).

For Ringo2 the factor was 0.76 (Steele et al., 2006). We attribute the improved correction to the better contrast ratio in the new Ringo3 Polaroid.

Correcting for Instrumental Angle

The angle measured by the Ringo Polarimeters is relative to the positioning of the telescope and instrument. The position of the telescope, i.e. the rotation of the Cassegrain, was quantified using the ROTSKYPA fits header, which gives the angle of rotation East of North on the sky. To account for the angle of the instrument itself, it was necessary to measure the polarisation angle of a polarised standard (PA_S) and note the shift of the measured position angle to that in the literature (PA_T).

$$PA_T = PA_S + ROTSKYPA + K \qquad (4.1)$$

An average of this value, K, over a period of stability (i.e. during which the polarimeter

---

[2]http://james.as.arizona.edu/ psmith/Fermi/
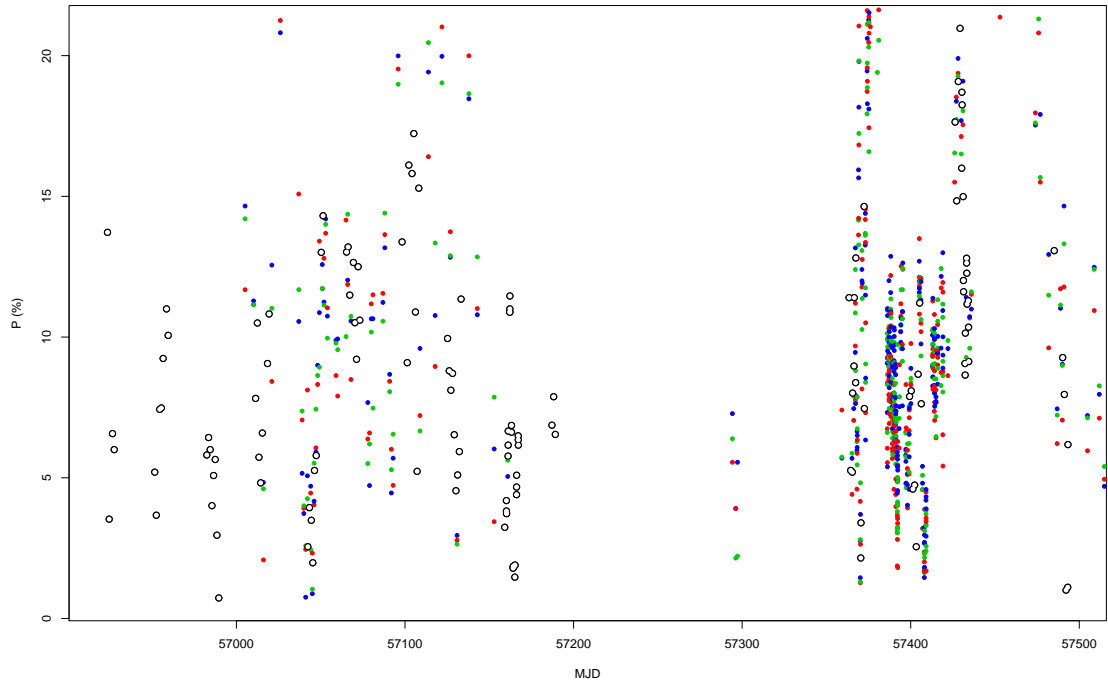
Figure 4.9: Comparison of Ringo3 (colours) and Steward (black) polarisation data for a high degree of polarisation period for OJ287 as a consistency check. The 0.96 polarisation correction factor used in this work will calculate lower polarisation values than those using a 0.75-0.84 factor (Słowikowska et al., 2016). Since the polarisations measured on the same night as the Steward Observatory (SO) values are sometimes higher than those measured by the SO it is safe to assume that our greater factor is sufficient and does not need to be smaller (which would predict even higher values of polarisation).
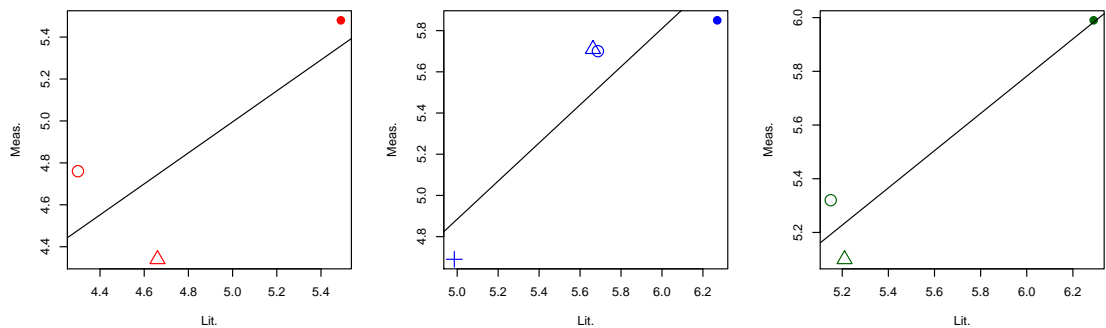
Figure 4.10: Comparison of literature and measured degree of polarisation values for the sources in Table 4.3. The colours represent the three different cameras and the different symbols represent different standard stars (as shown in Table 4.3).

Ringo3 Period	red	green	blue	red	green	blue
	K value (degrees)			standard deviation		
<20130123	NA	NA	NA	NA	NA	NA
>20130123 <20131212	NA	NA	NA	NA	NA	NA
>20131212 <20140608	57.39	54.58	54.93	4.26	3.60	3.94
>20140608 <20150629	115.15	115.95	115.42	3.75	3.25	2.92
>20150629	125.61	124.80	124.90	4.63	5.05	4.89

Table 4.2: Table of K values (polarisation angle zeropoint) for Ringo3 in each period and camera with the standard deviation for each period/camera. Again the NA values represent periods during which the instrumental polarisation is not constrainable.

was not removed from the telescope), was then used for every measurement to correct for the instrumental position angle. Figure 4.11 shows the K values for the Ringo3 polarimeter and Table 4.2 shows the numerical values and the standard deviation. The standard deviation on the K values was used to calculate the minimum error on the position angle. A combination of the standard deviations for each camera gives a minimum error of red = 4.2°, green = 4.0° and blue = 3.9°. Standard deviation was used here to represent the error, rather than standard error on the mean, as the standard deviation is a better description of the repeatability of the instrument as a whole, rather than the standard error on the mean which reflects the accuracy of the measurement of K.

Once the calibration parameters were defined, the polarisation extraction method described in Section 2.2.2 was used to calculate the Ringo3 angle and degree of polarisation.

Telescope Mirror Realuminising and motor speed changes

During a site visit in July 2015, both the primary and secondary mirrors were removed from the LT and taken to the William Herschel Telescope (WHT) for realuminisation. This was the first time the secondary mirror had been recoated, and its old coating was removed and replaced, resulting in a ~2x increase in sensitivity. In addition to this
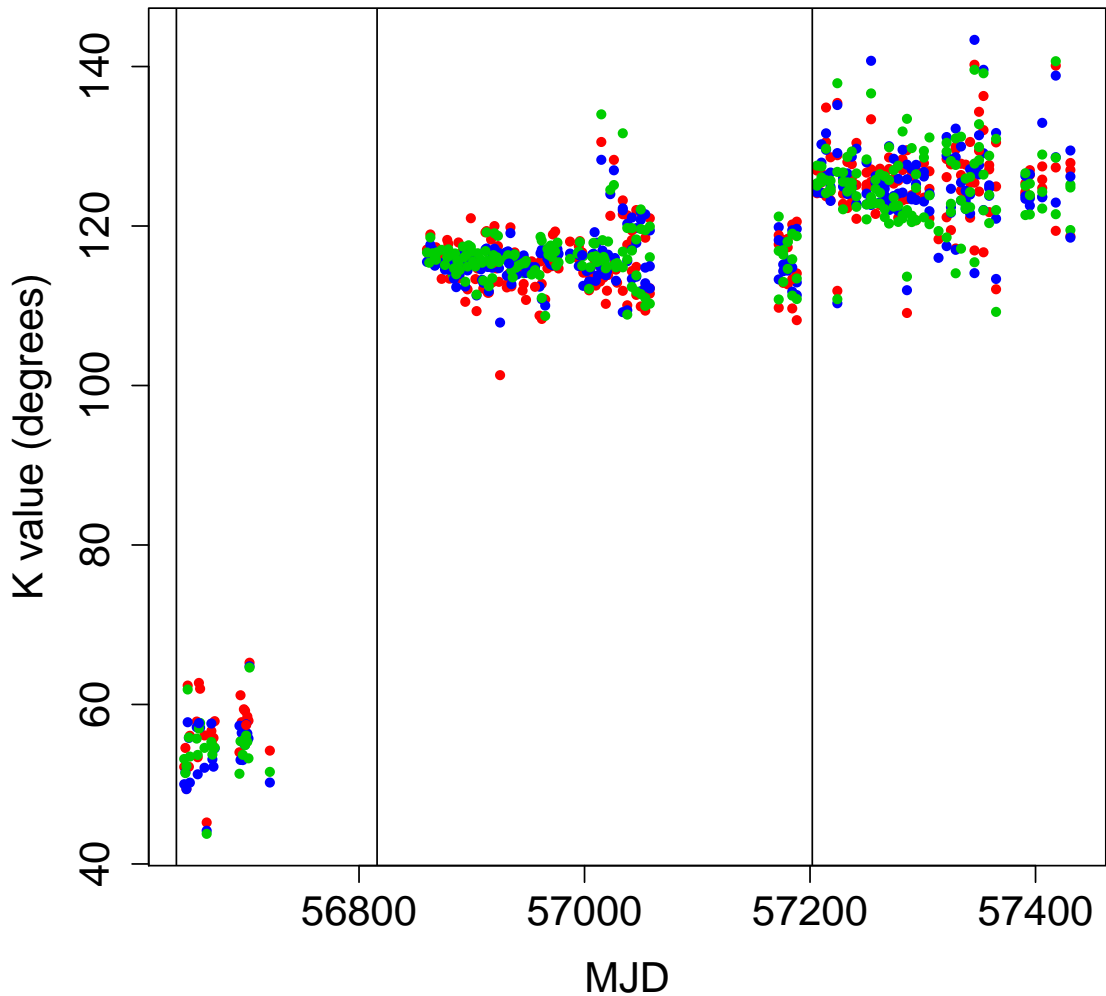
Figure 4.11: A plot of the K values for polarised standard BD+64 106. The vertical black lines show when the instrument was removed from the telescope and thus changes the K value. The periods after MJD∼56800 have less variation in the K values as the Polaroid was not removed from the polarimeter during these maintenance runs. Coloured points represent the red, green and blue cameras.

Star	Red (m = 1.15)		Blue (m = 0.89)		Green (m = 0.82)	
	Lit. Pol.	Meas. Pol.	Lit. Pol.	Meas. Pol.	Lit. Pol.	Meas. Pol.
BD+25 727 ●	5.49±0.037	5.48	6.28±0.037	5.85	6.18±0.033	5.99
BD+64 106 ○	4.696±0.052	4.76	5.687±0.037	5.70	5.150±0.098	5.32
Hilt 960 △	4.455±0.030	4.34	5.663±0.021	5.71	5.210±0.029	5.10
HD155528 +	4.18±0.06	3.95	4.94±0.06	4.69	4.75±0.05	4.78

Table 4.3: Table of standard star polarisation values for each of the 3 Ringo3 colours. Symbols are to aid comparison with Figure 4.10. References : HD155528 Chavero et al. (2006), BD+64 106 and HILT 960 Schmidt et al. (1992) and BD+25 727 Wisniewski (2005).

improvement, the motor for the Ringo3 Polaroid (which had operated at one rotation per second; its slowest speed) was replaced with another motor which could slow the rotation even further, allowing more counts to be collected in each rotor position and thus increase sensitivity. The Polaroid rotation was slowed to one rotation every 4 seconds. As a result of the introduction of a new motor that rotates the Polaroid in the reverse direction, the Stokes u parameter values became negative. To correct for this a negative sign was added to all u values after July 2015 (MJD = 57202).

4.1.3   Three-colour magnitude calibration

To calibrate the secondary star magnitudes for use with Ringo3 data reduction it was necessary to have three different reference secondary standard star magnitudes for each blazar in each Ringo3 waveband. These values were not available since the wavebands themselves are non-standard, so the following procedure was carried out to calibrate the 3 band magnitudes for the secondary stars for each source. In this work we refer to the Ringo3 wave bands as blue = 350-640 nm (b*), green = 650-760 nm (g*) and red = 770-1000 nm (r*).

Three spectral type A0 standard stars were selected from the Virtual Observatory SIM-BAD database; HD24083, HD50188 and HD92573. These stars have magnitudes in each band that are the same (to two decimal places). They therefore are 'natural 'calibrators in the Vega photometric system. These stars were observed on three photometric nights and once the data were quality checked, the counts (adjusted to match EMGAIN values of the blazar frames) for each star were used to calculate the nightly zeropoint for each camera as a function of wavelength (see Section 2.2.2 for zeropoint calculation). Figure 4.12 shows the zeropoints for the three different wavebands.

These zeropoints were then plotted against the corresponding airmasses to give an equation to calculate the zeropoint for the blazar sources (on the same or nearest dates)
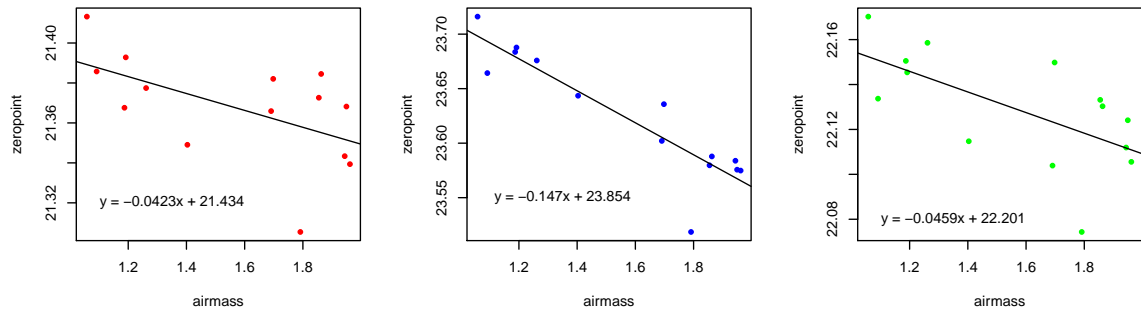
Figure 4.12: Ringo3 zeropoints as a function of airmass for the three different cameras (red, green and blue) using three different standard stars. Displayed on the plots are the linear fit equations which are shown as the black lines on each plot.

according to the airmass of the source observation. Once the respective zeropoint was calculated, it was used in the equation m = zp - 2.5 * $\log_{10}$(sec. star counts) to calculate the secondary star magnitude (in red, green and blue) on these dates (and the respective mean was taken). The secondary star magnitudes calculated in this way are shown in Table 4.4. For further clarity, Figure 4.13 shows the B-R magnitudes from the USNO-B1 catalogue against the b* - r* magnitudes from the b* and r* Ringo3 cameras respectively. There are two sources for which the B-R, b*-r* magnitudes do not follow a roughly linear correlation. These sources are ON231 (which only has one secondary star in the field) and 3C279 (which is in a field with secondary stars that also have B magnitude - R magnitude indices greater than the b* magnitude - r* magnitude indices).

4.2 Analysis

A similar analysis to that in Chapter 3 was conducted for the Ringo3 data, with additional study of the colour properties of the sources. The definition of EVPA rotations and γ-ray flares are kept the same as for the Ringo2 analysis (see Section 3.3.1) for continuity purposes.

Source	Star RA	Star Dec	red mag	blue mag	green mag	R mag[1]	B mag[1]
(1) 3C66A	02:22:40.5	+43:01:35.9	16.58	17.60	16.80	16.60	17.59
(2) IC310	03:16:47.19	+41:19:57.4	15.10	16.50	15.48	15.20	16.77
(3) 3C120	04:33:12.445	+05:21:16.14	15.70	17.08	16.07	15.97	17.64
(4) PKS 0502+049	05:05:24	+4:58:54.95	13.05	15.14	13.75	14.08	16.19
(5) S5 0716+014	07:21:54.35	+71:19:20.8	13.03	13.91	13.23	13.99	14.75
(6) PKS 0736 +01	07:39:16.10	+01:37:35.66	14.80	15.54	14.98	15.02	15.63
(7) OJ287	08:54:46.12	+20:07:19.97	15.49	16.65	15.78	15.68	16.97
(8) S4 0954+658	09:58:44.52	+65:33:28.39	15.99	17.32	16.34	16.05	17.74
(9) 1ES 1011+496	10:15:08.03	+49:25:42.1	13.89	14.83	14.16	13.74	14.89
(10) Mrk 180	11:36:40.52	+70:10:16.01	13.72	14.59	13.95	14.30	14.87
(11) 1ES 1218+304	12:21:23.09	+30:10:38.97	15.14	16.83	15.56	15.48	17.59
(12) ON231	12:21:27.83	+28:14:37.9	17.19	18.08	17.35	17.75	20.94
(13) PKS 1222+216	12:25:01.68	+21:23:24.31	15.59	16.75	15.88	15.97	17.09
(14) 3C279	12:56:14.73	-05:47:36.72	16.75	19.52	17.78	17.27	19.48
(15) 1ES 1426+428	14:28:32	+42:39:36	16.50	17.64	16.79	16.72	17.88
(16) PKS 1510-089	15:12:51.669	-09:05:23.33	14.18	15.14	14.39	13.90	14.81
(17) PG1553+113	15:55:46.09	+11:11:19.6	15.35	16.57	15.63	15.07	16.35
(18) Mrk 501	16:53:56.18	+39:44:59.10	15.52	16.98	16.02	15.41	17.11
(19) BL Lac	22:02:53.556	+42:17:46.92	13.51	14.67	13.76	13.82	15.64

Table 4.4: Table of the Ringo3 sources and the secondary star used for magnitude calibration (with right ascension and declination co-ordinates). The R and B magnitude values are taken from the USNO-B1 catalogue [1]Monet et al. (2003). The r*, b* and g* magnitudes are found using the gradient of zeropoint and airmass values calculated using standard stars.
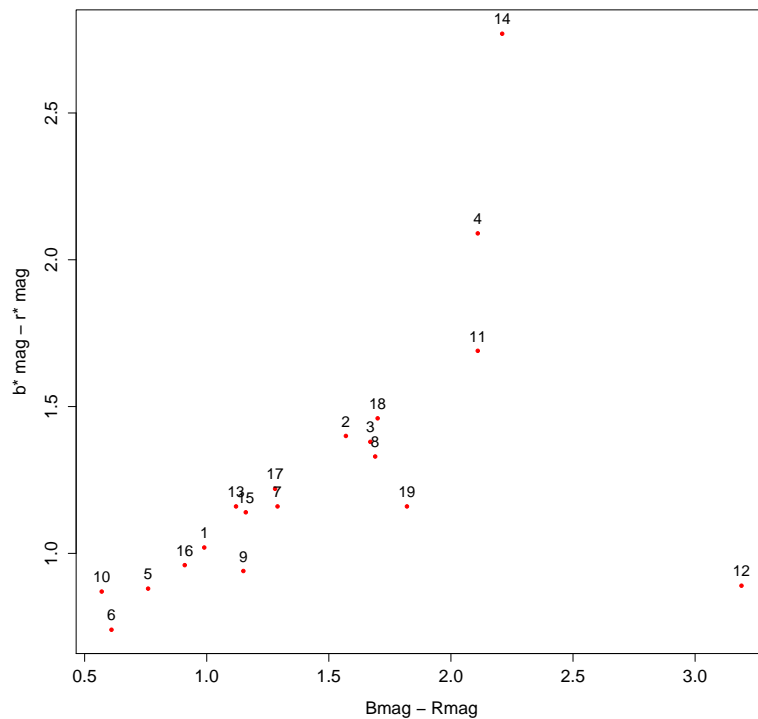
Figure 4.13: B-R colour magnitude plot.
B magnitude - R magnitude (USNO-B1) and b* magnitude - r* magnitude comparison plot for source in Table 4.4. Numerical notation matches those in the Table.

Name	z	Type	r* Mag. range	g* Mag. range	b* Mag. range	r* Pol. range (%)	g* Pol. range (%)	b* Pol. range (%)	Fermi range phot. cm^{-2} s^{-1}	Observation Period (MJD)	Absent data
3C66a	0.444	ISP	14.38 - 12.57	14.68 - 13.22	15.43 - 13.99	0.75 - 13.54	0.71 - 12.32	0.31 - 12.44	5.41x10^{-8} - 1.65x10^{-7}	56267.924 - 57406.978	...
IC310	0.019	HSP	13.11 - 12.12	13.75 - 12.69	15.17 - 13.72	0.71 - 7.58	0.21 - 16.54	0.55 - 19.72	3.04x10^{-13} - 1.93x10^{-8}	57036.863 - 57391.908	...
3C120	0.034	LSP (FSRQ)	14.18 - 13.61	14.13 - 13.41	15.43 - 14.81	0.06 - 4.25	0.10 - 4.11	0.25 - 4.42	...	57036.860 - 57391.910	Fermi
PKS 0502+049	0.954	LSP (FSRQ)	19.03 - 14.23	18.93 - 14.68	19.14 - 15.31	2.13 - 36.83	2.53 - 30.27	0.70 - 25.29	4.08x10^{-8} - 4.26x10^{-6}	56693.892 - 57427.923	...
S5 0716+714	0.31	ISP	14.51 - 11.32	14.97 - 11.72	15.72 - 12.50	0.72 - 27.56	0.90 - 27.67	1.37 - 27.89	6.16x10^{-8} - 2.17x10^{-6}	56267.973 - 57413.033	...
PKS 0736+017	0.189	LSP (FSRQ)	16.32 - 14.41	17.32 - 14.87	17.96 - 15.66	0.60 - 24.81	0.62 - 28.28	0.63 - 40.26	5.43x10^{-8} - 5.02x10^{-6}	57007.998 - 57413.024	...
OJ287	0.306	LSP	15.09 - 13.15	15.55 - 13.64	16.35 - 14.39	1.27 - 40.98	1.04 - 41.00	0.76 - 43.12	4.86x10^{-8} - 4.21x10^{-7}	57005.122 - 57435.987	...
S4 0954+65	0.367	LSP	16.23 - 13.80	16.76 - 14.37	17.46 - 15.06	0.39 - 33.28	0.83 - 34.78	0.53 - 33.76	6.47x10^{-8} - 2.57x10^{-6}	57160.904 - 57426.040	...
1ES 1011+496	0.212	HSP	15.51 - 14.88	15.81 - 15.25	16.44 - 15.78	0.38 - 16.96	0.27 - 25.05	0.45 - 11.95	3.77x10^{-8} - 1.04x10^{-7}	56268.254 - 57454.025	...
Mrk 180	0.045	HSP	16.11 - 10.97	16.76 - 10.02	17.91 - 10.04	0.50 - 9.29	0.16 - 7.51	0.20 - 6.22	...	56321.980 - 57427.020	Fermi
1ES 1218+304	0.164	HSP	16.67 - 15.79	16.67 - 16.10	17.45 - 16.82	1.10 - 42.25	0.68 - 14.22	0.19 - 24.11	1.12x10^{-8} - 1.29x10^{-8}	56268.274 - 57421.185	...
ON231	0.102	ISP	15.55 - 14.65	16.02 - 14.70	16.77 - 15.52	0.63 - 8.39	1.29 - 9.75	0.90 - 9.52	2.12x10^{-8} - 4.74x10^{-8}	57206.950 - 57454.065	...
PKS 1222+216	0.432	LSP (FSRQ)	14.95 - 14.28	15.18 - 14.50	15.81 - 15.12	4.12 - 10.58	6.15 - 8.91	5.70 - 9.46	3.67x10^{-8} - 9.18x10^{-6}	56268.280 - 57427.202	...
3C279	0.536	LSP (FSRQ)	16.06 - 13.88	16.31 - 14.01	18.02 - 15.26	6.19 - 30.78	5.35 - 32.81	6.06 - 27.38	1.52x10^{-7} - 6.42x10^{-5}	56268.281 - 57433.148	...
1ES 1426+428	0.129	HSP	16.35 - 15.87	16.81 - 16.42	17.71 - 17.35	0.45 - 7.02	0.13 - 4.68	0.22 - 6.57	...	57041.170 - 57427.250	Fermi
PKS 1510-089	0.36	LSP (FSRQ)	16.91 - 13.38	16.61 - 13.83	17.20 - 14.69	0.77 - 35.69	0.87 - 39.36	0.54 - 35.08	1.36x10^{-7} - 2.12x10^{-5}	56288.285 - 57435.248	...
PG1553+113	0.78	HSP	14.34 - 12.80	14.59 - 12.84	15.23 - 13.42	0.57 - 13.17	0.21 - 11.27	0.50 - 10.94	4.60x10^{-8} - 1.33x10^{-7}	56285.286 - 57452.273	...
Mrk 501	0.034	HSP	14.02 - 11.29	14.20 - 12.22	15.54 - 12.54	0.30 - 4.71	0.30 - 4.96	0.24 - 6.18	3.68x10^{-8}- 1.88x10^{-7}	56487.90 - 57414.27	...
BL Lac	0.069	ISP	16.46-14.22	16.86- 14.50	17.19 - 14.71	0.44 - 35.74	0.86 - 20.52	1.01 - 18.73	9.02x10^{-8} - 4.07x10^{-6}	56393.240 - 57258.070	...

Table 4.5: The full Ringo3 catalogue with redshift, source type, optical magnitude range (for each camera), Polarisation range (for each camera), Fermi range (where available), observation period information and details of unavailable data. References for the redshift values can be found in individual source descriptions in Chapter 3 and current Chapter.

4.3 Description of data

The full histories of the first fifteen sources were discussed in Chapter 3 in the Ringo2 analysis. The general behaviour of the source during the Ringo3 observing period, compared to that of Ringo2, is discussed here. When rotations are referred to as 'downward' or 'upward' this merely refers to their direction on the plot and due to different orientations in different sources this is not comparable source to source and only shows a change in direction in a single source.

4.3.1 3C66A

Figure 4.14 shows the optical and γ-ray properties of 3C66A during the Ringo3 period. The source had an overall lower γ-ray flux during the later Ringo3 period (MJD$\sim$56300-57400). In the Ringo2 observing period (MJD$\sim$55000-56200) the source peaked at a Fermi flux of $\sim$100 x10^{-8} phot cm^{-2}s^{-1} while during the Ringo3 period the source peaked at $\sim$20x10^{-8} phot cm^{-2}s^{-1}. The range of the optical magnitude R$\sim$15-14 was similar for both periods.

There were two EVPA rotations across the whole Ringo2 and Ringo3 monitoring period. Early in the Ringo2 period (see 3.12) there was a rapid rotation in the 'upward' direction ($\sim$170° over 9 days from MJD$\sim$55070-55079). During the Ringo3 period (MJD$\sim$56840-56920) there seemed to be a more gradual, though scattered (due to low values of the degree polarisation), rotation with a similar length ($\sim$120°) in the 'downward' direction over $\sim$80 days.

The source reached a higher degree of polarisation $\sim$25% during the Ringo2 period and generally showed similar variability albeit with a lower peak value.

Figure 4.14: The multicolour light curve and polarisation plot for BL Lac source 3C66A. See Section 4.3.1 for a full description of the source.

4.3.2 IC310

IC310 is an S0 galaxy (i.e. a lenticular galaxy that appears to be between a spiral and elliptical type) at a redshift of z=0.0189 with a supermassive black hole of $3\text{x}10^8\text{M}_\odot$ (Aleksić et al., 2014a). IC310 is part of the Perseus Cluster and as such the jet direction is determined by its motion through the intracluster medium (Kadler et al., 2012). In 2010 the presence of very high-energy (VHE) γ-rays was discovered by the MAGIC collaboration (Mariotti, 2010) and very long baseline array (VLBA) studies by Kadler et al. (2012) suggest the orientation angle between the jet-axis and the line-of-sight to be $10 \lesssim \theta \lesssim 20$ degrees; making IC310 at the borderline between radio galaxies and BL Lacs. While radio polarisation measurements have been made, there are no optical polarisation measurements in the literature. After the detection of an exceptionally bright γ-ray flare and rapid variability in November 2012, the source was added to the Ringo monitoring campaign. IC310's light curve and polarisation plots are shown in Figure 4.15.

IC310 is particularly interesting as variability (on the scale of a few minutes) constraints suggest the radius of the emission region is $\sim$20% of the event horizon of the black hole. This variability cannot be easily explained by the standard shock-in-jet model (Eisenacher Glawion et al., 2015). In the Ringo3 data we saw that the source often reached the highest degree of polarisation values ($\sim$15-20%) in blue and green filters. This was coincident with the presence of a full moon in the sky, which also affects the magnitude, and was the result of an imperfect sky subtraction by Source Extractor. The scattering of blue/green light from the moon may be the cause of these bright polarisation events.

The EVPA was stable (within the conditions of the definition of a rotation) until MJD$\sim$57250 when there was a slight increase in γ-ray flux (the source is relatively faint in γ-rays), and the source showed an interesting rotation; seen most clearly in the

interpretation of the blue EVPA points (see Figure 4.16). The behaviour seen in the green camera was a result of the scatter/errors on the datapoints and is not indicative of intrinsic behaviour of IC310.

The EVPA rotated $\sim$700°, which is not uncommon in blazars (Marscher et al., 2010), however in amongst this rotation (after MJD$\sim$57290) there were smaller $\sim$100° quasi-rotations. The definition of a rotation adopted in this work is that a $\geq$90° rotation must consist of 4 or more points with a considerable rotation between them. In the case of these quasi-rotations it is likely that the sampling of data caused the appearance of quick short rotations that may be part of one long rotation. It is also possible that these small rotations are stochastic behaviour of the EVPA exhibiting a random walk-like behaviour.

The optical magnitude showed 'dips' every $\sim$29 days, which were more pronounced in the blue filter, but barely noticeable in the red filter (see Figure 4.15). These are attributable to the periods of the full moon and are residuals left over from an imperfect sky subtraction using Source Extractor.

4.3.3 3C120

3C120 is a radio galaxy with an FR-I morphology (i.e. a bright core) at a redshift of z=0.033 (Lavaux & Hudson, 2011). Its radio jet has blazar-like superluminal components when viewed on parsec scales (Gómez et al., 2000, 2001, 2011). The Ringo3 observations (see Figure 4.17) began in October 2014 after a period of prolonged γ-ray activity in the source (Casadio et al., 2015b). Fermi γ-ray data for this source are not presented in this work due to its absence from the 3FGL (third Fermi LAT catalogue) from which we take the γ-ray data. Outside of flaring periods the source is very faint in γ-rays, monitoring of the source in optical continues in the anticipation of future flares-for which we can gather γ-ray data when the source is brighter. There are no recent
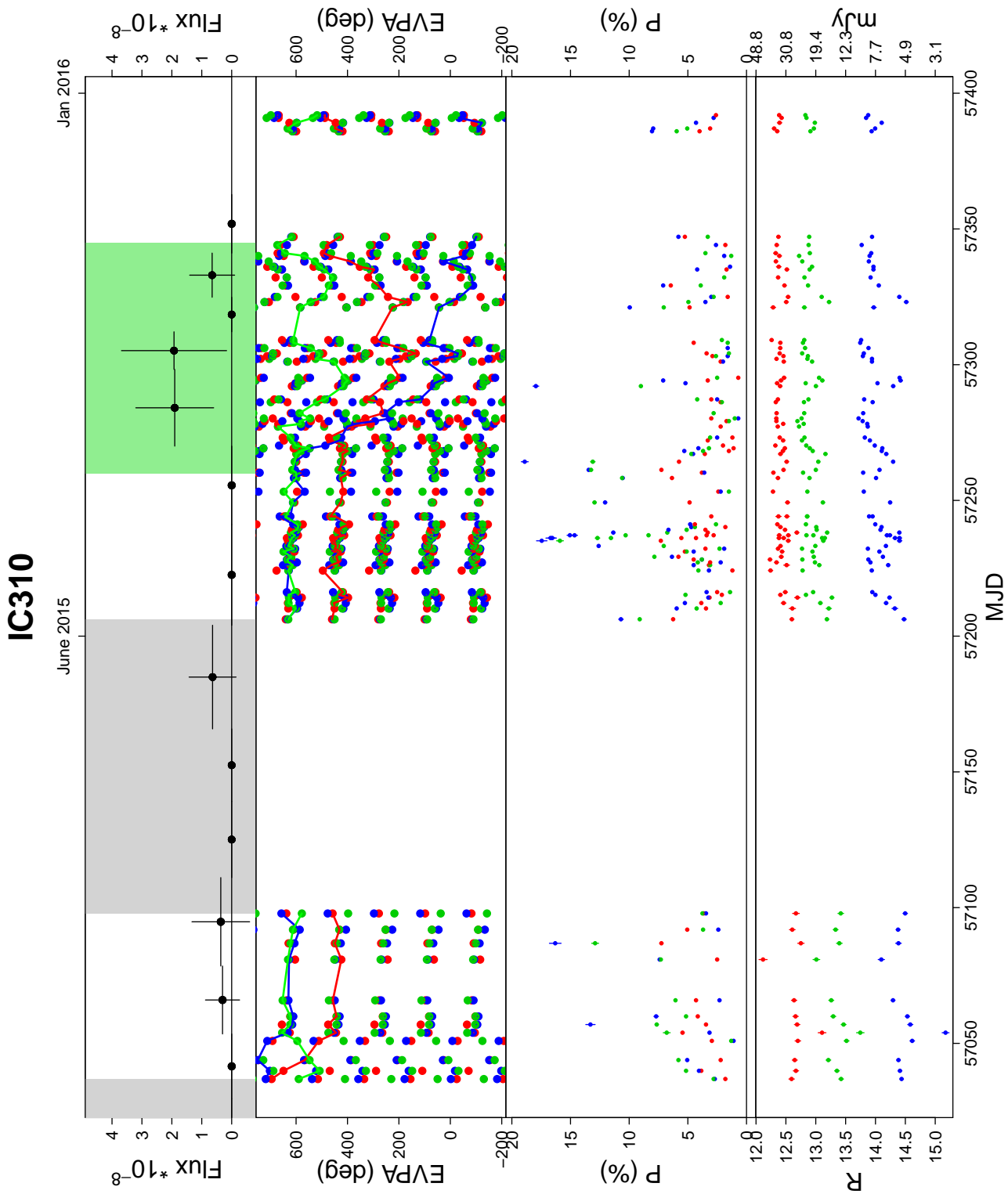
Figure 4.15: The multicolour EVPA plot for radio galaxy source IC310 showing the different interpretation of the EVPA by the automated code depending on the different data. See Section 4.3.2 for a full description of the source.
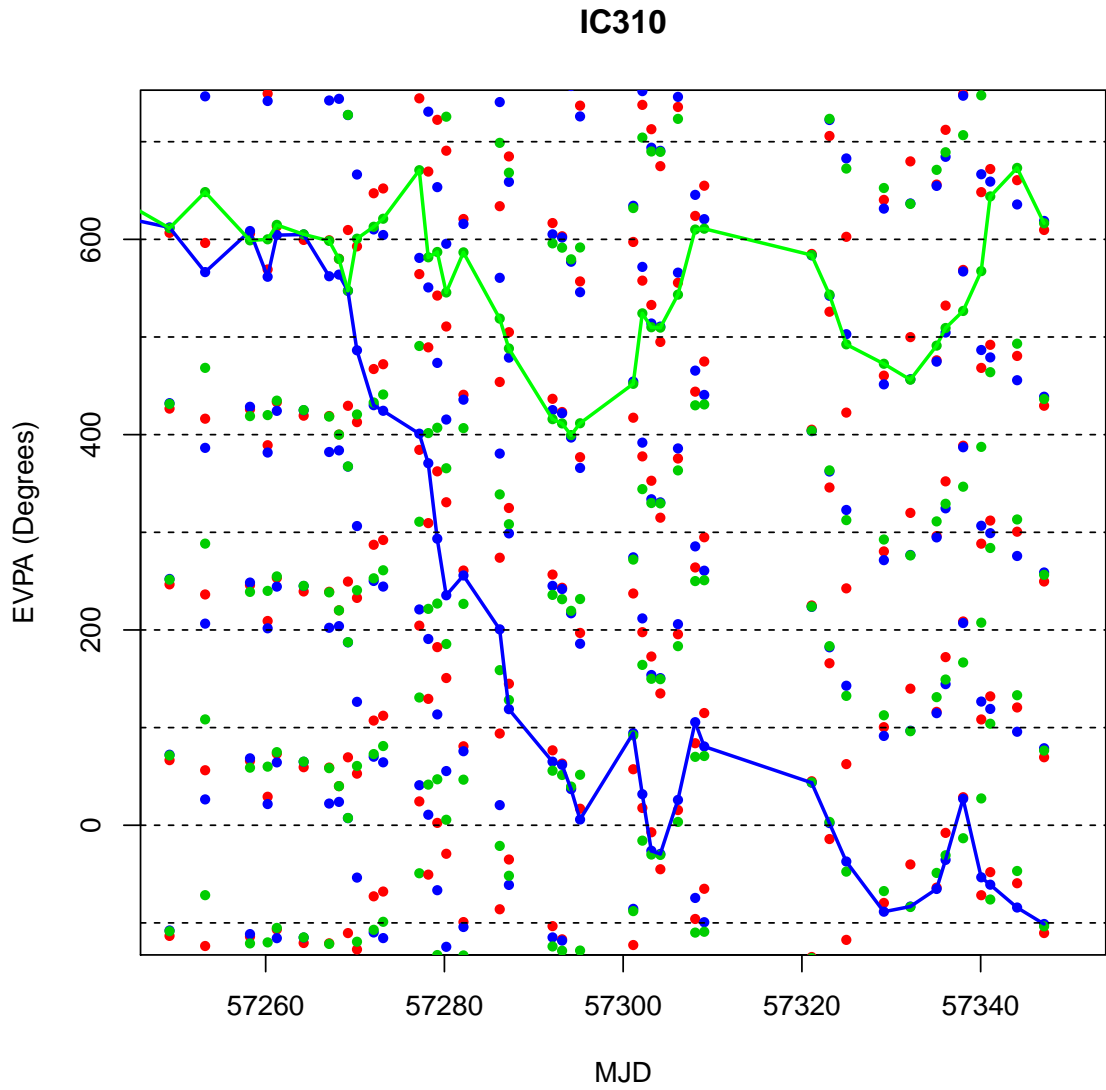
Figure 4.16: The EVPA plot for the radio galaxy source IC310 showing the green and blue measured rotations (these differences are not intrinsic source behaviour and are due to scatter on the datapoints. See Section 4.3.2 for a full description of the source.)

optical polarisation studies of this source in the literature. The optical photometric and polarimetric data presented in this work showed no EVPA rotations and low levels of polarisation. No optical flares were observed as the source appears to be in a period of quiescence.

4.3.4   PKS 0502+049

The flat spectrum radio quasar, PKS 0502+049, at z=0.954 (Drinkwater et al., 1997), is one of the most distant blazars in the sample. It was added to the sample in 2013 when it was reported to undergo an increase in its γ-ray flux (Ojha & Dutka, 2013). There are no publications of long-term photometric or polarimetric monitoring of PKS 0502+049. Few data have been taken so far with the Ringo3 program, however, Figure 4.18 shows that during a large γ-ray flare (MJD$\sim$56900) there was a large optical flare which increased the optical magnitude by $\sim$3 magnitudes and corresponded with a degree of polarisation peak of 30%. Any perceived rotations were discounted due to the few points making up the rotation.

4.3.5   S5 0716+714

In Figure 4.19 S5 0716+714 continued to show many γ-ray flares with 17 identified in this work over the Ringo3 period of $\sim$1200 days. In the Ringo3 data, there was a tendency for γ-ray flares to be correlated with optical flares. The degree of polarisation peaked at $\sim$25%, which was higher than the $\sim$20% maximum during the Ringo2 period. The source showed a minimum $\sim$150° 'downward' rotation early in the monitoring period at MJD$\sim$56600. This period was not as well sampled and this rotation may be part of a larger rotation. There was a large EVPA rotation of $\sim$500° (shown in the blue filter) beginning at MJD$\sim$56900. The end of this rotation was coincident with a large γ-ray flare of $\sim$200 x10^{-8} phot cm$^{-2}s^{-1}$. The EVPA underwent a noisy

Figure 4.17: The multicolour light curve and polarisation plot for FSRQ source 3C120. See Section 4.3.3 for a full description of the source.

Figure 4.18: The multicolour light curve and polarisation plot for FSRQ source PKS 0502+049. See Section 4.3.4 for a full description of the source.

'downward' ∼100 rotation over the period of 100 days from MJD∼57250-57350. During this period the degree of polarisation was very variable (from 0.72-25.6%) which might explain the noisy rotation.

4.3.6 PKS 0736+017

PKS 0736+017 is a FSRQ with a redshift of z=0.189 (Ho & Kim, 2009). It was reported to have increased γ-ray emission in November 2014. It was then added to the Ringo3 monitoring campaign and continued to show bright γ-ray flares (see Figure 4.20). There is little in the literature about PKS 0736+017, particularly lacking is optical polarisation monitoring. In Figure 4.20 the Ringo3 data showed high levels of optical polarisation of ∼30% and one occurrence of ∼40%.

There was a large 'downward' rotation of ∼725° starting at MJD∼57050, this was preceded by an 'upward' ∼250° rotation. There was a ∼500 x10^{-8} phot cm^{-2} s^{-1} γ-ray flare towards the end of the rotation (similar to that seen in S5 0716+714). After MJD∼57270, there were stochastic variations in the EVPA which can be interpreted as short rotations; one 'upward' rotation of ∼90° from MJD = 57290 - 57310 and another 'upward' rotation of ∼90° from MJD = 57338 - 57345.

4.3.7 OJ287

OJ287 was relatively quiescent from the start of the Ringo3 period until MJD∼57300 (although there were gaps in the monitoring, see Figure 4.23). The source showed similar variation in optical magnitude and degree of polarisation (DOP) to its behaviour in the Ringo2 period, reaching DOP∼30%. It was not until late 2015 that OJ287 started to show some more activity. Between MJD 57369-57381 there was a brief 'downward' EVPA rotation of ∼200° which occurred during a flaring period.

Figure 4.19: The multicolour light curve and polarisation plot for BL Lac source S5 0716+714.
See Section 4.3.5 for a full description of the source.

Figure 4.20: The multicolour light curve and polarisation plot for BL Lac source PKS 0736+017. See Section 4.3.6 for a full description of the source.

Of the 19 blazars in this sample, at least 7 (3C66A, 3C279, S5 0716+714, OJ287, ON231, Mrk 421, and Mrk 501) are believed to be part of a binary system due to the variations/periodicity in their light curves (Hudec, 2011). OJ287 is a binary supermassive black hole system and has twelve-yearly outbursts with an orbital eccentricity (apocentre/pericentre) of 0.700±0.001 (Valtonen et al., 2016). It can be modelled as the secondary supermassive black hole (M = 1.5±0.1x $10^8 M_\odot$) passing through the accretion disk of the primary supermassive black hole (M = 1.83±0.01 x $10^{10} M_\odot$) (see Figure 4.21). The periodic optical outbursts can be predicted using previous observations (over >100 years), and the accurate measurement of the timing of the outbursts can constrain the spin of the primary black hole according to the precession of the secondary's orbit. Part of this project was to intensively monitor OJ287 when triggered by the larger community's observations. Ringo3 polarimetric data were used in Valtonen et al. (2016).

Nightly observations by the OJ287 collaboration began in September 2015 and the source's activity was monitored closely. Between 18th and 25th November 2015 (MJD 57344 - 57351), the source began to brighten, prompting an increase in cadence of the observations using the Liverpool Telescope and Ringo3. The source hit maximum brightness on 4th December (MJD= 57360, see black arrow in Figure 4.23) and continued to be active for weeks afterwards.

The impacting secondary black hole on the accretion disk generates thermal emission (the first flare), however, the result of the interaction on the magnetic field/accretion disk is more complicated as it has a less direct route than the thermal emission (Valtonen et al., 2016). Figure 4.23 shows the intensive polarimetric and photometric monitoring using Ringo3. During this monitoring the source reached the highest polarisation ever observed (Valtonen et al., 2016) at MJD~57380, approximately 20 days after the first flare. During the first optical flare the degree of polarisation was ~10%, which is low for OJ287 (see Figures 3.14 and 4.23, no Ringo3 data were available at time).
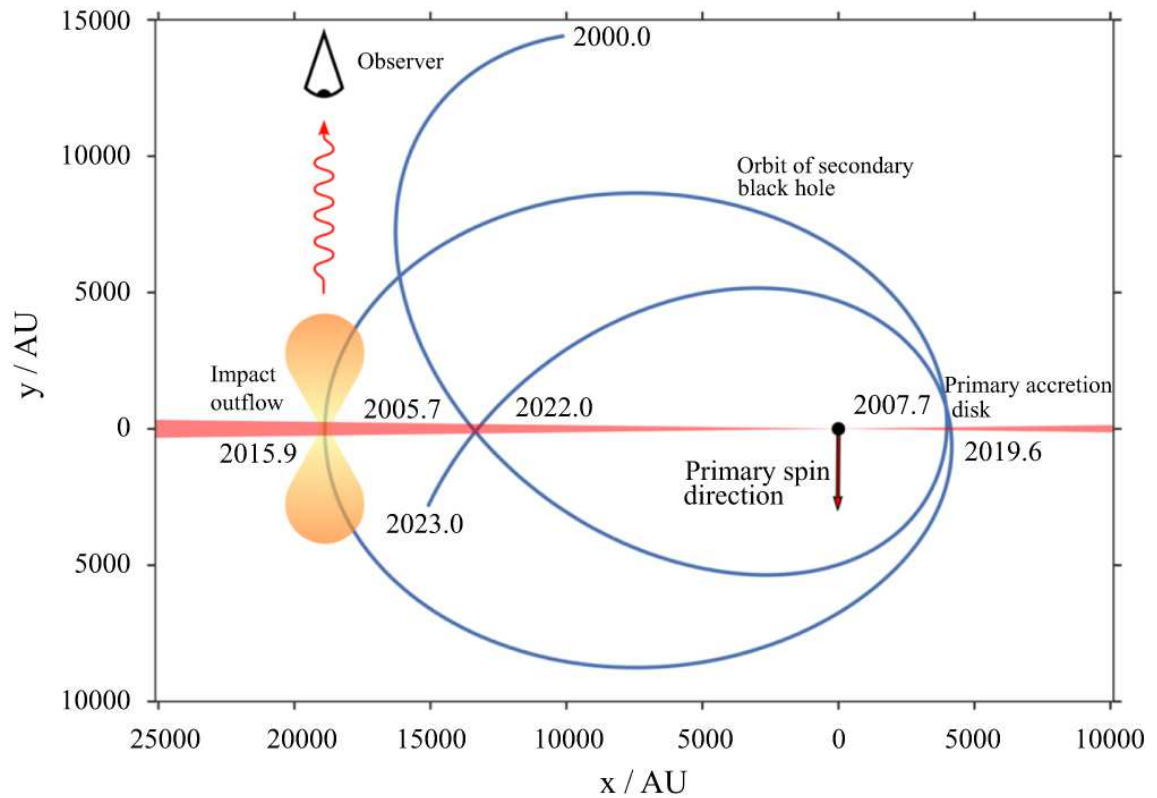
Figure 4.21: Diagram showing the orbital motion of the secondary SMBH in the blazar OJ288, indicating where and when it will interact with the primary accretion disk. Taken from Valtonen et al. (2016).

This might suggest that the intensive thermal emission was diluting the non-thermal emission from the primary's jet. During the second peak (see second black arrow on Figure 4.23) there was a maximum of 43% polarisation (the highest on record for OJ287).

The first flare appeared to be predominantly thermal and showed low degree of polarisation. This suggests that the typical non-thermal emission from the primary jet is diluted by the increase in thermal emission from the impact of the secondary supermassive black hole (SMBH2) on the primary's accretion disk. There was no associated, strong, polarised emission at the time of the impact. The impact of the SMBH2 on the SMBH1 accretion disk causes a 'bubble' of gas from the accretion disk to tear away and expand. As the bubble cools it becomes transparent at optical wavelengths and produces the shape of the peak in the optical magnitude (Valtonen et al., 2010a;
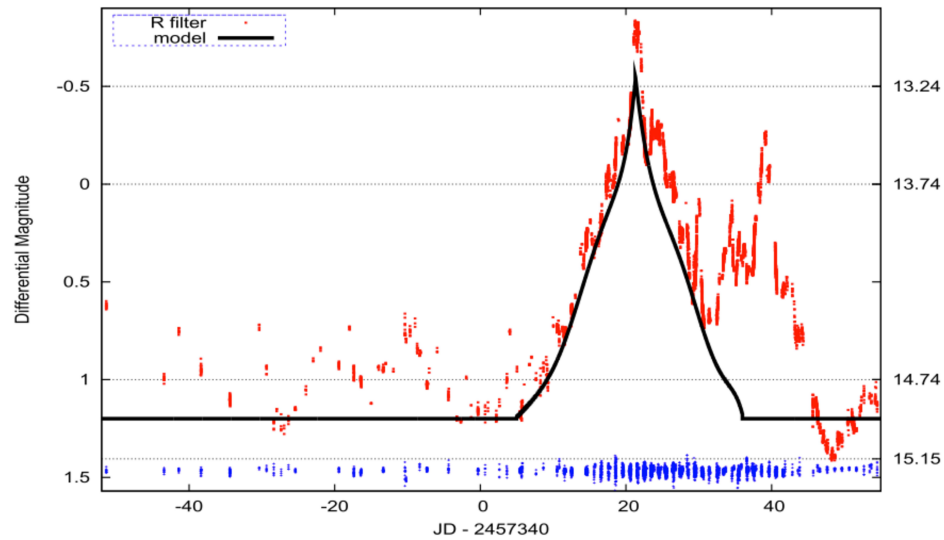
Figure 4.22: The optical light curve for OJ287 during the double flare believed to be caused by the interaction of a secondary supermassive black hole with the primary supermassive black hole. The black line is a model based on a uniform expanding sphere of plasma (Pihajoki, 2016; Valtonen et al., 2016). The red line shows the optical differential magnitude of the source over the period of October - December 2015 with respect to the check star GSC 1400-444. This Figure was taken from Valtonen et al. (2016).

Pihajoki, 2016). Figure 4.22 shows the shape of the optical magnitude peak with data taken from a variety of observatories, see Valtonen et al. (2016) for more details.

To explain the second, strongly polarised, non-thermal flare there must be an ordered magnetic field or magnetic reconnection to create such high polarisation. It is possible that the polarisation flare originated from the primary jet, but it is not possible that this was caused by the impact (due to light crossing times across the accretion disk). It may be coincidental that the primary jet flares shortly after the impact, however, the second strongly polarised peak is also present during the 1984 (Smith et al., 1987) outburst, which suggests the events are connected.

We associate the strongly polarised flare with the SMBH2 and its impact with the accretion disk. It is possible that the gravitational influence of the SMBH2 accretes matter from the primary accretion disk and creates a relativistic jet which is, during the interaction, orientated toward the observer, or, the magnetic fields associated with SMBH1 and SMBH2 interact and create polarised emission by magnetic reconnection.

With the simultaneous Fermi γ-ray data (see Figure 4.23) we saw that the gamma-ray flux stayed low and only increased marginally at the time of the flare. This might suggest that the highly polarised emission cannot be associated with magnetic reconnection, however, it is possible that if the blob of gamma-ray emission is close to the launching region of the jet the gamma-rays would be absorbed.

4.3.8   S4 0954+658

S4 0954+658 (z=0.367 Lawrence et al. (1986) - although this has been contended by Landoni et al. (2015) who suggest a lower limit of z$\geq$0.45) is an intermediate spectral peaked (ISP) BL Lac source. It was added to the Ringo3 monitoring campaign in May 2015 after a large γ-ray flare reaching $\sim$250 x10^{-8} phot. cm^{-2}s^{-1} (see Figure 4.24). After the outburst (which lasted $\sim$40 days) the γ-rays returned to a low level, with one much smaller flare occurring just after MJD$\sim$57300.

The source has been extensively studied in optical wavelengths and was first found to show large variations of optical magnitude on nightly timescales by Wagner et al. (1993) during a 4 week monitoring program. Intensive monitoring by Raiteri et al. (1999) between 1994-1998 showed intranight variability and high activity. They also measured colour variations but found no correlation with magnitude. Larionov et al. (2011) reported a rise in R magnitude from $\sim$17.6 to 14.8 with flare-like behaviour and we saw similar behaviour in the Ringo3 data, although with poor cadence. The optical magnitude varied between 17.5 and 13.8 across the three wavelength bands. The degree of polarisation reached $\sim$27% during one EVPA rotation but otherwise fluctuated between 0.4 - 26%. The EVPA showed one 'upward' (MJD = 57175-57190) and one 'downward' (MJD = 57332 - 57344) rotation of $\sim$300° each, although the poor cadence may mean that other rotations (or longer rotations) may have been missed.

oj287

Figure 4.23: The multicolour light curve and polarisation plot for FSRQ source OJ287. See Section 4.3.7 for a full description of the source.
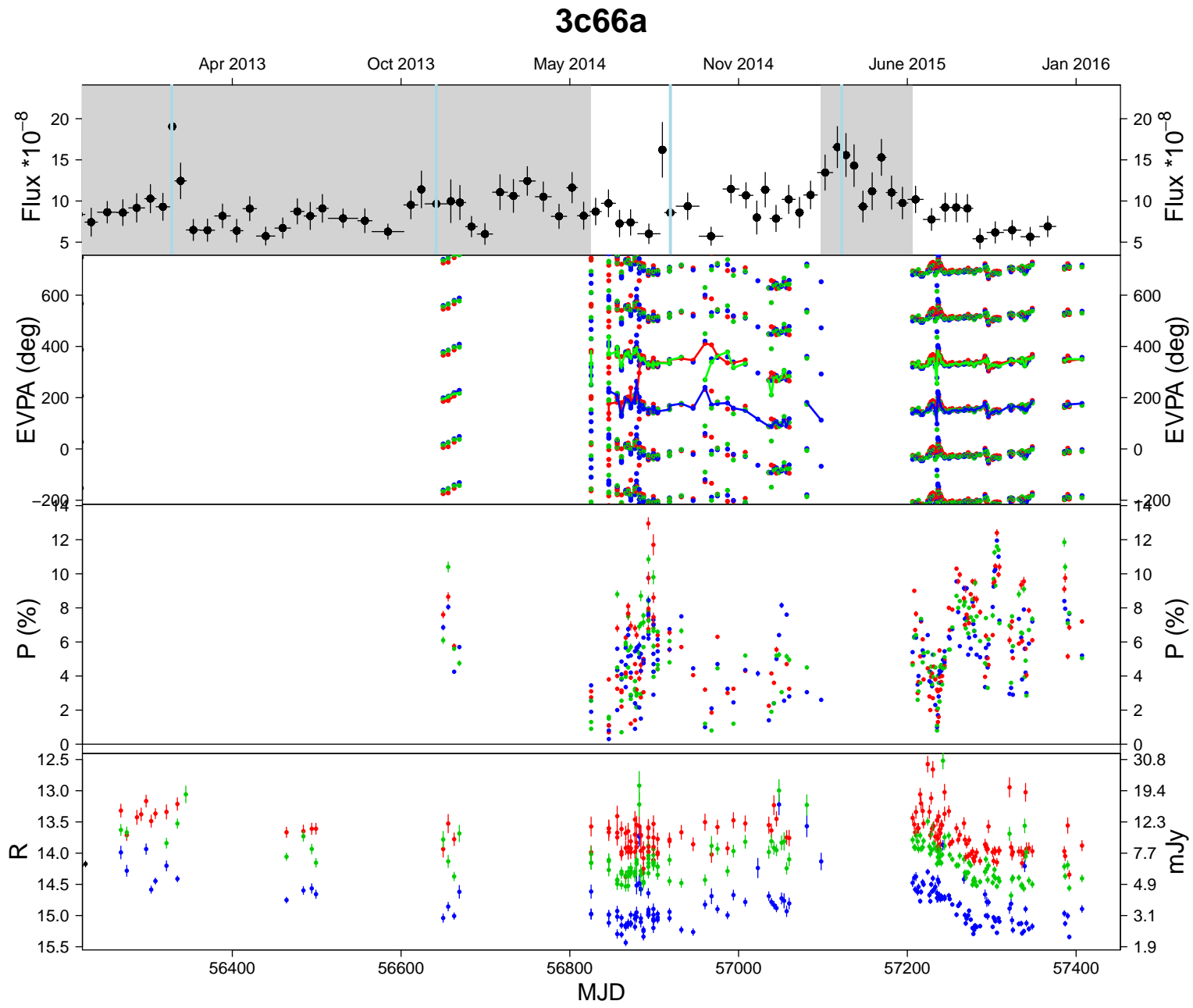
Figure 4.24: The multicolour light curve and polarisation plot for BL Lac source S4 0954+658. See Section 4.3.8 for a full description of the source.

(a) Field of view   (b) Field of view
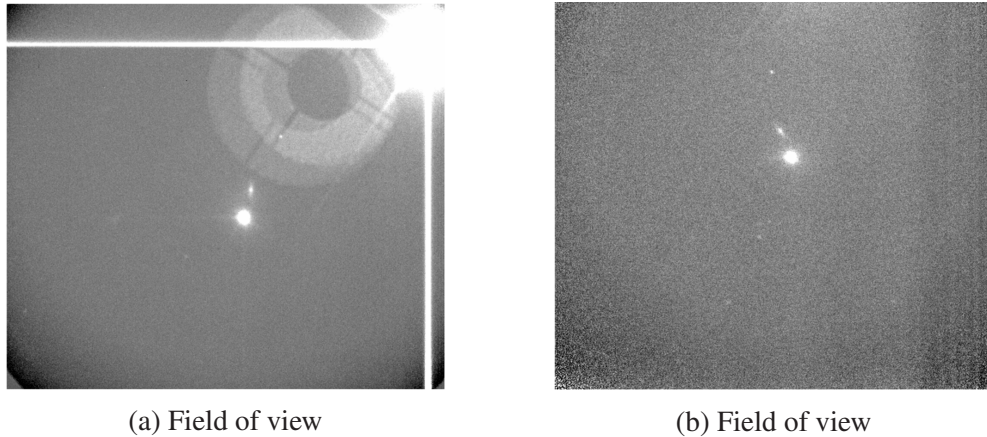
Figure 4.25: Two images of the Mrk 421 field of view (∼4x4 arcsecs) from the Ringo3 instrument on the Liverpool Telescope at differing rotator angles.

4.3.9 Mrk 421

The Ringo3 field of Mrk 421 is shared by a foreground star whose brightness causes diffraction spikes and very bright ghosts on the images (see Figure 4.25a). Even when the foreground star is not in the frame (see Figure 4.25b) the source does not have a secondary star in the frame (just a faint galaxy) which meant that photometry was not possible. Due to the nature of the foreground star and lack of secondaries in the frame, a WCS fit using the LT pipeline was not possible. It was also extremely difficult to manually identify the source by setting pixel or right ascension (RA) and declination (Dec) constraints because the ghosts can appear in the centre of the frame. By removing those frames with extensive ghosting (e.g. see Figure 4.25a) and setting tight RA and Dec constraints, it was possible to isolate Mrk 421 in the frame (this was checked visually for each new frame). For the SkyCamZ data we identified a suitable secondary star from the larger field of view (one that was consistently in every image).

Figure 4.26 shows the behaviour of Mrk 421 during the Ringo3 observing period. There were 14 γ-ray flaring episodes reaching a similar level of γ-ray flux during the Ringo2 period. The EVPA underwent a long 'downward' ∼350° rotation from MJD=57375 - 57480, which consisted of smaller (and often scattered) 'upward' and 'downward' rotations. The degree of polarisation reached a maximum of 15.5%, lower

than that during the Ringo2 period.

4.3.10   1ES1011+496

The Ringo2 and early Ringo3 periods showed a stable EVPA of ~110° which changed at MJD~57000 and underwent a 'downward' 120° rotation, followed by an 'upward' rotation of ~170° and then immediately followed by another 'downward' ~410° rotation (see Figure 4.27). The EVPA then returned to its previous stable value at ~100°. The degree of polarisation varied between 0 and 20%; a higher level than during the Ringo2 period. The optical magnitude showed a similar small variation throughout the ~1500 days.

4.3.11   Mrk 180

In the Ringo3 period we saw a stable optical magnitude with little variation (see Figure 4.28). The source was very faint in γ-rays so there was just one binned point. There were two EVPA rotations: a 'downward' rotation of ~210° then a second 'downward' rotation of ~280°. The polarisation stayed low and did not change greatly over the entire period; ranging between 0 and 7%. The large error bars associated with the larger polarisation values were associated with larger photometric errors. It is possible that this was caused by the close proximity of Mrk 180 on sky with another source (which was affecting the counts measured in Source Extractor).

4.3.12   1ES1218+304

The γ-ray flux for 1ES1218+304 is low and continued to be so through the Ringo2 and Ringo3 periods (see Figure 4.29). The EVPA stayed relatively stable at ~79° until MJD~57050-57150 when the EVPA underwent an 'upward' rotation of ~240°
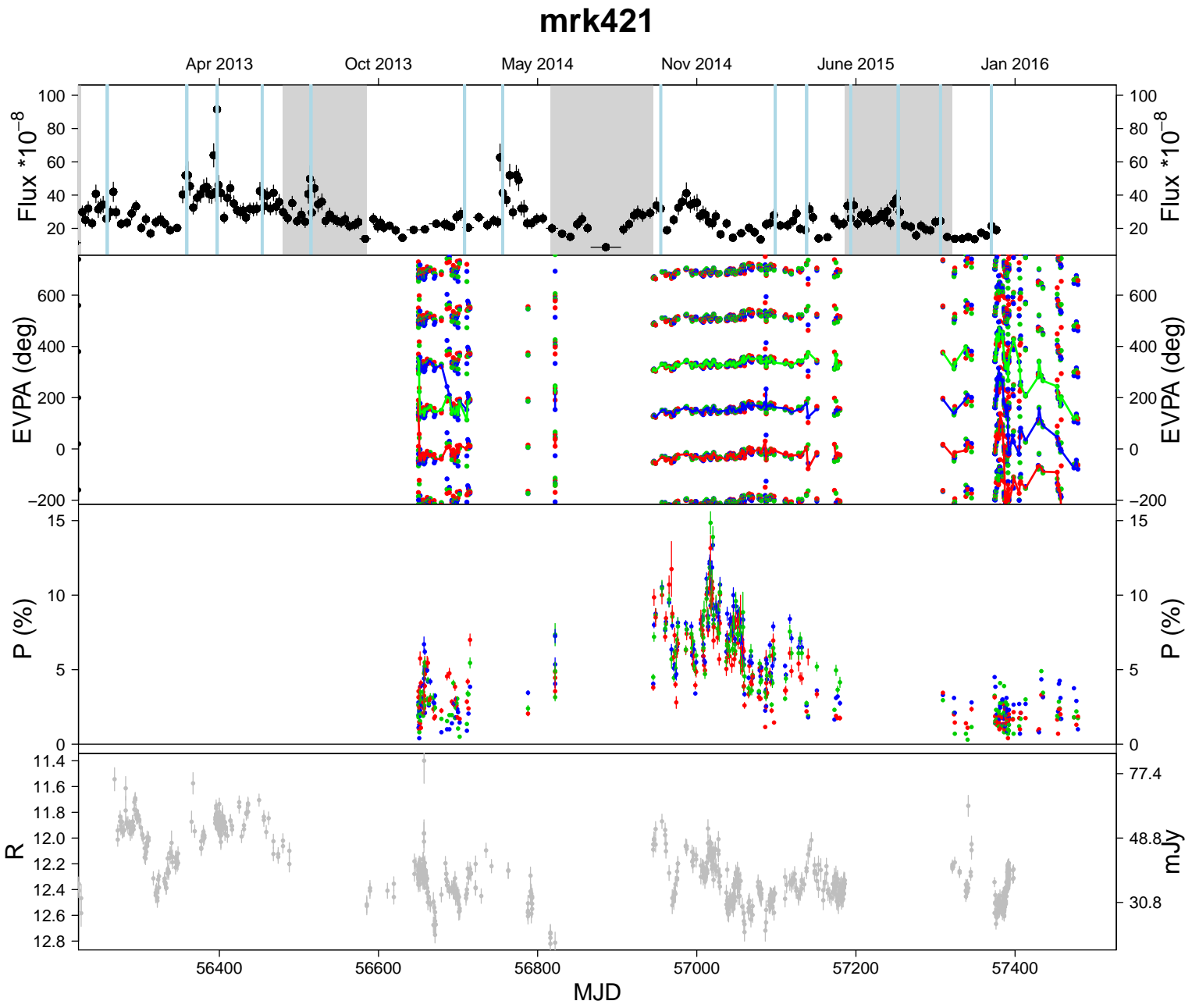
mrk421

Figure 4.26: The multicolour light curve and polarisation plot for BL Lac source MRK 421.
See Section 4.3.9 for a full description of the source.
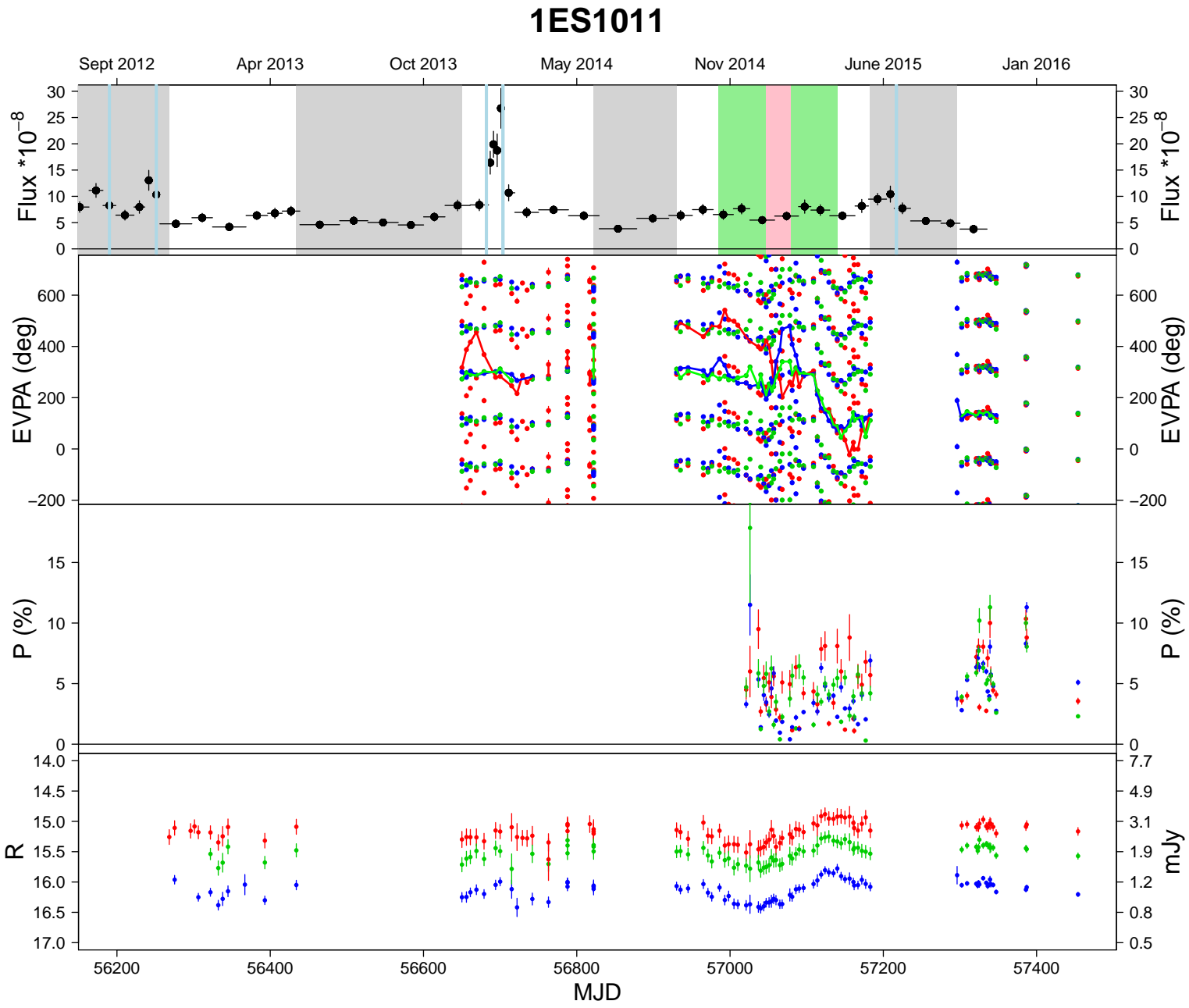
Figure 4.27: The multicolour light curve and polarisation plot for BL Lac source 1ES 1011. See Section 4.3.10 for a full description of the source.
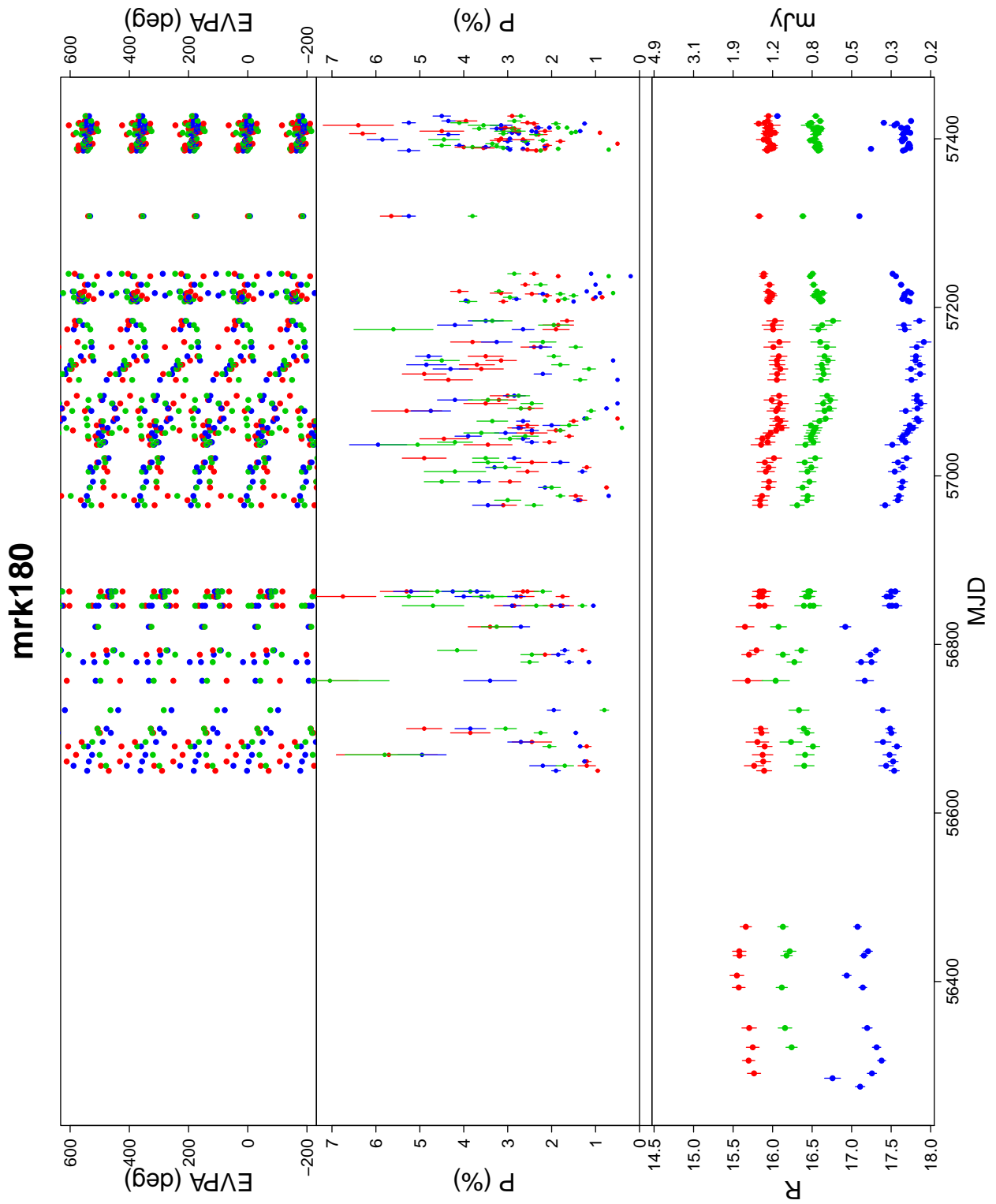
Figure 4.28: The multicolour light curve and polarisation plot for BL Lac source Mrk 180. See Section 4.3.11 for a full description of the source.

immediately followed by a 'downward' rotation of $\sim210°$. The degree of polarisation was variable and in general stayed below 15%. The optical magnitude showed very little variation.

4.3.13 ON231

A short period of observations was available for ON231 during the Ringo3 period (see Figure 4.30). The Ringo2 period showed no EVPA rotations, the Ringo3 period showed 'downward' then 'upward' noisy rotations from MJD$\sim$57380 onwards, during which the degree of polarisation was $\lesssim$10%. The optical magnitude showed little variation.

4.3.14 PKS 1222+216

The Ringo3 field for PKS 1222+216 contains one secondary star source which is often cropped out of the frame with the rotation of the telescope/instrument. This results in a lower quantity of datapoints for this source than for other blazars.

The optical magnitude showed little variation in each wavelength. The EVPA showed no rotations and was stable. The degree of polarisation was typically $\leq$15% (which is within the errors of the maximum degree of polarisation during the Ringo2 period), with the exception of one event, on MJD = 57129, where the degree of polarisation reached 28.6%, 26.7% and 23.9% in red, green and blue bands respectively.

The γ-ray data showed 10 flaring events, some (such as the event near MJD$\sim$56500) peaked over a wide period of time and hence the light blue line in Figure 4.31 does not appear on the largest flare. The two largest flares occurred while the source was not observable in the optical (due to physical location or observing restrictions).
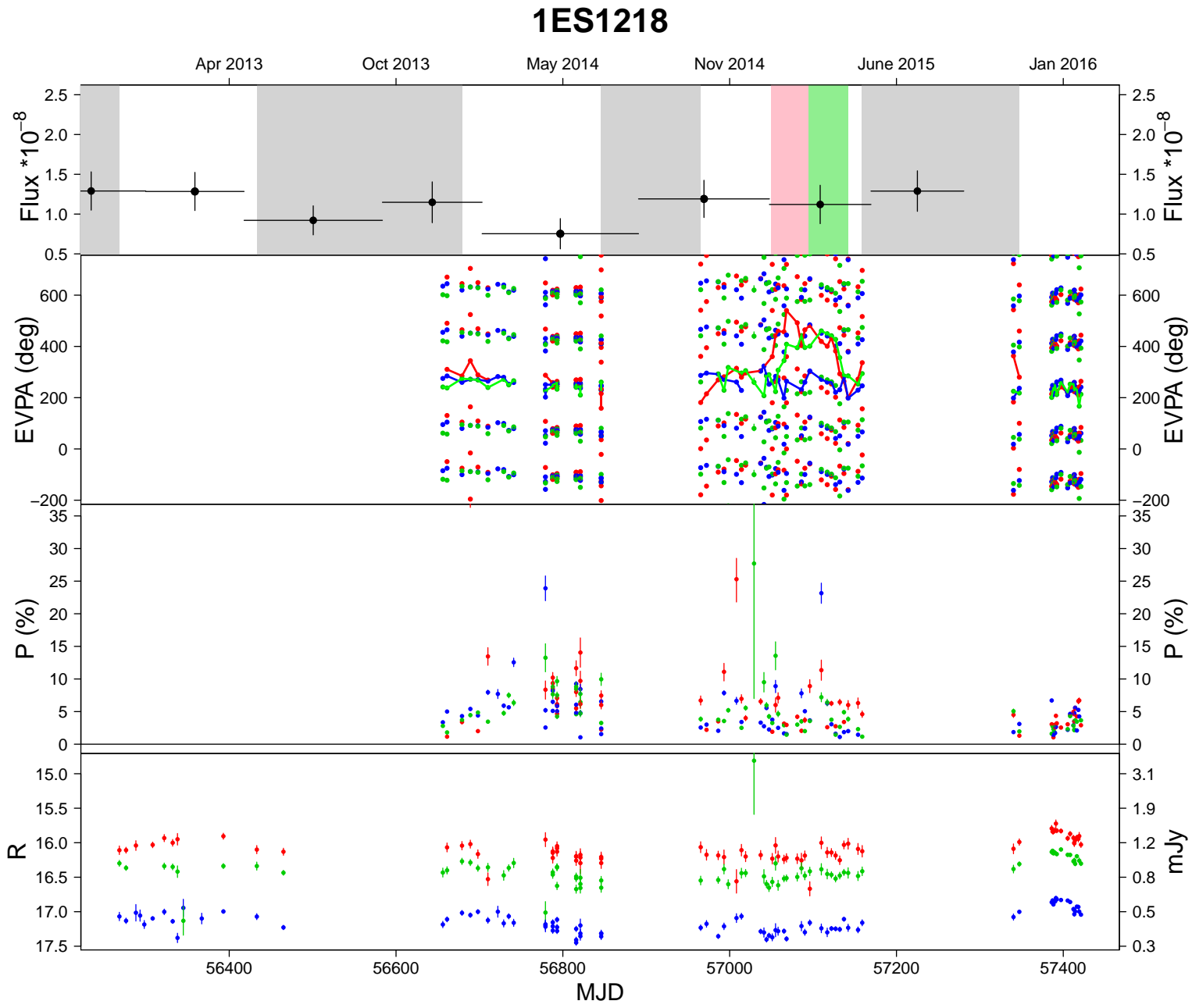
Figure 4.29: The multicolour light curve and polarisation plot for BL Lac source 1ES1218. See Section 4.3.12 for a full description of the source.
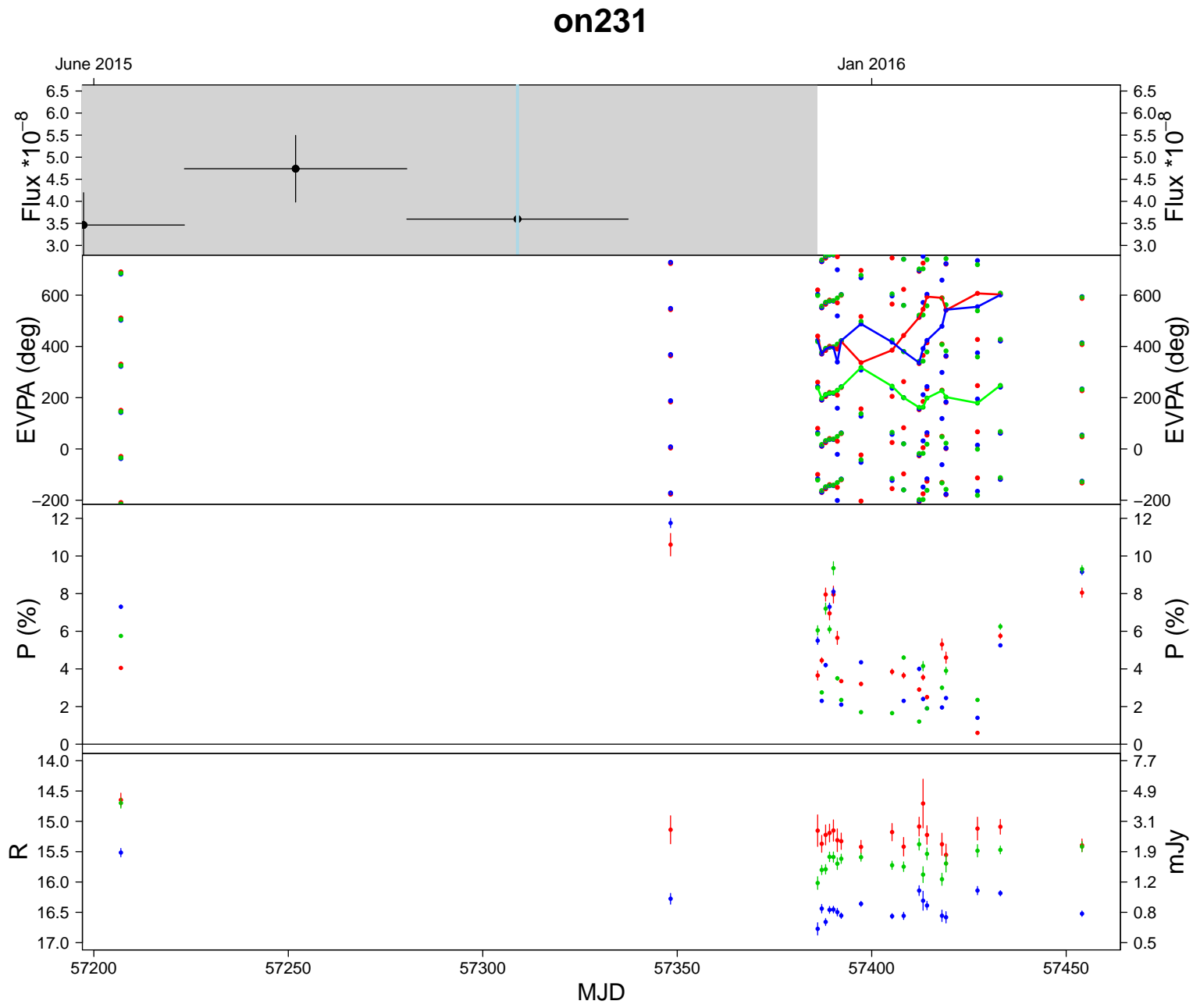
on231

Figure 4.30: The multicolour light curve and polarisation plot for BL Lac source ON 231. See Section 4.3.13 for a full description of the source.
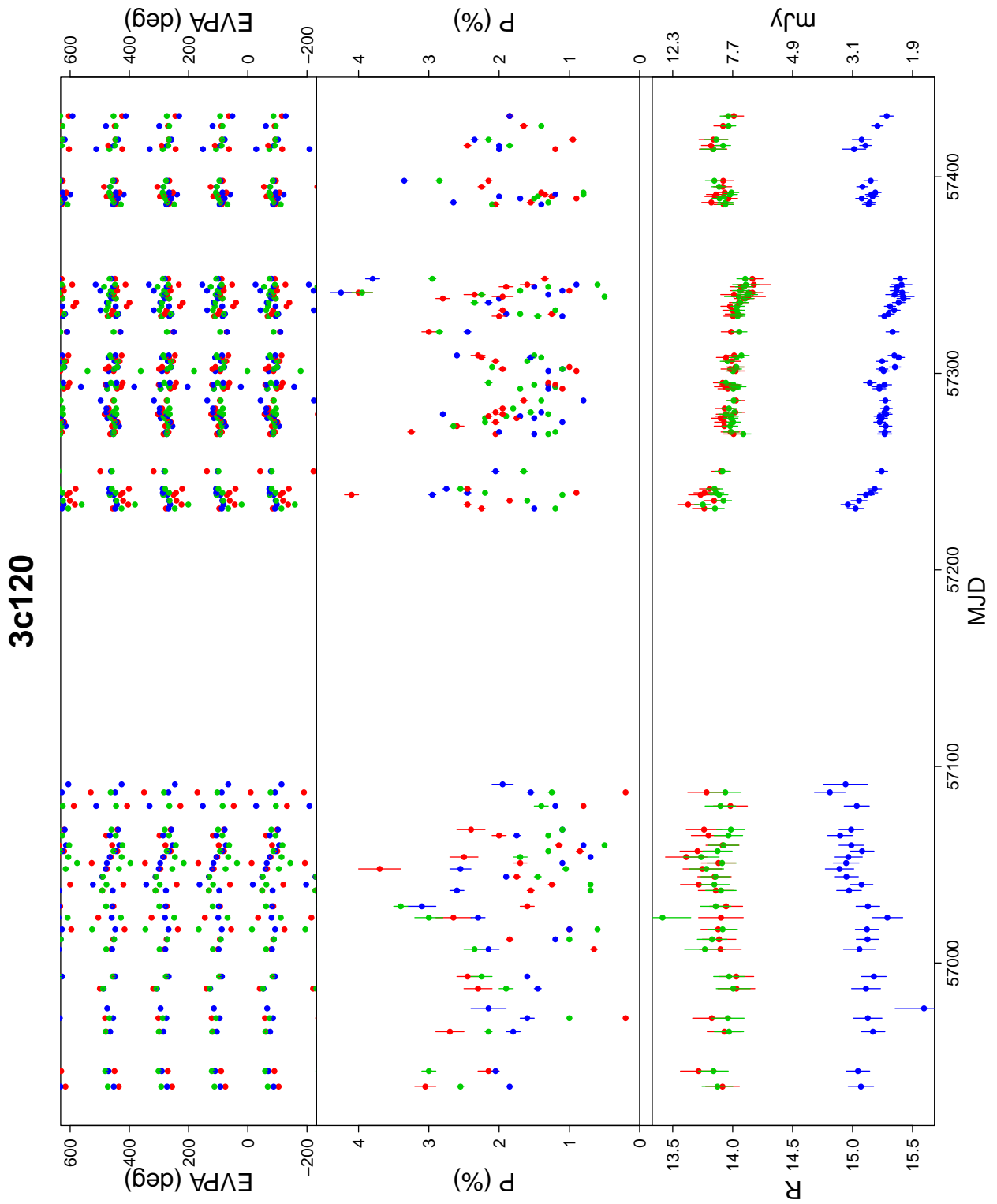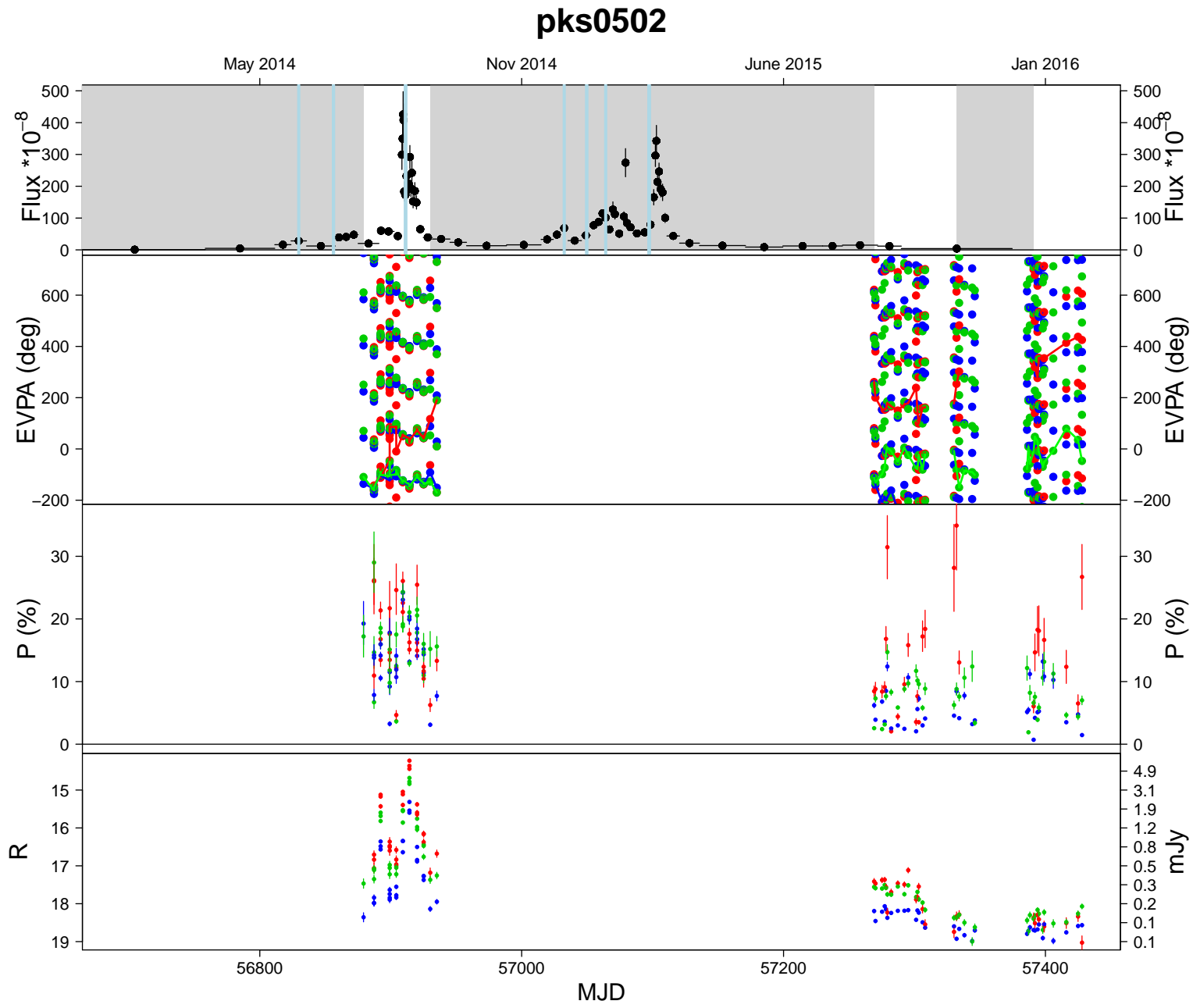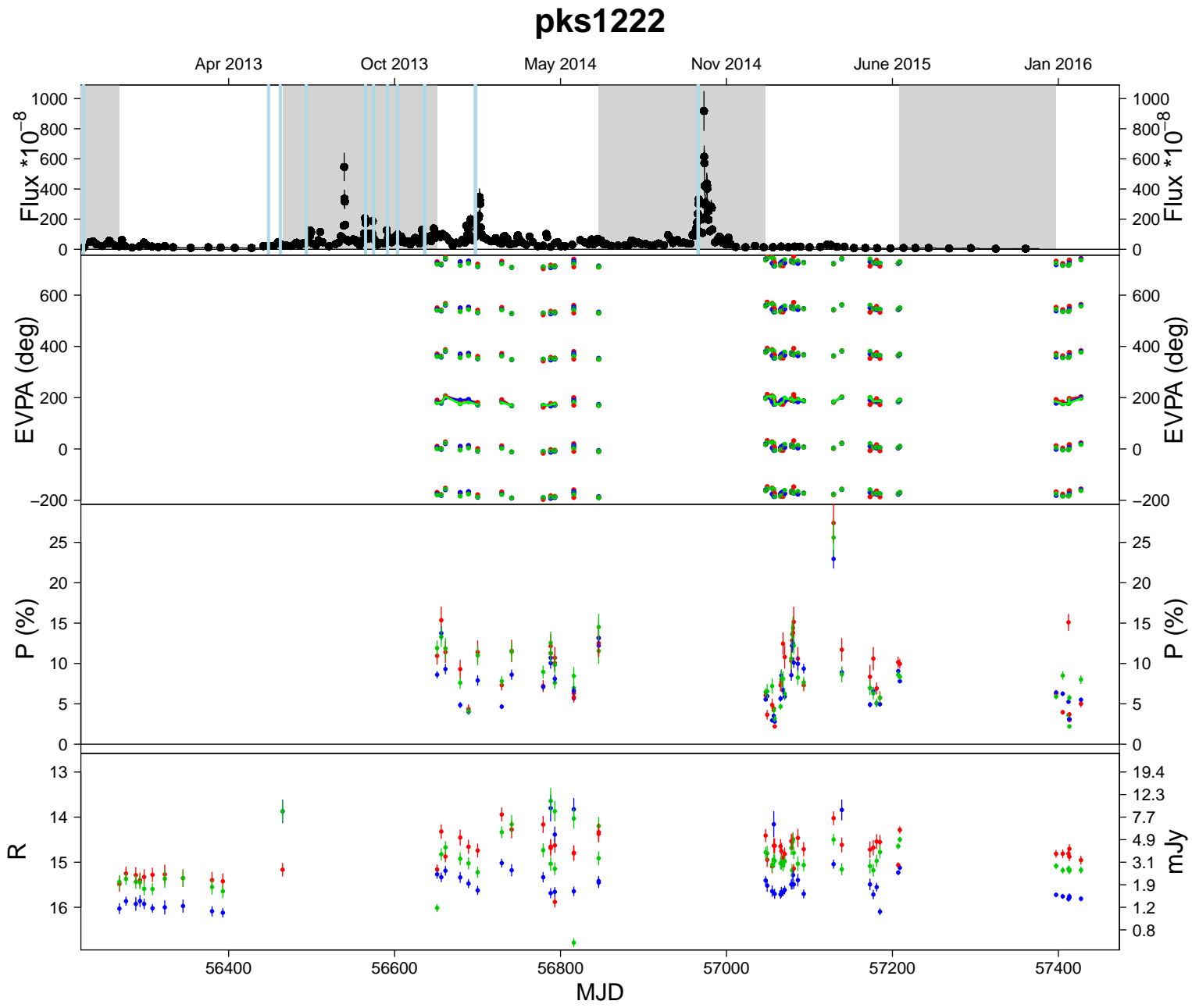
Figure 4.31: The multicolour light curve and polarisation plot for FSRQ source PKS 1222. See Section 4.3.14 for a full description of the source.

4.3.15   3C279

3C279 is a very active source in γ-rays; there were 16 flares in the Ringo3 period, some too small to discern by eye due to the magnitude of the large flares (reaching $\sim$3.0 x 10^{-4} phot. cm^{-2} s^{-1}, see Figure 4.32). During the Ringo3 period the EVPA remained stable and showed very little variation and no rotations. The degree of polarisation reached similar levels ($\sim$30%) as it did during the Ringo2 period. The optical magnitude appeared more variable in the blue, and had a larger standard deviation of 0.72 magnitudes compared with sd=0.55 (green) and sd=0.51 (red).

4.3.16   1ES 1426+426

1ES 1426+426 is too faint in γ-rays to have Fermi LAT data. The optical magnitude showed little variation and the degree of polarisation was low: $\leq$7%, (see Figure 4.33) similar to during the Ringo2 period.

The EVPA trace code suggested a long 'upward' rotation of $\sim$400° between MJD$\sim$57040-57090 from the red points, however, the blue points suggested the angle rotates 'downward' by $\sim$300° before rotating 'upward' again by the same amount. A tracing of the green points suggested an even smaller rotation 'downward' then 'upward' of $\sim$100° each. For this work the blue camera interpretation was used; first a 'downward' rotation of $\sim$305° (from MJD 57040 - 57080) followed by an 'upward' rotation of $\sim$300° (from MJD 57093 - 57185).

A similar ambiguous interpretation was the case for the next two sets of rotations (MJD$\sim$57210-57245 and $\sim$57390-57350), this is due to the low degree of polarisation causing larger scatter on the EVPA points. The 'downward' rotation from MJD = 57200 - 57225 was $\sim$170° and the 'upward' rotation from MJD = 57225 - 57242 was $\sim$120°. From MJD = 57380 onwards there were various fluctuations in the EVPA,
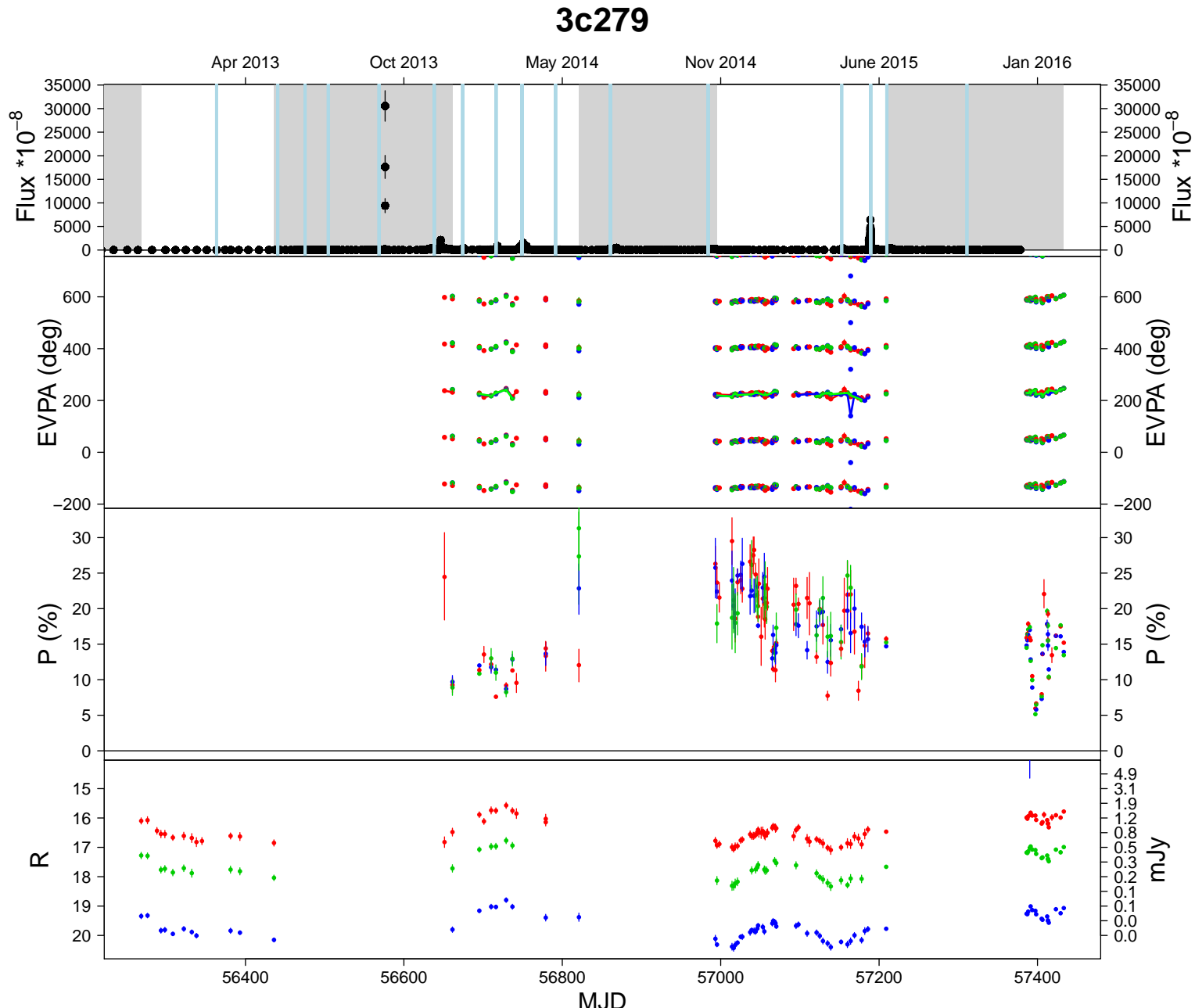
3c279
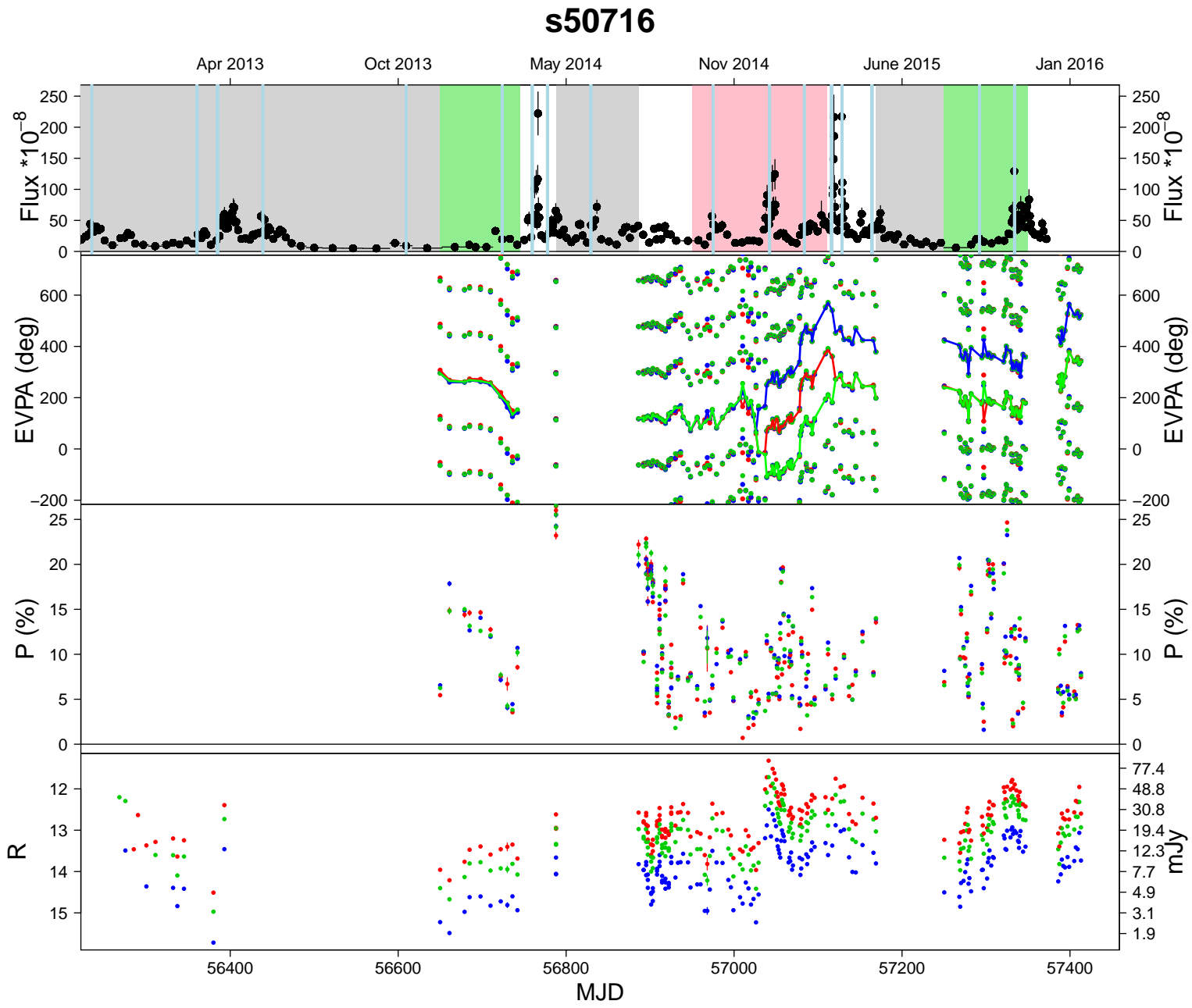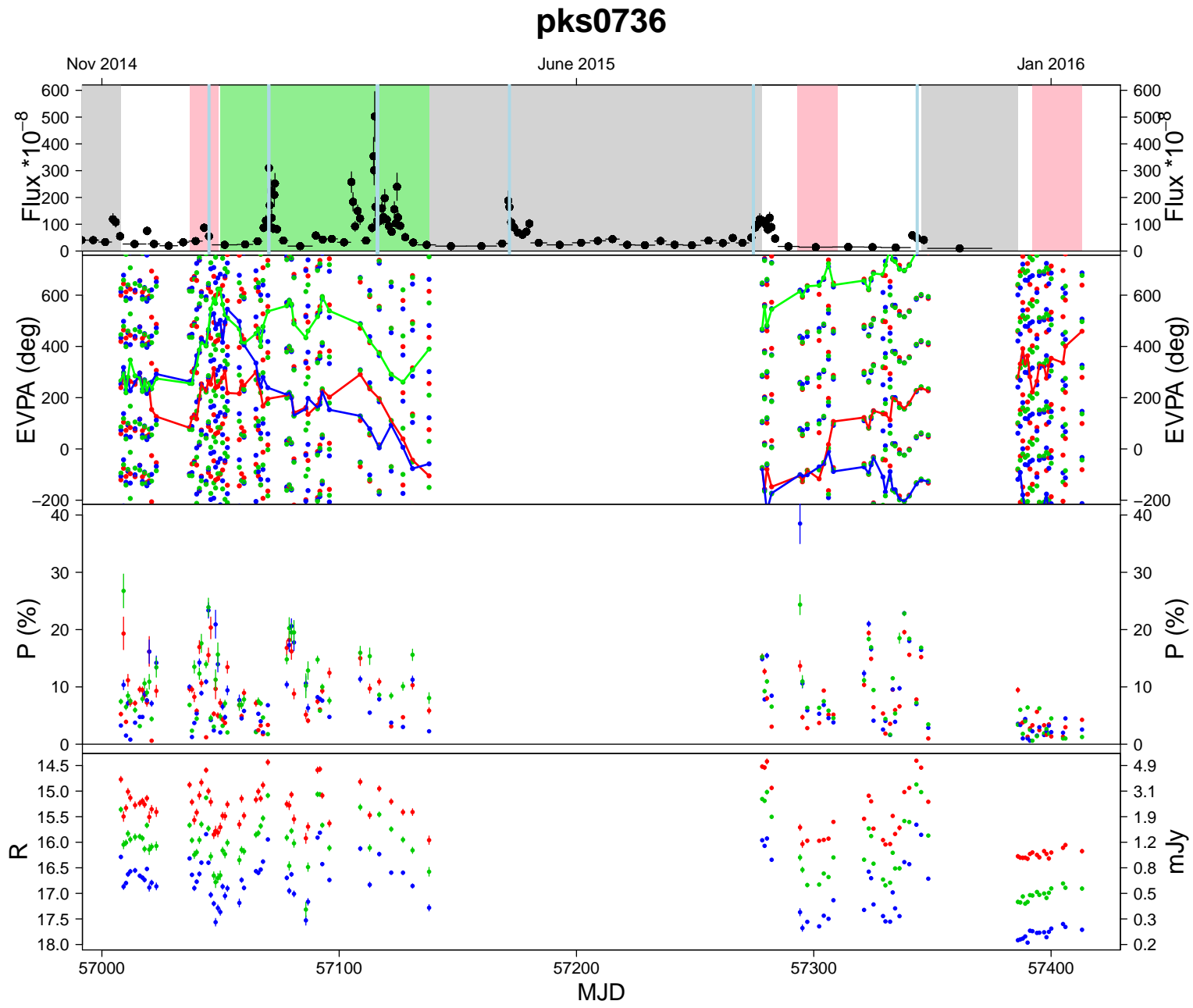

Figure 4.32: The multicolour light curve and polarisation plot for FSRQ source 3C279. See Section 4.3.15 for a full description of the source.

however only one rotation met the criteria specified in this work and that was the 'upward' $\sim 200°$ rotation from MJD = 57412-57427.

4.3.17   PKS 1510-089

PKS 1510-089 is very active in γ-rays, showing a lot of flare activity (25 flaring events in ~ 1200 days; see Figure 4.35). The largest flares were followed by an increase in the optical magnitude which otherwise, prior to this increase, stayed relatively stable.

From the variety of rotations that occurred between MJD= 56650 - 56900, only one met the criteria specified in this work and that was a 'downward' rotation of $\sim 180°$ from MJD = 56660 - 56730 (blue camera interpretation).

At MJD = 57120 the source underwent a substantial rotation for ~ 2 months, which depending on interpretation in the three different colours, showed a minimum 'upward' rotation of $\sim 400°$ ($\sim 480°$ in the blue camera). This is not unusual for PKS 1510-089 which has previously undergone a larger 'upward' rotation of $\sim 720°$ (Marscher et al., 2010) (from here 'rot1'). The rotation seen in the Ringo3 data (from here 'rot2') reached its highest (observable) angle at MJD$\sim$57250 which was coincident with an increase in the optical magnitude from b* magnitude$\sim$16.5-15.2 and a flare in the degree of polarisation reaching $\sim 30\%$. Rot1 showed similar characteristics with the peak angle corresponding with an optical flare and the degree of polarisation reaching $\geq 30\%$. Figure 4.34 shows the γ-ray activity during 'rot1' and 'rot2'. The flaring activity in γ-rays prior to 'rot1' occurred for ~ 60 days and showed multiple γ-ray flares. The γ-ray activity prior to 'rot2' showed flares which occurred over a ~ 200 day period. This may suggest that the emission was tracing the same shocked region but with different speeds.
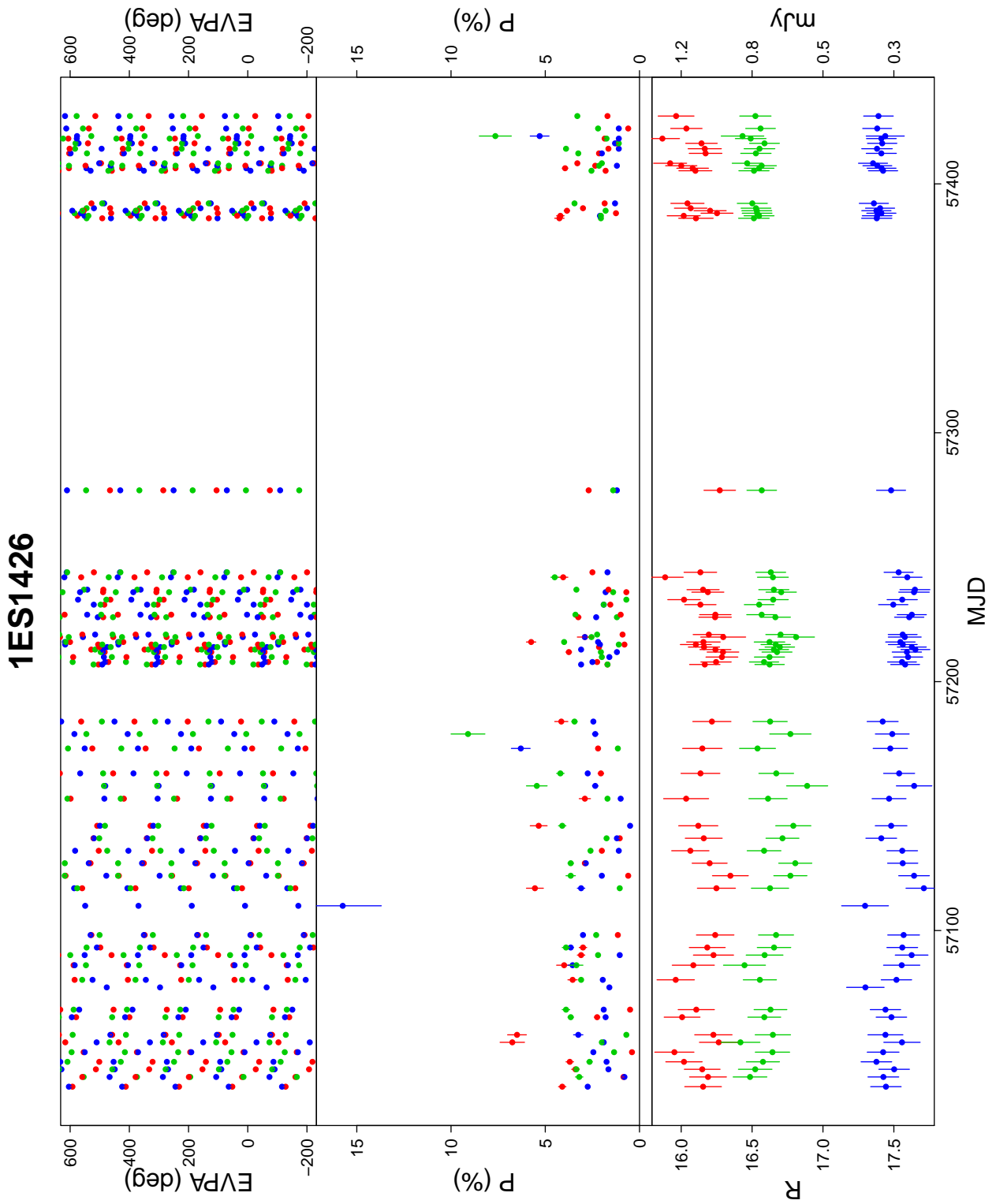
Figure 4.33: The multicolour light curve and polarisation plot for BL Lac source 1ES 1426.
See Section 4.3.16 for a full description of the source.
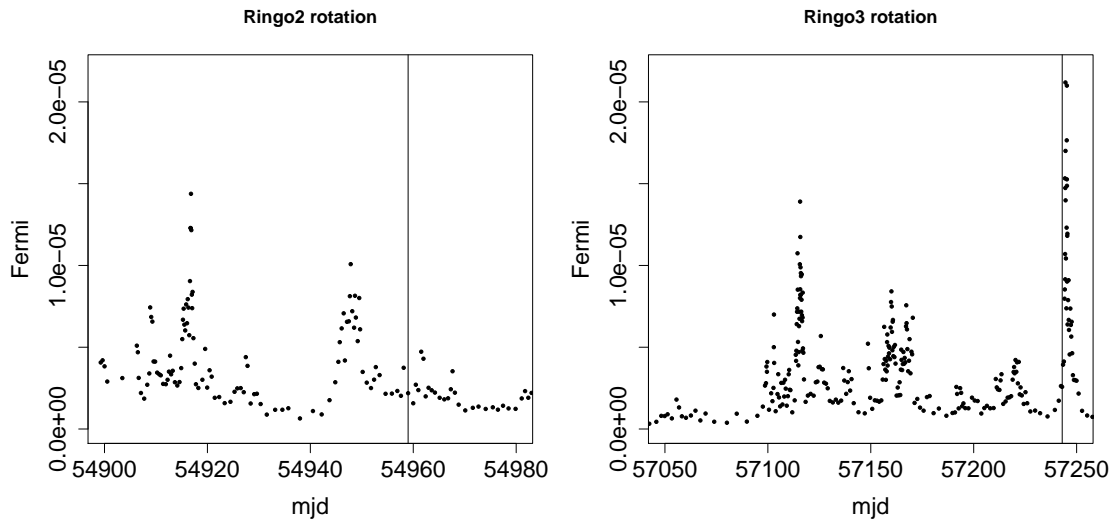
Figure 4.34: Comparison of the γ-ray activity in PKS 1510-089 during 'rot1' (the vertical line in the first plot) and 'rot2' (the vertical line in the second plot).

4.3.18 PG 1553+113

PG 1553+113, throughout the Ringo2 and Ringo3 periods of observation, showed a low γ-ray flux and a relatively stable optical magnitude (see Figures 3.24 and 4.36). The optical magnitude increased with the rise in γ-ray flux at MJD$\sim$57000. The polarisation was variable but low $\lesssim$12%.

From MJD$\sim$56775, the interpretation of the EVPA rotation (from the blue camera) showed a $\sim$350° rotation, but due to the poor sampling there were $\sim$1 month gaps in the data so they were classed as 2 separate rotations of $\sim$150°. From MJD$\sim$57200 onwards the EVPA rotated 'upward' by $\sim$100°.

4.3.19 Mrk 501

Mrk 501 showed a low level of γ-ray flux throughout the Ringo2 and Ringo3 periods, with 3 small flaring episodes and some small variations (see Figure 4.37). The EVPA showed no rotations and the polarisation was the lowest of the sample at $\lesssim$ 6%. The optical magnitude showed very little variation. These behaviours were very similar to
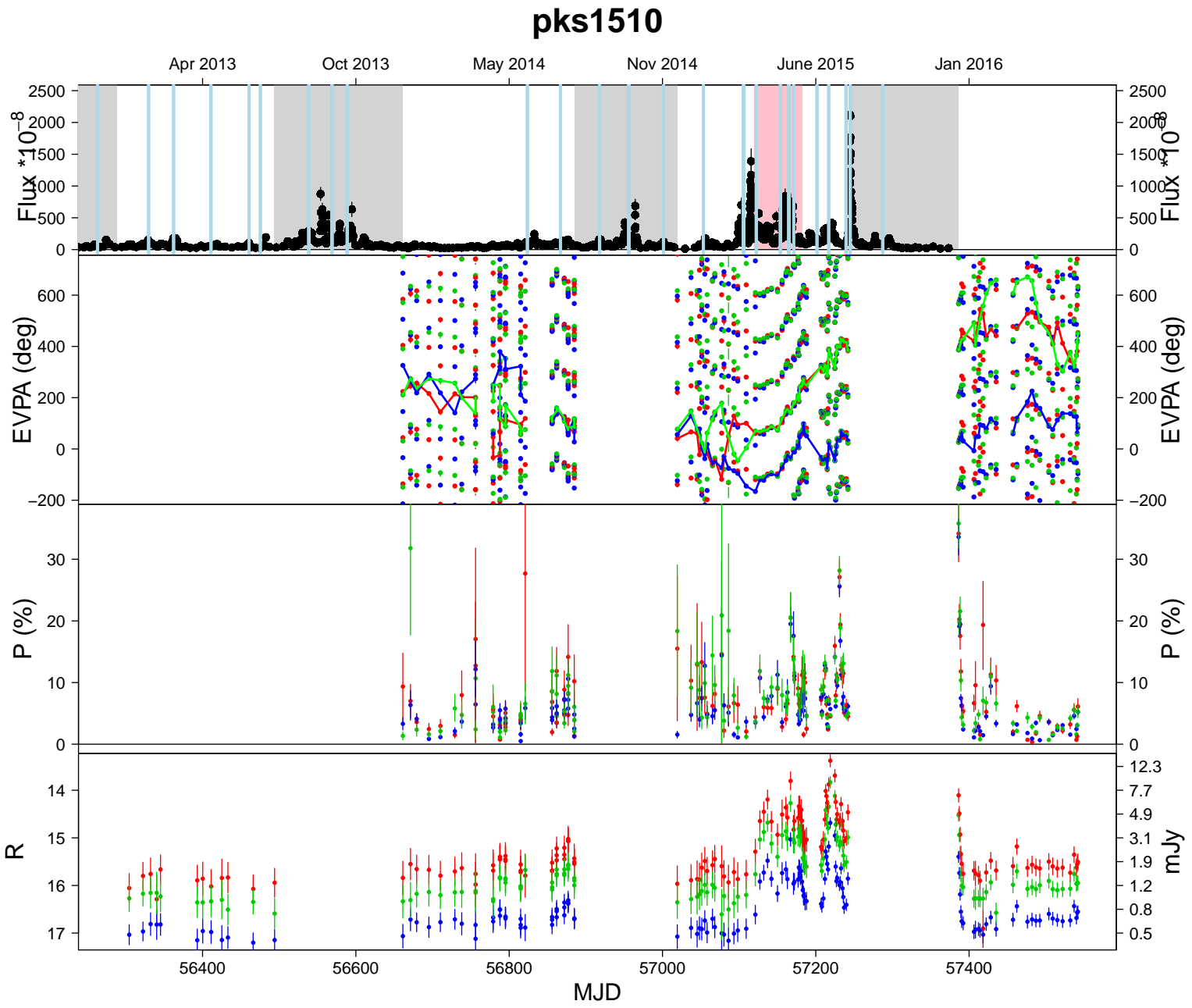
Figure 4.35: The multicolour light curve and polarisation plot for FSRQ source PKS 1510-089. See Section 4.3.17 for a full description of the source.
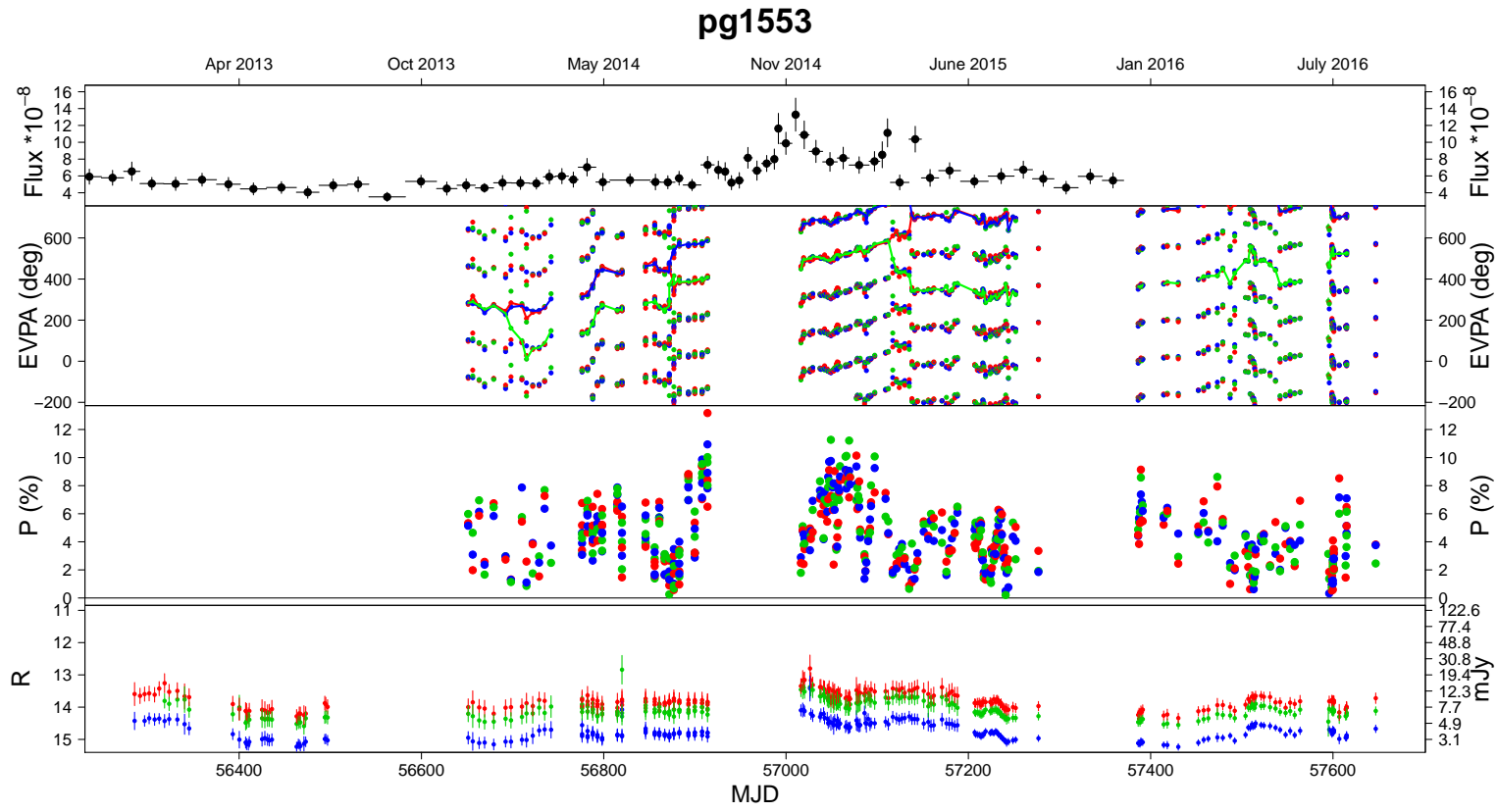
Figure 4.36: The multicolour light curve and polarisation plot for BL Lac source PG 1553. See Section 4.3.18 for a full description of the source.

those seen in the Ringo2 period of monitoring.

4.3.20 BL Lac

BL Lac showed similar γ-ray flare amplitude and variation in the Ringo3 as the Ringo2 period, with more flaring episodes (16) during the Ringo3 period (see Figure 4.39). The degree of polarisation underwent a ~month long increase from 1.4% to ~15%, (from MJD = 57205- 57229) and it then dropped to low polarisation levels before rising to 15.6% a few days later on MJD = 57236.

Intranightly measurements on MJD = 56816 appeared to show the EVPA undergoing a rapid ~100° rotation (from the EVPA interpretation using the red and green cameras, the blue camera showed the same points as scatter). The corresponding degree of polarisation measurements were between 1.5 and 9.4% and suggested that the EVPA points were exhibiting scatter associated with low polarisation. A similar rotation event occurred (in blue and green cameras) on MJD = 56892-56893 (in six measurements), again these measurements corresponded with low degree of polarisation; 0.4-5.3%. Other ~100° rotations between MJD~56900-57000 did not meet the requirements for rotation classification due to their being composed of just three points.

On MJD~57150, the datapoints from the three cameras were interpreted as showing a ~100° 'downward' rotation. Later on, denser sampling (and post telescope primary and secondary mirror realuminisation from MJD = 57202 onwards) showed a rapid EVPA rotation of ~200° from MJD = 57239 - 57242 (see Figure 4.38). The gaps in the sampling make a rotation definition difficult, however the eye can see where an 'upward' ~250° rotation could be traced. In Figure 4.38 the EVPA nearest neighbour interpretation is shown for each Ringo3 camera, along with a solid black line upward which traces a rough path of a ~250° rotation which occurs in ~48 hours. We do not attribute the difference between the EVPA in the green and the red camera to be intrinsic
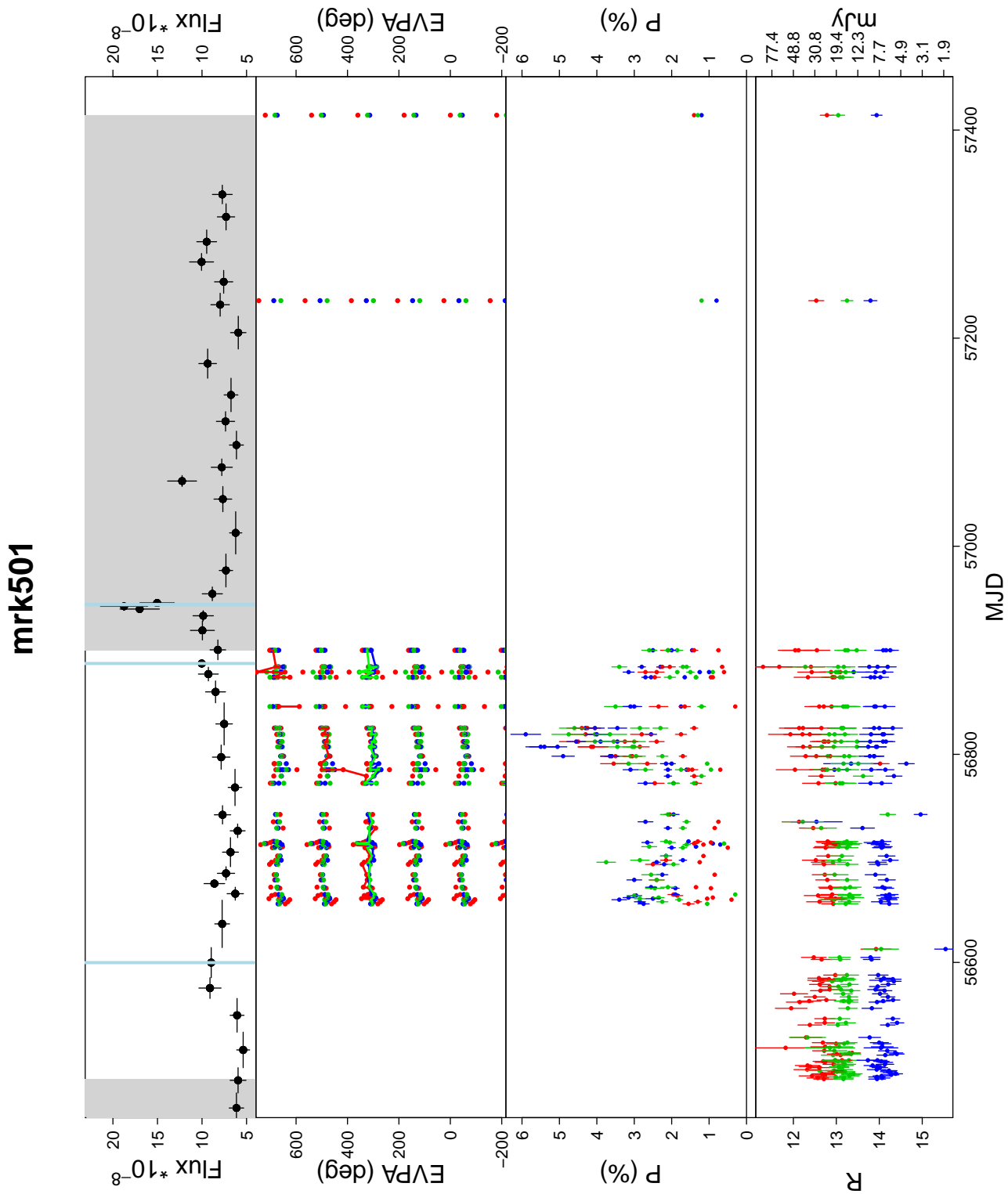
Figure 4.37: The multicolour light curve and polarisation plot for BL Lac source Mrk 501. See Section 4.3.19 for a full description of the source.

to the source, but simply due to the limited cadence of the observations.

For this analysis we used the EVPA interpretation from the red camera; a 'downward' rotation of $\sim$110°.
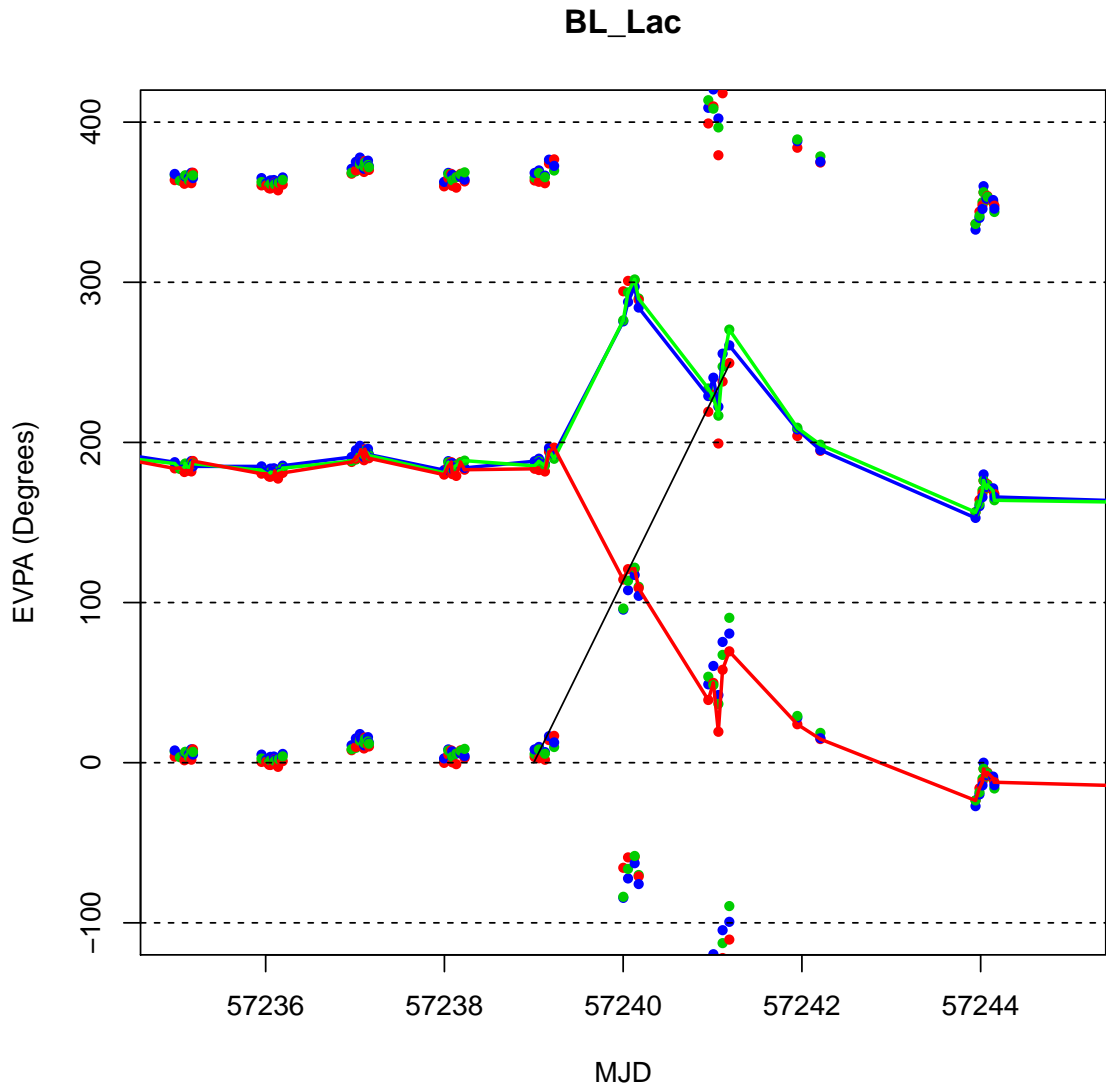
Figure 4.38: Comparison of the interpretation of an EVPA rotation in BL Lac in each of the three cameras (red, green and blue). This is an example of how the scatter on the data points can result in a different interpretation of the EVPA, and does not indicate different behaviours at different wavelengths.
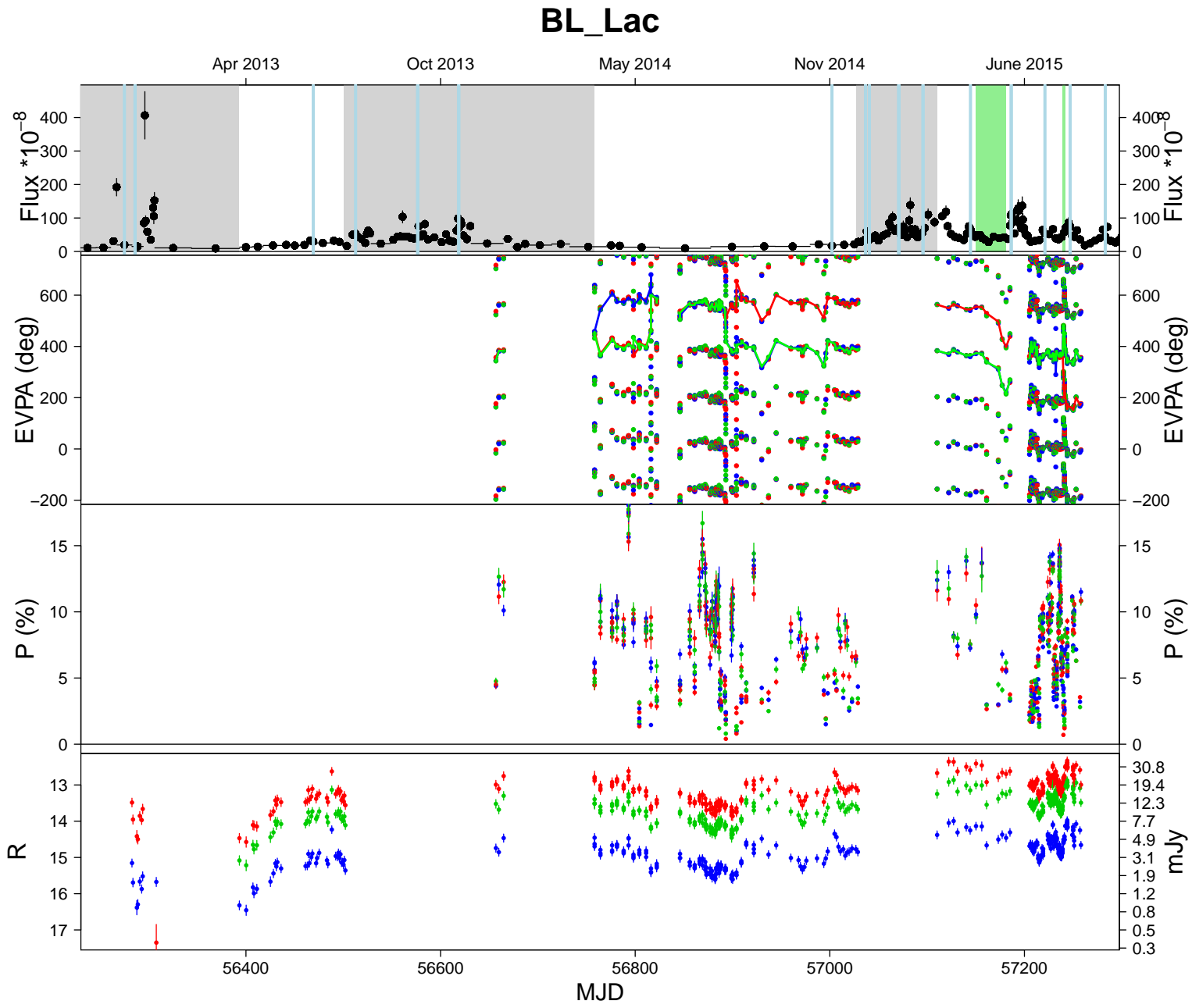
BL_Lac
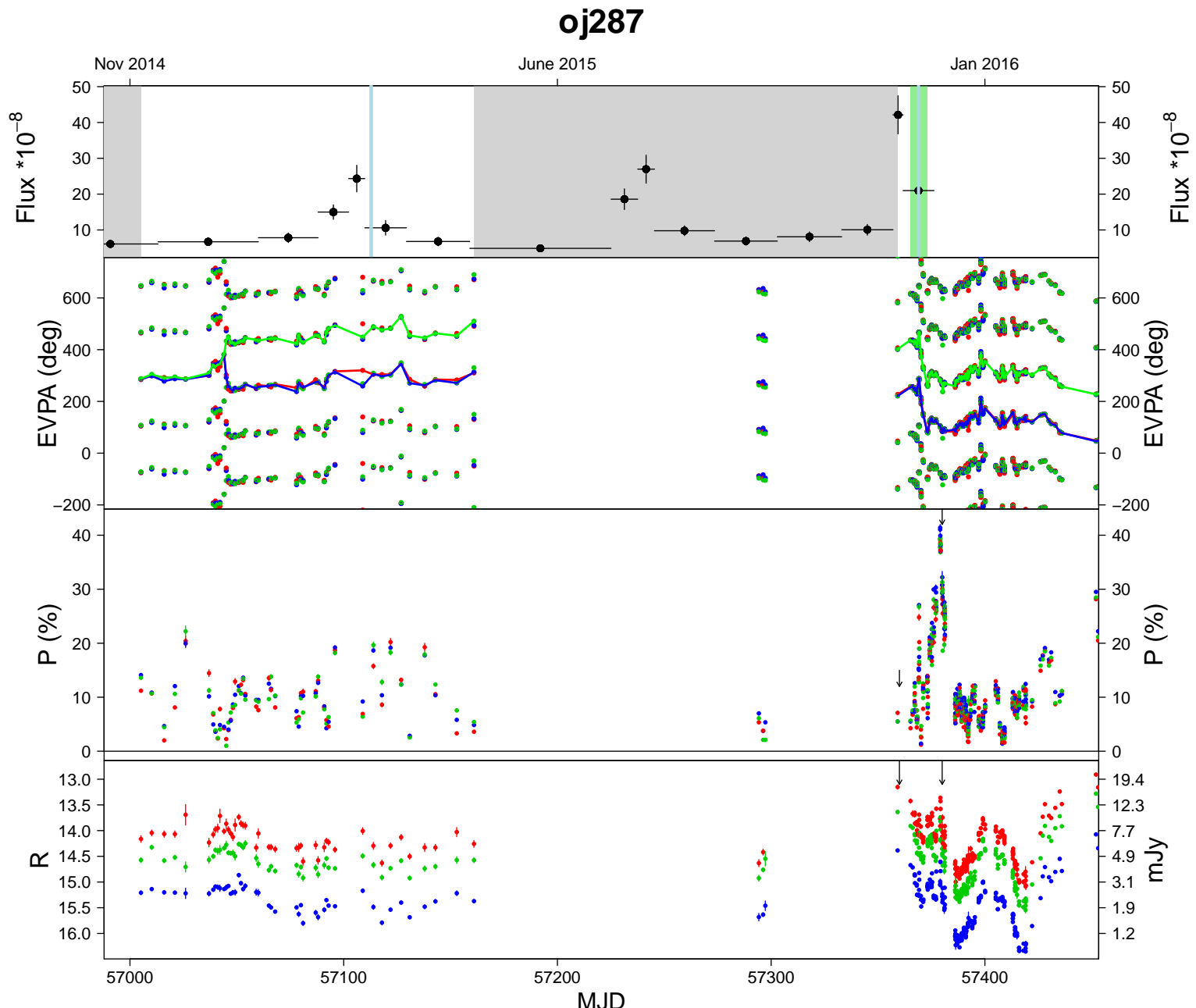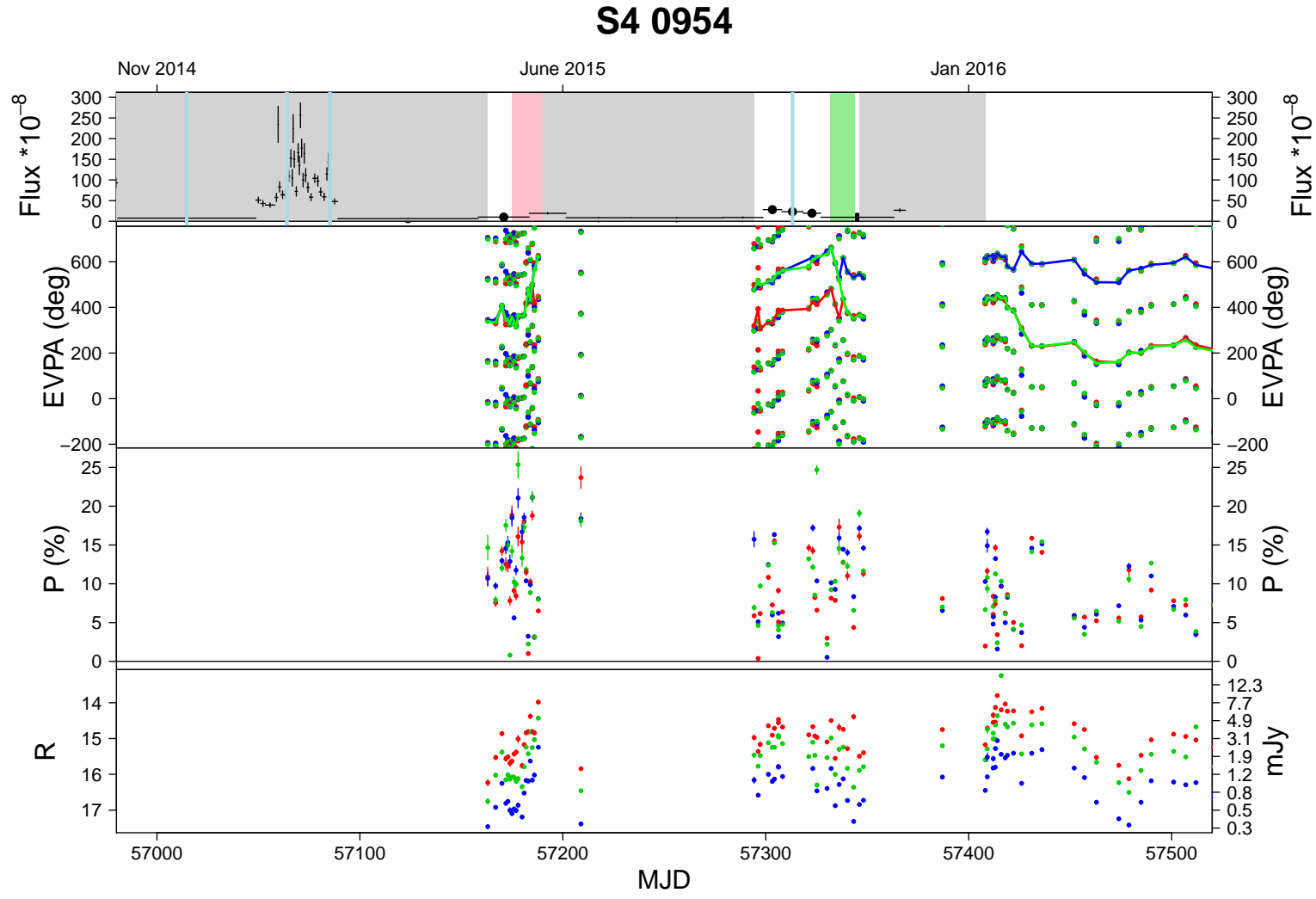

Figure 4.39: The multicolour light curve and polarisation plot for BL Lac. See Section 4.3.20 for a full description of the source.

4.4 Discussion

The correlation analysis performed on Ringo2 data in Chapter 3 was performed on the Ringo3 data and is discussed in this section. For the correlation plots comparing γ-ray and magnitude, γ-ray and degree of polarisation and magnitude and degree of polarisation the values from the green camera (central wavelengths) were used. As in Chapter 3, we plot the data with their non-distance-corrected values and distance-corrected values (i.e. absolute magnitude).

We continued to use the same method for interpolating Fermi γ-ray data to coincide with the optical observation dates (see Section 3.5.1). Mrk 180, 1ES 1426+496 and 3c120 are too faint in γ-rays for Fermi data so they were excluded from the γ-ray analysis.

With multicolour information in the Ringo3 data, an additional analysis was conducted which compares the spectral changes in the different blazar subclasses with changes in optical magnitude and degree of polarisation.

Mrk 421 does not have secondary stars in the frame so photometric calibration of Ringo3 data cannot occur, this means that colour information is not available.

The same notation and interpretation of the Spearman rank coefficients and KS test p values from the Chapter 3 are used in this Chapter.

4.4.1 Optical magnitude and γ-ray flux correlations

Figure 4.40 shows the Fermi γ-ray (interpolated) flux plotted against optical apparent magnitude for all sources and for the different subclasses: BL Lacs, FSRQs, LSP, ISP and HSPs. As was seen in the same plot for the Ringo2 data, the first plot in Figure 3.2 appears to show two subclasses, which are then shown in panels 2 and 3 to be the FSRQ and BL Lac sources respectively. From the figure it is also possible to separate
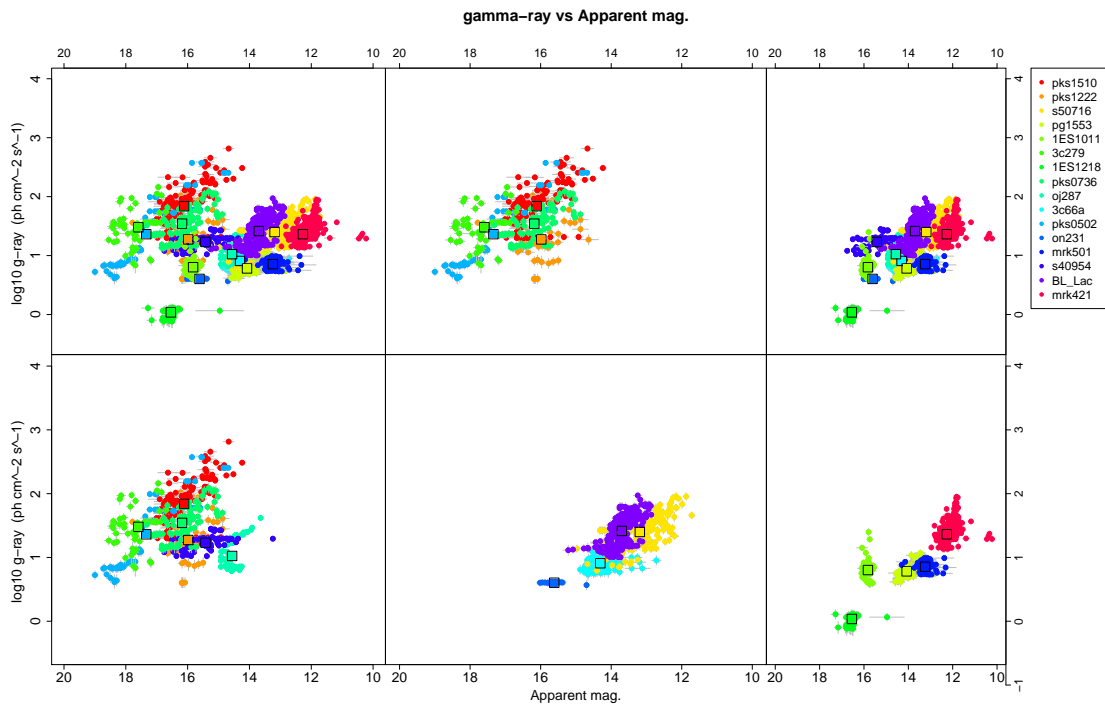
Figure 4.40: Plot of $\log_{10}\gamma$-ray flux against g* apparent magnitude for all sources and seasons, separated into different subclasses. The colour key identifies the sources and the black squares show the mean of each source.

the three spectral peak subclasses with a shift toward higher magnitudes with higher spectral peak.

Similar to the Ringo2 data, Figure 4.41 shows this apparent trend is no longer visible when the absolute magnitude is plotted. This means that the trends seen by eye in the apparent magnitude plots were caused by distance effects.

Table 4.6 shows the range of Spearman rank coefficient ρ and p values for different classes for the optical g* magnitude and γ-ray flux. Focussing on those ρ values where $p \leq 0.05$, there were 9 positive correlations and 1 negative correlation. The mean ρ values varied from 0.487-0.611 between the different classes. The source with a significant negative correlation was a FSRQ, with ρ=-0.270

Figures 4.42, 4.43 and 4.44 show the individual plots for each season of each source. In this plot it is clear that in general the data from each wavelength band are in the order blue, green, red in increasing brightness (this can also be seen in the individual
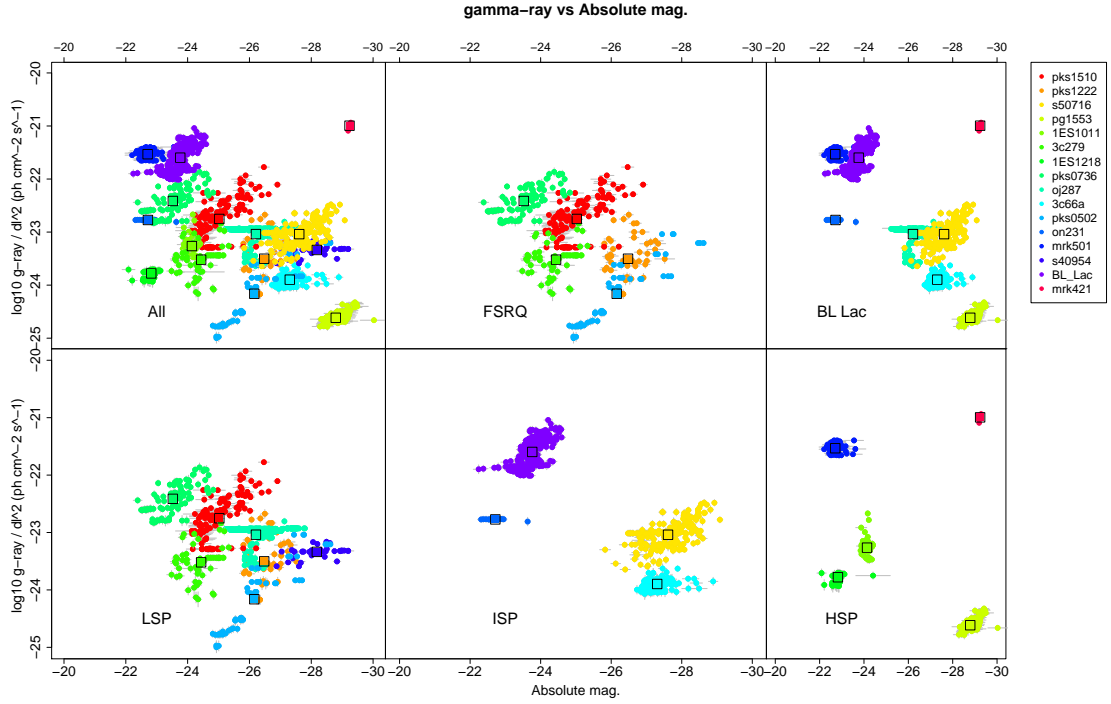
Figure 4.41: Plot of distance corrected $\log_{10}\gamma$-ray flux against g* absolute magnitude for all sources and seasons, separated into different subclasses. The colour key identifies the sources and the black squares show the mean of each source.

	Type	All p Range p	Range ρ	Mean p	Mean ρ	Quantity -ρ,+ρ	Quantity	p≤0.05 Range ρ	Mean ρ	Quantity -ρ,+ρ	Quantity
mag-gam	HSP	0.000 - 0.810	-0.172 - 0.687	0.363	0.144	4,2	6	0.486 - 0.687	0.587	0,2	2
	ISP	0.000 - 0.269	0.267 - 0.742	0.0673	0.525	0,4	4	0.473 - 0.742	0.611	0,3	3
	LSP	0.000 - 0.497	-0.270 - 0.866	0.112	0.340	2,6	8	-0.270 - 0.866	0.518	1,4	5
	FSRQ	0.000 - 0.497	-0.270 - 0.866	0.132	0.363	1,5	6	-0.270 - 0.866	0.487	1,3	4
	BL Lac	0.000 - 0.810	-0.172 - 0.742	0.213	0.293	5,7	12	0.473 - 0.742	0.608	0,6	6
	All	0.000 - 0.810	-0.270 - 0.866	0.186	0.316	6,12	18	-0.270 - 0.866	0.559	1,9	10
deg-gam	HSP	1.65×10^{-7} - 0.835	-0.592 - 0.256	0.339	-0.0591	3,3	6	-0.592 - 0.256	-0.168	1,1	2
	ISP	0.00052 - 0.739	-0.277 - -0.0197	0.403	-0.130	4,0	4	-0.277 - -0.277	-0.277	1,0	1
	LSP	4.54×10^{-8} - 0.484	-0.320 - 0.647	0.116	0.19	3,5	8	-0.320 - 0.647	0.305	1,4	5
	FSRQ	4.54×10^{-8} - 0.484	-0.100 - 0.647	0.107	0.318	1,5	6	0.306 - 0.516	0.411	0,4	2
	BL Lac	1.65×10^{-7} - 0.835	-0.592 - 0.256	0.327	-0.105	9,3	12	-0.592 - 0.256	-0.233	3,1	4
	All	4.54×10^{-8} - 0.835	-0.592 - 0.647	0.254	0.0359	10,8	18	-0.592 - 0.647	0.114	3,5	8
deg-mag	HSP	0.00416 - 0.917	-0.342 - 0.167	0.315	0.036	1,5	6	-0.342 - -0.342	-0.342	1,0	1
	ISP	2.97×10^{-5} - 0.991	-0.332 - -0.00351	0.499	-0.108	4,0	4	-0.332 - -0.332	-0.332	0,1	1
	LSP	3.09×10^{-8} - 0.112	-0.416 - 0.653	0.0234	0.119	3,5	8	-0.416 - 0.653	0.154	2,4	6
	FSRQ	3.09×10^{-8} - 0.112	-0.386 - 0.653	0.0309	0.178	2,4	6	-0.386 - 0.326	-0.03	1,1	2
	BL Lac	1.83×10^{-7} - 0.991	-0.416 - 0.303	0.324	-0.0275	6,6	12	-0.416 - 0.303	-0.197	2,4	6
	All	3.09×10^{-8} - 0.991	-0.416 - 0.653	0.226	0.0409	8,10	18	-0.416 - 0.653	0.0315	3,5	8

Table 4.6: Summary of results from the Spearman Rank correlation test showing the p and ρ values for different subclasses for optical vs γ-ray data, degree of polarisation vs Fermi γ-ray flux and optical magnitude vs optical degree of polarisation. The full dataset is presented in Tables 4.17, 4.16 and 4.18.

source light curves). The red, green and blue magnitude plotted against γ-ray flux tend to show similar correlations and increase and decrease in a similar pattern. Tables 4.16, 4.17 and 4.18 give the Spearman Rank coefficient test ρ and p values for the three waveband optical and γ-ray correlations. Those ρ values that have significant p values (i.e. p$\leq$0.05) are shown in bold in the table.

4.4.2 Optical degree of polarisation and γ-ray flux correlations.

Figure 4.45 shows the γ-ray flux vs degree of polarisation for all sources. Similar to the Ringo2 data the HSP sources showed a lower maximum value of polarisation ($\sim$10%), which increased to a maximum of $\sim$30% and $\sim$40% for ISP and LSP sources respectively.

In Figure 4.46 we show the distance-corrected γ-ray flux against the degree of polarisation. The sources separate due to their differing γ-ray fluxes, but no new trends are visible by eye.

The individual sources and seasons are shown in Figures 4.47, 4.48 and 4.49 and show that the relationship between the degree of polarisation and γ-ray flux for each camera is more scattered than that of the optical magnitude and γ-rays in Figures 4.42, 4.43 and 4.44. For the degree of polarisation and γ-ray correlation there is no uniform behaviour of the properties in each filter, as can be seen in the optical magnitude and γ-ray correlations.

A full list of the Spearman rank coefficient values for each season is in Tables 4.16, 4.17 and 4.18 and also in Table 4.6 for each subclass. In Table 4.6 there are 5/8 positive ρ values and the mean ρ values vary between positive and negative values. The significant ρ values from the Ringo2 analysis in Table 4 (Section 4.1.1), where available, are all negative except the ISP sources' correlation which is positive.
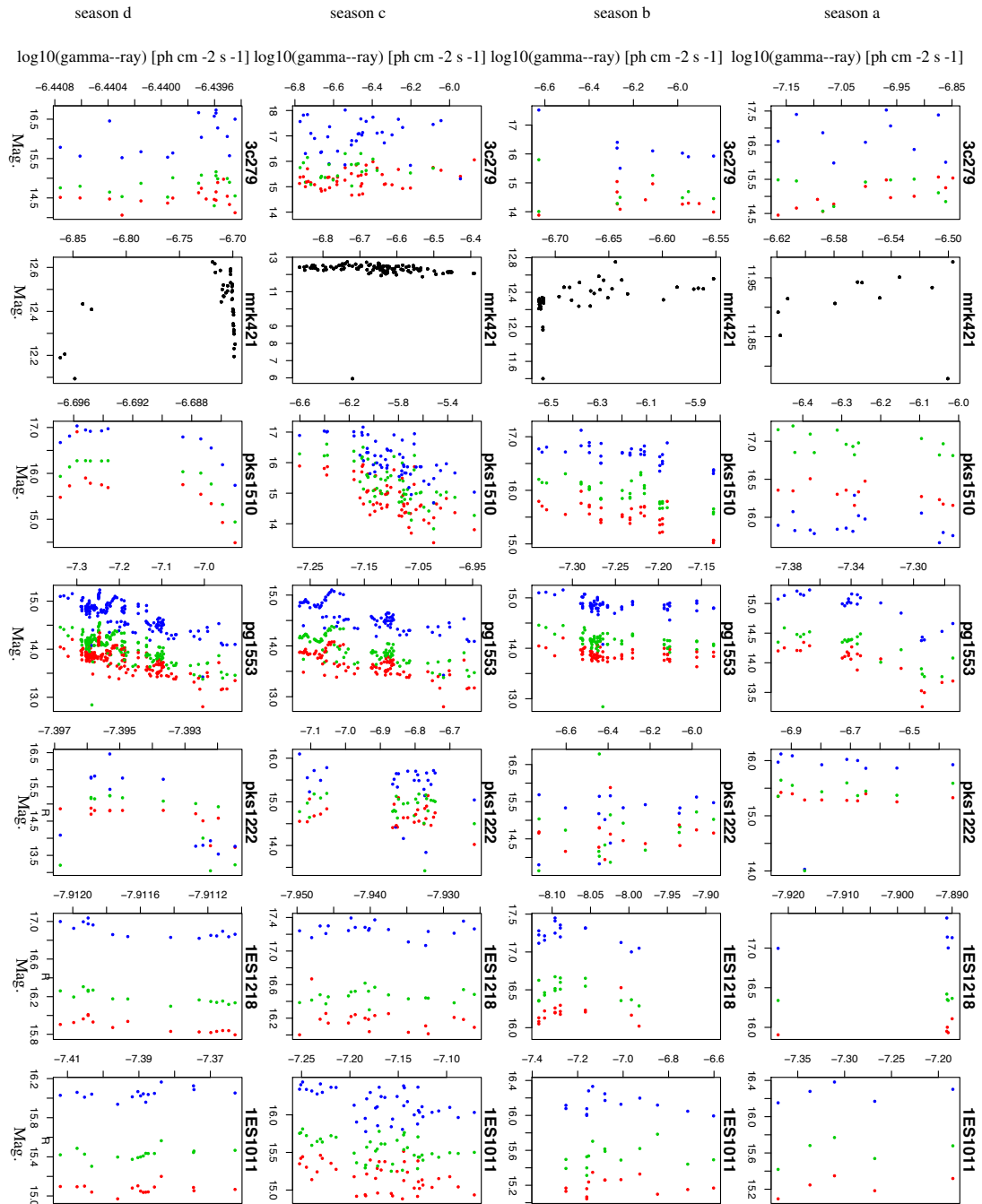
Figure 4.42: Plot of $\log_{10}\gamma$-ray flux against b*, g* and r* magnitude for all sources and seasons. The cameras are identified by each of their colours (red, green and blue) except for Mrk 421 which does not have multicolour information.
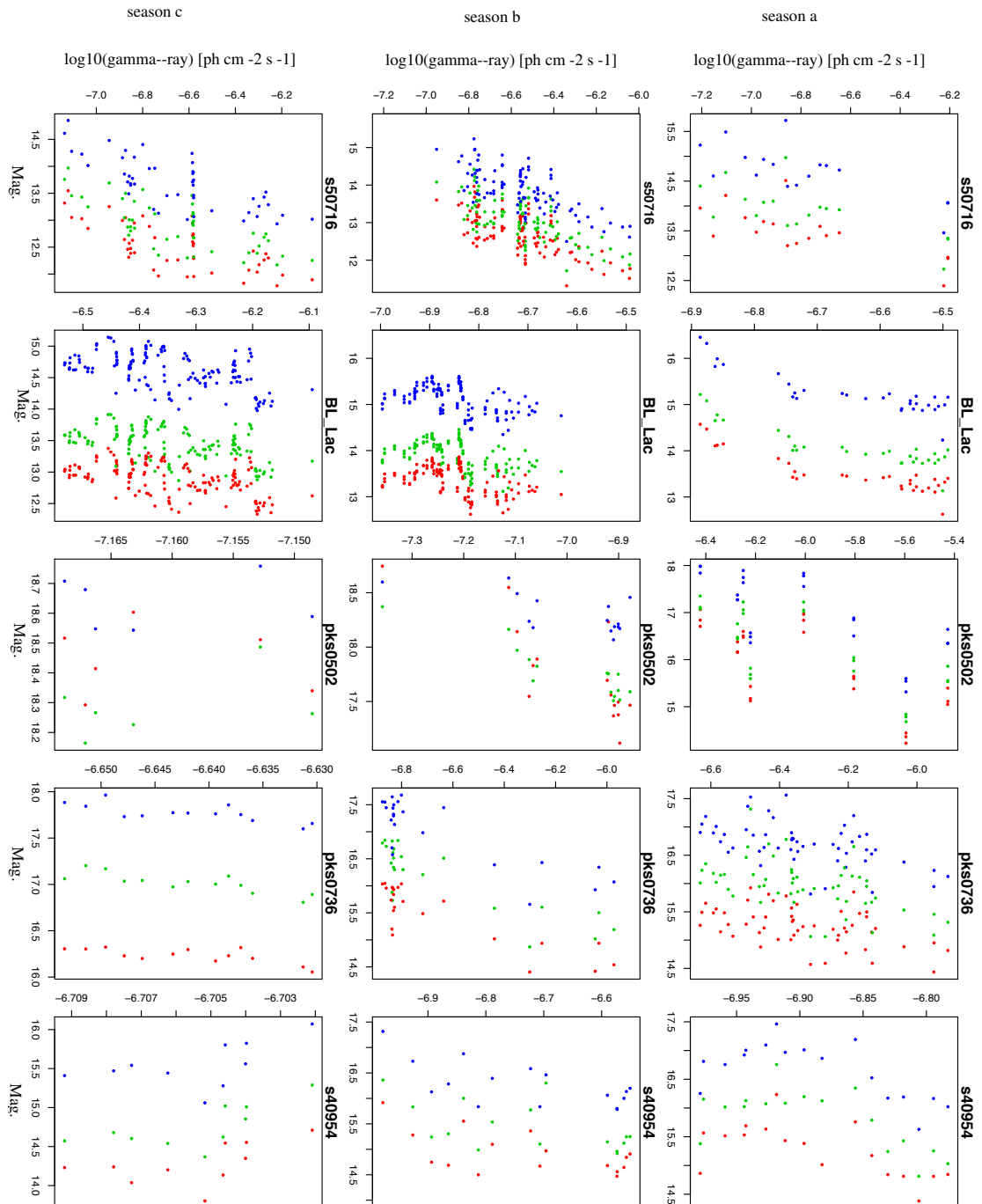
Figure 4.43: Figure 4.42 continued...

Season b

Season a
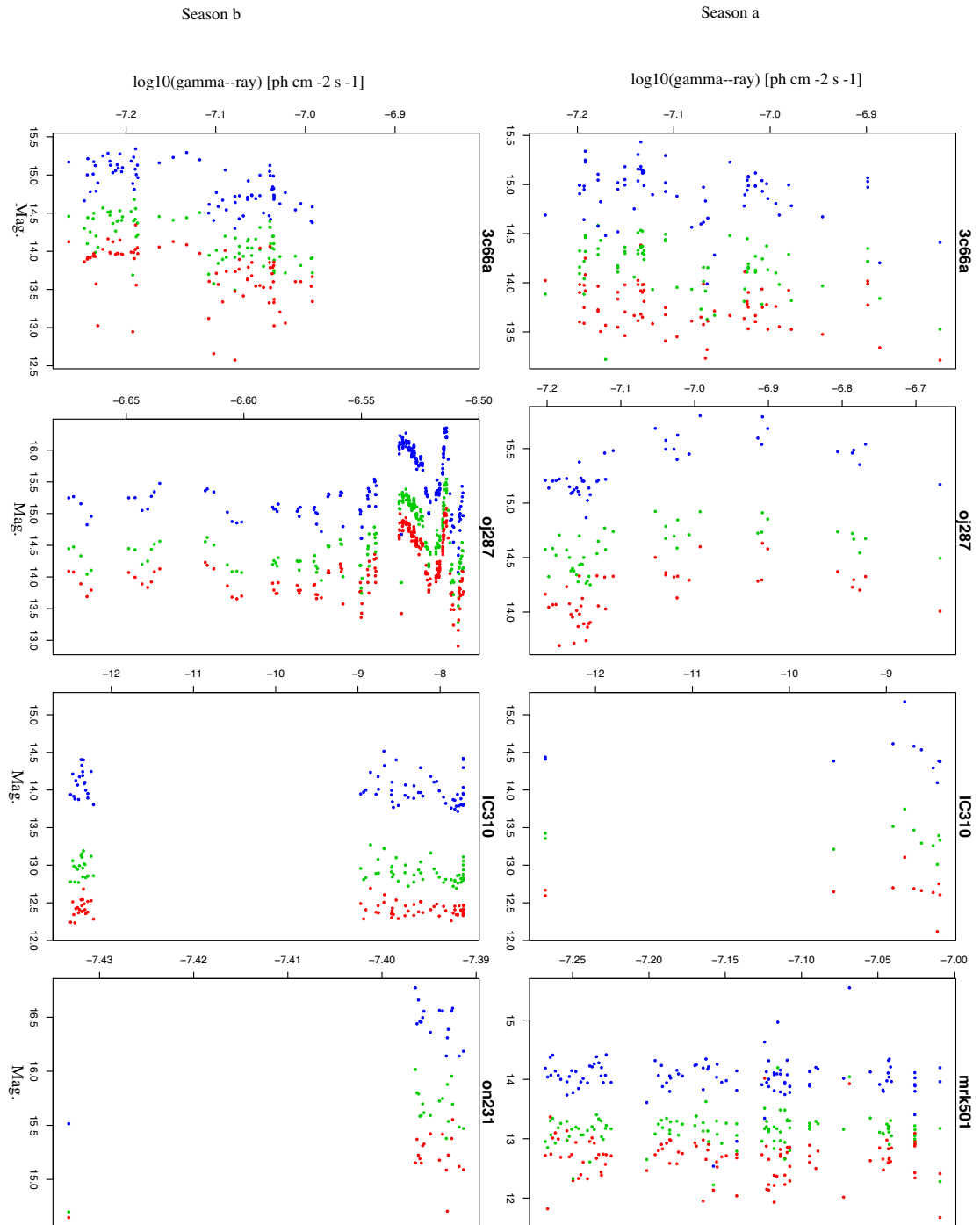
Figure 4.44: Figure 4.42 continued...
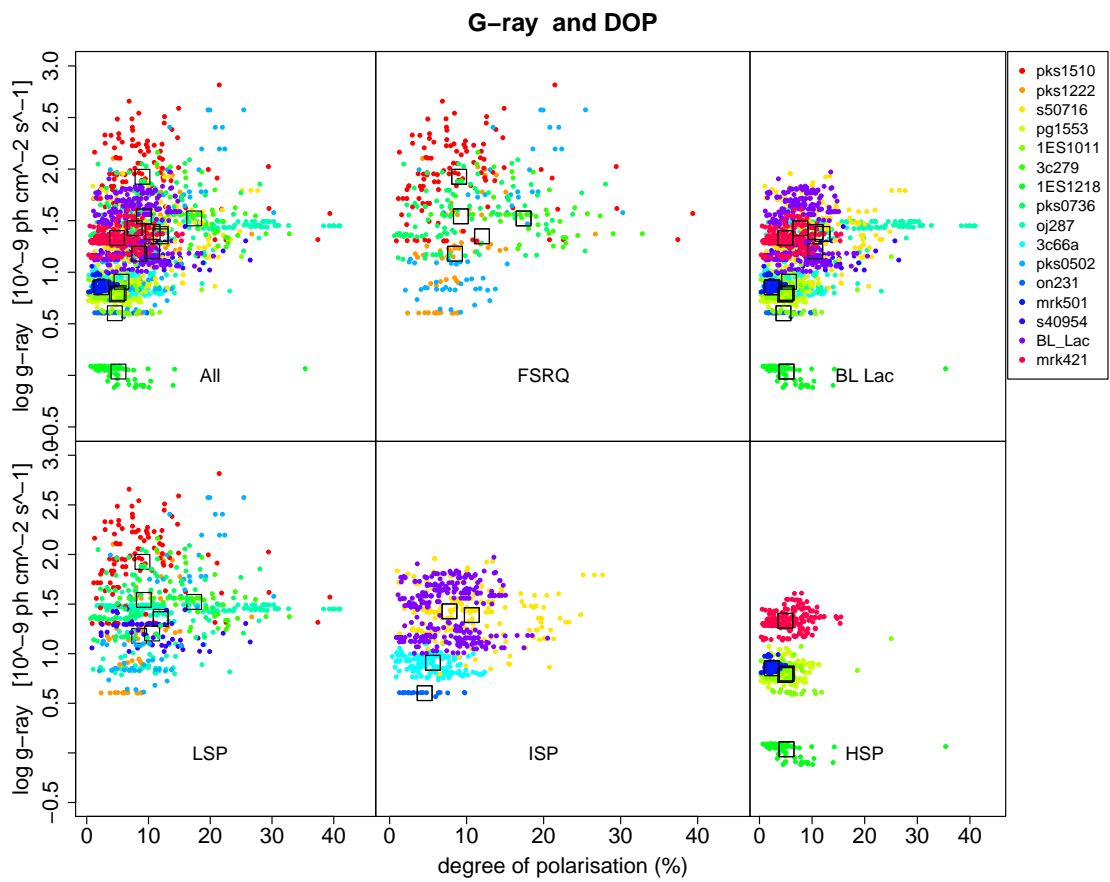
Figure 4.45: Plot of $\log_{10}\gamma$-ray flux against g* band degree of polarisation for all sources, separated into different subclasses. The colour key identifies the sources and the black squares show the mean of each source.
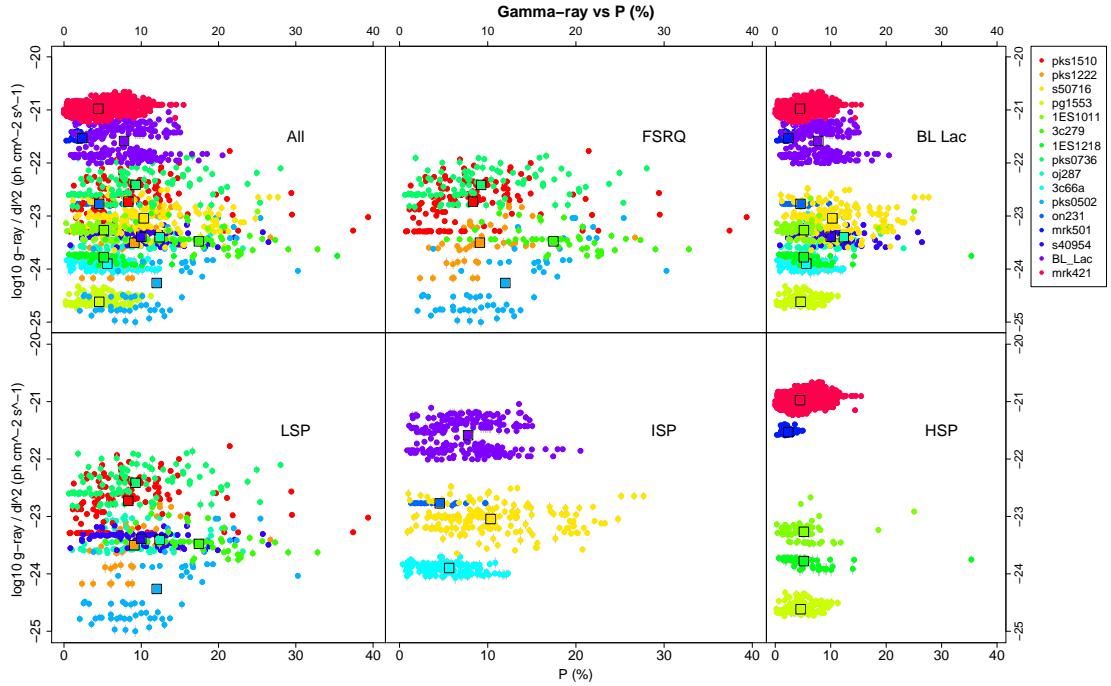
Figure 4.46: Plot of distance-corrected $\log_{10}\gamma$-ray flux against g* band degree of polarisation for all sources, separated into different subclasses. The colour key identifies the sources and the black squares show the mean of each source.

4.4.3 Optical magnitude and degree of polarisation correlations

Figure 4.50 shows the optical apparent magnitude against degree of polarisation for each subclass. Figure 4.51 shows the same data where the magnitude has been converted to absolute magnitude to account for distance affects. There are no apparent correlations between the magnitude and degree of polarisation for either plot.

Figures 4.52, 4.53 and 4.54 show correlations for individual sources and each season (for all three colours).

A full list of the Spearman rank coefficient values are in Tables 4.17, 4.18 and 4.16 and also in Table 4.6 for each subclass. Table 4.6 shows the significant correlation coefficients (i.e where p$\leq$0.05) have 5/8 positive ρ values. The significant ρ values from the Ringo2 analysis in Table 4 (Section 4.1.1), where available, were all positive with the ISP sources' correlation being close to zero. In both the Ringo2 and Ringo3 data there were more positive than negative correlations between the optical magnitude
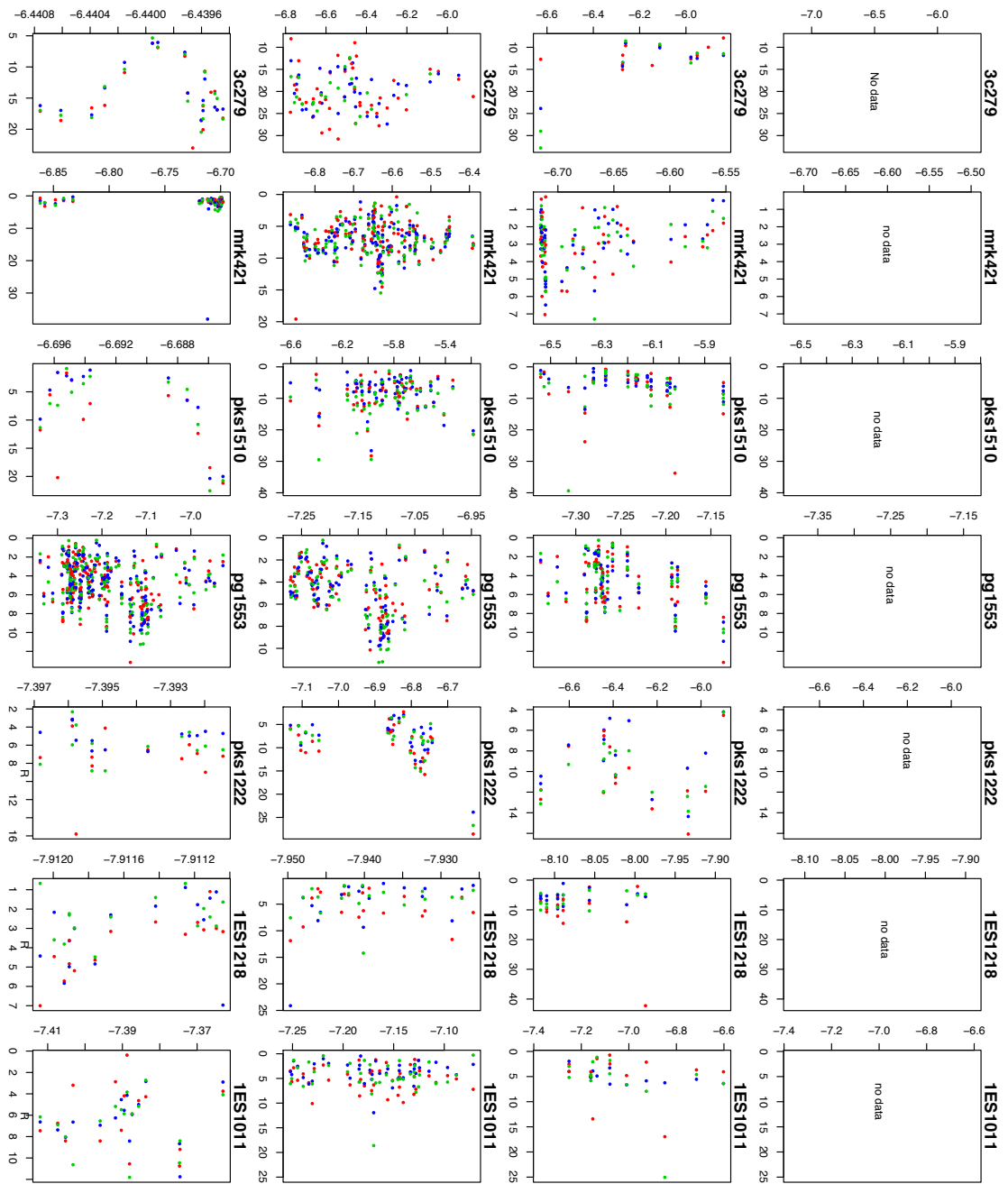
Figure 4.47: Plot of $\log_{10}\gamma$-ray flux against b*, g* and r* band degree of polarisation for all sources and seasons. The cameras are identified by each of their colours (red, green and blue) except for Mrk 421 which does not have multicolour information.
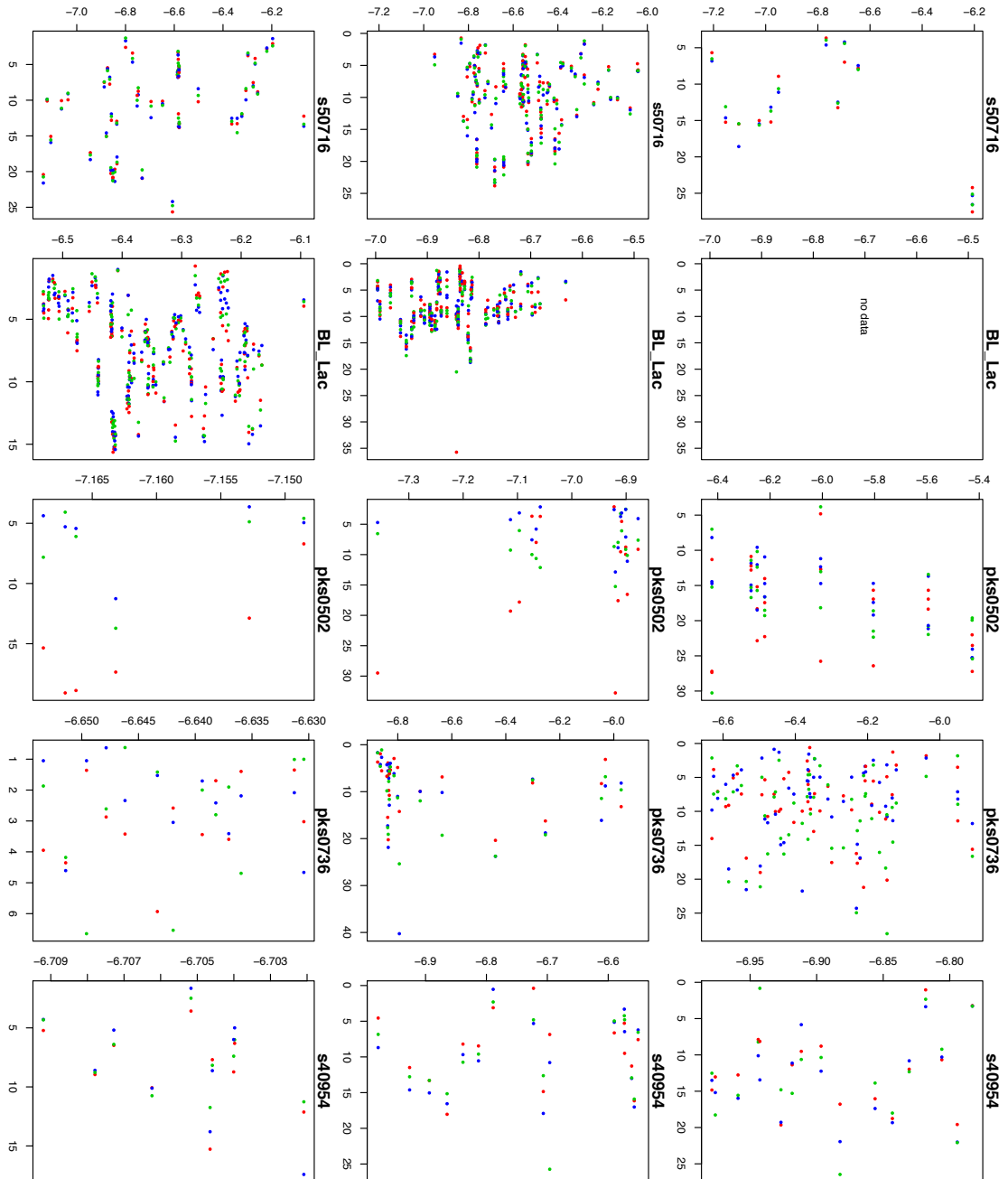
Figure 4.48: Figure 4.47 continued...
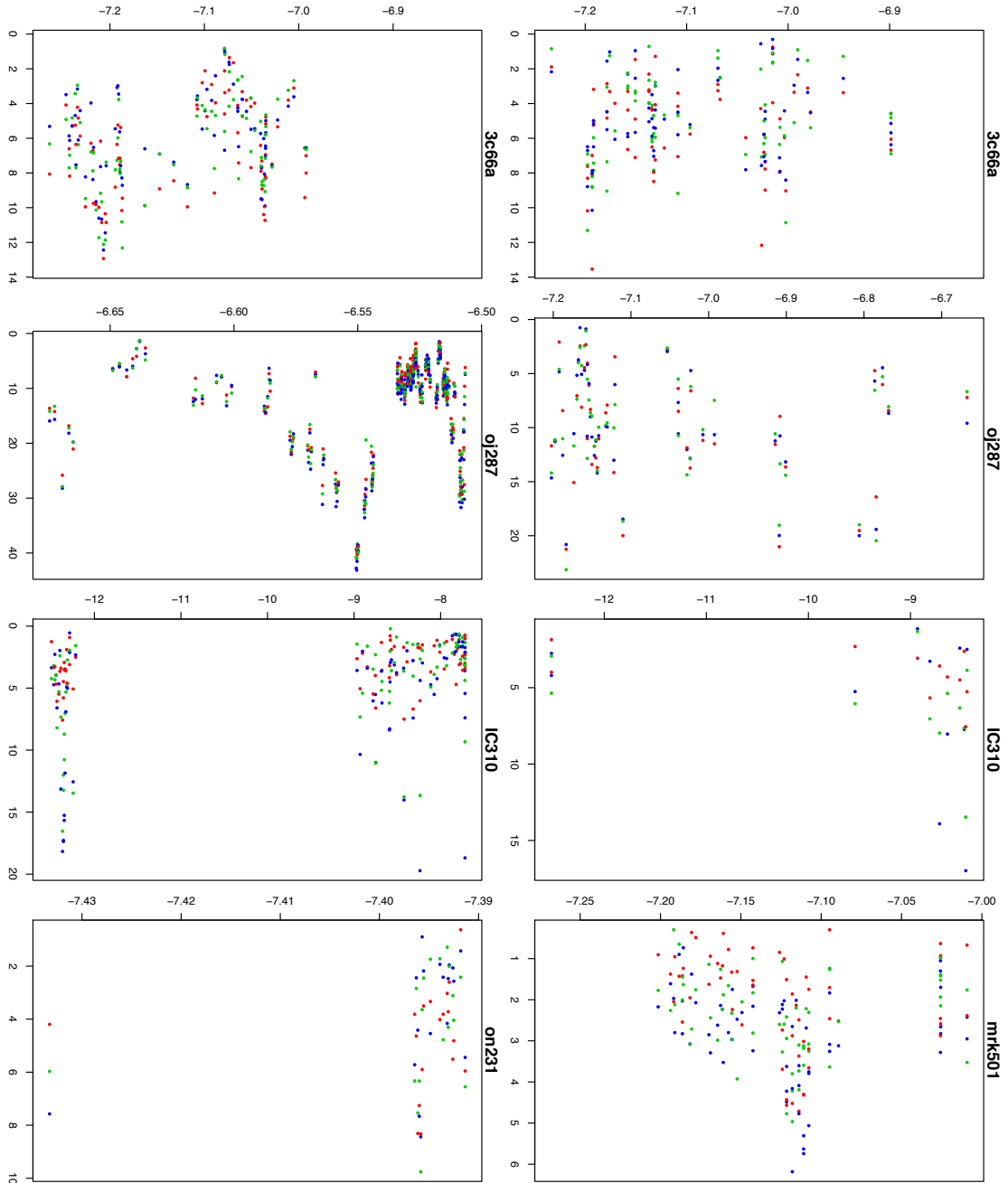
Figure 4.49: Figure 4.47 continued...
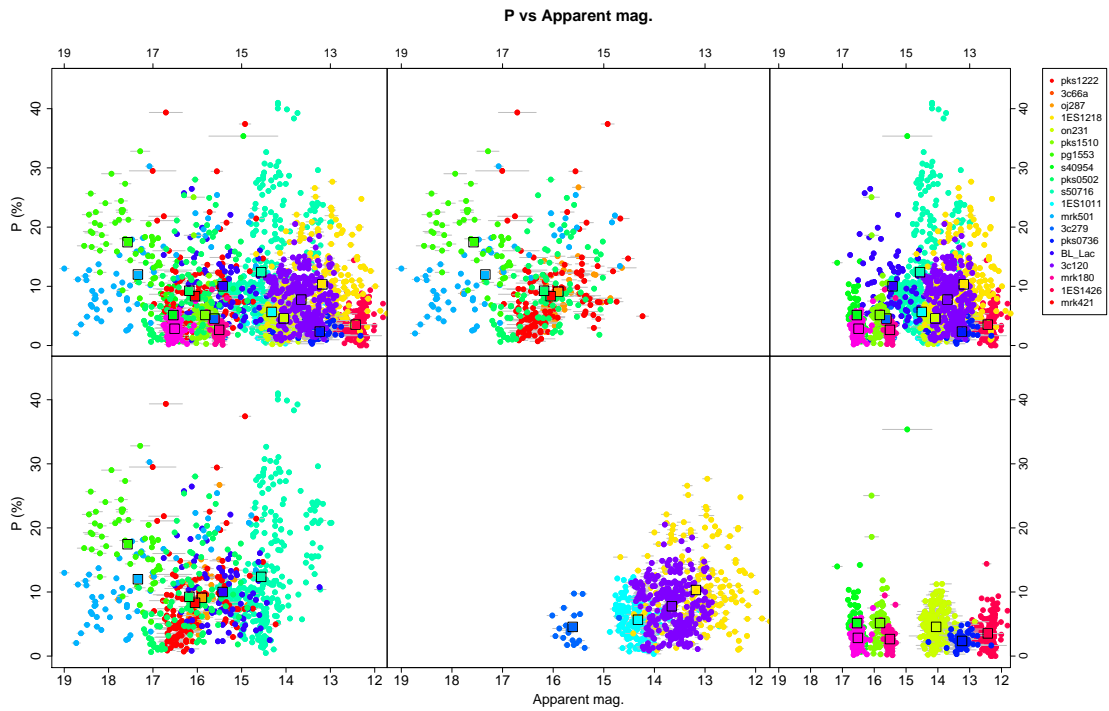
Figure 4.50: Plot of degree of polarisation against apparent magnitude in the g* band for all sources, separated into different subclasses. The colour key identifies the sources and the black squares show the mean of each source.

and degree of polarisation.
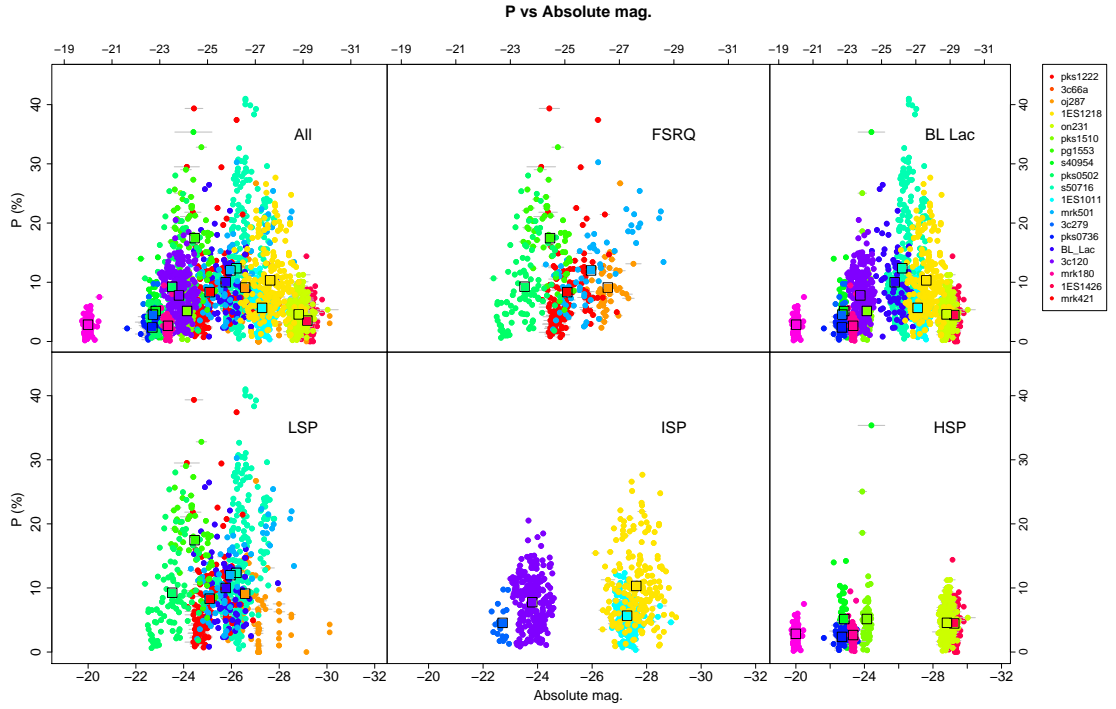
P vs Absolute mag.

Figure 4.51: Plot of absolute magnitude against degree of polarisation in the g* band for all sources, separated into different subclasses. The colour key identifies the sources and the black squares show the mean of each source.

1. Source	2. Rot ↑ (anti-c-wise)	3. Rot ↓ (c-wise)	4. Flares	5. Type	6. Fermi mon. period (days)	7. Max. deg.	8. Flare rate flares/day (year)	9. Days between rot & flare	10. Flares during rot
3C 66A	0	0	4	ISP	1134	13.5	...	...	...
IC310	0	1	0	HSP	1101	19.7	9×10^{-3}	...	...
PKS 0502+049	0	0	7	HSP	1074	36.8	...	...	...
S5 0716+714	1	2	17	ISP	1144	27.9	0.015	25, 23, 5	7
PKS 0736+017	1	1	6	LSP (FSRQ)	1102	40.3	0.0054	...	4
OJ287	1	0	2	LSP	1137	43.1	0.0018	...	1
S4 0954+65	1	1	3	ISP	964	26.5	0.0031	...	1
Mrk 421	0	1	14	HSP	1149	15.5	0.0122	0	1
1ES1011+496	1	2	5	HSP	1088	25.0	0.0046	...	0
1ES1426+304	2	1	0	HSP	...	7.0	...	...	...
1ES1218+304	1	1	0	HSP	991	24.11	...	...	...
ON231	1	1	1	ISP	1058	9.8	...	...	...
PKS 1222+216	0	0	10	LSP (FSRQ)	1128	28.6		...	...
3C 279	0	0	16	LSP (FSRQ)	1145	32.9	...	...	...
PKS 1510-089	1	1	25	LSP (FSRQ)	1144	39.4	0.022	103	9
PG 1553+113	3	0	4	HSP	1123	13.2	0.0036	...	3
Mrk 501	0	0	3	HSP	1105	6.2	...	...	...
BL Lac	2	0	16	ISP	1142	20.5			

Table 4.7: Tabulated data of the upward and downward EVPA rotations and γ-ray flares for different blazar subclasses for the 11 sources that have EVPA rotation/γ-ray flare events. Also included are the length of the Fermi monitoring period in days, the maximum degree of polarisation, the flare rate (and mean flare rate), days between rotations and flares (and mean of this value) and number of flares during a rotation.
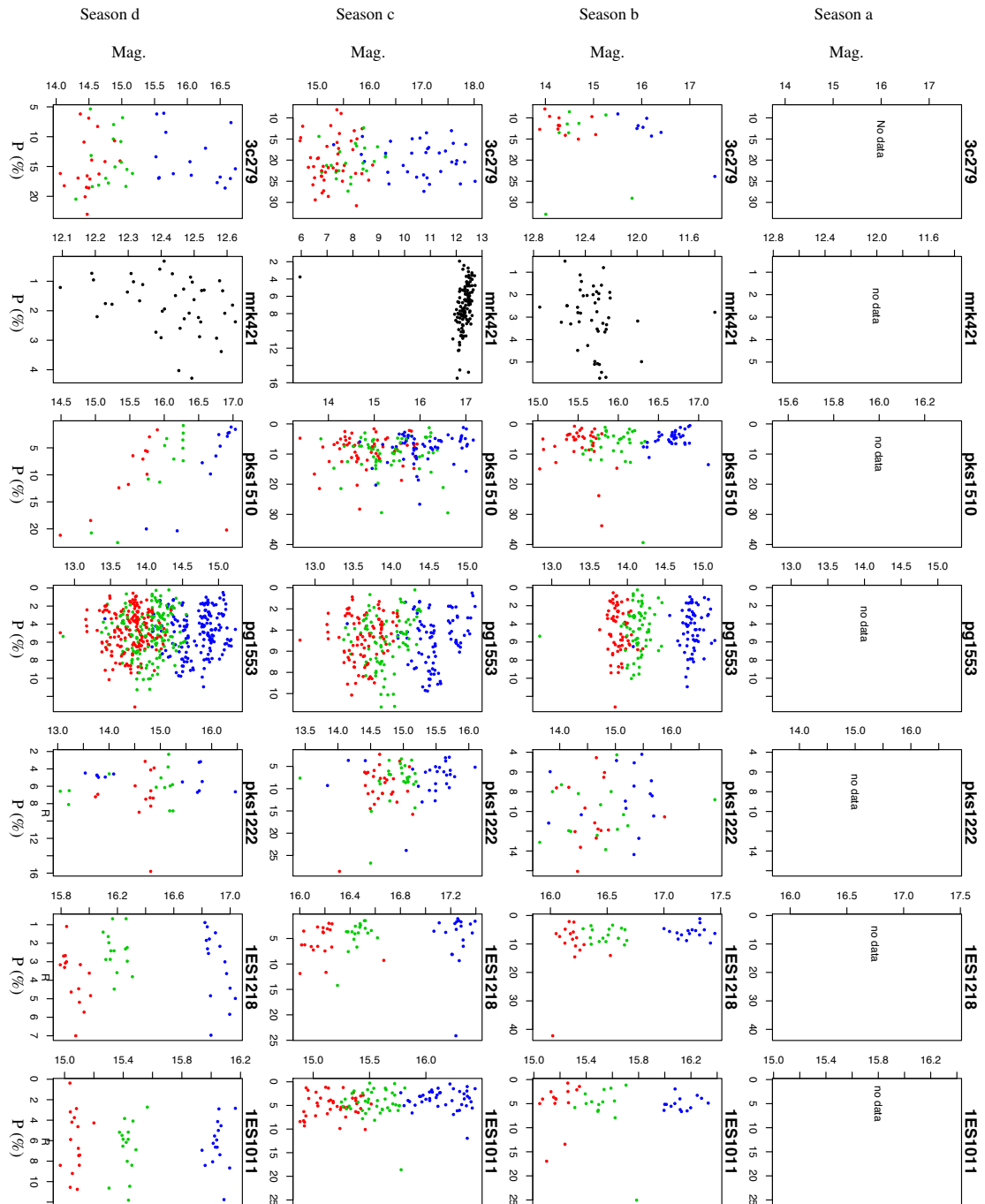
Figure 4.52: Plot of g* band magnitude against g* band degree of polarisation for all sources. The cameras are identified by each of their colours (red, green and blue) except for Mrk 421 which does not have multicolour information.
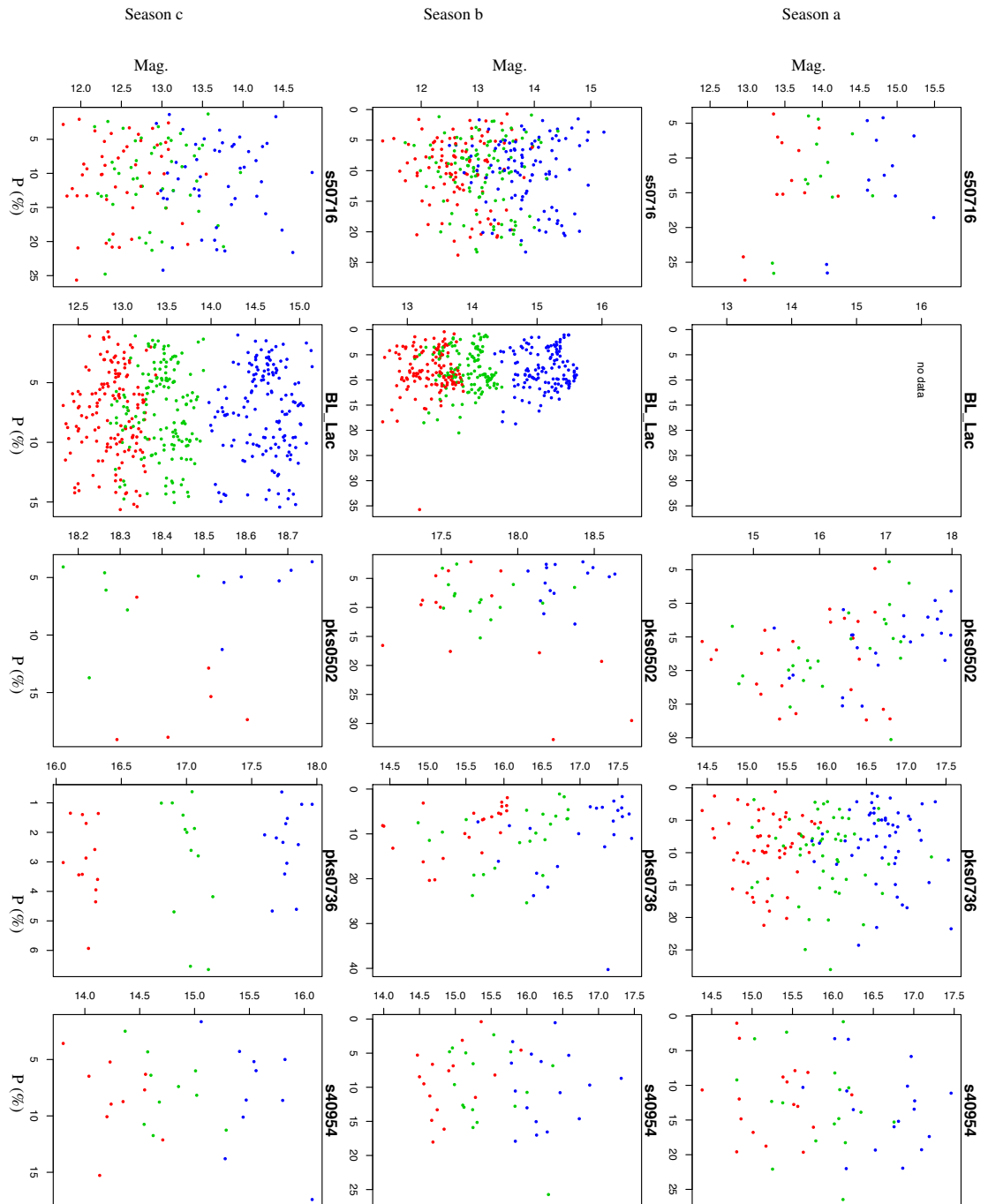
Figure 4.53: Figure 4.52 continued...
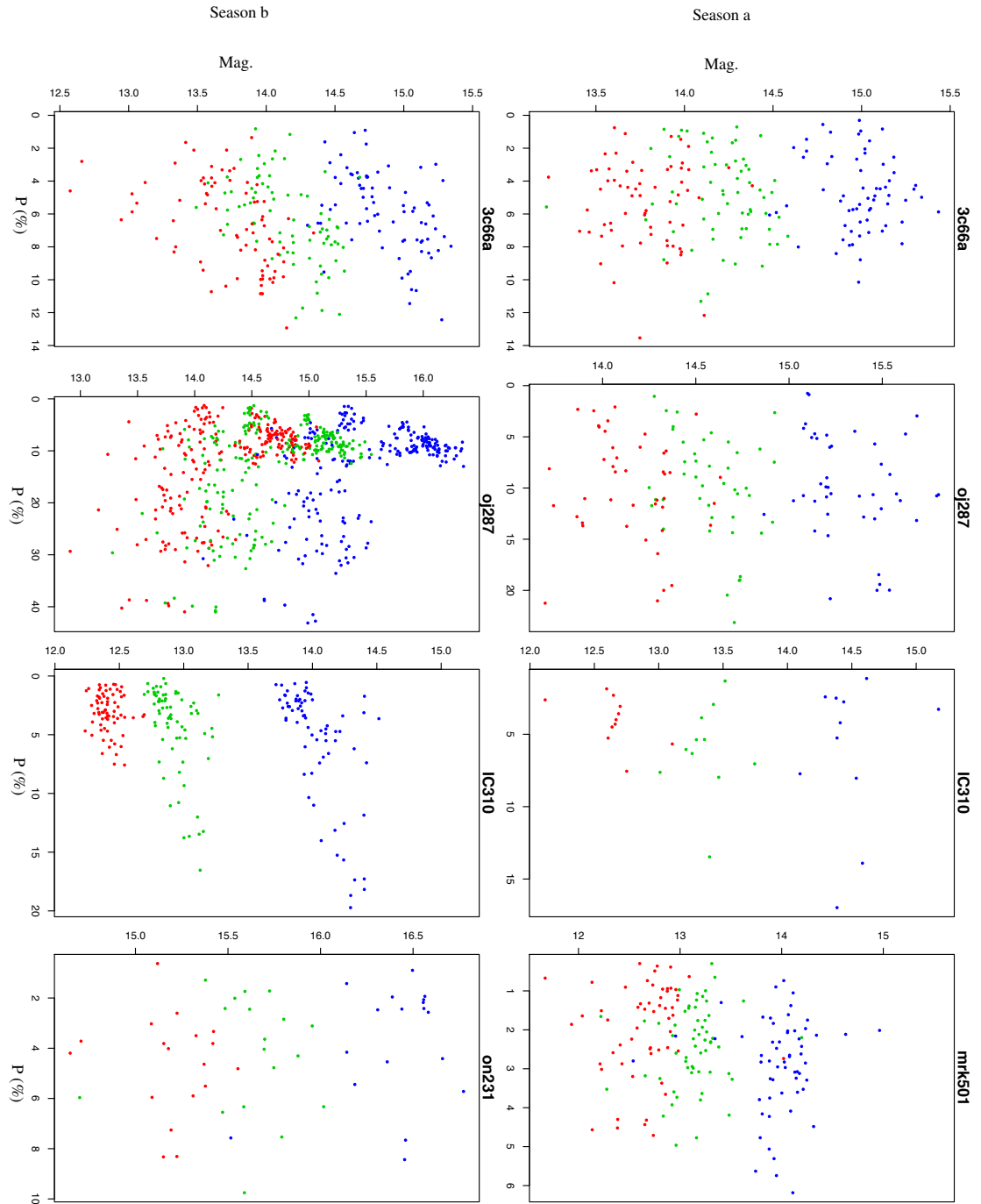
Figure 4.54: Figure 4.52 continued...

4.5 Colour analysis

In addition to the correlation analysis, the three wavebands of the Ringo3 instrument allowed spectral analysis of the blazars in this sample. Blazar magnitude variations are usually accompanied by changes in the spectral shape (Zhang et al., 2015a). The spectral properties of a source can be directly related to the colour of a source, i.e. the magnitude in one band subtracted from the magnitude in another band. This affords information about the origin of the light and which part of the source is changing.

There are various physical components of a blazar which contribute to the lower energy emission in the spectral energy distribution (SED). The dominant emission is non-thermal synchrotron emission from the jet, along with infrared light reflected from the dusty torus and ultra-violet light from the accretion disk. The synchrotron emission from the jet spans infrared (lower energy photons) to X-ray wavelengths (higher energy photons). Exploring the spectral changes during blazar variability allows the exploration of the synchrotron emission component of the SED and hence identification of the emitting regions of the source.

If different blazar subclasses (for example FSRQs and BL Lacs) have different physical properties then the small part of the optical spectrum which is probed using the Ringo3 instrument can give information about the emitting components of the source (see Figure 1.2 in the Introduction). This will be discussed in more detail at the end of this Chapter.

Through the analysis performed in this work an interesting discovery was made. When colour plots were made that included the same camera on both the x and y axes, the location of outliers is amplified, resulting in a false correlation. Initially plots were made of b* magnitude - r* magnitude, b* magnitude - g* magnitude and g* magnitude - r* magnitude against b* magnitude and r* magnitude to compare with the analysis made by Gupta et al. (2016). Strangely the plots suggested that the sources were both
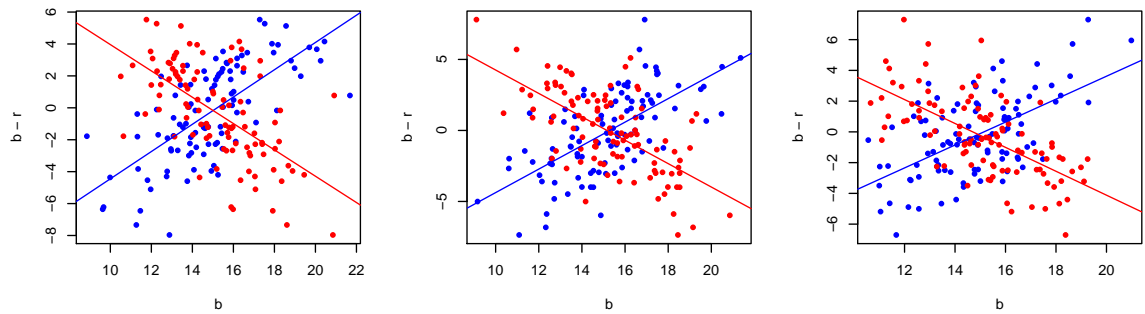
Figure 4.55: Plots of randomly generated 'b' and 'r' values in the form x= b y= b-r (blue) and x = r y = b-r (red). This shows three iterations of the code and the tendency of the fit to be positive (blue) or negative (red).

bluer and redder depending on the x axis magnitude (b* magnitude and r* magnitude respectively).

A rudimentary code was written that generated two variables (b and r) of random magnitudes and error values, and plotted these variables against each other in the form b, b-r and r, b-r (similar to the form taken in the colour-magnitude plots). A linear regression was fitted to each set of datapoints and this showed the preference for false fits (dependent on the x axis colour). Figure 4.55 shows an example of 3 runs with 100 magnitude values centred on 15 and 100 error values centred on 2.

This highlights the necessity to have an independent magnitude (i.e. one not contained in the colour index, and thus one with different errors) on the x axis to avoid false trends in the data caused by outliers. For this reason the colour-magnitude and colour-degree of polarisation analysis conducted in this section is such that all three colours are involved in each correlation analysis.

4.5.1 Photometric colour vs magnitude

Figures 4.56, 4.57 and 4.58 show the b* magnitude - g* magnitude vs r* magnitude, b* magnitude - r* magnitude vs g* magnitude and g* magnitude - r* magnitude vs b* magnitude respectively for all sources except for Mrk 421 (which lacks secondary stars in the frame so photometric calibration and thus 3 waveband analysis is not possible).
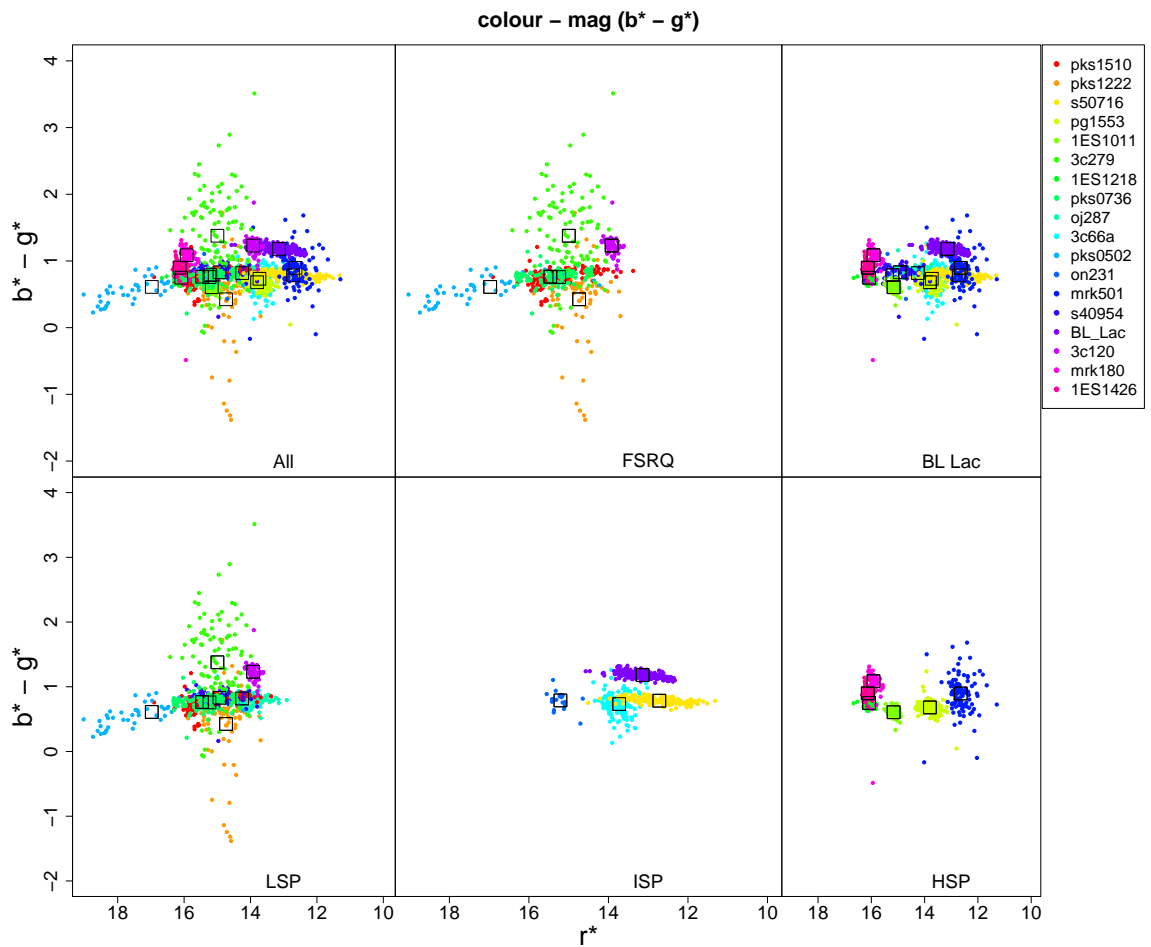
Figure 4.56: Plot of b* magnitude - g* magnitude vs r* magnitude for all sources, separated into different subclasses. The colour key identifies the sources and the black squares show the mean of each source.

The sources were separated into FSRQs, BL Lacs and LSP, ISP and HSP sources.

Figure 4.56 shows the b* magnitude - g* magnitude vs r* magnitude correlations. Most sources had a colour index between -0.5 and 2, but for the FSRQs PKS 1222+216 (orange points) and 3c279 (green points), the index was between -1.4 and 1.7 and -0.08 - 3.5 respectively. Table 4.8 shows the significant Spearman correlation coefficients and there were three positive correlations. These were for three FSRQs PKS 1222+216, 3c279 and PKS 1510-089. These positive correlations suggest that the three FSRQ sources are 'redder' when brighter, whereas the other sources are 'bluer' when brighter.

Figure 4.57 shows the b* magnitude - r* magnitude vs g* magnitude colour-magnitude plots. Again the FSRQs showed the greatest colour index with PKS 1222+216 (orange)
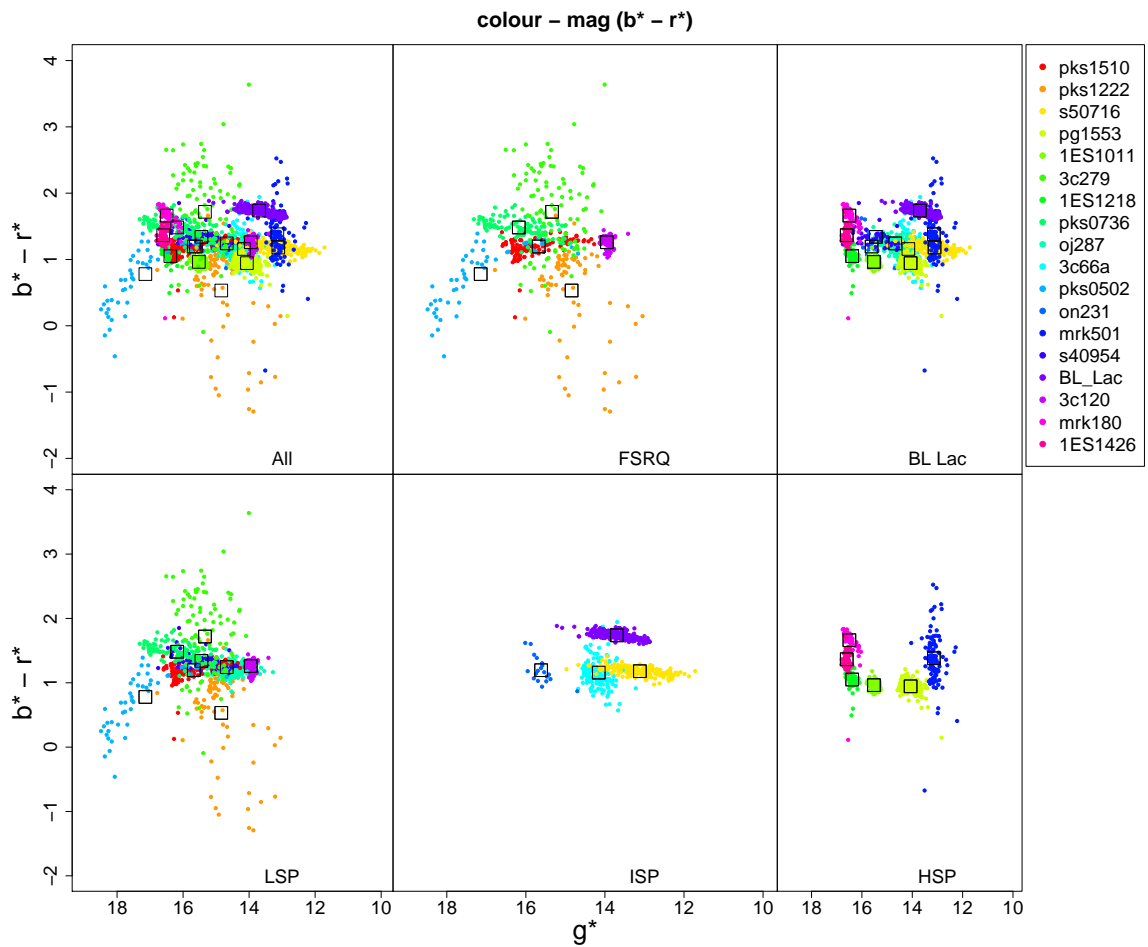
Figure 4.57: Plot of b* magnitude - r* magnitude vs g* magnitude for all sources, separated into different subclasses. The colour key identifies the sources and the black squares show the mean of each source.

and 3c279 (green) showing variations between -1.3 - 1.7 and -0.09 - 3.6 respectively. Mrk 501 (dark blue points) also showed a larger index (-0.7 - 2.5). In Table 4.8 the mean significant ρ values show only two sources had positive correlations; the FS-RQs PKS 1510-089 and PKS 0502+049. This suggests that these two FSRQs exhibit 'redder' when brighter behaviour while the other sources show 'bluer' when brighter behaviour.

Figure 4.58 shows the g* magnitude - r* magnitude vs b* magnitude correlations. In these correlations there were the lowest index values out of the 3 indices used in this analysis. This may be due to the 'blueness' of many of these sources and this index not including the b* magnitude. The greatest variation (i.e. magnitude>2) was shown by
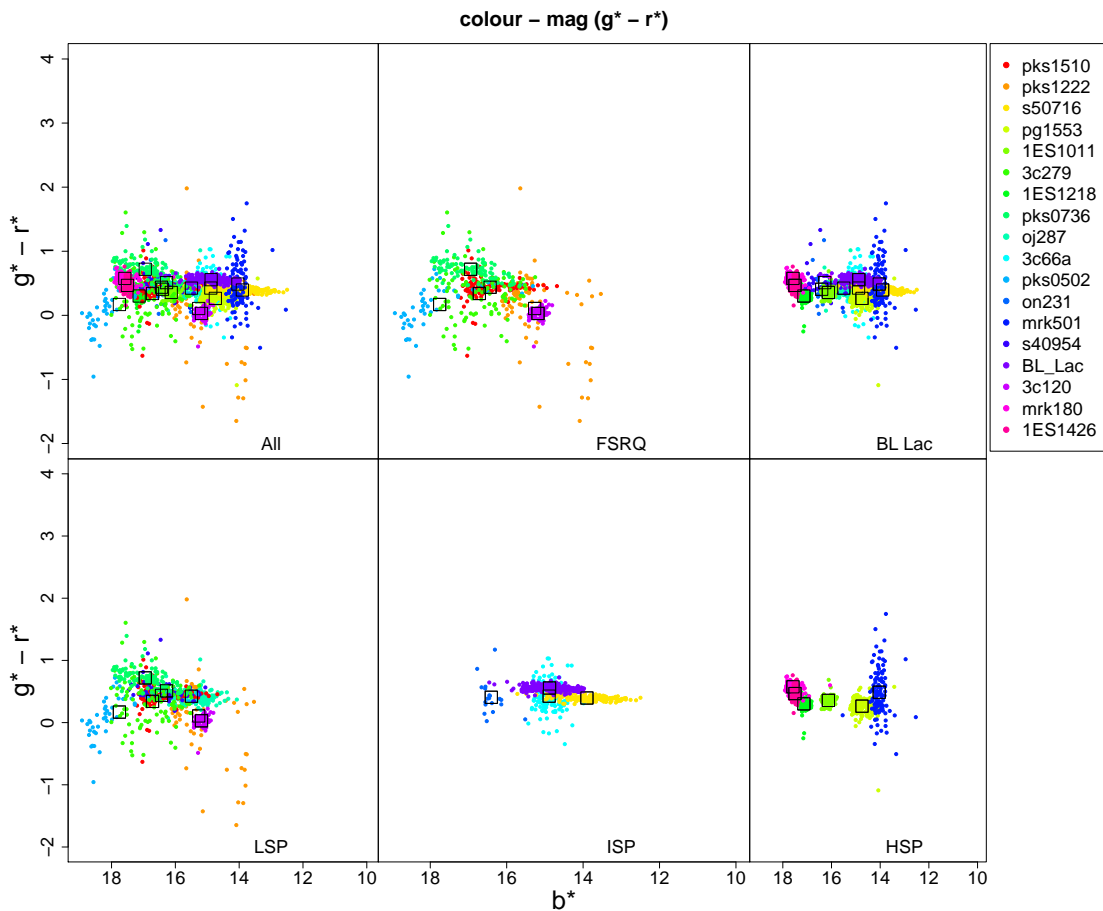
Figure 4.58: Plot of g* magnitude - r* magnitude vs b* magnitude for all sources, separated into different subclasses. The colour key identifies the sources and the black squares show the mean of each source.

PKS 1222+216 (-1.6 <magnitude<2.0), 3c279 (-0.5 <magnitude<1.6), FSRQs and Mrk 501 (-0.5 <magnitude<1.7), a BL Lac source.

In Table 4.8 the only two significant positive correlations were for PKS 0502+049 and 3c120, both FSRQs, suggesting a redder when brighter behaviour for these sources.

This analysis showed that in our sample, during the periods observed, the sources that showed 'redder' when brighter behaviour were FSRQs or the BL Lac, HSP source Mrk 501. All other sources showed 'bluer' when brighter behaviour.

A more detailed analysis of each source is shown in Figure 4.59 with the corresponding Spearman Rank coefficient test results and gradient of a linear fit for each source in Table 4.9. A p value of ≤0.05 signals a statistically significant correlation.
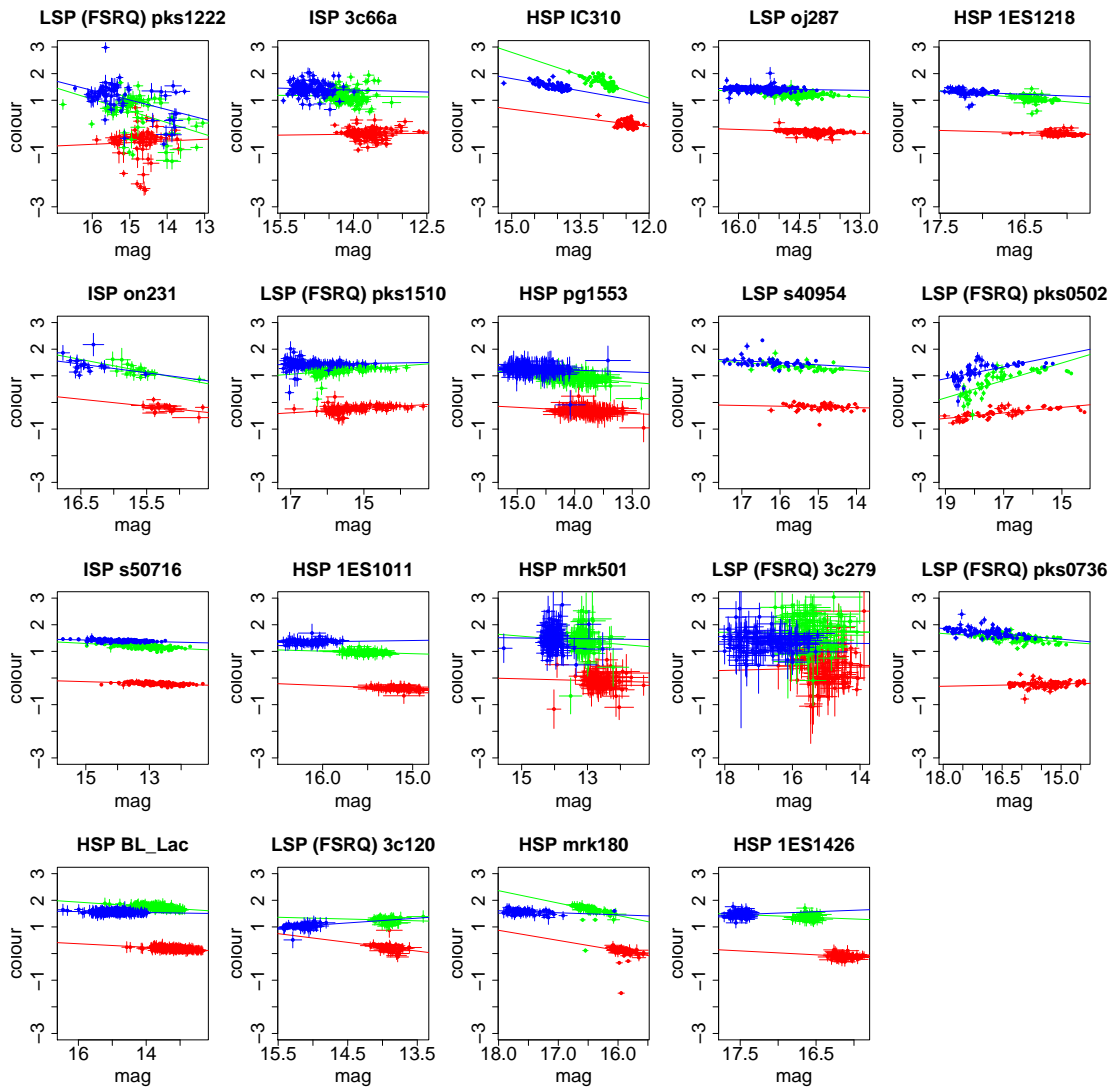
Figure 4.59: b* magnitude - r* vs g* magnitude (green points), b* magnitude - g* magnitude vs r* magnitude (red points) and g* magnitude - r* magnitude vs b* magnitude (blue points) for all sources (except Mrk 421). The lines are a linear regression fit to the data. The values for these plots are shown in Table 4.9.

		All p						$p \leq 0.05$			
	Type	Range p	Range ρ	Mean p	Mean ρ	Quantity $-\rho,+\rho$	Quantity	Range ρ	Mean ρ	Quantity $-\rho,+\rho$	Quantity
b* - g*	HSP	2.75×10^{-9} - 0.129	-0.560 - -0.145	0.0429	-0.302	6,0	6	-0.56 - -0.271	-0.361	4,0	4
	ISP	0.000 - 0.939	-0.589 - -0.00624	0.277	-0.351	4,0	4	-0.589 - -0.48	-0.534	2,0	2
	LSP	0.000 - 0.907	-0.461 - 0.762	0.153	0.0877	4,4	8	-0.461 - 0.762	0.137	2,3	5
	FSRQ	0.000 - 0.907	-0.461 - 0.762	0.175	0.211	2,4	6	-0.461 - 0.762	0.263	1,3	4
	BL Lac	0.000 - 0.939	-0.589 - -0.00624	0.128	-0.315	12,0	12	-0.589 - -0.271	-0.412	7,0	7
	All	0.000 - 0.939	-0.589 - 0.762	0.144	-0.140	14,4	18	-0.589 - 0.762	-0.166	8,3	11
b* - r*	HSP	0.000 - 0.236	-0.699 - -0.115	0.0864	-0.332	6,0	6	-0.699 - -0.347	-0.502	3,0	3
	ISP	0.000 - 0.115	-0.600 - -0.129	0.0307	-0.467	4,0	4	-0.6 - -0.545	-0.58	3,0	3
	LSP	0.000 - 0.454	-0.504 - 0.862	0.0914	-0.0249	5,3	8	-0.504 - 0.862	0.0034	3,2	5
	FSRQ	0.000 - 0.454	-0.504 - 0.862	0.122	0.112	3,3	6	0.53 - 0.862	0.696	0,2	2
	BL Lac	0.000 - 0.236	-0.699 - -0.115	0.0534	-0.395	12,0	12	-0.699 - -0.347	-0.515	8,0	8
	All	0.000 - 0.454	-0.699 - 0.862	0.0762	-0.226	15,3	18	-0.699 - 0.862	-0.294	9,2	11
g* - r*	HSP	0.0236 - 0.935	-0.271 - 0.0971	0.329	-0.0781	4,2	6	-0.271 - -0.228	-0.249	2,0	2
	ISP	2.57×10^{-7} - 0.359	-0.385 - -0.0752	0.143	-0.229	4,0	4	-0.385 - -0.152	-0.269	0,2	2
	LSP	0.000 - 0.981	-0.576 - 0.808	0.186	-0.00275	4,4	8	-0.576 - 0.808	0.0024	3,2	5
	FSRQ	0.000 - 0.981	-0.576 - 0.808	0.241	0.078	2,4	6	0.27 - 0.808	0.539	0,2	2
	BL Lac	2.57×10^{-7} - 0.935	-0.385 - 0.0971	0.216	-0.156	10,2	12	-0.385 - -0.152	-0.254	6,0	6
	All	0 - 0.981	-0.576 - 0.808	0.224	-0.0782	12,6	18	-0.576 - 0.808	-0.114	7,2	9

Table 4.8: Summary of results from the Spearman Rank correlation test showing the p and ρ values for different subclasses for colour-magnitude correlations. The full dataset for each source and each season is presented in Table 4.9.

With the exception of three FSRQ sources; PKS 1510-089, PKS 0736+017 and PKS 0502+049, looking at only *significant* values, all sources showed negative correlations between the colour indices and the magnitude. This suggests that, within this sample, as all BL Lac and some FSRQ sources get brighter (i.e. increase along the x-axis) the source gets bluer. This can be interpreted as bluer synchrotron emission from the jet (i.e. higher energy particles) in general. However, in the case of FSRQs, a bluer when brighter trend may be caused by the contribution of thermal emission from the accretion disk.

PKS 1510-089 and PKS 0502+049 both showed positive correlations. This suggests that unlike the 'bluer' when brighter sources these FSRQs become 'redder' when brighter, suggesting an increase in the red, non-thermal synchrotron emission from the jet. PKS 0736+017 showed a positive correlation in the blue - green index and negative correlations in both the other indices. This suggests that there may be multiple emission components, some which are associated with accelerated regions ('bluer' when brighter) or less accelerated regions ('redder' when brighter). Alternatively the source may also exhibit different behaviour (i.e. 'bluer' or 'redder' when brighter) depending on whether the source is in a period of flaring or quiescence.

Source	Type	Line colour (cameras)	ρ	p	linear fit gradient
PKS 1222+216	LSP (FSRQ)	red (blue - green)	0.223	0.0956	-0.132
PKS 1222+216	LSP (FSRQ)	green (blue - red)	0.101	0.454	0.343
PKS 1222+216	LSP (FSRQ)	blue (green - red)	**0.00331**	0.981	0.348
3C66A	ISP	red (blue - green)	-0.00637	0.402	-0.0832
3C66A	ISP	green (blue - red)	**-0.191**	0.0114	0.113
3C66A	ISP	blue (green - red)	**-0.160**	0.0350	0.522
IC310	HSP	red (blue - green)	**-0.235**	0.0318	0.218
IC310	HSP	green (blue - red)	**-0.733**	2.20×10^{-16}	0.572
IC310	HSP	blue (green - red)	**-0.708**	2.20×10^{-16}	0.307
OJ287	LSP	red (blue - green)	**-0.375**	6.94×10^{-11}	0.0499
OJ287	LSP	green (blue - red)	**-0.388**	1.25×10^{-11}	0.0731
OJ287	LSP	blue (green - red)	**-0.197**	0.000808	0.0215
1ES 1218+304	HSP	red (blue - green)	**-0.219**	0.0323	0.146
1ES 1218+304	HSP	green (blue - red)	-0.0484	0.640	0.272
1ES 1218+304	HSP	blue (green - red)	**-0.271**	0.029	-0.212
ON231	ISP	red (blue - green)	-0.312	0.157	0.0601
ON231	ISP	green (blue - red)	-0.406	0.0619	0.0759
ON231	ISP	blue (green - red)	-0.252	0.256	-0.125
PKS 1510-089	LSP (FSRQ)	red (blue - green)	**0.478**	1.20×10^{-9}	-0.0538
PKS 1510-089	LSP (FSRQ)	green (blue - red)	**0.442**	2.70×10^{-8}	-0.103
PKS 1510-089	LSP (FSRQ)	blue (green - red)	0.0737	0.373	-0.0112
PG 1553+113	HSP	red (blue - green)	**-0.229**	0.00110	-0.108
PG 1553+113	HSP	green (blue - red)	**-0.305**	1.13×10^{-5}	0.122
PG 1553+113	HSP	blue (green - red)	**-0.157**	0.0255	0.366
S4 0954+65	LSP	red (blue - green)	-0.201	0.121	0.0210
S4 0954+65	LSP	green (blue - red)	**-0.382**	0.00240	0.407
S4 0954+65	LSP	blue (green - red)	-0.242	0.0602	0.550
PKS 0502+049	LSP (FSRQ)	red (blue - green)	**0.282**	0.0250	-0.00845
PKS 0502+049	LSP (FSRQ)	green (blue - red)	0.234	0.0654	0.367
PKS 0502+049	LSP (FSRQ)	blue (green - red)	0.204	0.109	0.549
S5 0716+714	ISP	red (blue - green)	**-0.454**	2.38×10^{-10}	0.262
S5 0716+714	ISP	green (blue - red)	**-0.548**	2.20×10^{-16}	-0.0475
S5 0716+714	ISP	blue (green - red)	**-0.361**	7.94×10^{-7}	-0.101
1ES 1011+496	HSP	red (blue - green)	-0.144	0.151	-0.472
1ES 1011+496	HSP	green (blue - red)	**-0.201**	0.0435	0.224
1ES 1011+496	HSP	blue (green - red)	0.0881	0.380	0.383
Mrk 501	HSP	red (blue - green)	-0.117	0.223	-0.0221
Mrk 501	HSP	green (blue - red)	-0.139	0.146	0.388
Mrk 501	HSP	blue (green - red)	-0.0344	0.720	0.466
3C279	LSP (FSRQ)	red (blue - green)	-0.0114	0.907	0.0285
3C279	LSP (FSRQ)	green (blue - red)	-0.164	0.0916	0.101
3C279	LSP (FSRQ)	blue (green - red)	0.132	0.175	0.0670
PKS 0736+017	LSP (FSRQ)	red (blue - green)	**0.205**	0.0458	-0.029
PKS 0736+017	LSP (FSRQ)	green (blue - red)	**-0.504**	2.56×10^{-7}	0.103
PKS 0736+017	LSP (FSRQ)	blue (green - red)	**-0.576**	1.053×10^{-9}	0.134
BL Lac	HSP	red (blue - green)	**-0.570**	2.20×10^{-16}	-0.0531
BL Lac	HSP	green (blue - red)	**-0.535**	2.20×10^{-16}	-0.205
BL Lac	HSP	blue (green - red)	-0.0683	0.214	-0.163
3C120	LSP (FSRQ)	red (blue - green)	**-0.255**	0.0218	-0.877
3C120	LSP (FSRQ)	green (blue - red)	0.00967	0.932	-0.536
3C120	LSP (FSRQ)	blue (green - red)	0.169	0.132	0.106
Mrk 180	HSP	red (blue - green)	**-0.321**	0.000594	-0.501
Mrk 180	HSP	green (blue - red)	**-0.567**	2.20×10^{-16}	0.111
Mrk 180	HSP	blue (green - red)	**-0.305**	0.00111	0.609
1ES 1426+428	HSP	red (blue - green)	-0.0654	0.604	-0.00583
1ES 1426+428	HSP	green (blue - red)	**0.00730**	0.954	0.112
1ES 1426+428	HSP	blue (green - red)	-0.155	0.217	-0.105

Table 4.9: Full table of Spearman rank coefficient values for the colour-magnitude correlations along with linear fit gradients.

		All p						p<0.05			
	Type	Range p	Range ρ	Mean p	Mean ρ	Quantity -ρ,+ρ	Quantity	Range ρ	Mean ρ	Quantity -ρ,+ρ	Quantity
colour-colour	HSP	2.66×10^{-7} - 0.0734	0.224 - 0.492	0.0125	0.367	0,6	6	0.335 - 0.492	0.395	0,5	5
	ISP	0.000579 - 0.0344	-0.261 - 0.491	0.0114	0.157	1,3	4	-0.261 - 0.491	0.157	1,3	4
	LSP	1.52×10^{-6} - 0.381	-0.549 - 0.465	0.0612	0.205	1,7	8	-0.549 - 0.465	0.228	1,5	6
	FSRQ	1.52×10^{-6} - 0.349	-0.120 - 0.465	0.0746	0.287	1,5	6	0.323 - 0.465	0.406	1,4	5
	BL Lac	2.66×10^{-7} - 0.381	-0.261 - 0.492	0.0422	0.273	1,11	12	-0.261 - 0.492	0.300	1,9	10
	All	2.66×10^{-7} - 0.381	-0.549 - 0.492	0.0339	0.248	2,16	18	-0.549 - 0.492	0.265	2,13	15

Table 4.10: Summary of results from the Spearman Rank correlation test showing the p and ρ values for different subclasses for the colour-colour correlation (see Figure 4.60).

4.5.2 Photometric colour-colour

Figure 4.60 shows g* magnitude - r* magnitude vs b* magnitude - g* magnitude for all sources (except Mrk 421). The Spearman rank coefficient results are shown in Table 4.10. The significant ρ values were predominantly positive, and with the exception of one ISP and one LSP source, the mean values for each subclass were all positive. This suggests that when the majority of sources' emission gets 'redder' in one band, it simultaneously gets 'redder' in the other bands which suggests the slope of the synchrotron SED is getting steeper.

4.5.3 Polarimetric colour vs degree of polarisation

Figures 4.61, 4.62 and 4.63 show the correlations of 'polarimetric colour' (i.e. degree of polarisation measured in 2 bands subtracted from each other) plotted against the degree of polarisation in the third remaining band. The Spearman rank coefficient values are shown in Table 4.11.

Figure 4.61 shows the relationship between the polarisation b* degree - g* degree index against r* degree. The greatest polarimetric colour change was seen in LSP/FSRQ sources. The ISP and HSP sources showed $<\pm10\%$ variation in the polarisation index, whereas in the LSP/FSRQ sources the colour change was between $\pm20\%$.

Table 4.11 shows the range of Spearman rank coefficient values for the different subclasses. The p values of the correlations for the b* degree - g* degree were between
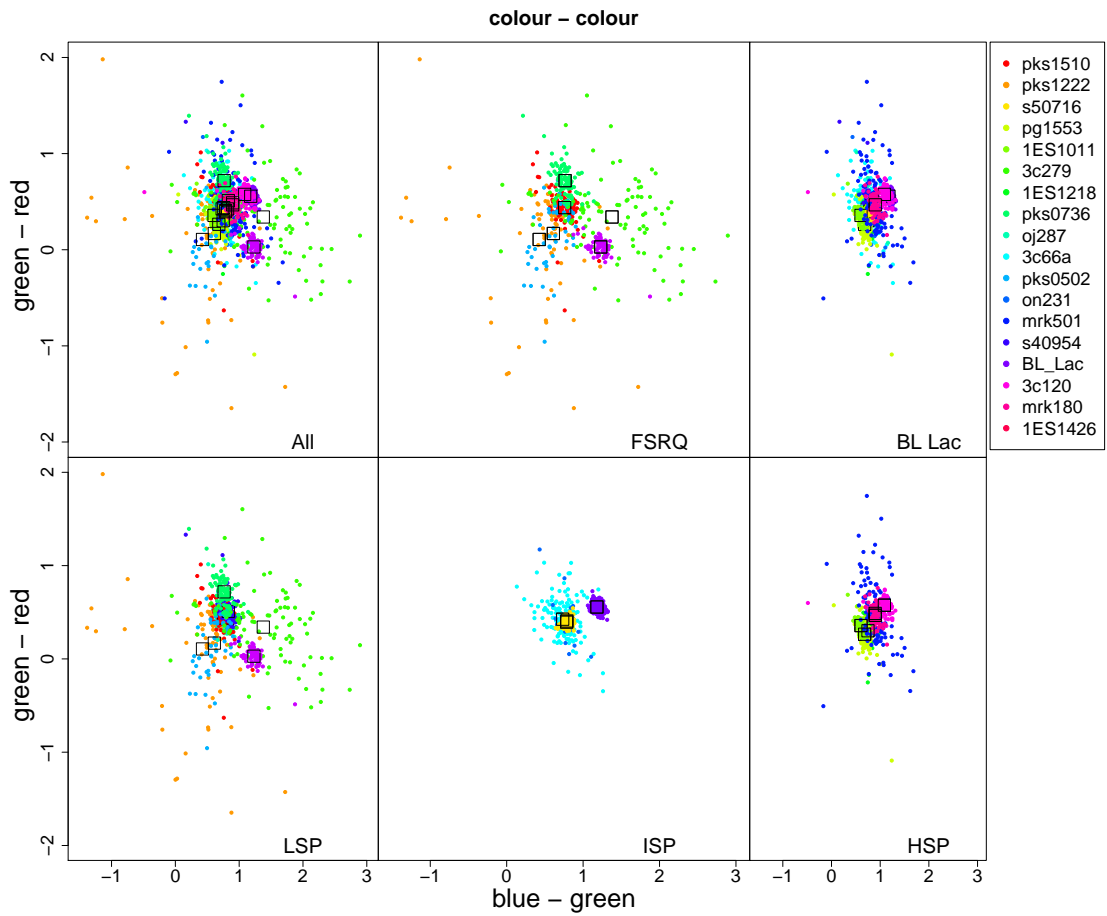
Figure 4.60: Colour-colour plot for all sources (except Mrk 421) and subclasses. Here blue, green and red are the Ringo3 bands (b*, g* and r* respectively). See Table 4.10 for coefficient values.
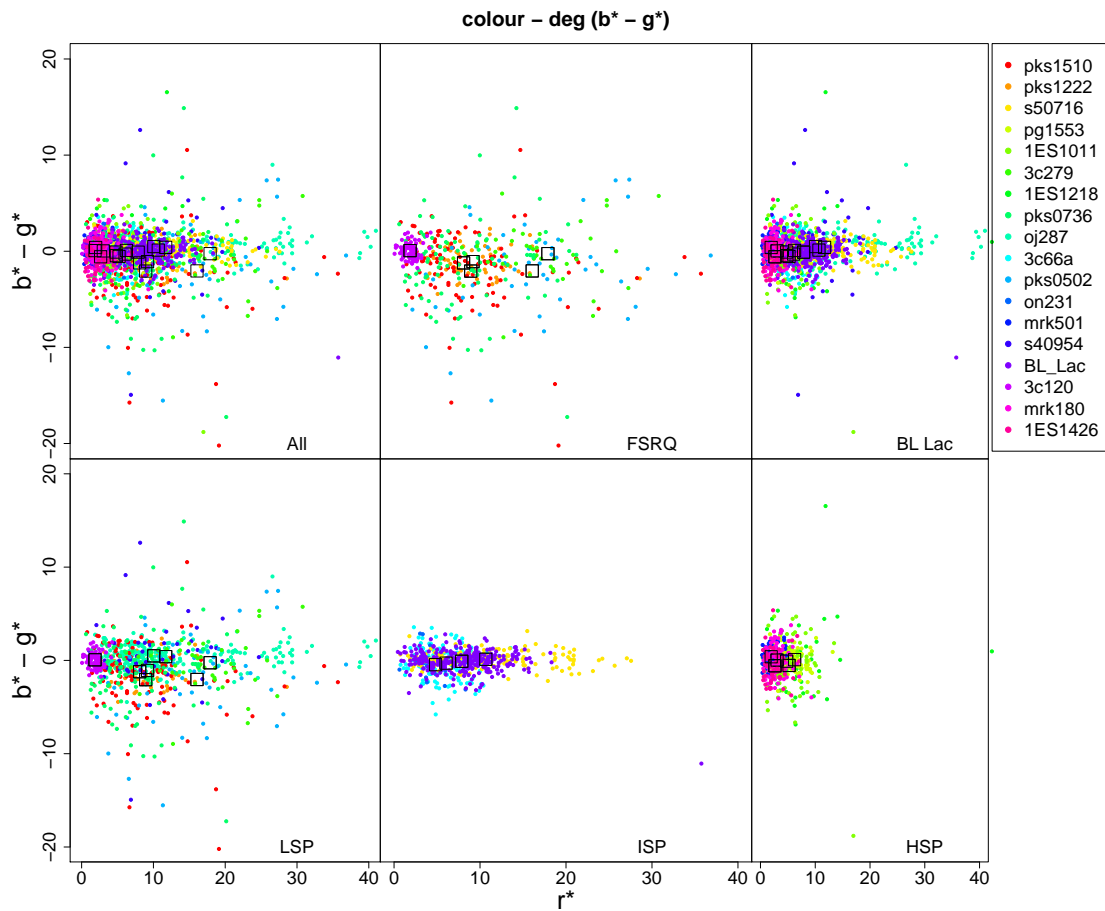
Figure 4.61: Plot of b* degree of polarisation - g* degree of polarisation vs r* degree of polarisation for all sources, separated into different subclasses. The colour key identifies the sources and the black squares show the mean of each source.

0.00316 - 0.826 with two significant correlations, one positive, one negative. The FSRQ PKS 1510-089 showed a negative correlation of (ρ=-0.263), which implies a 'redder' polarisation when the polarisation increases. The BL Lac source OJ287 showed a positive correlation (ρ=0.130), which suggests a 'bluer' when increasing polarisation.

Figure 4.62 shows the polarisation colour index b* degree - r* degree against the degree of polarisation measured in the g* band. As with the b* degree - g* degree index there was a greater b* degree - r* degree index value for LSP/FSRQ sources than for ISP/HSP sources. The LSP/FSRQ sources showed more 'reddening' than the ISP/HSP sources, with an index that reached ∼-30%.
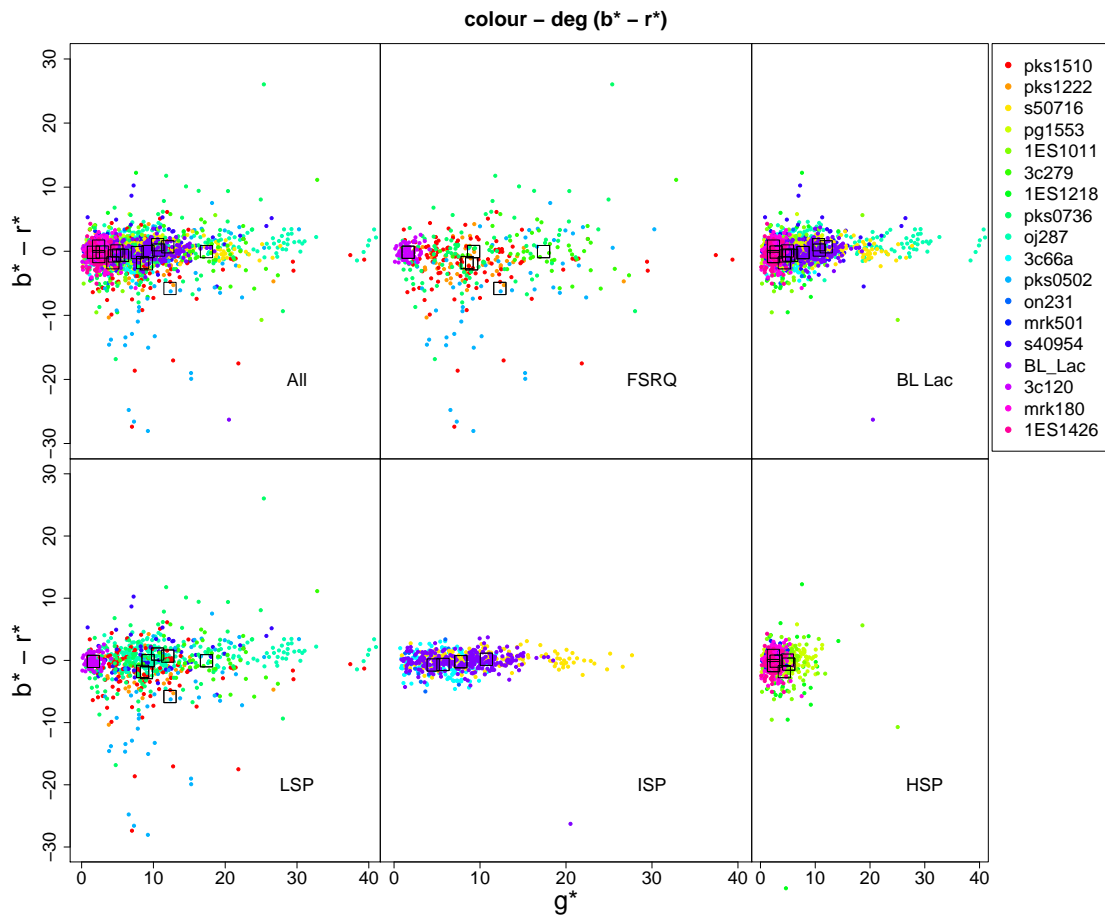
Figure 4.62: Plot of b* degree of polarisation - r* degree of polarisation vs g* degree of polarisation for all sources, separated into different subclasses. The colour key identifies the sources and the black squares show the mean of each source.

Table 4.11 shows 4 significant ρ values which were all positive; 1 HSP source and 3 LSP sources. OJ287 (LSP) had $\rho=0.129$, PG 1553+113 (HSP) had $\rho=0.157$, PKS 0502+049 (LSP) had $\rho=0.479$ and PKS 0736+017 (LSP) had $\rho=0.277$.

Figure 4.63 shows the g* degree - r* degree against the b* degree. Here the polarisation indices for the LSP/FSRQ sources were again the largest with the ISP/HSP sources having values $\gtrsim \pm 10\%$. Table 4.11 shows positive values for the 3 significant ρ values. These were for HSP (PG 1553+113, $\rho=0.176$), ISP (ON231, $\rho=0.465$) and LSP (PKS 0736, $\rho=0.301$) sources alike. This suggests that a 'bluer' polarisation is correlated with an increase in polarisation in at least one LSP, ISP and HSP source.

Figure 4.64 shows three polarisation colour-degree of polarisation correlations for all
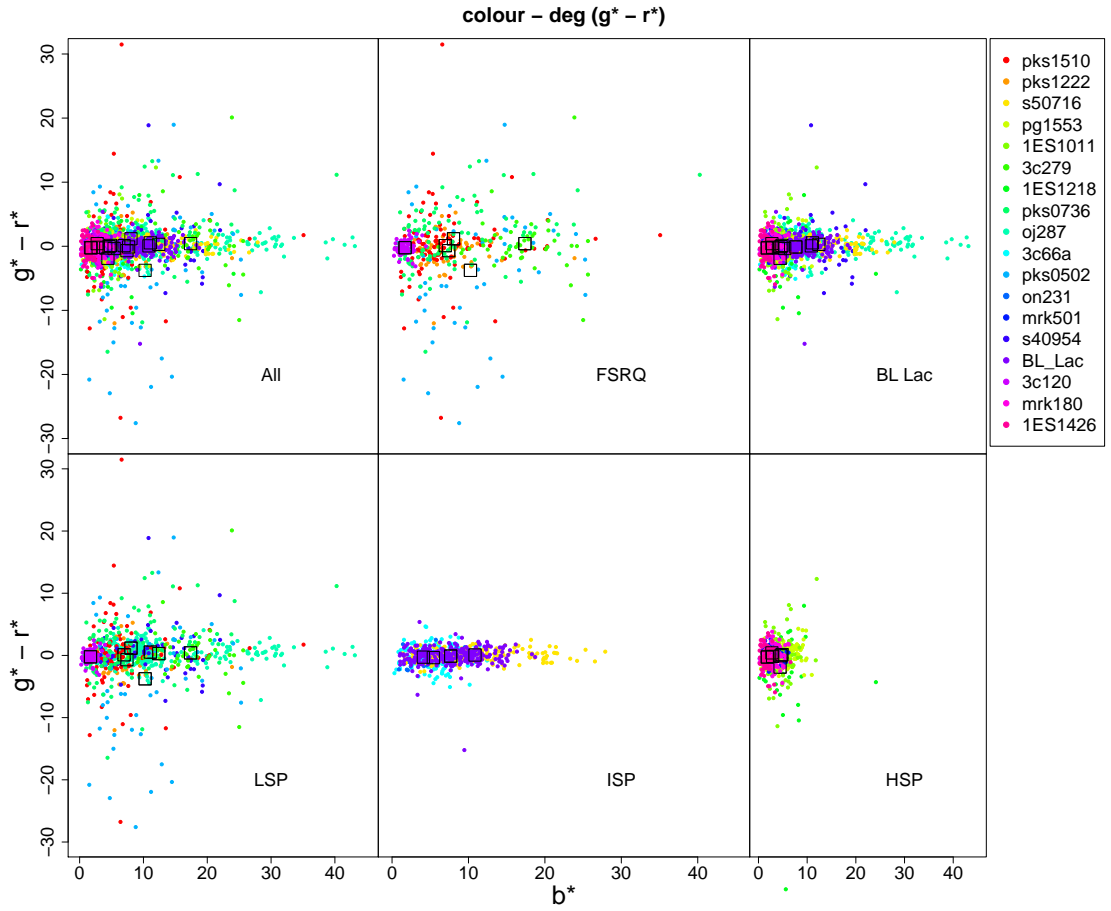
Figure 4.63: Plot of g* degree of polarisation - r* degree of polarisation vs b* degree of polarisation for all sources, separated into different subclasses. The colour key identifies the sources and the black squares show the mean of each source.

		All p						p$\leq$0.05			
	Type	Range p	Range ρ	Mean p	Mean ρ	Quantity $-\rho,+\rho$	Quantity	Range ρ	Mean ρ	Quantity $-\rho,+\rho$	Quantity
b* - g*	HSP	0.124 - 0.801	-0.059 - 0.194	0.525	0.0438	2,4	6	NA - NA	NA	0,0	0
	ISP	0.145 - 0.719	-0.347 - -0.0213	0.421	-0.130	4,0	4	NA - NA	NA	0,0	0
	LSP	0.00316 - 0.826	-0.263 - 0.263	0.392	0.0231	4,4	8	-0.263 - 0.130	-0.0665	1,1	2
	FSRQ	0.00316 - 0.826	-0.263 - 0.263	0.472	-0.0164	4,2	6	-0.263 - -0.263	-0.263	1,0	1
	BL Lac	0.0274 - 0.801	-0.347 - 0.194	0.429	0.0022	6,6	12	0.130 - 0.130	0.130	0,1	1
	All	0.00316 - 0.826	-0.347 - 0.263	0.443	-0.00401	10,8	18	-0.263 - 0.130	-0.0665	1,1	2
b* - r*	HSP	0.0443 - 0.835	-0.0764 - 0.157	0.459	0.0558	2,4	6	0.157 - 0.157	0.157	0,1	1
	ISP	0.152 - 0.918	-0.108 - 0.0847	0.525	0.00531	2,2	4	NA - NA	NA	0,0	0
	LSP	0.000379 - 0.961	-0.185 - 0.479	0.208	0.113	2,6	8	0.129 - 0.479	0.295	0,3	3
	FSRQ	0.000379 - 0.961	-0.185 - 0.479	0.239	0.0982	2,4	6	0.277 - 0.479	0.378	0,2	2
	BL Lac	0.0289 - 0.918	-0.108 - 0.182	0.424	0.0556	4,8	12	0.129 - 0.157	0.143	0,2	2
	All	0.000379 - 0.961	-0.185 - 0.479	0.362	0.0698	6,12	18	0.129 - 0.479	0.261	0,4	4
g* - r*	HSP	0.0241 - 0.917	-0.0812 - 0.176	0.615	0.0149	4,2	6	0.176 - 0.176	0.176	0,1	1
	ISP	0.0465 - 0.761	0.0256 - 0.465	0.36	0.16	0,4	4	0.465 - 0.465	0.465	0,1	1
	LSP	0.00304 - 0.925	-0.145 - 0.301	0.342	0.103	1,7	8	0.301 - 0.301	0.301	0,1	1
	FSRQ	0.00304 - 0.620	-0.145 - 0.301	0.220	0.128	1,5	6	0.301 - 0.301	0.301	0,1	1
	BL Lac	0.0241 - 0.925	-0.0812 - 0.465	0.546	0.0654	4,8	12	0.176 - 0.465	0.321	0,2	2
	All	0.00304 - 0.925	-0.145 - 0.465	0.437	0.0864	5,13	18	0.176 - 0.465	0.314	0,3	3

Table 4.11: Summary of results from the Spearman Rank correlation test showing the p and ρ values for different subclasses for polarisation colour-polarisation correlations.

sources (except Mrk 421). Table 4.12 shows the Spearman rank coefficient values and the gradient of a linear fit. All significant ρ values (i.e. with p$\leq$0.05) showed positive correlations except for PKS 1510-089 (FSRQ) which showed a negative correlation in b* - g* vs r*. A bluer polarisation is indicative of higher energy particles within the jet emission, the greater the energy of the photons, the higher the frequency and hence the stronger emission in the blue region. These results showed that most sources had a positive correlation between the degree of polarisation increasing and a bluer polarisation, except for one FSRQ which showed that with an increase in degree of polarisation the polarisation gets redder (which would suggest the particles in the jet have less energy).

A postive correlation between the level of polarisation and the colour of the polarisation (i.e. the energy of the particles in the jet) suggests the presence of either a transient shock event (i.e. shell interactions or a magnetic reconnection event) or emission coming from an accelerating region or a permanent shock structure such as a Mach disk, as discussed by Marscher (2014).

Polarimetric colour-colour

The polarimetric colour-colour plot shown in Figure 4.65 shows the b* degree - g* degree index on the x axis and the g* degree - r* degree index on the y axis. The overall correlation was similar to the colour-colour magnitude plot (see Figure 4.60) insomuch as it also shows the sources get redder. It also highlights the larger indices in LSP/FSRQ sources, which is in part explained by the fact that the maximum polarisation values for HSP/ISP sources are less than those for the LSP sources (e.g. see Figure 4.45). Table 4.13 shows that all 14 significant correlations were negative.

Source	Type	Line colour (cameras)	ρ	p	gradient
PKS 1222+216	LSP (FSRQ)	red (blue - green)	-0.0366	0.809	-0.022
PKS 1222+216	LSP (FSRQ)	green (blue - red)	0.185	0.217	-0.028
PKS 1222+216	LSP (FSRQ)	blue (green - red)	-0.145	0.335	-0.002
3C66A	ISP	red (blue - green)	-0.116	0.169	-0.062
3C66A	ISP	green (blue - red)	-0.108	0.200	-0.058
3C66A	ISP	blue (green - red)	0.0256	0.761	0.006
IC310	HSP	red (blue - green)	0.194	0.0774	0.233
IC310	HSP	green (blue - red)	**0.622**	2.20×10^{-16}	0.888
IC310	HSP	blue (green - red)	**0.637**	2.20×10^{-16}	0.455
OJ287	LSP	red (blue - green)	**0.130**	0.0274	0.024
OJ287	LSP	green (blue - red)	**0.129**	0.0289	0.026
OJ287	LSP	blue (green - red)	0.0409	0.490	0.001
1ES 1218+304	HSP	red (blue - green)	-0.059	0.662	0.061
1ES 1218+304	HSP	green (blue - red)	-0.0764	0.571	0.079
1ES 1218+304	HSP	blue (green - red)	-0.0174	0.898	-0.114
ON231	ISP	red (blue - green)	-0.347	0.145	-0.232
ON231	ISP	green (blue - red)	0.0526	0.832	0.151
ON231	ISP	blue (green - red)	**0.465**	0.00465	0.303
PKS 1510-089	LSP (FSRQ)	red (blue - green)	**-0.263**	0.00316	-0.115
PKS 1510-089	LSP (FSRQ)	green (blue - red)	-0.151	0.0931	-0.039
PKS 1510-089	LSP (FSRQ)	blue (green - red)	0.135	0.133	0.097
PG 1553+113	HSP	red (blue - green)	-0.0489	0.533	-0.008
PG 1553+113	HSP	green (blue - red)	**0.157**	0.0443	0.080
PG 1553+113	HSP	blue (green - red)	**0.176**	0.0241	0.094
S4 0954+65	LSP	red (blue - green)	0.153	0.282	0.051
S4 0954+65	LSP	green (blue - red)	0.182	0.200	0.059
S4 0954+65	LSP	blue (green - red)	0.0135	0.925	0.018
PKS 0502+049	LSP (FSRQ)	red (blue - green)	0.263	0.0594	0.180
PKS 0502+049	LSP (FSRQ)	green (blue - red)	**0.479**	0.000379	0.568
PKS 0502+049	LSP (FSRQ)	blue (green - red)	0.196	0.164	0.281
S5 0716+714	ISP	red (blue - green)	-0.0351	0.653	-0.009
S5 0716+714	ISP	green (blue - red)	-0.00807	0.918	-0.002
S5 0716+714	ISP	blue (green - red)	0.0458	0.557	0.007
1ES 1011+496	HSP	red (blue - green)	0.0636	0.582	-0.271
1ES 1011+496	HSP	green (blue - red)	0.0770	0.505	-0.062
1ES 1011+496	HSP	blue (green - red)	0.0653	0.572	0.324
Mrk 501	HSP	red (blue - green)	0.194	0.124	0.210
Mrk 501	HSP	green (blue - red)	0.138	0.278	0.153
Mrk 501	HSP	blue (green - red)	-0.0426	0.737	-0.085
3C279	LSP (FSRQ)	red (blue - green)	-0.0636	0.582	0.032
3C279	LSP (FSRQ)	green (blue - red)	**-0.00727**	0.961	0.015
3C279	LSP (FSRQ)	blue (green - red)	0.0732	0.620	-0.024
PKS 0736+017	LSP (FSRQ)	red (blue - green)	0.049	0.635	0.023
PKS 0736+017	LSP (FSRQ)	green (blue - red)	**0.277**	0.00637	0.289
PKS 0736+017	LSP (FSRQ)	blue (green - red)	**0.301**	0.00304	0.247
BL Lac	HSP	red (blue - green)	-0.0213	0.719	-0.068
BL Lac	HSP	green (blue - red)	0.0847	0.152	-0.051
BL Lac	HSP	blue (green - red)	0.105	0.0772	0.025
3C120	LSP (FSRQ)	red (blue - green)	-0.0784	0.497	0.044
3C120	LSP (FSRQ)	green (blue - red)	0.162	0.158	0.273
3C120	LSP (FSRQ)	blue (green - red)	0.210	0.0675	0.221
Mrk 180	HSP	red (blue - green)	0.0794	0.449	-0.038
Mrk 180	HSP	green (blue - red)	0.0671	0.522	-0.026
Mrk 180	HSP	blue (green - red)	-0.0109	0.917	0.021
1ES 1426+428	HSP	red (blue - green)	0.0337	0.801	0.057
1ES 1426+428	HSP	green (blue - red)	-0.0279	0.835	-0.118
1ES 1426+428	HSP	blue (green - red)	-0.0812	0.543	-0.246

Table 4.12: Table of polarisation colour - degree of polarisation Spearman rank coefficient values and gradients for all sources.
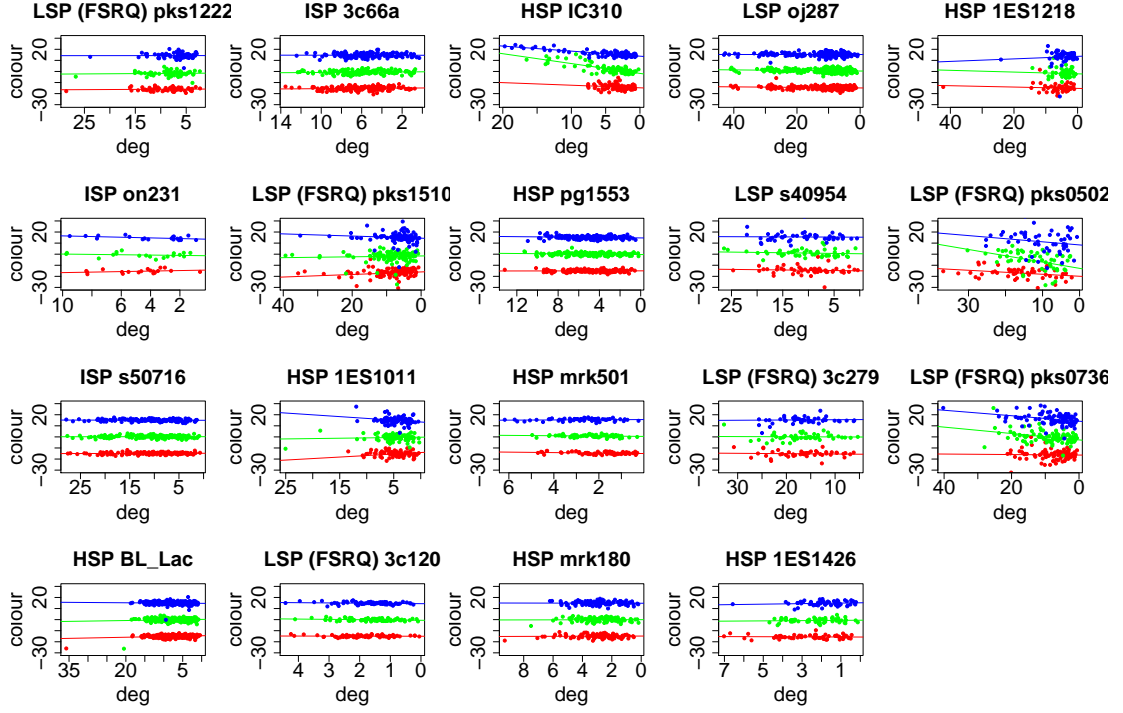
Figure 4.64: b* degree of polarisation - g* polarisation vs r* polarisation (red points), b* polarisation - r* polarisation vs g* polarisation (green points) and g* polarisation - r* polarisation vs b* polarisation for all sources (except Mrk 421). Blue points are shifted up (+15) and red points are shifted down (-15) for clarity. The coloured lines represent a linear regression fit to the data. The values for these plots are shown in Table 4.12.

		All p					p≤0.05			
	Type	Range p	Range ρ	Mean p	Mean ρ	Quantity $-\rho,+\rho$	Quantity	Range ρ	Mean ρ	Quantity $-\rho,+\rho$	Quantity
colour-colour	HSP	4.46×10^{-10} - 0.00502	-0.579 - -0.369	0.000917	-0.458	6,0	6	-0.579 - -0.369	-0.458	6,0	6
	ISP	3.03×10^{-11}- 0.590	-0.516 - -0.122	0.177	-0.270	4,0	4	-0.516 - -0.309	-0.412	2,0	2
	LSP	7.67×10^{-6} - 0.00722	-0.572 - -0.227	0.00134	-0.414	8,0	8	-0.572 - -0.227	-0.414	8,0	8
	FSRQ	7.67×10^{-6} - 0.0023	-0.572 - -0.39	0.000567	-0.451	6,0	6	-0.390 - -0.572	-0.451	6,0	6
	BL Lac	3.03×10^{-11} - 0.590	-0.579 - -0.122	0.0601	-0.369	12,0	12	-0.579 - -0.227	-0.417	10,0	10
	All	3.03×10^{-11}- 0.590	-0.579 - -0.122	0.0402	-0.396	18,0	18	-0.579 - -0.227	-0.43	16,0	16

Table 4.13: Summary of results from the Spearman Rank correlation test showing the p and ρ values for different subclasses for the polarimetric colour-colour correlation (see Figure 4.60).
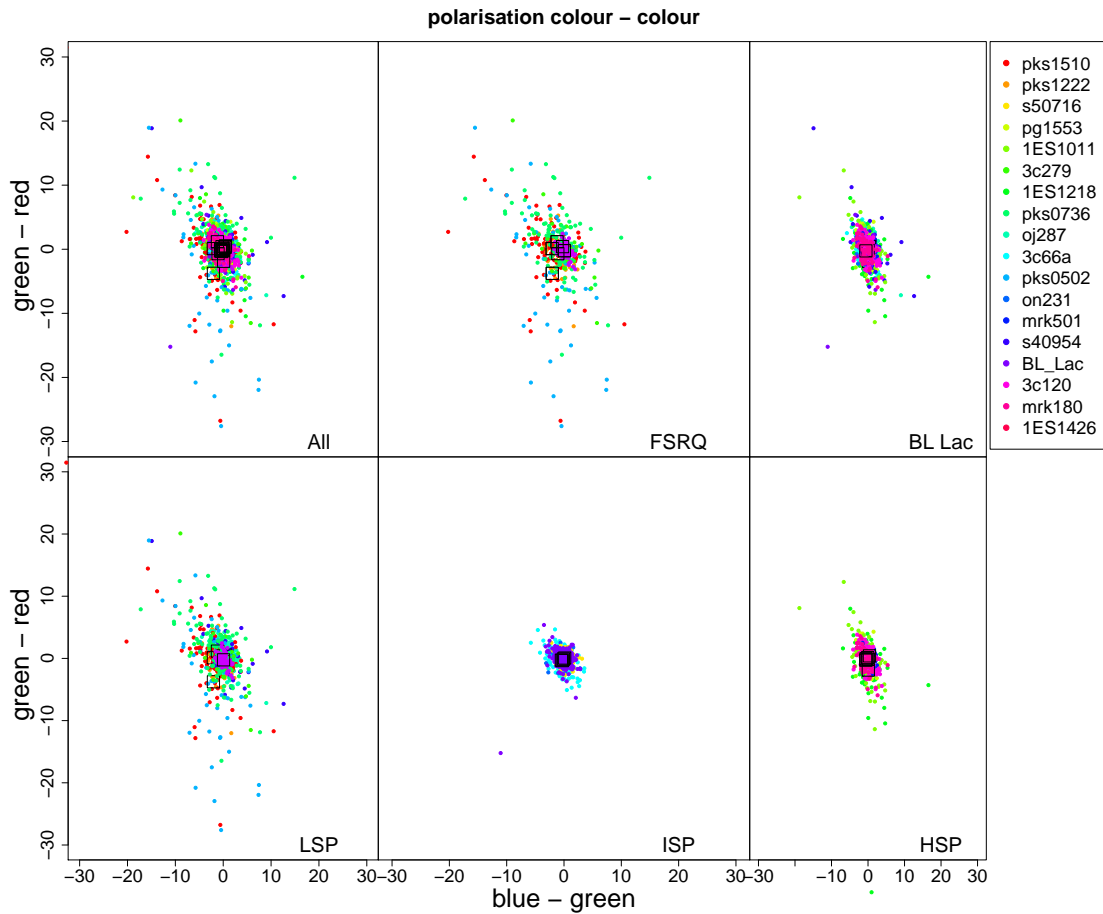
Figure 4.65: Degree of polarisation colour-colour plot for all sources separated into subclasses.

Polarimetric colour vs magnitude

The final comparison to make is between the polarimetric colours and the magnitude, to explore the connection between polarisation changes and the brightness of the source. Figures 4.66, 4.67 and 4.68 show the polarisation colour - magnitude relations for b* - g* degree vs r* magnitude, b* -r* degree vs g* magnitude and g* - r* degree vs b* magnitude respectively. Table 4.14 shows the correlation coefficients for each source along with their p value.

Of the significant ρ values for the b* degree - g* degree vs r* magnitude, there were two correlations found in BL Lac (ISP and HSP) sources that were positive and negative. These were for 3c66a (ISP, ρ=0.174) and 1ES 1426+428 (HSP, ρ=-0.278), the two most scattered sources in Figure 4.66, suggesting two different behaviours in these sources.
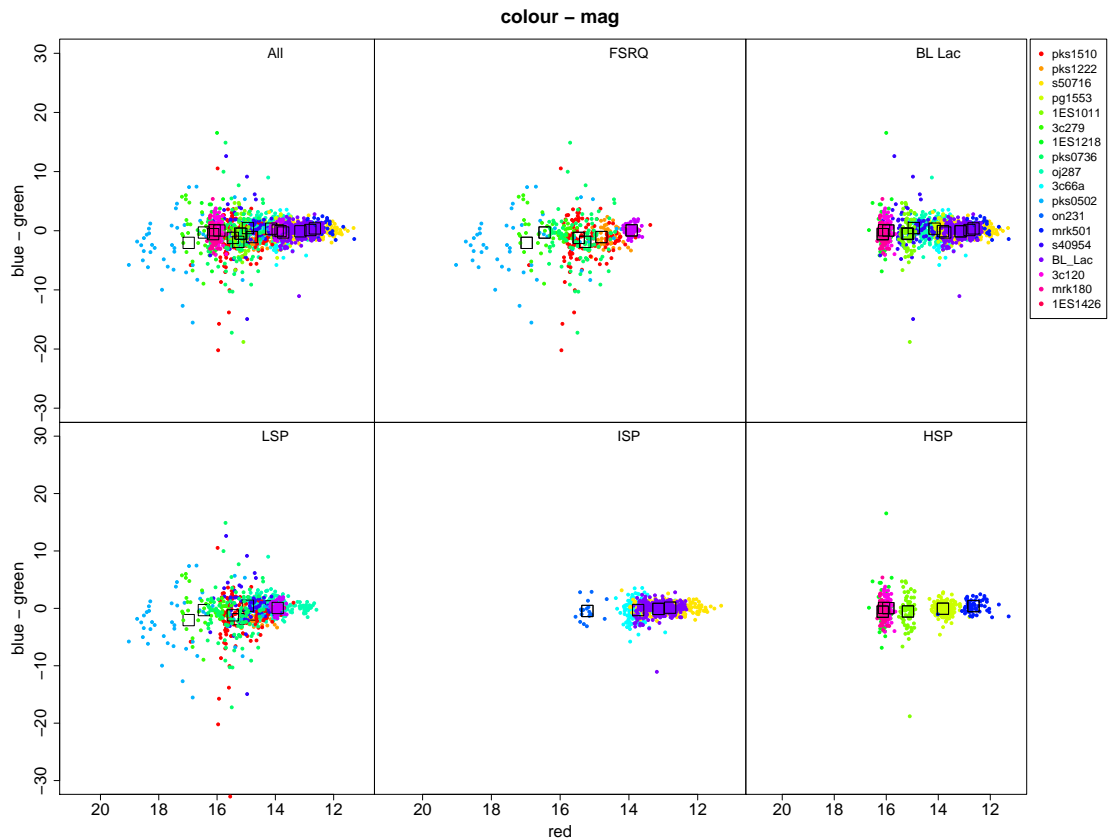
Figure 4.66: Plot of b* degree of polarisation - g* degree of polarisation vs r* magnitude for all sources, separated into different subclasses. The colour key identifies the sources and the black squares show the mean of each source.

The polarisation gets 'redder' with increasing brightness (a negative correlation) or 'bluer' (a positive correlation). The individual sources and their correlations can be seen in Table 4.15 and Figure 4.69.

Of the significant ρ values for the b* degree - r* degree vs g* magnitude there were six significant correlations found, two positive in FSRQ sources and one positive and three negative in BL Lac sources. The FSRQ sources are PKS 1510-089 and PKS 0502+049. This positive correlation suggests as the source gets brighter, the polarisation gets 'bluer'. The polarisation was also 'bluer' when higher for one BL Lac source, ON231 (ISP) , whereas the other BL Lac sources; OJ287 (LSP), S4 0954+65 (LSP) and 1ES 1426+428 (HSP), showed negative correlations suggesting a 'redder' polarisation when brighter.
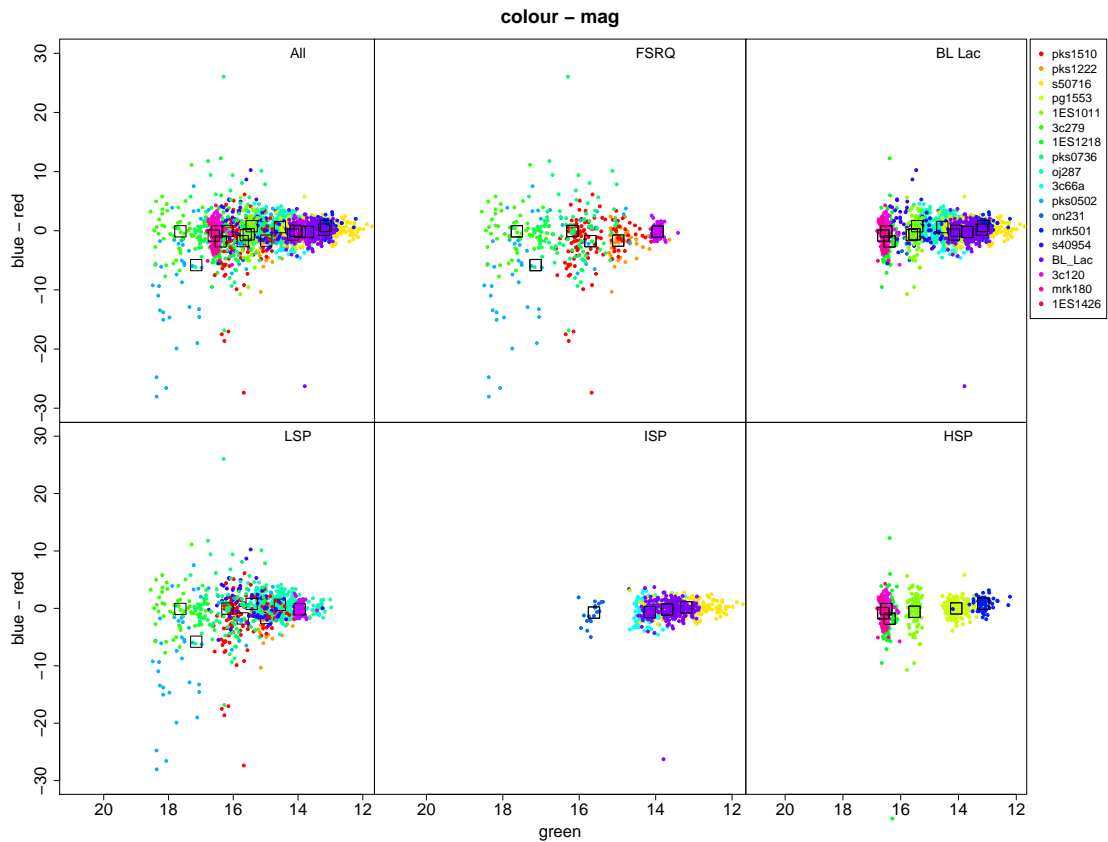
Figure 4.67: Plot of b* degree of polarisation - r* degree of polarisation vs g* magnitude for all sources, separated into different subclasses. The colour key identifies the sources and the black squares show the mean of each source.

The 'bluer' colour suggests higher energy particles in the jet and/or an increase in the temperature of the disk; this indicates a recent acceleration process in the jet or injection into the disk. The high values of polarisation suggest the presence of an ordered magnetic field. The polarisation is associated with synchrotron emission from the jet; the change in colour of the magnitude can be due to changes in the jet or the disk, therefore it is difficult to disentangle the origin of the emission and whether it is associated with the polarisation.

Of the significant ρ values for the g* degree - r* degree vs b* magnitude plots there were four correlations; two negative and two positive. The FSRQs showed one negative (3C279) correlation. The BL Lac sources showed two negative; OJ287 (LSP) and S4 0954+65 (LSP), correlations and one positive correlation (PG 1553+113, HSP).
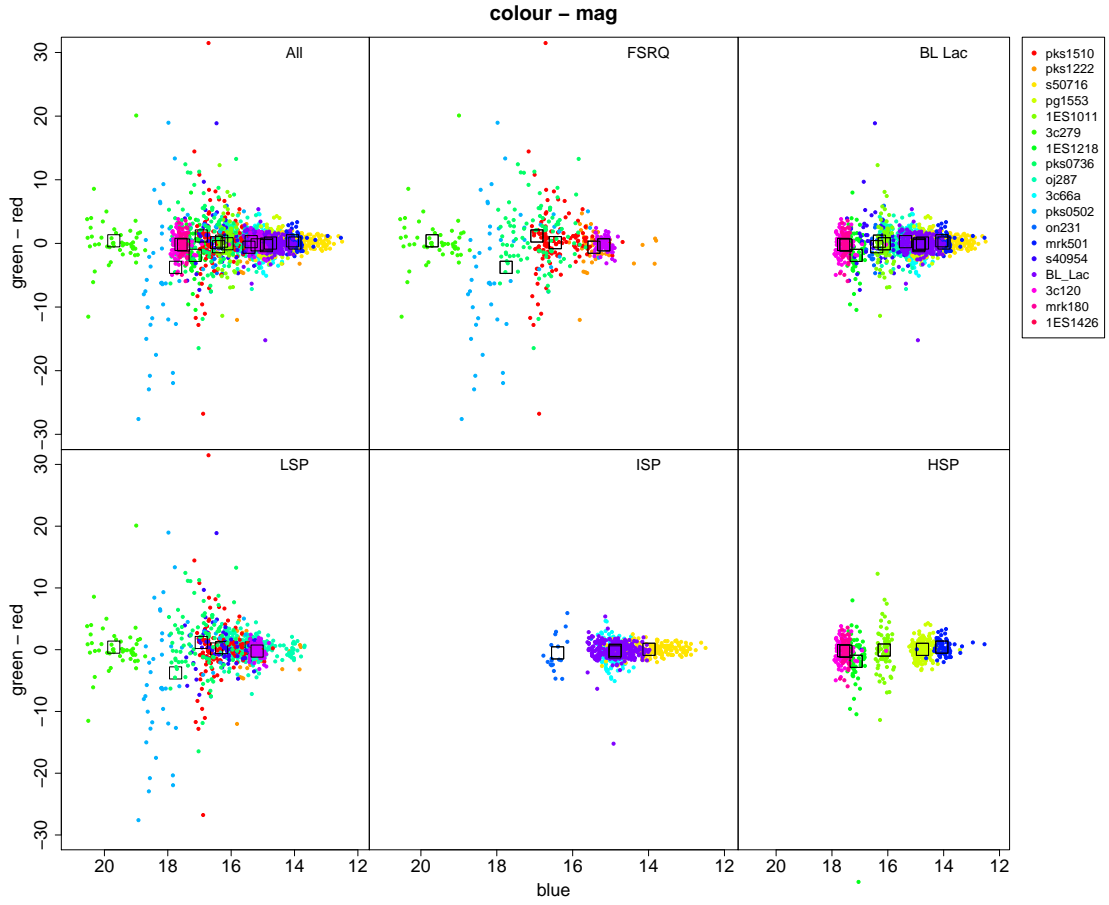
Figure 4.68: Plot of g* degree of polarisation - r* degree of polarisation vs b* magnitude for all sources, separated into different subclasses. The colour key identifies the sources and the black squares show the mean of each source.

		All p						p≤0.05			
	Type	Range p	Range ρ	Mean p	Mean ρ	Quantity $-\rho,+\rho$	Quantity	Range ρ	Mean ρ	Quantity $-\rho,+\rho$	Quantity
b* - g*	HSP	0.035 - 0.777	-0.278 - 0.0677	0.409	-0.0574	3,3	6	-0.278 - -0.278	-0.278	1,0	1
	ISP	0.0381 - 0.612	-0.0396 - 0.174	0.378	0.0839	1,3	4	0.174 - 0.174	0.174	0,1	1
	LSP	0.089 - 0.722	-0.123 - 0.227	0.355	0.0563	3,5	8	NA - NA	NA	0,0	0
	FSRQ	0.089 - 0.722	-0.0367 - 0.227	0.382	0.109	1,5	6	NA - NA	NA	0,0	0
	BL Lac	0.035 - 0.777	-0.278 - 0.174	0.377	-0.0179	6,6	12	-0.278 - 0.174	-0.052	1,1	2
	All	0.035 - 0.777	-0.278 - 0.227	0.378	0.0245	7,11	18	-0.278 - 0.174	-0.052	1,1	2
b* - r*	HSP	0.0205 - 0.569	-0.305 - 0.207	0.283	0.00965	2,4	6	-0.305 - -0.305	-0.305	1,0	1
	ISP	0.0141 - 0.616	-0.0392 - 0.56	0.339	0.171	1,3	4	0.56 - 0.56	0.56	0,1	1
	LSP	0.000106 - 0.834	-0.413 - 0.518	0.311	0.0372	3,5	8	-0.413 - 0.518	0.0473	2,2	4
	FSRQ	0.000106 - 0.834	-0.0684 - 0.518	0.414	0.148	1,5	6	0.259 - 0.518	0.389	0,2	2
	BL Lac	0.0028 - 0.616	-0.413 - 0.560	0.255	0.0130	5,7	12	-0.413 - 0.56	-0.0832	3,1	4
	All	0.000106 - 0.834	-0.413 - 0.560	0.308	0.0578	6,12	18	-0.413 - 0.56	0.074	3,3	6
g* - r*	HSP	0.0272 - 0.742	-0.0969 - 0.172	0.456	0.0127	3,3	6	0.172 - 0.172	0.172	0,1	1
	ISP	0.222 - 0.910	-0.0723 - 0.17	0.516	0.0107	2,2	4	NA - NA	NA	0,0	0
	LSP	0.00231 - 0.623	-0.278 - 0.416	0.283	-0.00755	5,3	8	-0.278 - 0.416	0.00367	2,1	3
	FSRQ	0.00231 - 0.623	-0.105 - 0.416	0.365	0.0574	3,3	6	0.416 - 0.416	0.416	0,1	1
	BL Lac	0.0272 - 0.910	-0.278 - 0.172	0.407	-0.0238	7,5	12	-0.278 - 0.172	-0.0777	2,1	3
	All	0.00231 - 0.910	-0.278 - 0.416	0.393	0.00326	10,8	18	-0.278 - 0.416	0.0457	2,2	4

Table 4.14: Summary of results from the Spearman Rank correlation test showing the p and ρ values for different subclasses for polarisation colour-magnitude correlations.
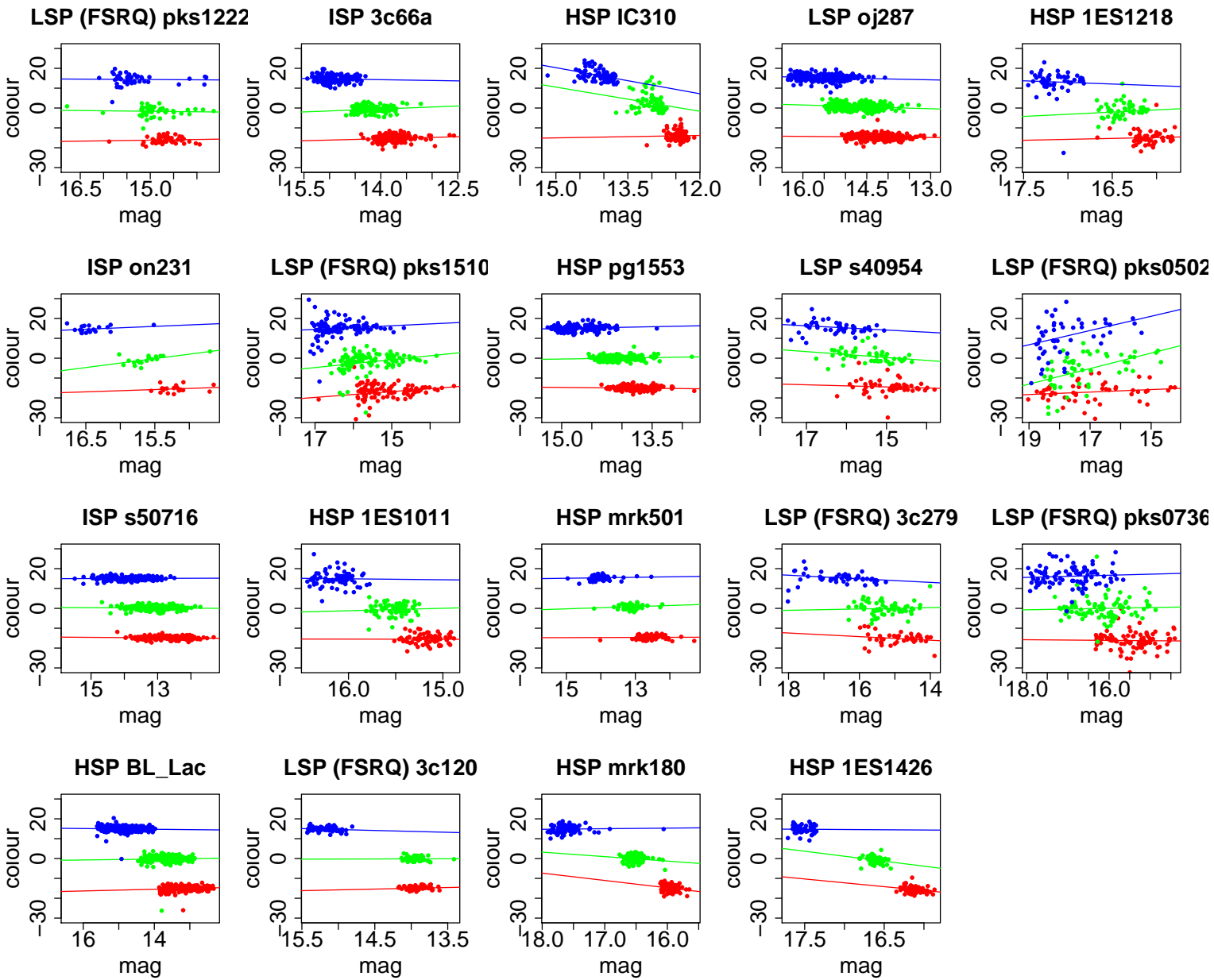
Figure 4.69: b* degree of polarisation - g* polarisation vs r* magnitude (red points), b* po-larisation - r* polarisation vs g* magnitude (green points) and g* polarisation - r* polarisation vs b* magnitude for all sources (except Mrk 421). Blue points are shifted up (+15) and red points are shifted down (-15) for clarity. The coloured lines represent a linear regression fit to the data. The values for these plots are shown in Table 4.15.

Source	Type	Line colour (cameras)	ρ	P	gradient
pks1222	LSP (FSRQ)	red (blue - green)	0.0939	0.533	-0.340
pks1222	LSP (FSRQ)	green (blue - red)	-0.0684	0.651	0.246
pks1222	LSP (FSRQ)	blue (green - red)	-0.0743	0.623	0.137
3c66a	ISP	red (blue - green)	**0.174**	0.0381	-0.674
3c66a	ISP	green (blue - red)	0.135	0.108	-0.986
3c66a	ISP	blue (green - red)	-0.0638	0.449	0.403
IC310	HSP	red (blue - green)	-0.0888	0.421	-0.408
IC310	HSP	green (blue - red)	**-0.369**	0.000590	4.054
IC310	HSP	blue (green - red)	**-0.472**	7.74×10^{-6}	4.377
oj287	LSP	red (blue - green)	-0.0827	0.162	0.178
oj287	LSP	green (blue - red)	**-0.175**	0.00304	0.636
oj287	LSP	blue (green - red)	**-0.127**	0.0320	0.436
1ES1218	HSP	red (blue - green)	0.0677	0.616	-0.943
1ES1218	HSP	green (blue - red)	0.207	0.122	-2.196
1ES1218	HSP	blue (green - red)	-0.0445	0.742	1.618
on231	ISP	red (blue - green)	0.139	0.570	-1.155
on231	ISP	green (blue - red)	**0.560**	0.0141	-4.495
on231	ISP	blue (green - red)	0.170	0.485	-1.448
pks1510	LSP (FSRQ)	red (blue - green)	0.153	0.0890	-1.465
pks1510	LSP (FSRQ)	green (blue - red)	**0.259**	0.00363	-1.978
pks1510	LSP (FSRQ)	blue (green - red)	0.117	0.194	-0.913
pg1553	HSP	red (blue - green)	-0.0909	0.246	0.297
pg1553	HSP	green (blue - red)	0.0861	0.271	-0.483
pg1553	HSP	blue (green - red)	**0.172**	0.0272	-0.598
s40954	LSP	red (blue - green)	-0.123	0.389	0.543
s40954	LSP	green (blue - red)	**-0.413**	0.00280	1.474
s40954	LSP	blue (green - red)	**-0.278**	0.0486	1.063
pks0502	LSP (FSRQ)	red (blue - green)	0.227	0.105	-0.625
pks0502	LSP (FSRQ)	green (blue - red)	**0.518**	0.000106	-3.902
pks0502	LSP (FSRQ)	blue (green - red)	**0.416**	0.00231	-3.583
s50716	ISP	red (blue - green)	-0.0396	0.612	0.124
s50716	ISP	green (blue - red)	-0.0392	0.616	0.082
s50716	ISP	blue (green - red)	0.00887	0.910	-0.050
1ES1011	HSP	red (blue - green)	0.0603	0.602	0.055
1ES1011	HSP	green (blue - red)	0.0658	0.569	-1.231
1ES1011	HSP	blue (green - red)	0.0509	0.660	0.478
mrk501	HSP	red (blue - green)	0.0365	0.777	-0.052
mrk501	HSP	green (blue - red)	0.108	0.394	-0.563
mrk501	HSP	blue (green - red)	-0.0955	0.452	-0.244
3c279	LSP (FSRQ)	red (blue - green)	0.0649	0.660	0.906
3c279	LSP (FSRQ)	green (blue - red)	0.0268	0.834	-0.335
3c279	LSP (FSRQ)	blue (green - red)	-0.105	0.465	0.903
pks0736	LSP (FSRQ)	red (blue - green)	-0.0367	0.722	0.164
pks0736	LSP (FSRQ)	green (blue - red)	0.0616	0.550	-0.375
pks0736	LSP (FSRQ)	blue (green - red)	0.0777	0.451	-0.542
BL Lac	HSP	red (blue - green)	0.0624	0.292	-0.425
BL Lac	HSP	green (blue - red)	0.0297	0.616	-0.221
BL Lac	HSP	blue (green - red)	-0.0723	0.222	0.180
3c120	LSP (FSRQ)	red (blue - green)	0.154	0.181	-0.792
3c120	LSP (FSRQ)	green (blue - red)	0.0885	0.443	-0.101
3c120	LSP (FSRQ)	blue (green - red)	-0.0868	0.452	0.928
mrk180	HSP	red (blue - green)	-0.140	0.181	3.701
mrk180	HSP	green (blue - red)	-0.104	0.319	2.255
mrk180	HSP	blue (green - red)	0.0904	0.388	-0.291
1ES1426	HSP	red (blue - green)	**-0.278**	0.0350	3.870
1ES1426	HSP	green (blue - red)	**-0.305**	0.0205	5.019
1ES1426	HSP	blue (green - red)	-0.0969	0.468	0.245

Table 4.15: Table of polarisation colour - magnitude Spearman rank coefficient values and gradients for all sources.

Over all the quantity of positive and negative correlations are equal and show no particular preference for any subclass of blazar in this sample.

4.5.4 Optical and γ-ray properties during EVPA rotations

Figure 4.70 shows the distribution of the degree of polarisation (top panel), g* band optical magnitude (mid panel) and γ-ray flux (bottom panel) during (column 1) and outside of (column 2) periods of EVPA rotations. Each measurement that coincided with the 'during' or 'outside' period was used in each histogram in the form of $\frac{value-min(values)}{range(all)}$ where 'value(s)' are the single measurement of degree of polarisation, optical magnitude or γ-ray flux and 'all' is all of the 'values' during the particular period. The quantity of data points was adjusted so that the number of measurements outside a rotation was the same as the number of measurements during a rotation by dividing the histogram counts by the ratio of the lengths of the outside and during data sets. The third panel shows the ratio of the means $\frac{mean(value-min(values))}{range(all)}$ during the rotation/non-rotation periods for each source.

Figure 4.70 shows the distribution of properties during and outside of EVPA rotation events for the 10 sources that have rotation events (see Table 4.7, note IC310 is included). The first histogram of the top panel shows that the degree of polarisation favoured lower values during rotation events with a mean of 0.20. There were few degree of polarisation values that were >80% of the maximum value.

The degree of polarisation data outside of rotations (second histogram on top panel) appeared to show a similar distribution to the degree of polarisation data during rotations, with a suppressed high polarisation tail. The mean of the outside of rotations distribution was slightly higher (0.28).

A KS test performed on the two distributions had a p value (p = 0.057) that was slightly larger than the significance threshold (p = 0.05) and thus the null hypothesis cannot be rejected.

The third histogram shows that 7/9 sources had mean degree of polarisation values during rotations that were lower than outside of rotations.
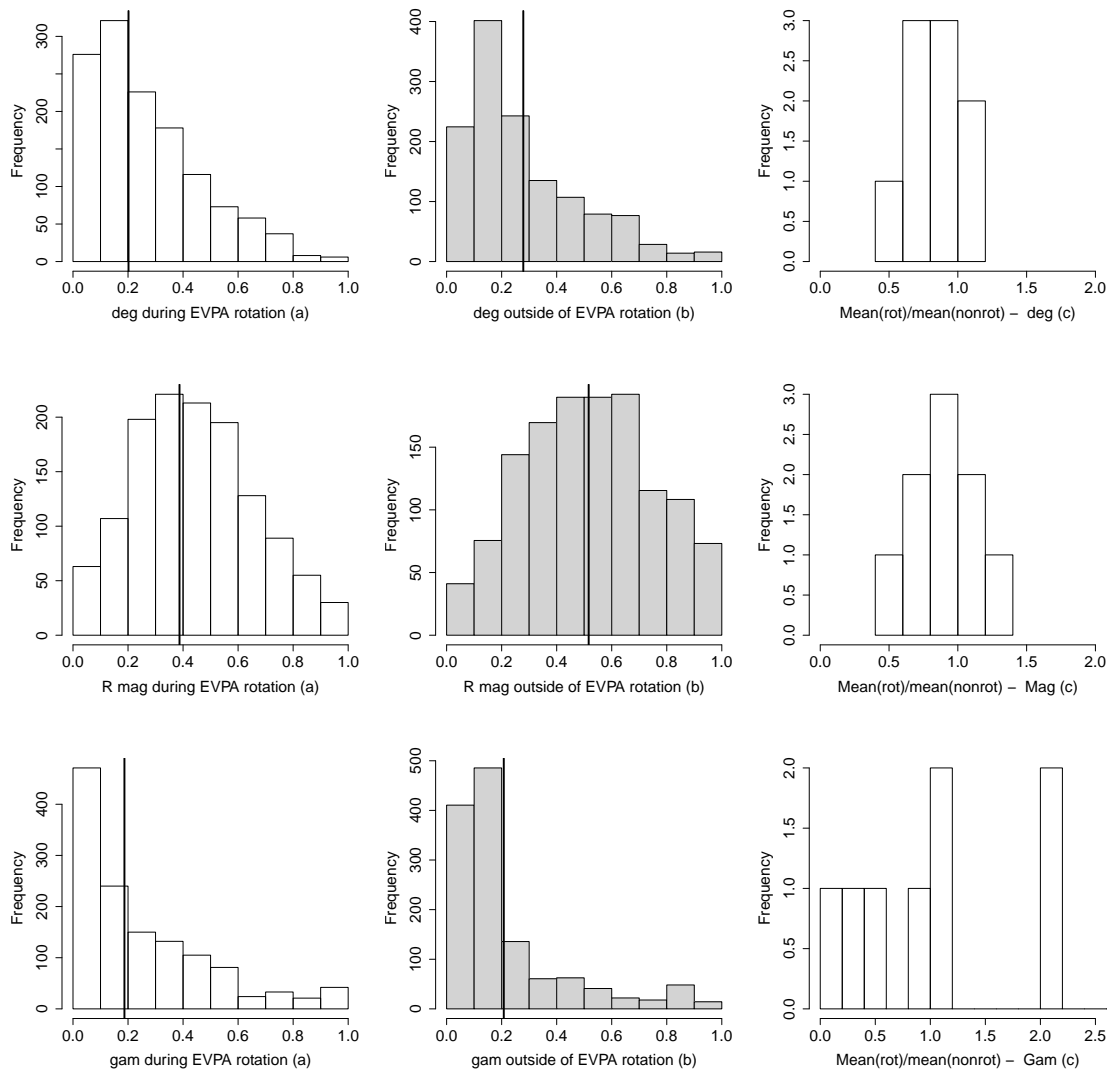
Figure 4.70: The degree of polarisation (top), optical magnitude (middle) and γ-ray flux (bottom) displayed as a fraction of the normalised range for a) during EVPA rotations (white) and b) outside of EVPA rotations (grey) and c) as a ratio of the mean of each property during a rotation over the mean of each property outside of a rotation for each individual source (see Section 4.5.4 for more details). The black vertical lines in the first two columns show the mean of the histograms.

For the optical (g* band) magnitude values there was a similar shape between the during and outside rotation histograms. It can be seen that the peak of the 'during' histogram was shifted toward brighter magnitude values, and the peak of the 'outside' histogram was shifted toward fainter magnitude values. There were a larger number of data points >80% of the total range for 'outside' values. The mean for the 'outside' distribution (0.52) was greater than the mean for the 'during' distribution (0.44).

A KS test on the two distributions gave a small p value of $<2.2\times10^{-16}$, which indicates that the null hypothesis (that the two distributions are related) can be rejected and the two distributions appeared to come from different distributions.

The third histogram in the second panel shows that in 6/9 sources the mean optical magnitude value was lower during rotations than outside of rotations.

The third panel shows the distribution of γ-ray flux values during (a) and outside (b) rotations. The distributions looked similar but had KS test p values of $<2.2\times10^{-16}$, which indicates they come from different parent distributions. The means of each distribution were similar, with values of 0.19 and 0.21 for during and outside rotations respectively.

The third histogram shows that half the sources had mean γ-ray flux values during rotations greater than outside rotations.

To explore the relationship between γ-ray flares and optical rotations, the rotations were corrected for their observing seasons by dividing the number of rotations by the duty cycle (i.e. number of days in optical period divided by number of days in γ-ray period). In Section 3.5.2, Figure 3.10 shows a significant positive correlation between the corrected number of optical rotations and the number of γ-ray flares. This was repeated for the Ringo3 period (see Figure 4.71), however, the results of the Spearman Rank Coefficient test were insignificant and were close to a significant *lack* of correlation (ρ=-0.0268, p= 0.919).
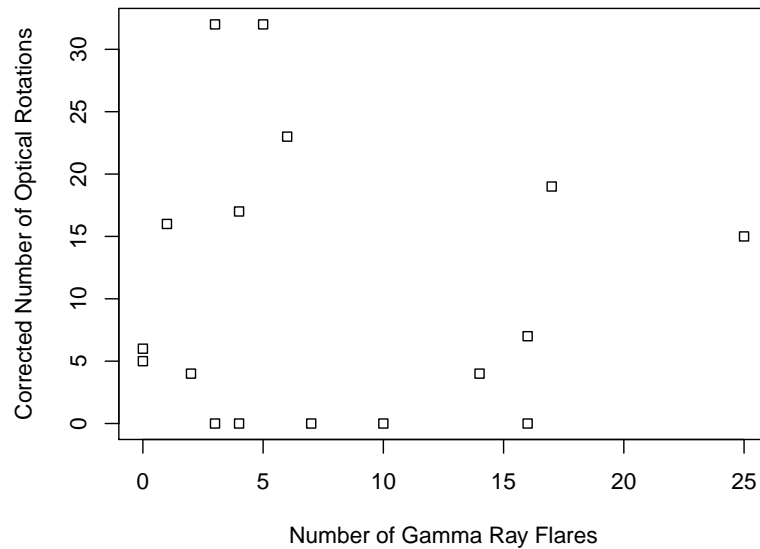
Figure 4.71: Corrected (for duty cycle) number of optical rotations against number of γ-ray flares for the 17 sources with available γ-ray data. There is no significant correlation (ρ=-0.0268, p=0.919).

4.5.5 Lag analysis

In order to explore the possibility that the data could be better correlated with a positive or negative lag (suggesting a physical separation of the emission regions or a delay in emission) a code was written which shifted one variable (e.g. γ-ray flux, magnitude or degree of polarisation) by incremental steps of 1 day from -50 days to +50 days, and applied the Spearman correlation test to each lagged set. The significant (i.e $p \leq 0.05$) ρ values and their corresponding lag values are shown in Figure 4.72.

The positive correlations peaked strongly around zero days. This gives strong confidence to their validity, and indicates a relatively close association between the optical and γ-ray emitting regions. The negative correlations had a much wider distribution of lag time and might be more attributable to coincidence. The decrease in the strength of correlation with lag suggests that, though the ρ values were close to zero, they are in fact likely to be real rather than stochastic correlations.

Source	Season	MJD range	ρ	p value	Season	MJD range	ρ	p value	Season	MJD range	ρ	p value	Season	MJD range	ρ	p value
3c66a mag-gam	a	56825.208 - 57097.865	0.08074	0.44169	b	57206.208 - 57406.978	0.50636	0.00000	c	NA - NA	NA	NA	d	NA - NA	NA	NA
3c66a deg-gam	a	56825.208 - 57097.865	-0.06285	0.61813	b	57206.208 - 57406.978	-0.12495	0.27827	c	NA - NA	NA	NA	d	NA - NA	NA	NA
3c66a mag-deg	a	56825.208 - 57097.865	0.02072	0.86966	b	57206.208 - 57406.978	-0.51446	0.00000	c	NA - NA	NA	NA	d	NA - NA	NA	NA
3c279 mag-gam	a	56268.281 - 56435.943	0.17183	0.07824	b	56656.277 - 56820.969	0.02747	0.93499	c	56995.27 - 57208.895	-0.37970	0.00531	d	57386.176 - 57433.148	0.43333	0.06528
3c279 deg-gam	a	56268.281 - 56435.943	0.30614	0.01872	b	56656.277 - 56820.969	-0.16364	0.63387	c	56995.27 - 57208.895	0.00316	0.98383	d	57386.176 - 57433.148	0.39525	0.10553
3c279 mag-deg	a	56268.281 - 56435.943	0.25856	0.05241	b	56656.277 - 56820.969	0.19091	0.57626	c	56995.27 - 57208.895	-0.46640	0.00140	d	57386.176 - 57433.148	-0.02167	0.93446
pks1510 mag-gam	a	56288.285 - 56493.972	0.12208	0.59687	b	56661.283 - 56884.905	0.59328	0.00028	c	57019.294 - 57243.926	0.56799	0.00000	d	57386.277 - 57541.938	0.00876	0.96558
pks1510 deg-gam	a	56288.285 - 56493.972	-0.40175	0.08931	b	56661.283 - 56884.905	0.31826	0.06705	c	57019.294 - 57243.926	-0.13618	0.30289	d	57386.277 - 57541.938	0.64164	0.00042
pks1510 mag-deg	a	56288.285 - 56493.972	0.00702	0.97988	b	56661.283 - 56884.905	-0.01451	0.93538	c	57019.294 - 57243.926	0.03068	0.81716	d	57386.277 - 57541.938	0.18987	0.34128
oj287 mag-gam	a	57005.122 - 57160.938	-0.55278	0.00013	b	57359.153 - 57531.872	-0.05071	0.43683	c	NA - NA	NA	NA	d	NA - NA	NA	NA
oj287 deg-gam	a	57005.122 - 57160.938	0.19013	0.21564	b	57359.153 - 57531.872	-0.15459	0.01731	c	NA - NA	NA	NA	d	NA - NA	NA	NA
oj287 mag-deg	a	57005.122 - 57160.938	-0.17533	0.25404	b	57359.153 - 57531.872	0.38845	0.00000	c	NA - NA	NA	NA	d	NA - NA	NA	NA
s50716 mag-gam	a	56661.027 - 56787.887	0.57739	0.00369	b	56886.233 - 57168.892	0.63181	0.00000	c	57250.238 - 57413.033	0.57186	0.00002	d	NA - NA	NA	NA
s50716 deg-gam	a	56661.027 - 56787.887	0.18881	0.55783	b	56886.233 - 57168.892	0.03432	0.73294	c	57250.238 - 57413.033	-0.37112	0.00902	d	NA - NA	NA	NA
s50716 mag-deg	a	56661.027 - 56787.887	0.23077	0.47091	b	56886.233 - 57168.892	-0.04778	0.63462	c	57250.238 - 57413.033	0.09153	0.53051	d	NA - NA	NA	NA
BL Lac mag-gam	a	56393.242 - 56501.086	0.62088	0.02687	b	56758.24 - 57026.824	0.50342	0.00000	c	57110.247 - 57258.072	0.47436	0.00000	d	NA - NA	NA	NA
BL Lac deg-gam	a	56393.242 - 56501.086	-0.41209	0.16339	b	56758.24 - 57026.824	-0.15567	0.07816	c	57110.247 - 57258.072	0.24844	0.00223	d	NA - NA	NA	NA
BL Lac mag-deg	a	56393.242 - 56501.086	-0.25275	0.40433	b	56758.24 - 57026.824	-0.02009	0.82103	c	57110.247 - 57258.072	-0.02793	0.73410	d	NA - NA	NA	NA
mrk421 mag-gam	a	56226.255 - 56479.889	0.49000	0.00000	b	56585.242 - 56815.969	0.32300	0.97100	c	56945.2481134 - 57185.9647569	-0.07100	0.55000	d	57321.2585069 - 57398.0890972	0.41100	0.99000
mrk421 deg-gam	a	56226.255 - 56479.889	0.26400	0.00100	b	56585.242 - 56815.969	-0.08600	0.43100	c	56945.2481134 - 57185.9647569	-0.00700	0.06300	d	57321.2585069 - 57398.0890972	-0.12700	0.55900
mrk421 mag-deg	a	56226.255 - 56479.889	-0.03000	0.71700	b	56585.242 - 56815.969	0.03000	0.15900	c	56945.2481134 - 57185.9647569	0.09000	0.66200	d	57321.2585069 - 57398.0890972	-0.03000	0.14600
mrk180 mag-gam	a	56275.255 - 56464.979	0.04000	0.32800	b	56650.116 - 56845.931	0.04000	0.32800	c	56856.884 - 57239.876	0.04000	0.32800	d	57386.047 - 57427.023	-0.10800	0.54400
mrk180 deg-gam	a	56275.255 - 56464.979	-0.08000	0.61100	b	56650.116 - 56845.931	-0.08000	0.61100	c	56856.884 - 57239.876	-0.08000	0.61100	d	57386.047 - 57427.023	0.09300	0.48100
mrk180 mag-deg	a	56275.255 - 56464.979	0.10466	0.52470	b	56650.116 - 56845.931	0.29670	0.32465	c	56856.884 - 57239.876	-0.21498	0.13358	d	57386.047 - 57427.023	0.18077	0.38548
mrk501 mag-gam	a	56487.895 - 56884.052	0.17183	0.07824	b	NA - NA	NA	NA	c	NA - NA	NA	NA	d	NA - NA	NA	NA
mrk501 deg-gam	a	56487.895 - 56884.052	0.30614	0.01872	b	NA - NA	NA	NA	c	NA - NA	NA	NA	d	NA - NA	NA	NA
mrk501 mag-deg	a	56487.895 - 56884.052	0.25856	0.05241	b	NA - NA	NA	NA	c	NA - NA	NA	NA	d	NA - NA	NA	NA
on231 mag-gam	a	57386.102 - 57454.065	0.12208	0.59687	b	NA - NA	NA	NA	c	NA - NA	NA	NA	d	NA - NA	NA	NA
on231 deg-gam	a	57386.102 - 57454.065	-0.40175	0.08931	b	NA - NA	NA	NA	c	NA - NA	NA	NA	d	NA - NA	NA	NA
on231 mag-deg	a	57386.102 - 57454.065	0.00702	0.97988	b	NA - NA	NA	NA	c	NA - NA	NA	NA	d	NA - NA	NA	NA
pg1553 mag-gam	a	56285.286 - 56495.05	0.00876	0.96558	b	56651.289 - 56913.851	0.32312	0.00839	c	57016.284 - 57276.875	0.67283	0.00000	d	57386.276 - 57452.273	-0.21667	0.58094
pg1553 deg-gam	a	56285.286 - 56495.05	0.64164	0.00042	b	56651.289 - 56913.851	0.27070	0.03082	c	57016.284 - 57276.875	0.26199	0.01445	d	57386.276 - 57452.273	-0.09524	0.84013
pg1553 mag-deg	a	56285.286 - 56495.05	0.18987	0.34128	b	56651.289 - 56913.851	-0.17321	0.17069	c	57016.284 - 57276.875	0.11819	0.27501	d	57386.276 - 57452.273	0.57143	0.15114
pks1222 mag-gam	a	56268.279729 - 56464.986273	0.49085	0.00000	b	56651.232878 - 56845.945352	-0.13571	0.62972	c	57047.149809 - 57208.893548	0.15195	0.50925	d	57397.21779 - 57427.20169	0.20000	0.91667
pks1222 deg-gam	a	56268.279729 - 56464.986273	0.26432	0.00112	b	56651.232878 - 56845.945352	0.06786	0.81294	c	57047.149809 - 57208.893548	0.56883	0.00812	d	57397.21779 - 57427.20169	0.60000	0.41667
pks1222 mag-deg	a	56268.279729 - 56464.986273	-0.09286	0.74345	b	56651.232878 - 56845.945352	0.20714	0.45777	c	57047.149809 - 57208.893548	0.19740	0.38933	d	57397.21779 - 57427.20169	-0.20000	0.91667
1ES1011 mag-gam	a	56268.254 - 56434.016	0.57186	0.00002	b	56650.127 - 56821.944	-0.11801	0.59968	c	56930.245 - 57182.925	0.42468	0.00541	d	57296.254 - 57454.025	0.09706	0.72136
1ES1011 deg-gam	a	56268.254 - 56434.016	-0.37112	0.00902	b	56650.127 - 56821.944	-0.09481	0.68204	c	56930.245 - 57182.925	0.04675	0.76814	d	57296.254 - 57454.025	0.04412	0.87374
1ES1011 mag-deg	a	56268.254 - 56434.016	0.09153	0.53051	b	56650.127 - 56821.944	0.06494	0.77988	c	56930.245 - 57182.925	0.12244	0.43851	d	57296.254 - 57454.025	-0.10588	0.69677
1ES1218 mag-gam	a	56268.274 - 56433.045	-0.05071	0.43683	b	56679.052 - 56845.953	-0.06522	0.76175	c	56965.253 - 57158.932	0.08427	0.65106	d	57347.278 - 57421.185	0.72549	0.00141
1ES1218 deg-gam	a	56268.274 - 56433.045	-0.15459	0.01731	b	56679.052 - 56845.953	0.17441	0.48735	c	56965.253 - 57158.932	0.08348	0.69739	d	57347.278 - 57421.185	-0.78431	0.00030
1ES1218 mag-deg	a	56268.274 - 56433.045	0.38845	0.00000	b	56679.052 - 56845.953	-0.25903	0.29805	c	56965.253 - 57158.932	0.03739	0.86275	d	57347.278 - 57421.185	-0.52206	0.03365
1ES1426 mag-gam	a	57037.266 - 57276.88	-0.18800	0.68900	b	57386.178 - 57427.254	0.08200	0.31400	c	NA - NA	NA	NA	d	NA - NA	NA	NA
1ES1426 deg-gam	a	57037.266 - 57276.88			b	57386.178 - 57427.254	-0.58700	0.99900	c	NA - NA	NA	NA	d	NA - NA	NA	NA
1ES1426 mag-deg	a	57037.266 - 57276.88	-0.00365	0.98204	b	57386.178 - 57427.254	0.25275	0.38246	c	NA - NA	NA	NA	d	NA - NA	NA	NA
IC310 mag-gam	a	57036.863 - 57097.86	0.13636	0.69351	b	57206.209 - 57391.908	0.12865	0.28779	c	NA - NA	NA	NA	d	NA - NA	NA	NA
IC310 deg-gam	a	57036.863 - 57097.86	0.57273	0.07060	b	57206.209 - 57391.908	-0.41363	0.00042	c	NA - NA	NA	NA	d	NA - NA	NA	NA
IC310 mag-deg	a	57036.863 - 57097.86	-0.52727	0.10013	b	57206.209 - 57391.908	-0.14926	0.21696	c	NA - NA	NA	NA	d	NA - NA	NA	NA
pks0502 mag-gam	a	56887.219 - 56930.128	0.34834	0.07497	b	57269.153 - 57332.105	0.83571	0.00013	c	57390.956 - 57427.923	0.11976	0.77758	d	NA - NA	NA	NA
pks0502 deg-gam	a	56887.219 - 56930.128	0.26231	0.20449	b	57269.153 - 57332.105	-0.18571	0.50667	c	57390.956 - 57427.923	-0.65714	0.17500	d	NA - NA	NA	NA
pks0502 mag-deg	a	56887.219 - 56930.128	0.08231	0.69487	b	57269.153 - 57332.105	-0.40714	0.13331	c	57390.956 - 57427.923	0.20000	0.71389	d	NA - NA	NA	NA
pks0736 mag-gam	a	57007.998 - 57137.87	0.43114	0.00140	b	57278.24 - 57345.228	0.70553	0.00025	c	57387.007 - 57413.024	0.62088	0.02687	d	NA - NA	NA	NA
pks0736 deg-gam	a	57007.998 - 57137.87	-0.00548	0.96904	b	57278.24 - 57345.228	0.30138	0.16199	c	57387.007 - 57413.024	-0.41209	0.16339	d	NA - NA	NA	NA
pks0736 mag-deg	a	57007.998 - 57137.87	0.01911	0.89181	b	57278.24 - 57345.228	0.66206	0.00078	c	57387.007 - 57413.024	-0.25275	0.40433	d	NA - NA	NA	NA
s40954 mag-gam	a	57162.991 - 57187.899	0.61325	0.00186	b	57294.224 - 57346.103	0.43684	0.06295	c	57408.13 - 57426.04	-0.71818	0.01680	d	NA - NA	NA	NA
s40954 deg-gam	a	57162.991 - 57187.899	-0.10049	0.70134	b	57294.224 - 57346.103	0.00351	0.99138	c	57408.13 - 57426.04	0.27273	0.44827	d	NA - NA	NA	NA
s40954 mag-deg	a	57162.991 - 57187.899	-0.09069	0.72970	b	57294.224 - 57346.103	0.37368	0.11574	c	57408.13 - 57426.04	-0.23636	0.51390	d	NA - NA	NA	NA
3c120 mag-gam	a	56937.078 - 57086.854	0.04000	0.32800	b	57231.23 - 57345.094	0.04000	0.32800	c	57386.942 - 57430.908	-0.13200	0.81400	d	NA - NA	NA	NA
3c120 deg-gam	a	56937.078 - 57086.854	-0.08000	0.61100	b	57231.23 - 57345.094	-0.08000	0.61100	c	57386.942 - 57430.908	-0.00300	0.02600	d	NA - NA	NA	NA
3c120 mag-deg	a	56937.078 - 57086.854	-0.07510	0.73298	b	57231.23 - 57345.094	0.10466	0.52470	c	57386.942 - 57430.908	0.09100	0.63700	d	NA - NA	NA	NA

Table 4.16: Table of correlation values for the parameters in the red camera as shown.

Source	Season	MJD range	ρ	p value	Season	MJD range	ρ	p value	Season	MJD range	ρ	p value	Season	MJD range	ρ	p value
3c66a mag-gam	a	56825.208 - 57097.865	0.14670	0.16057	b	57206.208 - 57406.978	0.54613	0.00000	c	NA - NA	NA	NA	d	NA - NA	NA	NA
3c66a deg-gam	a	56825.208 - 57097.865	-0.13241	0.25359	b	57206.208 - 57406.978	-0.04433	0.69752	c	NA - NA	NA	NA	d	NA - NA	NA	NA
3c66a mag-deg	a	56825.208 - 57097.865	-0.00834	0.94296	b	57206.208 - 57406.978	-0.43357	0.00008	c	NA - NA	NA	NA	d	NA - NA	NA	NA
3c279 mag-gam	a	56268.281 - 56435.943	0.12207	0.20787	b	56656.277 - 56820.969	-0.01099	0.97831	c	56995.27 - 57208.895	-0.04370	0.75542	d	57386.176 - 57433.148	-0.06842	0.78126
3c279 deg-gam	a	56268.281 - 56435.943	0.31724	0.01469	b	56656.277 - 56820.969	-0.54762	0.17098	c	56995.27 - 57208.895	-0.19694	0.26314	d	57386.176 - 57433.148	-0.71765	0.00244
3c279 mag-deg	a	56268.281 - 56435.943	0.08153	0.53832	b	56656.277 - 56820.969	-0.26190	0.53641	c	56995.27 - 57208.895	-0.09947	0.57436	d	57386.176 - 57433.148	0.50000	0.05085
pks1510 mag-gam	a	56288.285 - 56493.972	0.29091	0.20016	b	56661.283 - 56884.905	0.56211	0.00067	c	57019.294 - 57243.926	0.73269	0.00000	d	57386.277 - 57541.938	-0.22551	0.24747
pks1510 deg-gam	a	56288.285 - 56493.972	-0.51053	0.02719	b	56661.283 - 56884.905	0.44752	0.00850	c	57019.294 - 57243.926	0.12671	0.33798	d	57386.277 - 57541.938	0.29721	0.12455
pks1510 mag-deg	a	56288.285 - 56493.972	0.16842	0.48911	b	56661.283 - 56884.905	0.29167	0.09437	c	57019.294 - 57243.926	0.17054	0.19604	d	57386.277 - 57541.938	0.34483	0.07291
oj287 mag-gam	a	57005.122 - 57160.938	-0.64186	0.00000	b	57359.153 - 57531.872	-0.05509	0.39824	c	NA - NA	NA	NA	d	NA - NA	NA	NA
oj287 deg-gam	a	57005.122 - 57160.938	0.15405	0.31694	b	57359.153 - 57531.872	-0.17822	0.00600	c	NA - NA	NA	NA	d	NA - NA	NA	NA
oj287 mag-deg	a	57005.122 - 57160.938	-0.24341	0.11129	b	57359.153 - 57531.872	0.31376	0.00000	c	NA - NA	NA	NA	d	NA - NA	NA	NA
s50716 mag-gam	a	56661.027 - 56787.887	0.64783	0.00082	b	56886.233 - 57168.892	0.63429	0.00000	c	57250.238 - 57413.033	0.72101	0.00000	d	NA - NA	-0.10800	0.54400
s50716 deg-gam	a	56661.027 - 56787.887	0.12587	0.69971	b	56886.233 - 57168.892	0.04523	0.65283	c	57250.238 - 57413.033	-0.41694	0.00311	d	NA - NA	0.09300	0.48100
s50716 mag-deg	a	56661.027 - 56787.887	0.22378	0.48491	b	56886.233 - 57168.892	0.00369	0.97076	c	57250.238 - 57413.033	-0.00520	0.97186	d	NA - NA	0.17000	0.76200
BL Lac mag-gam	a	56393.242 - 56501.086	0.70879	0.00883	b	56758.24 - 57026.824	0.50439	0.00000	c	57110.247 - 57258.072	0.49085	0.00000	d	NA - NA	-0.10800	0.54400
BL Lac deg-gam	a	56393.242 - 56501.086	0.45604	0.11975	b	56758.24 - 57026.824	-0.16986	0.05439	c	57110.247 - 57258.072	0.26432	0.00112	d	NA - NA	0.09300	0.48100
BL Lac mag-deg	a	56393.242 - 56501.086	0.23077	0.44777	b	56758.24 - 57026.824	0.01933	0.82765	c	57110.247 - 57258.072	-0.02982	0.71684	d	NA - NA	0.17000	0.76200
mrk421 mag-gam	a	56226.2550115 - 56479.8890625	0.49000	0.00000	b	56585.2418402 - 56815.9689236	0.32300	0.97100	c	56945.2481134 - 57185.9647569	-0.07100	0.55000	d	57321.2585069 - 57398.0890972	0.41100	0.99000
mrk421 deg-gam	a	56226.2550115 - 56479.8890625	0.26400	0.00100	b	56585.2418402 - 56815.9689236	-0.08600	0.43100	c	56945.2481134 - 57185.9647569	-0.00700	0.06300	d	57321.2585069 - 57398.0890972	-0.12700	0.55900
mrk421 mag-deg	a	56226.2550115 - 56479.8890625	-0.03000	0.71700	b	56585.2418402 - 56815.9689236	0.03000	0.15900	c	56945.2481134 - 57185.9647569	0.09000	0.66200	d	57321.2585069 - 57398.0890972	-0.03000	0.14600
mrk180 mag-gam	a	56275.255 - 56464.979	0.04000	0.32800	b	56650.116 - 56845.931	0.04000	0.32800	c	56856.884 - 57239.876	0.04000	0.32800	d	57386.047 - 57427.023	-0.10800	0.54400
mrk180 deg-gam	a	56275.255 - 56464.979	-0.08000	0.61100	b	56650.116 - 56845.931	-0.08000	0.61100	c	56856.884 - 57239.876	-0.08000	0.61100	d	57386.047 - 57427.023	0.09300	0.48100
mrk180 mag-deg	a	56275.255 - 56464.979	-0.02854	0.86288	b	56650.116 - 56845.931	0.09706	0.72136	c	56856.884 - 57239.876	0.11549	0.42334	d	57386.047 - 57427.023	-0.02077	0.92234
mrk501 mag-gam	a	56487.895 - 56884.052	0.12207	0.20787	b	NA - NA	0.08200	0.31400	c	NA - NA	NA	NA	d	NA - NA	NA	NA
mrk501 deg-gam	a	56487.895 - 56884.052	0.31724	0.01469	b	NA - NA	-0.58700	0.99900	c	NA - NA	NA	NA	d	NA - NA	NA	NA
mrk501 mag-deg	a	56487.895 - 56884.052	0.08153	0.53832	b	NA - NA	-0.17400	0.61600	c	NA - NA	NA	NA	d	NA - NA	NA	NA
on231 mag-gam	a	57386.102 - 57454.065	0.29091	0.20016	b	NA - NA	0.08200	0.31400	c	NA - NA	NA	NA	d	NA - NA	NA	NA
on231 deg-gam	a	57386.102 - 57454.065	-0.51053	0.02719	b	NA - NA	-0.58700	0.99900	c	NA - NA	NA	NA	d	NA - NA	NA	NA
on231 mag-deg	a	57386.102 - 57454.065	0.16842	0.48911	b	NA - NA	-0.17400	0.61600	c	NA - NA	NA	NA	d	NA - NA	NA	NA
pg1553 mag-gam	a	56285.286 - 56495.05	-0.22551	0.24747	b	56651.289 - 56913.851	0.42695	0.00040	c	57016.284 - 57276.875	0.72005	0.00000	d	57386.276 - 57452.273	-0.73333	0.03112
pg1553 deg-gam	a	56285.286 - 56495.05	0.29721	0.12455	b	56651.289 - 56913.851	0.25673	0.03926	c	57016.284 - 57276.875	0.27820	0.00887	d	57386.276 - 57452.273	-0.23810	0.58214
pg1553 mag-deg	a	56285.286 - 56495.05	0.34483	0.07291	b	56651.289 - 56913.851	0.13304	0.28997	c	57016.284 - 57276.875	0.09609	0.37248	d	57386.276 - 57452.273	0.64286	0.09618
pks1222 mag-gam	a	56268.279729 - 56464.986273	0.46784	0.00000	b	56651.232878 - 56845.945352	-0.23571	0.39655	c	57047.149809 - 57208.893548	0.20130	0.37988	d	57397.21779 - 57427.20169	-0.00000	1.00000
pks1222 deg-gam	a	56268.279729 - 56464.986273	0.26330	0.00117	b	56651.232878 - 56845.945352	-0.10714	0.70483	c	57047.149809 - 57208.893548	0.55714	0.00977	d	57397.21779 - 57427.20169	1.00000	0.08333
pks1222 mag-deg	a	56268.279729 - 56464.986273	0.23929	0.38923	b	56651.232878 - 56845.945352	0.07500	0.79257	c	57047.149809 - 57208.893548	0.44805	0.04305	d	57397.21779 - 57427.20169	-0.00000	1.00000
1ES1011 mag-gam	a	56268.254 - 56434.016	0.72101	0.00000	b	56650.127 - 56821.944	-0.20384	0.36121	c	56930.245 - 57182.925	0.46876	0.00194	d	57296.254 - 57454.025	-0.52059	0.04101
1ES1011 deg-gam	a	56268.254 - 56434.016	-0.41694	0.00311	b	56650.127 - 56821.944	0.67857	0.00690	c	56930.245 - 57182.925	-0.03509	0.82504	d	57296.254 - 57454.025	-0.19412	0.47003
1ES1011 mag-deg	a	56268.254 - 56434.016	-0.00520	0.97186	b	56650.127 - 56821.944	-0.00714	0.98466	c	56930.245 - 57182.925	0.04141	0.79409	d	57296.254 - 57454.025	0.21471	0.42321
1ES1218 mag-gam	a	56268.274 - 56433.045	-0.05509	0.39824	b	56679.052 - 56845.953	0.35565	0.08869	c	56965.253 - 57158.932	0.03306	0.85982	d	57347.278 - 57421.185	0.65931	0.00502
1ES1218 deg-gam	a	56268.274 - 56433.045	-0.17822	0.00600	b	56679.052 - 56845.953	-0.04522	0.83406	c	56965.253 - 57158.932	-0.28077	0.17352	d	57347.278 - 57421.185	-0.44363	0.07617
1ES1218 mag-deg	a	56268.274 - 56433.045	0.31376	0.00000	b	56679.052 - 56845.953	0.10783	0.61477	c	56965.253 - 57158.932	0.15692	0.45206	d	57347.278 - 57421.185	-0.62500	0.00869
1ES1426 mag-gam	a	57037.266 - 57276.88	-0.18800	0.68900	b	57386.178 - 57427.254	0.08200	0.31400	c	NA - NA	NA	NA	d	NA - NA	NA	NA
1ES1426 deg-gam	a	57037.266 - 57276.88			b	57386.178 - 57427.254	-0.58700	0.99900	c	NA - NA	NA	NA	d	NA - NA	NA	NA
1ES1426 mag-deg	a	57037.266 - 57276.88	0.06186	0.68213	b	57386.178 - 57427.254	-0.09286	0.74345	c	NA - NA	NA	NA	d	NA - NA	NA	NA
IC310 mag-gam	a	57036.863 - 57097.86	0.46364	0.15433	b	57206.209 - 57391.908	0.31394	0.00837	c	NA - NA	NA	NA	d	NA - NA	NA	NA
IC310 deg-gam	a	57036.863 - 57097.86	0.20000	0.55755	b	57206.209 - 57391.908	-0.42885	0.00024	c	NA - NA	NA	NA	d	NA - NA	NA	NA
IC310 mag-deg	a	57036.863 - 57097.86	0.00909	0.98919	b	57206.209 - 57391.908	-0.67285	0.00000	c	NA - NA	NA	NA	d	NA - NA	NA	NA
pks0502 mag-gam	a	56887.219 - 56930.128	0.58120	0.00179	b	57269.153 - 57332.105	0.53214	0.04379	c	57390.956 - 57427.923	-0.09524	0.84013	d	NA - NA	NA	NA
pks0502 deg-gam	a	56887.219 - 56930.128	0.46667	0.01721	b	57269.153 - 57332.105	0.07857	0.78268	c	57390.956 - 57427.923	-0.07143	0.88199	d	NA - NA	NA	NA
pks0502 mag-deg	a	56887.219 - 56930.128	0.40855	0.03925	b	57269.153 - 57332.105	0.22500	0.41896	c	57390.956 - 57427.923	-0.00000	1.00000	d	NA - NA	NA	NA
pks0736 mag-gam	a	57007.998 - 57137.87	0.54435	0.00003	b	57278.24 - 57345.228	0.59289	0.00343	c	57387.007 - 57413.024	0.70879	0.00883	d	NA - NA	NA	NA
pks0736 deg-gam	a	57007.998 - 57137.87	-0.06176	0.65956	b	57278.24 - 57345.228	0.50889	0.01423	c	57387.007 - 57413.024	0.45604	0.11975	d	NA - NA	NA	NA
pks0736 mag-deg	a	57007.998 - 57137.87	-0.07402	0.59739	b	57278.24 - 57345.228	0.41897	0.04776	c	57387.007 - 57413.024	0.23077	0.44777	d	NA - NA	NA	NA
s40954 mag-gam	a	57162.991 - 57187.899	0.47053	0.02346	b	57294.224 - 57346.103	0.34974	0.14216	c	57408.13 - 57426.04	-0.62727	0.04399	d	NA - NA	NA	NA
s40954 deg-gam	a	57162.991 - 57187.899	-0.16176	0.53392	b	57294.224 - 57346.103	-0.17353	0.51936	c	57408.13 - 57426.04	0.52727	0.10013	d	NA - NA	NA	NA
s40954 mag-deg	a	57162.991 - 57187.899	-0.19853	0.44347	b	57294.224 - 57346.103	0.00882	0.97815	c	57408.13 - 57426.04	-0.30000	0.37107	d	NA - NA	NA	NA
3c120 mag-gam	a	56937.078 - 57086.854	0.04000	0.32800	b	57231.23 - 57345.094	0.04000	0.32800	c	57386.942 - 57430.908	-0.13200	0.81400	d	NA - NA	NA	NA
3c120 deg-gam	a	56937.078 - 57086.854	-0.08000	0.61100	b	57231.23 - 57345.094	-0.08000	0.61100	c	57386.942 - 57430.908	-0.00300	0.02600	d	NA - NA	NA	NA
3c120 mag-deg	a	56937.078 - 57086.854	-0.07308	0.72787	b	57231.23 - 57345.094	-0.02854	0.86288	c	57386.942 - 57430.908	0.09100	0.63700	d	NA - NA	NA	NA

Table 4.17: Table of correlation values for the parameters in the blue camera as shown.

Source	Season	MJD range	ρ	p value	Season	MJD range	ρ	p value	Season	MJD range	ρ	p value	Season	MJD range	ρ	p value
3c66a mag-gam	a	56825.208 - 57097.865	0.13286	0.20422	b	57206.208 - 57406.978	0.56276	0.00000	c	NA - NA	NA	NA	d	NA - NA	NA	NA
3c66a deg-gam	a	56825.208 - 57097.865	-0.20755	0.07816	b	57206.208 - 57406.978	-0.21025	0.06305	c	NA - NA	NA	NA	d	NA - NA	NA	NA
3c66a mag-deg	a	56825.208 - 57097.865	-0.14285	0.22742	b	57206.208 - 57406.978	-0.54469	0.00000	c	NA - NA	NA	NA	d	NA - NA	NA	NA
3c279 mag-gam	a	56268.281 - 56435.943	-0.01326	0.89199	b	56656.277 - 56820.969	0.26923	0.37330	c	56995.27 - 57208.895	0.00395	0.97775	d	57386.176 - 57433.148	0.07544	0.75917
3c279 deg-gam	a	56268.281 - 56435.943	0.17967	0.17672	b	56656.277 - 56820.969	-0.16667	0.70332	c	56995.27 - 57208.895	-0.17984	0.40983	d	57386.176 - 57433.148	0.03529	0.89972
3c279 mag-deg	a	56268.281 - 56435.943	0.20367	0.12501	b	56656.277 - 56820.969	-0.61905	0.11498	c	56995.27 - 57208.895	0.17787	0.41507	d	57386.176 - 57433.148	0.17059	0.52660
pks1510 mag-gam	a	56288.285 - 56493.972	0.41429	0.06309	b	56661.283 - 56884.905	0.70145	0.00001	c	57019.294 - 57243.926	0.68205	0.00000	d	57386.277 - 57541.938	-0.01970	0.92127
pks1510 deg-gam	a	56288.285 - 56493.972	-0.32508	0.18789	b	56661.283 - 56884.905	0.39740	0.02064	c	57019.294 - 57243.926	-0.13366	0.31196	d	57386.277 - 57541.938	0.49145	0.01001
pks1510 mag-deg	a	56288.285 - 56493.972	-0.12074	0.63252	b	56661.283 - 56884.905	0.10863	0.53941	c	57019.294 - 57243.926	-0.02484	0.85158	d	57386.277 - 57541.938	0.23504	0.23690
oj287 mag-gam	a	57005.122 - 57160.938	-0.54785	0.00015	b	57359.153 - 57531.872	-0.05923	0.36371	c	NA - NA	NA	NA	d	NA - NA	NA	NA
oj287 deg-gam	a	57005.122 - 57160.938	0.16589	0.28082	b	57359.153 - 57531.872	-0.16813	0.00958	c	NA - NA	NA	NA	d	NA - NA	NA	NA
oj287 mag-deg	a	57005.122 - 57160.938	-0.30247	0.04640	b	57359.153 - 57531.872	0.35945	0.00000	c	NA - NA	NA	NA	d	NA - NA	NA	NA
s50716 mag-gam	a	56661.027 - 56787.887	0.32435	0.12221	b	56886.233 - 57168.892	0.62985	0.00000	c	57250.238 - 57413.033	0.70247	0.00000	d	NA - NA	NA	NA
s50716 deg-gam	a	56661.027 - 56787.887	0.16783	0.60373	b	56886.233 - 57168.892	0.04591	0.64799	c	57250.238 - 57413.033	-0.41263	0.00312	d	NA - NA	NA	NA
s50716 mag-deg	a	56661.027 - 56787.887	0.29371	0.35433	b	56886.233 - 57168.892	-0.00911	0.92788	c	57250.238 - 57413.033	0.02204	0.87905	d	NA - NA	NA	NA
BL Lac mag-gam	a	56393.242 - 56501.086	0.80769	0.00142	b	56758.24 - 57026.824	0.53562	0.00000	c	57110.247 - 57258.072	0.46784	0.00000	d	NA - NA	NA	NA
BL Lac deg-gam	a	56393.242 - 56501.086	-0.26374	0.38349	b	56758.24 - 57026.824	-0.18417	0.03681	c	57110.247 - 57258.072	0.26330	0.00117	d	NA - NA	NA	NA
BL Lac mag-deg	a	56393.242 - 56501.086	-0.45604	0.11975	b	56758.24 - 57026.824	-0.08104	0.36079	c	57110.247 - 57258.072	-0.04047	0.62256	d	NA - NA	NA	NA
mrk421 mag-gam	a	56226.2550115 - 56479.8890625	0.49000	0.00000	b	56585.2418402 - 56815.9689236	0.32300	0.97100	c	56945.2481134 - 57185.9647569	-0.07100	0.55000	d	57321.2585069 - 57398.0890972	0.41100	0.99000
mrk421 deg-gam	a	56226.2550115 - 56479.8890625	0.26400	0.00100	b	56585.2418402 - 56815.9689236	-0.08060	0.43100	c	56945.2481134 - 57185.9647569	-0.00700	0.06300	d	57321.2585069 - 57398.0890972	-0.12700	0.55900
mrk421 mag-deg	a	56226.2550115 - 56479.8890625	-0.03000	0.71700	b	56585.2418402 - 56815.9689236	0.03000	0.15900	c	56945.2481134 - 57185.9647569	0.09000	0.66200	d	57321.2585069 - 57398.0890972	-0.03000	0.14600
mrk180 mag-gam	a	56275.255 - 56464.979	0.04000	0.32800	b	56650.116 - 56845.931	0.04000	0.32800	c	56856.884 - 57239.876	0.04000	0.32800	d	57386.047 - 57427.023	-0.10800	0.54400
mrk180 deg-gam	a	56275.255 - 56464.979	-0.08000	0.61100	b	56650.116 - 56845.931	-0.08000	0.61100	c	56856.884 - 57239.876	-0.08000	0.61100	d	57386.047 - 57427.023	0.09300	0.48100
mrk180 mag-deg	a	56275.255 - 56464.979	-0.01883	0.90948	b	56650.116 - 56845.931	0.05495	0.85568	c	56856.884 - 57239.876	0.31333	0.02714	d	57386.047 - 57427.023	0.23923	0.24830
mrk501 mag-gam	a	56487.895 - 56884.052	-0.01326	0.89199	b	NA - NA	0.08200	0.31400	c	NA - NA	NA	NA	d	NA - NA	NA	NA
mrk501 deg-gam	a	56487.895 - 56884.052	0.17967	0.17672	b	NA - NA	-0.58700	0.99900	c	NA - NA	NA	NA	d	NA - NA	NA	NA
mrk501 mag-deg	a	56487.895 - 56884.052	0.20367	0.12501	b	NA - NA	-0.17400	0.61600	c	NA - NA	NA	NA	d	NA - NA	NA	NA
on231 mag-gam	a	57386.102 - 57454.065	0.41429	0.06309	b	NA - NA	0.08200	0.31400	c	NA - NA	NA	NA	d	NA - NA	NA	NA
on231 deg-gam	a	57386.102 - 57454.065	-0.32508	0.18789	b	NA - NA	-0.58700	0.99900	c	NA - NA	NA	NA	d	NA - NA	NA	NA
on231 mag-deg	a	57386.102 - 57454.065	-0.12074	0.63252	b	NA - NA	-0.17400	0.61600	c	NA - NA	NA	NA	d	NA - NA	NA	NA
pg1553 mag-gam	a	56285.286 - 56495.05	-0.01970	0.92127	b	56651.289 - 56913.851	0.46966	0.00008	c	57016.284 - 57276.875	0.69195	0.00000	d	57386.276 - 57452.273	-0.80000	0.01383
pg1553 deg-gam	a	56285.286 - 56495.05	0.49145	0.01001	b	56651.289 - 56913.851	0.24961	0.04520	c	57016.284 - 57276.875	0.33331	0.00169	d	57386.276 - 57452.273	-0.30952	0.46181
pg1553 mag-deg	a	56285.286 - 56495.05	0.23504	0.23690	b	56651.289 - 56913.851	0.11503	0.36063	c	57016.284 - 57276.875	0.15331	0.15602	d	57386.276 - 57452.273	0.42857	0.29921
pks1222 mag-gam	a	56268.279729 - 56464.986273	0.46784	0.00000	b	56651.232878 - 56845.945352	-0.32500	0.23698	c	57047.149809 - 57208.893548	-0.01818	0.93929	d	57397.21779 - 57427.20169	0.40000	0.75000
pks1222 deg-gam	a	56268.279729 - 56464.986273	0.26530	0.00117	b	56651.232878 - 56845.945352	-0.09286	0.74345	c	57047.149809 - 57208.893548	0.47662	0.03036	d	57397.21779 - 57427.20169	0.40000	0.75000
pks1222 mag-deg	a	56268.279729 - 56464.986273	0.23929	0.38923	b	56651.232878 - 56845.945352	0.12500	0.65752	c	57047.149809 - 57208.893548	0.16623	0.46972	d	57397.21779 - 57427.20169	-0.60000	0.41667
1ES1011 mag-gam	a	56268.254 - 56434.016	0.70247	0.00000	b	56650.127 - 56821.944	-0.17448	0.43565	c	56930.245 - 57182.925	0.44688	0.00328	d	57296.254 - 57454.025	-0.52941	0.03728
1ES1011 deg-gam	a	56268.254 - 56434.016	-0.41263	0.00312	b	56650.127 - 56821.944	0.32747	0.25296	c	56930.245 - 57182.925	0.07836	0.62075	d	57296.254 - 57454.025	-0.25000	0.34913
1ES1011 mag-deg	a	56268.254 - 56434.016	0.02204	0.87905	b	56650.127 - 56821.944	0.04176	0.89152	c	56930.245 - 57182.925	0.03071	0.84663	d	57296.254 - 57454.025	0.05588	0.83930
1ES1218 mag-gam	a	56268.274 - 56433.045	-0.05923	0.36371	b	56679.052 - 56845.953	0.16435	0.44110	c	56965.253 - 57158.932	-0.20183	0.27622	d	57347.278 - 57421.185	0.72304	0.00149
1ES1218 deg-gam	a	56268.274 - 56433.045	-0.16813	0.00958	b	56679.052 - 56845.953	-0.47218	0.03709	c	56965.253 - 57158.932	0.10154	0.62037	d	57347.278 - 57421.185	-0.17143	0.54061
1ES1218 mag-deg	a	56268.274 - 56433.045	0.35945	0.00000	b	56679.052 - 56845.953	-0.22256	0.34403	c	56965.253 - 57158.932	0.25197	0.21347	d	57347.278 - 57421.185	-0.32500	0.23698
1ES1426 mag-gam	a	57037.266 - 57276.88	-0.18800	0.68900	b	57386.178 - 57427.254	0.08200	0.31400	c	NA - NA	NA	NA	d	NA - NA	NA	NA
1ES1426 deg-gam	a	57037.266 - 57276.88			b	57386.178 - 57427.254	-0.58700	0.99900	c	NA - NA	NA	NA	d	NA - NA	NA	NA
1ES1426 mag-deg	a	57037.266 - 57276.88	-0.12353	0.42869	b	57386.178 - 57427.254	0.23929	0.38923	c	NA - NA	NA	NA	d	NA - NA	NA	NA
IC310 mag-gam	a	57036.863 - 57097.86	0.30000	0.37107	b	57206.209 - 57391.908	0.30232	0.01123	c	NA - NA	NA	NA	d	NA - NA	NA	NA
IC310 deg-gam	a	57036.863 - 57097.86	0.44545	0.17279	b	57206.209 - 57391.908	-0.47804	0.00004	c	NA - NA	NA	NA	d	NA - NA	NA	NA
IC310 mag-deg	a	57036.863 - 57097.86	0.12727	0.71379	b	57206.209 - 57391.908	-0.56966	0.00000	c	NA - NA	NA	NA	d	NA - NA	NA	NA
pks0502 mag-gam	a	56887.219 - 56930.128	0.56044	0.00277	b	57269.153 - 57332.105	0.82500	0.00022	c	57390.956 - 57427.923	-0.16667	0.70332	d	NA - NA	NA	NA
pks0502 deg-gam	a	56887.219 - 56930.128	0.46462	0.02034	b	57269.153 - 57332.105	-0.18214	0.51506	c	57390.956 - 57427.923	0.00000	1.00000	d	NA - NA	NA	NA
pks0502 mag-deg	a	56887.219 - 56930.128	0.46923	0.01900	b	57269.153 - 57332.105	-0.21429	0.44203	c	57390.956 - 57427.923	-0.40476	0.32684	d	NA - NA	NA	NA
pks0736 mag-gam	a	57007.998 - 57137.87	0.52314	0.00007	b	57278.24 - 57345.228	0.71640	0.00018	c	57387.007 - 57413.024	0.80769	0.00142	d	NA - NA	NA	NA
pks0736 deg-gam	a	57007.998 - 57137.87	0.12619	0.36686	b	57278.24 - 57345.228	0.44862	0.03302	c	57387.007 - 57413.024	-0.26374	0.38349	d	NA - NA	NA	NA
pks0736 mag-deg	a	57007.998 - 57137.87	0.00564	0.96812	b	57278.24 - 57345.228	0.54150	0.00851	c	57387.007 - 57413.024	-0.45604	0.11975	d	NA - NA	NA	NA
s40954 mag-gam	a	57162.991 - 57187.899	0.37940	0.07418	b	57294.224 - 57346.103	0.48421	0.03735	c	57408.13 - 57426.04	-0.72727	0.01502	d	NA - NA	NA	NA
s40954 deg-gam	a	57162.991 - 57187.899	-0.13725	0.59863	b	57294.224 - 57346.103	-0.10526	0.66747	c	57408.13 - 57426.04	0.34545	0.29939	d	NA - NA	NA	NA
s40954 mag-deg	a	57162.991 - 57187.899	-0.20833	0.42081	b	57294.224 - 57346.103	-0.20175	0.40584	c	57408.13 - 57426.04	-0.31818	0.34135	d	NA - NA	NA	NA
3c120 mag-gam	a	56937.078 - 57086.854	0.04000	0.32800	b	57231.23 - 57345.094	0.04000	0.32800	c	57386.942 - 57430.908	-0.13200	0.81400	d	NA - NA	NA	NA
3c120 deg-gam	a	56937.078 - 57086.854	-0.08000	0.61100	b	57231.23 - 57345.094	-0.08000	0.61100	c	57386.942 - 57430.908	-0.00300	0.02600	d	NA - NA	NA	NA
3c120 mag-deg	a	56937.078 - 57086.854	0.21937	0.31305	b	57231.23 - 57345.094	-0.01883	0.90948	c	57386.942 - 57430.908	0.09100	0.63700	d	NA - NA	NA	NA

Table 4.18: Table of correlation values for the parameters in the green camera as shown.

Figure 4.72: Plots of lag values for the Ringo3 sources separated into positive and negative lags for each of the three correlations: γ-ray flux and optical magnitude, γ-ray flux and degree of polarisation and optical magnitude and degree of polarisation.

4.6 Ringo3 results

As described in the previous Chapter's conclusions, it is important to bear in mind the caveats associated with the analysis conducted in this work. The properties of the sample in this work cannot be generalised to the blazar class as a whole due to the 'hand-picked' nature of the sample. For example, the HSP sources in this work typically displayed lower polarisation maxima ($\sim$10$) than the lower-peaked subclasses. The HSP polarisation values presented in this work are not representative of the entire HSP population, which contains some sources that can be $>10\%$ polarised (Heidt & Nilsson, 2011).

From the statistical study of the general sample properties with Ringo3 data the following principal results are reported:

1. With reference to item 1 from Section 3.6, the maximum degree of polarisation

for HSP, ISP and LSP sources was still ∼40%, ∼30% and ∼10% respectively, although this is simply representative of this particular sample and that HSP sources can reach higher maximum degree of polarisation (Heidt & Nilsson, 2011). The degree of polarisation can afford information about the magnetic field within the jet, although it may be an indicator of the luminosity/activity of the accretion disk, which is known to be greater in FSRQ sources (Maraschi & Tavecchio, 2003).

2. The optical degree of polarisation and γ-ray flux continued to show no strong correlations, and with an introduced lag of ± 50 days, the correlations did not significantly improve nor suggest that there was a lag between polarisation emission and γ-ray photons. 60% of significant correlations suggested an overall weak negative correlation. Figure 4.72 shows that with an introduced lag the sources tended toward a positive correlation and peak at zero lag.

3. 70% of optical magnitude and γ-ray flux correlations were significant (i.e. p$\leq$0.05) and of these 100% show a positive correlation with $\bar{\rho} = 0.619$ (see Table 4.6). This is in agreement with the Ringo2 results and those in the literature e.g. Hovatta et al. (2014); Cohen et al. (2014). Figure 4.72 shows that the favoured correlation between optical magnitude and γ-ray flux was positive and that the strongest correlations occurred at a lag of 0 days. Negative correlations were less prevalent and did not favour a particular lag.

4. There was a weak, almost zero, positive correlation (ρ=0.03) between the optical magnitude and degree of polarisation. 8/18 sources showed a significant correlation, of which 63% had positive correlations (see Table 4.6). The introduction of a ± 50 day lag showed that the strongest correlations were at ∼0 days lag. This implies that the weak correlations found in this work are likely to be real. The weak correlations suggested that some portion of the optical magnitude and degree of polarisation are associated, as one might assume since the source

of both of these is synchrotron radiation. This result shows that whilst a small quantity of optical magnitude and polarisation are correlated, the majority come from different emitting regions.

5. The relationships between γ-ray flares and rotation events were no different to those reported in Section 3.6. The data gaps caused by poor sampling and the source being close to the sun made it difficult to establish the connection between flares and rotations because rotation behaviour may be misinterpreted.

6. The mean degree of polarisation as a percentage of the total range of polarisation was 29% lower during rotation events compared with outside rotation events. This is comparable to the Ringo2 value of 26%. The mean optical (g*) magnitude was 16% lower during rotation events compared with outside rotation events, which again is comparable to the Ringo2 period value of 17%. The mean values of the γ-ray fluxes during rotations were 10% lower than outside of rotations. This differs from the larger Ringo2 value of 41%.

7. There was no significant correlation between the number of optical rotations and the number of γ-ray flares. This is different to the Ringo2 result and shows how a long time baseline will be needed to really untangle such behaviour.

8. In the colour analysis, it was found the that using data from the same waveband on both the x- or y- axis (be it polarisation or magnitude data), introduced a false correlation due to the outlying data being present on both axes. To avoid confusion the three colours are utilised in each colour-magnitude or colour-degree of polarisation plot.

9. FSRQs PKS 1222+216, 3C279 and Mrk 501 showed the largest range in colour indices. For the b* magnitude - g* vs r* magnitude correlations, these sources, along with PKS 1510-089, had positive correlations suggesting 'redder' when brighter behaviour. The other FSRQs and the BL Lac sources showed 'bluer'

when brighter behaviour.

10. In the b* magnitude - r* magnitude vs g* magnitude correlations, two FS-RQs (PKS 1510-089 & PKS 0502+049) and one BL Lac (Mrk 501) source showed 'redder' when brighter behaviour, but other sources showed 'bluer' when brighter behaviour.

11. The g* magnitude - r* magnitude vs b* magnitude correlations showed the smallest range of colour indices, suggesting that the b* magnitude dominates the variability of the indices. There were two significant correlations, which suggests that the FSRQ sources PKS 0502+049 and 3C120 showed a 'redder' when brighter property.

12. There were few significant correlations for the polarisation colour plots (12/57 significant correlations). With the exception of the b* - g* degree vs r* degree correlation for PKS 1510-089, there were negative correlations ($-0.637 < \rho < 0$). This suggests that the degree of polarisation becomes 'redder' when it increases in overall value. This suggests that when the polarisation is high, it is dominated by redder polarisation (i.e. non-thermal synchrotron emission from the jet).

4.7 Chapter conclusions

In this chapter a detailed discussion and explanation of the Ringo3 reduction and calibration procedure was presented. The calibration of the polarimetry was outlined along with the details of the instrument and instrumental constraints. The Ringo3 data were presented and the colour properties, correlations and EVPA and flare behaviour were discussed.

It was found that the optical and γ-ray fluxes were significantly correlated, whereas the γ-ray flux and degree of polarisation, and optical magnitude and degree of polarisation

were not. This is in keeping with the analysis with the Ringo2 data in Chapter 3 and suggests that there is a single emission region for the dominant emission in these blazars. The lack of strong correlations between the γ-ray flux/optical magnitude is also apparent over the Ringo2 and Ringo3 data. This implies that the magnetic field associated with the dominant emission is not highly ordered.

In the colour analysis, many FSRQ sources showed 'redder when brighter' properties, whereas most of the BL Lac sources (where significant) showed 'bluer when brighter' properties. This implies that FSRQs are initially dominated by blue emission from the accretion disk, but when the jet is injected with energised particles the emission becomes 'redder' (i.e. non-thermal) with a greater contribution from the synchrotron component in the jet .

The 'bluer' when brighter trend in BL Lac objects can usually be explained with shock-in-jet models Zhang et al. (2015a). This behaviour may imply the presence of two components contributing to the overall emission; a variable component with a constant and relatively blue color and an underlying red component (Ikejiri et al., 2011).

We explored the degree of polarisation 'colour' properties and it was found that the polarisation was generally 'redder' when higher. This implies that high levels of polarisation are associated with a larger quantity of lower energy electrons being injected into the region.

Unlike in the Ringo2 data analysis, a positive correlation between the corrected number of optical rotations and γ-ray flares was not found in the Ringo3 data analysis. These values were subject to correction for the duty cycle, which may show that there is important information lost when there are gaps in the data.

The following chapter brings together the results from Chapters 3 and 4 and applies the results to the physical properties of blazars and blazar subclasses.

Chapter 5

Conclusion

In this chapter, the results and discussion of the previous chapters are brought together. The similarities and differences between the Ringo2 and Ringo3 results are discussed, and the colour investigation results are concluded. The observational features of rotations and flares are discussed, along with their properties throughout the Ringo2 & Ringo3 monitoring campaigns.

Interesting events in individual sources are discussed and the instrumentation and data analysis findings are summarised.

5.1   Summary of results

The data taken as part of this project are one of the largest optical photometric and polarimetric samples of γ-ray bright blazars. The Ringo3 polarisation monitoring provides the first set of truly simultaneous, multicolour, optical polarisation measurements, opening a new window for blazar study.

We found that the maximum degree of polarisation of the blazars was dependent on the location of their synchrotron peak. Those sources that have SED synchrotron

peaks at lower frequencies (LSPs), have higher maximum degree of polarisation values ($\sim$40%). Those with synchrotron peaks at higher frequencies (HSPs), have lower maximum degree of polarisation values ($\sim$10%). Although Heidt & Nilsson (2011) showed that HSP blazars can have higher levels of polarisation ($\lesssim$20%), their values are still lower than our values for LSP blazars. Our results are consistent with other monitoring programs that found the polarisation was highest in LSP blazars (Ikejiri et al., 2011).

To explain the correlation between the maximum degree of polarisation and location of the synchrotron peak, Angelakis et al. (2016) proposed that the maximum polarisation values in these sources are a result of the viewing angle of the observer with respect to the jet axis. In their simple model they assume the cause of the polarisation is a shock-in-jet scenario (i.e. compression of the magnetic field makes it appear ordered). The higher energy electrons are in a small volume close to the compressed field, and the lower energy electrons in a large volume further downstream from the shock. The higher levels of polarisation are emitted in regions close to the shock, and blazars orientated with larger viewing angles should exhibit higher levels of activity at high synchrotron frequencies (Eldar & Levinson, 2000). This can be verified by measuring viewing angles of HSP blazars using very long baseline interferometry to measure the progression of jet emission features (Hovatta et al., 2009). If HSP sources are discovered with large viewing angles and low levels of polarisation, this model could be disregarded.

In $\sim$70% of source seasons across the Ringo2 and Ringo3 period, the optical magnitude and γ-ray flux were well correlated. This is in agreement with previous studies (Marscher et al., 2010; Abdo et al., 2010a; Cohen et al., 2014; Hovatta et al., 2014). We have shown that the introduction of a time lag (-50 to +50 days) between the γ-ray and optical data does not significantly increase the strength of the correlations. This suggests that in most cases, the optical and γ-ray emission is produced, simultaneously,

at a common emission site within the jet. This is consistent with synchrotron self-Compton emission models, where synchrotron electrons upscatter the photons produced by synchrotron electrons in their vicinity (Bloom & Marscher, 1996). It is also in agreement with Leptonic models of blazar emission, where γ-rays are produced by inverse Compton scattering by synchrotron electrons or by electrons from the jet sheath or other regions close to the jet (Sikora et al., 1994). However, the strongest correlations at zero lag suggest that the γ-ray emission is not produced by distant particles, such as those outside the jet in the broad line region.

Although it has been suggested that the *maximum* degree of polarisation is correlated with the γ-ray luminosity, we found that the γ-ray flux and optical degree of polarisation are not strongly correlated (and do not improve with an introduced lag). This can be explained by a spine-sheath model and differences in alignment of the jet magnetic fields of different blazar types (Itoh et al., 2016). The same authors also found some correlations between optical magnitude and degree of polarisation, but no strong correlations. Our lack of evidence for a strong correlation between γ-ray flux and degree of polarisation implies that in the region where the synchrotron radiation is upscattered to γ-ray energies (assuming a Leptonic origin of γ-ray emission), the magnetic field is not highly ordered. Hence there is no synchronous emission of high levels of polarisation with the γ-rays. Although synchrotron radiation is emitted at the same time as γ-ray emission (as shown in the correlations between optical magnitude and γ-ray flux), this particular synchrotron radiation is associated with disordered, or low-ordered, magnetic fields.

In a similar way, we found the optical magnitude was not strongly correlated with the optical degree of polarisation. Ikejiri et al. (2011) reported that small numbers of sources in their sample of 42 blazars showed weak positive ($\sim$30% of the sample) and negative ($\sim$12% of the sample) correlations between optical flux and polarisation degree. They suggested that there may be two components to explain the observed

polarisation: a short-term variation component that has a positive correlation between the flux and polarisation degree and a more long-term component (Uemura et al., 2010; Itoh et al., 2016).

In this work, we found similar results. There were significant correlations between optical magnitude and degree of polarisation for ∼half the sources in this sample. More of these correlations were positive than negative, and the correlations were weak (mean $\rho \lesssim 0.2$). This supports the idea of a short- and long-term component, and suggests that for these sources there is no large scale ordered magnetic field in the jet. There may be areas of low ordered or disordered magnetic fields that produce weakly polarised, synchrotron radiation.

In addition to the correlation properties, another aspect explored with these data was the relationship between γ-ray flares and optical rotations. Both of these properties are crucial for exploring the magnetic field of the jet, but both suffer from ambiguity in the way they are identified and quantified. In this work the γ-ray flares were identified by their separation from an established 'baseline' of γ-ray behaviour. This in itself is difficult to define, as prior- and post-flare, the level of the baseline changes. In this work the flares were grouped as flaring 'events' due to the nature of their occurrence and the necessity of applying a universal code to all sources. This is because the flaring was interpreted as an event in the jet that may cause more than one peak in the γ-ray light curve. The code needed to agree with what was seen by eye, and also establish a numerical constraint on the flare identification process. The technique used in this work was somewhat arbitrary and provides a rough guideline for identifying flares or flaring periods. This, too, is a complicated aspect of blazar polarimetry research, as it requires an all-encompassing description of a γ-ray flare.

A similar problem exists for the electric vector position angle (EVPA). Due to the 180° ambiguity, the evolution of the EVPA needs to be established using a careful technique. In this work the EVPA evolution was traced using a code that compares the

multiple possible successive EVPA values to the current one, and picks the point with the smallest difference. In general, EVPA interpretation methods are hugely affected by the cadence of the observations. Gaps in the data can mean that an EVPA rotation is missed. Conversely, the introduction of additional data points can 'break' the EVPA rotation. This is another reason why regular and intensive sampling is necessary to explore these variable sources.

During the Ringo2 period there was a correlation between the number of γ-ray flares and the number of optical rotations (having been corrected for their duty cycle). This was not the case during the Ringo3 period (where there was almost a significant *lack* of correlation). This is not a concerning result as, although corrected for the duty cycle, the gaps in the observing program result in missing data and therefore make the complete analysis more difficult.

PKS 1222+216 (FSRQ) showed no rotations across the Ringo2 and Ringo3 periods. 3C279, however, showed rotations during the Ringo2 period, and no rotations during the Ringo3 period (with an EVPA which was very stable). This behaviour suggests that some sources go through very different polarimetric behaviour over the period of years, possibly corresponding to a combination of short term and long term differing behaviour (Uemura et al., 2010; Itoh et al., 2016). These results further cement the requirement for a long baseline of data to establish the properties of these sources.

We found that the average polarisation during EVPA rotation events is lower than in the non-rotating state. This has been reported in Blinov et al. (2016)'s analysis of a larger sample of blazars. The lower polarisation during rotations can be explained using the Zhang et al. (2015b) model. This model explains a drop in degree of polarisation during EVPA rotation events may be due to light travel time effects, with different parts of the helical magnetic field being visible to an observer during the passage of an emission feature. This property was also observed and discussed in Marscher et al. (2008); the degree of polarisation is expected to drop to a minimum during an EVPA

rotation, as the mean magnetic field in the flaring region is transverse to that at the previous emission region.

The discussion in Section 4.3 of individual source behaviour (and histories for new sources added to the sample) showed that most sources have replicable or constant behaviour across the ~8 year period covered by KVA, Ringo2 and Ringo3. Some sources, for example, PKS 1510-089, showed greater γ-ray intensity and optical flares during long EVPA rotation events (see Figure 3.23 for the Ringo2 light curve and Figure 4.35 for the Ringo3 light curve). PKS 1510-089 also showed two particular episodes of γ-ray flaring that preceded an EVPA rotation (see Figure 4.34). These flares had similar γ-ray intensities but occurred over different timescales (~80 days for the first occurrence, ~200 days for the second occurrence). This difference in timescale may suggest that the particles are tracing the same magnetic field structure within the jet, but with different bulk motions of the emitting region. A longer baseline of observations for this source will allow the exploration of this recurrence.

The combination of multicolour photometry and polarimetry presented in this work can, in principle, allow the separation of emission from the host galaxy, accretion disk or external emission regions to that from the jet. The larger the degree of polarisation, the more ordered the magnetic field is in the emitting region. The jet emission (i.e. synchrotron radiation at optical wavelengths) can be shifted toward 'redder' or 'bluer' colours as a function of brightness of the source. This suggests that the charged particles in the jet are more energetic (bluer) or less energetic (redder) with increased flux. There is also a contribution from the accretion disk, particularly in FSRQs, which are considered beamed versions of Fanaroff & Riley FR-IIs and have more powerful accretion disks (Fanaroff & Riley, 1974; Padovani & Urry, 1990, 1991; Urry et al., 1991).

In FSRQ sources, the accretion disk emission is brighter, and on occasion this blue (thermal) emission can contribute to the spectral energy distribution of the blazar when

the jet emission is weak. In this work it was a selection of FSRQ sources and Mrk 501 (a BL Lac source) that showed the largest range of colour changes. We found that these sources showed 'redder' when brighter behaviour. This property, particularly for the FSRQs, suggests that the source is initially dominated by blue emission from the accretion disk, but when the jet is injected with energised particles the emission becomes 'redder' (i.e. non-thermal), with a greater contribution from the synchrotron component in the jet (Gaur et al., 2012).

The 'bluer' (BL Lacs) and 'redder' (FSRQs) when brighter magnitude properties found in this work are similar to those reported by Zhang et al. (2015a) and Ikejiri et al. (2011). Unlike other polarisation campaigns, with Ringo3 we were able to explore how the polarisation 'colour' changes with polarisation itself and with optical magnitude. There were no strong correlations between the magnitude and the polarisation 'colour', however, there were 'redder' when higher polarisation correlations, which suggests that the higher levels of polarisation are associated with larger numbers of lower energy electrons being injected, rather than the more obvious assumption that flares are associated with higher energy electron injections.

5.2 A consistent model of the γ-ray loud blazar jet

Detailed modelling of the physics of the relativistic blazar jet is beyond the scope of this work, however, by combining our results, and interpretation of these results, in terms of the published models detailed in Section 5.1, we have constructed a self-consistent model of the structures within the relativistic jet, which can be summarised as:

1. The strong, positive correlations between optical magnitude and γ-ray flux and the lag analysis performed in this work support the model of a single site for the

main γ-ray and optical emission that is located close to the base of the jet.

2. The weak correlations between optical degree of polarisation and optical magnitude/γ-ray flux indicate that the single site emission region is composed of weakly ordered magnetic fields.

3. The different maximum degree of polarisation for two synchrotron-peak-subclasses (as a function of viewing angle), is evidence that the polarisation is produced in (a) shocked region(s) within the jet, downstream of the main emission region.

4. The drop in polarisation degree during a polarisation angle rotation event indicates that the downstream magnetic field structure is either helical or compressed in a direction transverse to that of the jet.

5. The presence of possible repeated γ-ray flare temporal structures occurring across different timescales, prior to polarisation rotations, implies that the magnetic field structures are long-lasting, and the different timescales of flares are caused by the time variable bulk motions of the emission features down the jet.

6. The positive correlations between polarisation 'colour' (difference between the polarisation in two wavebands) and degree of polarisation suggest that the emission features travelling down the jet may have a higher density of lower energy electrons than the average energy of the jet.

5.3 Binary systems

During the most recent Ringo3 monitoring campaign, additional time was awarded for the monitoring of OJ287, a binary supermassive black hole (SMBH) system, which was predicted to undergo flaring activity in late 2015 (see Section 4.3.7) (Valtonen et al., 2016). Two optical flares were observed during the period of time the secondary SMBH was thought to impact the accretion disk of the primary SMBH. The optical

flare was accompanied by an increase in the γ-ray flux. During the first peak of the optical flare, the degree of polarisation was low (observations with the LT were not possible for this flare due to bad weather, however Figure 4.22 shows data taken from other optical campaigns), whereas the second peak coincided with a huge increase in the degree of polarisation to a maximum observed value for that source of 43%.

The peaks of these two flares were $\sim$20 days apart and suggest a rapid change in the system that manifests as a $\sim$30% degree of polarisation increase. Polarisation of such a high degree is attributable to non-thermal synchrotron emission, which is associated with magnetic fields; either in shocks or reconnection. During the period of the second flare, the colour - magnitude and colour - degree of polarisation correlations were comparable to those over the entire Ringo3 period, which suggests that there was no strong colour change during the intensive degree of polarisation 'flare'.

Light travel times across the accretion disk suggest that if the huge increase in polarisation is associated with the primary SMBH's jet, then that is coincidental, and the increase in polarisation is not associated with the impact of the secondary SMBH and the accretion disk. Other possible origins of the polarisation 'flare' are either the impact of the secondary SMBH on the primary accretion disk causing a shock due to magnetic reconnection or that a jet is formed close to the secondary supermassive black hole from the accretion of disk material during its approach (Pihajoki, 2016, e.g.). If a jet is formed, the degree of polarisation 'flare' is caused by the jet crossing the line of sight of the observer. The polarisation measurements taken with Ringo3 during this campaign, and for the following months, are crucial to understanding this system and work is ongoing in this area.

5.4 Sensitivity of results to sampling

As we have discussed, regular and intensive sampling is essential for monitoring these highly variable sources. In particular, with correlation analysis of optical data and γ-ray space telescope data, much more information can be afforded about the sources' behaviours with better sampling. The difficulty comes in matching the binned data from one telescope to another.

In addition, it is also particularly important to have intensive monitoring for the electric vector position angle (EVPA), a quantity that directly reflects the angle of the electric plane (and hence the angle of the magnetic field) of the electromagnetic wave of light. The 180° ambiguity associated with this measurement calls for the highest cadence of monitoring to capture the true nature of the electric plane. Gaps in data have been shown in this work to introduce false rotations, or miss rotations (the knowledge that a rotation was present comes from the addition of data from other groups). For example, recent preliminary results from monitoring of S5 0716+714, discussed by Gopal Bhatta at the 'Blazars Through Sharp Multi-Wavelength Eyes' conference, Malaga, June 2016, show a possible $\sim$400° rotation in the period of $\sim$24 hours (made possible by the collaboration of telescopes in Europe and America). Without intra-nightly monitoring (on this occasion during a γ-ray flare) this behaviour could not be detected.

In addition, as has been shown in Figure 3.1, data from the same event can be interpreted differently according to the sampling. This suggests that collaborations between the blazar optical polarimetric community would be the most beneficial to the study of these sources. The community have a variety of observational facilities available which allow intensive measurements (e.g. RoboPol/Steward Observatory) and regular sampling over long periods of time (e.g. this blazar group using the LT).

5.5 Instrumentation results

Another important aspect of this project was to calibrate the Ringo3 polarimeter data reduction process, and as a result there were a variety of 'lessons learned' from extensive use of this instrument, which will be applied to future polarimeter projects. In particular, the discovery of a significant instrumental polarisation caused by the impact of a rotating polarised beam on the dichroic mirrors has led to the exploration of an alternative method of modulating the incoming polarised beam of light. Replacing the polaroid with a rotating half wave plate and beam splitter will not only increase the quantity of photons hitting the detector but also reduce this scattering error (see Section 6 for more details).

The results of colour-magnitude analysis using the same waveband data on both axes, resulted in false correlations that were affected by the presence of outliers in both waveband data. This will be borne in mind for future multicolour polarimeter projects.

5.6 Chapter conclusions

This chapter presented the conclusions of this work; the comparison between the Ringo2 and Ringo3 results (including the trends within subclasses and the analysis of flares and rotations), the need for well sampled data with a regular cadence and presenting the limitations of the current polarimeter design and the colour analysis findings. In the next chapter the future work for this project will be presented.

Chapter 6

Future Work

In this final chapter the future avenues for this project are discussed. These include the design for a Ringo3 successor, MOPTOP, and finally concludes with a discussion of the future sources and science that could lead to a greater understanding of the jets of blazars.

6.1 MOPTOP

The following section details the MOPTOP design and specifics. This was submitted in an application for Royal Society Funding (Paul Instrument Fund) but was unfortunately unsuccessful. The information was presented in an SPIE paper (Jermak et al., 2016). Another application was submitted for the STFC PRD scheme in Summer 2016, in collaboration with Professor Iain Steele, and the outcome is awaited. The design was conceived in discussions initiated by myself, prompted by my findings from reducing and calibrating Ringo3 data. The full optical design itself was the work of Iain Steele.

Presented is the design and science case for the Liverpool Telescope's fourth-generation polarimeter; MOPTOP: a Multicolour OPTimised Optical Polarimeter, which is opti-

mised for sensitivity and bi-colour observations. We introduce an optimised polarimeter that is, as far as possible, limited only by the photon counting efficiency of the detectors. Using a combination of CMOS cameras, a continuously rotating half-wave plate and a wire grid polarising beamsplitter, we can accurately measure the polarisation of sources to $\sim 1\%$ at $\sim$19th magnitude in 10 minutes on a 2 metre telescope. For brighter sources we anticipate much lower systematics ($\lesssim 0.1\%$) than our current polarimeter. The design also gives the ability to measure polarisation and photometric variability on timescales as short as a few seconds. Overall the instrument will allow accurate measurements of the intra-nightly variability of the polarisation of sources such as gamma-ray bursts (GRBs) and blazars, allowing the constraint of magnetic field models, revealing more information about the formation, ejection and collimation of jets.

6.2 Science Case

The emerging importance of time domain astrophysics was recognised with the 2012 Royal Society meeting 'New windows on transients across the universe' and the subsequent meeting at the Kavli centre on "Interpreting signals from astrophysical transient experiments". Linear polarisation is now taking a leading role as a key diagnostic of physical conditions (for example magnetic field strength and geometry and relativistic plasma dynamics) in such transient sources as blazars, active galactic nuclei, X-ray binaries and GRBs. As an example, use of polarimetry as a diagnostic tool in time domain programmes has increased by a factor 5 on the Liverpool Telescope over the period 2012–2015. In all of these high energy sources, polarisation allows astronomers to probe the physical conditions at spatial scales that will never be accessible to direct imaging observations. For example, the Ringo2 polarimeter was used to make the first ever detections of polarisation in GRB ejecta emission (Steele et al., 2009) and its time

evolution (Mundell et al., 2013). Ringo2 and Ringo3 have also been used for leading programmes in blazar variability (Jermak et al., 2016). Ringo3 has also made the first high precision ($\pm 2°$) measurements of the inclination angle of the disk in a high mass X-ray binary (Slowikowska et al., 2016 in prep.).

For solar system sources such as asteroids and comets, the most important feature of a polarimeter is than it can measure low degrees of polarisation to an excellent accuracy (i.e. it is free from systematic errors). For comets, accurately measuring the polarisation strength can map the structure of a comet from the solar light scattered by dust particles in the coma. The linear polarisation depends on the intrinsic properties of the dust particles (their size, structure and composition) and also on their spatial distribution. The wider views of polarised light in the coma provide a study of the dust population distribution not available to the close-lying or in-situ measurements found by spacecraft such as the ESA Rosetta mission. Scattering is strongly wavelength dependent, making a multi-colour approach important. Similarly for the flood of new asteroids (many 10s per day) being discovered by the ESA Gaia Mission, polarimetric measurements at different phase angles can give the first measurements of the distribution of geometric albedo and surface roughness in large sample asteroid populations (Belskaya & Krugly, 2014, Proc. Gaia FUN SSO Workshop, 103).

A particular challenge presented by the GRB and blazar sources is the short timescales associated with them. For GRBs the early optical afterglow of the fireball fades on timescales of minutes (Piran, 1999), therefore both a rapid response and an observing approach that gathers maximum information in the time available is essential. This implies the need for maximum sensitivity combined with simultaneous, multicolour capability. By following the evolution of the light curve at several wavelengths as the synchrotron frequency evolves through the optical waveband, this allows us to distinguish between forward and reverse travelling (in the co-moving frame) shocks. This is important as the reverse shock explores the magnetic field structure in the jet

and the forward shock in the ambient media into which the jet is expanding.

The contribution of different components of an active galaxy to the overall bolometric flux can vary during periods of quiescence and flaring. The structure, conditions and properties of the components cause them to emit radiation at different wavelengths and consist of thermal and/or non-thermal radiation. When studying the jets of active galactic sources that are orientated on the sky so that their jet axes are within an opening angle of $\sim 10°$ of the observer, it is not possible to resolve the jet or emitting region, so the exploration of the point source object is through the total flux which is dominated by synchrotron emission from the highly relativistic, Doppler boosted and rapidly varying jet.

Simultaneously measuring multiple sections of the optical energy distribution of blazars over long time periods allows the exploration of the spectral changes in the source which afford information about the energy of the electron-emitting synchrotron radiation, the luminosity of the accretion disk and can help study the physical properties of different blazar subclasses (which have been classified by observational properties). Degree of polarisation measurements explore the magnetic field strength within the jet and the the electric vector position angle rotations, which can be as long as $\sim 700°$ in some sources (Jermak et al., 2016; Marscher et al., 2010), explore the order of the magnetic field. Flaring activity in optical wavelength bands can help explore the relationship between emitting regions of the jet and the formation of shocks.

6.3 Lessons learned from Ringo3

Since 2006, the Liverpool Telescope group have been working on a programme of research and development in instrumentation for time domain polarimetry and have developed a series of polarimeters of increasing sensitivity and wavelength coverage and exploring different polarimetric techniques.

The current polarimeter, Ringo3, is a multicolour device fitted with dichroic mirrors that split the polarised incoming beam of light into three optical wavebands: blue-visible (350-640 nm), green (650-760 nm) and red (770-1000 nm) (Arnold et al., 2012). This allows the measurement of polarisation degree and angle in three colours simultaneously (see Chapter 2 for more details).

The combination of a rapid rotating Polaroid and two dichroic mirrors introduced an unforeseen instrumental polarisation, which cannot be characterised by studying standard sources as the instrumental polarisation varied as a function of field rotation of the telescope. Since dichroic mirrors are successfully used in other polarimeters, e.g. DIPOL-2 (Piirola et al., 2014), this non-characterisable error has been attributed to an interaction between the *strongly polarised* and *time variable output* from the Polaroid (even for an un-polarised source) and the dichroic mirror coatings.

For Ringo3, to resolve this problem, a quasi-depolarising optic was introduced to the collimator lens to disrupt the polarised signal and produce 'scrambled' light. The throughput of the DPU-25 optic (from Thorlabs) is $\sim$82-84%, depending on wavelength. Since the polarisation is measured according to the intensity of light in each rotor position, scrambling the polarisation signal after the collimator lens does not prevent the measurement of polarisation. While providing a degree of correction, there are still small systematic errors remaining due to this effect. This limits the systematic error performance of Ringo3 to $\sim 0.5\%$.

6.4 Optical Design

The concept of MOPTOP was built from the problems experienced using, and calibrating, the Ringo3 data. Driven by the blazar monitoring project, discussions were undertaken during my PhD to explore the possible design of a new, 'optimised' polarimeter.
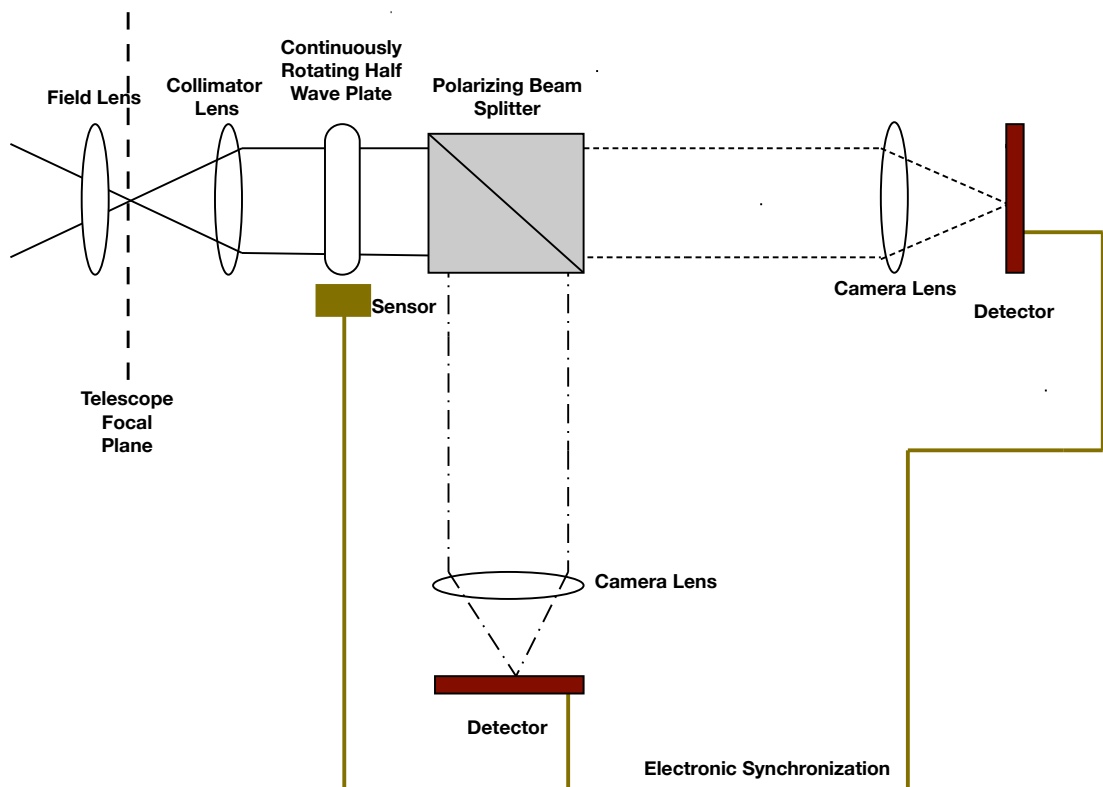
Figure 6.1: Schematic Layout of 'mini'-MOPTOP illustrating the design principle and showing the principal components. The incoming white light beam from the telescope is indicated with solid, black lines. A continuously rotating half wave plate modulates the polarisation angle of the incoming beam. One polarisation state is transmitted (dashed line) and the other reflected (dotted line) by the beam splitter. Each polarisation state is then simultaneously recorded by fast readout CMOS cameras synchronised to the wave plate angle.

The MOPTOP design aims to combine the advantages of a traditional dual-beam polarimeter in control of systematic errors, with the high time resolution of our Ringo series of designs. An outline of the design concept showing the components necessary to make polarisation measurements in a single band ('mini'-MOPTOP) is presented in Figure 6.1.

The optical design of the new polarimeter is such that the incoming beam of light enters the modulator element, a continuously revolving half-wave plate, which rotates the polarisation angle of the incoming beam. The beam then hits a wire grid polarising beam splitter, which divides the beam into the 'p' and 's' polarisation states. The two polarisation states are then imaged onto two fast readout, low noise imaging cameras, which are electronically synchronised to the wave plate angle.

The combination of a half wave plate and beamsplitter, instead of using a rotating Polaroid filter, allows the exploitation of $\sim$100% of the incoming beam of light (compared with the $\sim$50% transmission of the Ringo3 Polaroid). This immediately increases the sensitivity of the instrument.

By rotating a half wave plate by 22.5°, the polarisation angle of incident radiation can be rotated by 45°. Unlike other polarimeter designs, however, we will not step the plate between certain fixed positions (which has associated efficiency overheads) but instead rotate the wave plate continuously at $\sim$15 rpm. 16 points around the edge of the wave plate will trigger a fast proximity sensor every 22.5° of rotation. This trigger will synchronise the exposures to the fast readout cameras. Calculations show that using a continuous (as opposed to stepped) rotation has no effect on the accuracy of the measured polarisation. We have confirmed this with our simpler 8 position continuously rotating Polaroid system in Ringo2 (Steele et al., 2010). As well as increased observing efficiency, this use of rapid and continuous rotation is essential when observing rapidly variable objects. As an example, a Gamma-ray Burst optical counterpart can fade by 20% in one minute. A conventional, slowly stepped wave plate would misin-

terpret this variability as a polarisation signal of similar magnitude (since polarimetry is essentially a difference imaging technique). However, the high time resolution of MOPTOP ($\sim$1 second) means only a 0.3% error would be introduced into such measurement even when the data are subsequently temporally binned over the same one minute time period.

The beam-splitter separates the beam into 's' and 'p' polarisation states to be recorded on separate cameras. With the half wave plate in its initial position, the difference between the two images equals the Stokes Q parameter. The difference images at the subsequent half wave plate position (22.5°) equals the Stokes U parameter. The third wave plate position difference yields -Q and the fourth -U. The sum of all the images equals the Stokes I parameter. Suitable wire grid beam-splitters are available with very high throughput ($>$90%) for maximum sensitivity, a wide range of acceptance angles ($\pm$10°) for minimal field dependent instrumental depolarisation and a very high contrast ratio ($>$2000:1) over a wavelength range from 380 to 800 nm for very low overall instrumental depolarisation ($>$0.1%). As already described, by using a beam splitter in this role rather than a Polaroid we achieve double the throughput. We will also have much better control of systematic errors since our individual Stokes parameters will be formed from simultaneously obtained difference images and the rapidly alternating measurements of opposite signs of Q and U allows cancellation of offset biases and flat field errors.

It is possible to use a calcite beam splitter in place of the wire grid polariser. The calcite beam splitter has a wavelength range of (coated) $\sim$360-700 nm with a transmission of 75 - 95%, and uncoated $\sim$360-1000 nm with a transmission of 75 - 90%. A wire grid beam splitter has a range of $\sim$350-900 nm and a transmission of 40-90%.

6.4.1 CMOS Imaging Cameras

In Ringo2 we pioneered the use of fast readout, low noise detectors in a polarimeter. Such detectors have two key advantages in this application. Firstly they are able to observe rapidly varying sources at greater sensitivity. Secondly, and most importantly, the very low readout noise allows data to be taken a high frame rates ($\sim$0.1 - 1 Hz). This provides excellent temporal resolution when the source is sufficiently bright or, when the source is faint, allows temporal binning of high frame rate data without a significant read noise penalty to achieve the desired polarimetric accuracy. This gives huge dynamic range ($\sim$100000:1) and the resulting ability to observe transients of unknown and rapidly variable brightness. For Ringo2 and 3 we achieved the required low noise, fast readout using then state of the art Electron Multiplying CCD (EMCCD) technology. However due to their mode of operation EMCCDs suffer charge multiplication noise which causes a factor 2 reduction in the instrument sensitivity. For MOPTOP we will use newly available scientific CMOS (sCMOS) detectors for the first time in astronomical polarimetry. We have already carried out tests that show their readout can be synchronised electronically to the degree of precision necessary (see Steele, SPIE, 2016). sCMOS detectors maintain the rapid readout ($>$100 fps) and ultra low read noise ($<$0.9 electrons) advantages of EMCCD but add much greater sensitivity (quantum efficiency is $>$80% vs $\sim$40% for EMCCDs, because EMCCDs have a charge multiplication noise component that effectively reduces the QE by a factor 2.). In addition sCMOS detectors are available in much larger formats ($\sim$4 Mpix vs $\sim$1 Mpix from EMCCDs) allowing the full 8 arcmin telescope field of view to be sampled at optimal (Nyquist sampled) resolution.

6.5 MOPTOP

The previous polarimeters Ringo, Ringo2 and the current Ringo3 have been mounted on the Liverpool Telescope, which is the worlds largest fully robotic telescope. This is key in enabling them to responding autonomously to triggers from transient detection experiments such as the NASA Swift Satellite and the LIGO and VIRGO gravitational wave detectors. Response times for Gamma Ray Bursts are 2–3 minutes from satellite detection to our ground based optical observations, depending on the object location on the sky.

The design of MOPTOP takes our capability to a new level by meeting many ideal requirements (see below). It takes a number of already novel aspects from the Ringo series (a fast rotating element to allow high time resolution; the use of fast readout, very low noise cameras allowing a unique, post data acquisition, signal to noise ratio optimisation; the use of dichroic mirrors to provide multi-wavelength capability) and adds a unique optical dual-camera configuration to minimize systematic errors and provide the highest possible sensitivity.

We have identified the following requirements for the optimised polarimeter:

- Maximum sensitivity, such that the polarimetric accuracy obtained is dominated by the photon counting (Poisson) statistics of the light incident on the telescope.

- Very low systematic errors ($<0.1\%$) allowing measurement of low polarisation sources.

- Ability to measure a rapidly (~10 seconds) variable or fading source.

- Ability to measure all sources in the field of view without prior identification.

- Ability to measure sources over the widest possible dynamic range of photon counts and without prior knowledge of the source brightness.

- Ability to measure polarisation over a number of different wavelength ranges simultaneously.

- Be available to respond to transient events and other targets of opportunity.

- The widest possible field of view (as limited by the telescope optics).

- The best possible spatial resolution (as. limited by atmospheric effects).

While dual beam polarimeters have been built before, they have always combined the signal onto a single camera. This causes problems with source overlap and reduced sensitivity (since each object effectively receives double the background sky noise contribution compared to normal imaging). The traditional solution to this has been the use of a focal plane mask, but this reduces the field of view and means the instrument can not be used when the object localisation on the sky is poor (which is often the case for transient sources). Our dual camera design avoids these problems, providing full sensitivity with the full field of view.

Overall we anticipate the design to have four times the sensitivity of Ringo3 (a factor of two from the switch from Polaroid to beam splitting optics and a factor of two from the switch from EMCCD to sCMOS cameras). This implies a polarisation accuracy of $\sim 1\%$ should be obtainable with a 10 minute exposure at 19th magnitude. An example of how the MOPTOP design can be adapted to accommodate two sets of cameras for two colour operation is shown in Figure 6.2. An important advantage of the MOPTOP design over our previous Ringo3 polarimeters is that the polarisation angle of the incoming light to the dichroic mirrors is fixed (rather than rotating). This should eliminate the major cause of residual systematic error identified in Ringo3. This, plus the intrinsic advantage of a dual beam design in allowing differential correction of atmospheric and other time domain systematic effects, means that, for brighter objects, we anticipate the dual beam design should reduce systematic errors by a factor of 4 over Ringo3, reducing them to $\sim 0.1\%$.
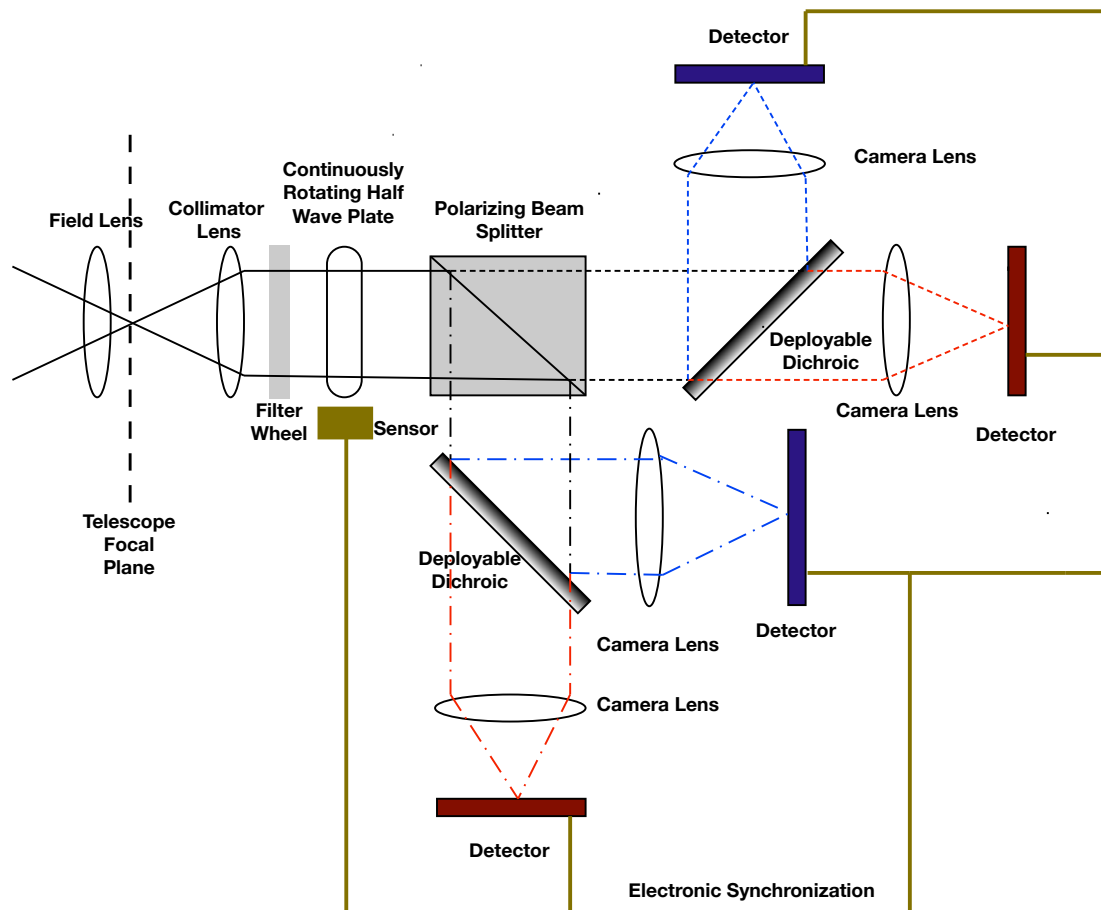
Figure 6.2: Schematic 2D rendering of a 2 camera set version of MOPTOP showing the principal components. The incoming white light beam from the telescope is indicated with solid, black lines. A continuously rotating half wave plate modulates the polarisation angle of the incoming beam. One polarisation state is transmitted (dashed line) and the other reflected (dotted line) by the beam splitter. Each polarisation state is then split by a dichroic mirror before being simultaneously recorded by fast readout CMOS cameras synchronised to the wave plate angle. Alternatively the dichroic mirrors may be removed from the beam and a specific wavelength range selected using the filter wheel.

6.6 Two vs Three band designs

The standard practice when exploring the variable spectral properties of blazars is to plot (B-V) vs V, (V-R) vs V, (R-I) vs V and (B-I) vs V using the Johnson and Cousin filters (Gaur et al., 2012). Or, depending on the wavelength, (J-R) vs J and vs R (Zhang et al., 2015a).

However, it is not widely appreciated that a 2-band approach for the study of spectral properties vs magnitude is susceptible to producing false correlations. As an example, following the same practice with our blazar sample using the (non-standard) Ringo3 optical wavebands: blue-visible 'b*' (350-640 nm), green 'g*' (650-760 nm) and red 'r*' (770-1000 nm) (Arnold et al., 2012) we found that the blazars seemed to show either a 'redder' *or* 'bluer' when brighter property depending on the magnitude or degree of polarisation used on the x axis (see Section 4.5 for full details)

This highlights the necessity to have an independent magnitude (i.e. one not contained in the colour index) on the x axis to avoid false trends in the data caused by outliers. For this reason MOPTOP's design will be extended to include at least 3 cameras.

6.7 Conclusion

We have presented how a unique combination of CMOS cameras, a continuously rotating half-wave plate and a wire grid polarising beamsplitter can be used to create a multicolour, optimised polarimeter which utilises more of the incoming light while retaining high time resolution. The throughput is calculated as follows: field & collimator lenses ∼95%, filters ∼75%, half wave plate ∼97%, beam splitter ∼70% and dichroics ∼95% giving a total throughput of ∼45%. The filter wheel is deployable and can be removed for sensitive observations.

We have begun testing the synchronisation of sCMOS cameras (see Steele, SPIE, 2016) necessary for the design. Our next step will be to do laboratory testing of the single band 'mini'-MOPTOP design before going on to build a multi-band version. To eliminate systematic errors in colour-brightness investigations we envisage the final MOPTOP design will have at least 3 wavebands.

6.7.1 Mini-MOPTOP

The development of MOPTOP will begin as an instrumentation PhD in 2017. The project aims to build a prototype MOPTOP (a mini-MOPTOP), which tests the synchronicity of the paired sCMOS cameras, both with image capture and sensitivity. The prototype will be tested in the laboratory and on sky on the Liverpool Telescope. The polarimeter will be used to make astrophysical measurements of magnetic field configurations in extragalactic time variable sources.

6.8 Future blazar work

I continue to be the PI of the blazar monitoring program. One particular scientific advantage would be to have an unbiased, statistically sound sample of blazars to do long-term monitoring of. This would be difficult to obtain observing time for using the Liverpool Telescope due to the large quantity of time required for the observations. This research is already underway with other blazar monitoring teams such as the RoboPol group, who use a specialised photopolarimeter designed specifically for the 1.3m telescope at the Skinakas Observatory (Blinov et al., 2015). The purpose of this blazar monitoring campaign is to explore these radio bright, active and variable source, and explore the relationship of γ-ray flares with polarisation properties. We continue to have access to the Fermi data, and endeavour to pursue a project aimed

at producing a 'polar' polarimeter- i.e. on that can exploit polar winters. This is an ambitious goal due to the limited choice of fair-weather locations which experience polar night, the isolation and the presence of aurora. It is a future project that will be explored. Continued observations allow the detailed study of these sources which often show variable properties on timescales of tens of years (e.g. OJ287, see Section 4.3.7).

The building of the MOPTOP instrument will allow greater sensitivity of measurements and shorter exposure times required to meet a particular SNR. This would allow more sources to be monitored in the same amount of time and with higher precision.

As part of this project we have monitored the brightest Narrow Line Seyfert1 galaxy in the northern sky, 1H 0323+342. This jetted source (detailed in the next section) is an interesting possible precursor to the blazar population and could afford information about the evolution of galaxies and AGN evolution.

6.9 Narrow-Line Seyfert 1 Galaxies

Narrow-Line Seyfert 1 (NLSy1) galaxies are an extreme form of Seyfert galaxy. Seyferts are active galaxies with spiral hosts and bright, starlike nuclei. Seyfert 1 galaxies have broad permitted lines and narrow permitted and forbidden lines. The HI Balmer lines are broader than the forbidden lines. The spectra of Seyfert 2 galaxies show permitted and forbidden narrow lines only (the electrons in the denser, broad-line region have a higher probability of being collisionally de-excited, whereas in the narrow-line regions the gas moves at lower velocities in a more rarified environment thus lowering the probability of collisions and so the electrons have a greater probability of being de-excited by forbidden transitions). The Balmer and forbidden line widths in Seyfert 2s are approximately the same size. The full widths at half maximum (FWHM) of the forbidden lines for Seyferts are 300-800 km s^{-1} and the HI lines in Seyfert 1 galaxies

are much broader ($\sim$1000-6000 km s^{-1}).

Seyfert galaxies can be classified as subclasses between Type 1 and Type 2, where the subclasses are based on the optical emission lines present in the spectra. Those subclasses closer to Type 2 (i.e. Type 1.8 and 1.9) have weaker broad-line components relative to the narrow-lines (Osterbrock, 1981). The accepted explanation for the difference in these galaxy types is the viewing angle. For Seyfert 1s it is believed that they are orientated so that the viewing angle is between the jet and the dusty torus, which means that emission from both the narrow line and broad line regions is visible. For Seyfert 2 galaxies, the viewing angle is such that the dusty torus blocks the light from the central regions: the accretion disk and the broad line region.

NLSy1s are an interesting class of Seyfert. Their forbidden lines have FWHM of $\sim$300 km s^{-1} (like Seyfert 2 galaxies) but they also have strong, featureless continua and strong emission lines from weakly ionised atoms (properties similar to Seyfert 1 galaxies). They have narrower than usual broad line region permitted lines, with the FWHM of Hβ <2000 km s^{-1} (Paliya et al., 2013a). NLSy1s also differ from the composite broad plus narrow HI spectra of the Seyfert 1.5 galaxies. It was in 1983, with the study of Markarian 359 that Osterbrock & Dahari (1983) classed sources with these properties as narrow-line Seyfert 1s. According to Goodrich (1989), the defining characteristics of a NLSy1 are : (1) the Balmer lines are slightly broader than the forbidden lines, (2) the ratio of the forbidden line [O III] (λ5007) to Hβ is <3 and (3) there are often emission lines from Fe II or higher ionisation lines.

Before the launch of the Fermi satellite, only radio galaxies and blazars were known to produce emission at gamma-ray wavelengths. However, Fermi-LAT discovered variable gamma-ray emission from a few radio loud (RL)-NLSy1s, including PMN J0948+0022 (Abdo et al., 2009c,b; Foschini et al., 2010). Although similarities between RL-NLSy1s and blazars had already been reported (Komossa et al., 2006), the discovery of gamma-ray emission was quite surprising since NLSy1s have spiral hosts

whereas radio galaxies and blazars have elliptical hosts. This brought into question the previously proposed connection between elliptical galaxies and jet formation. The combination of study of blazars and NLSy1s gives the opportunity to probe the nature of jet formation and structure by looking at two possible stages of AGN evolution, with the possibility of finding the missing link between radio-loud and radio-quiet AGN.

During this project the NLSy1 1H 0323+342 was monitored using Ringo3. A future aspect of this project will be to apply this analysis to the NLSy1 source and interpret its behaviour with respect to blazars. A collaborative project has been discussed with the University of Bologna, Italy.

6.10 Chapter summary

This final chapter has highlighted the future possibilities that this project can follow. The immediate intention is to continue the monitoring of the current sample of blazars using the Ringo3 polarimeter and, in the next LT observing semester, to apply for time on the IO:I and LOTUS instruments also.

This program has data for one NLSy1 source and also a radio galaxy, M87. Analysis of these addition sources of interest has begun or is due to begin imminently.

The application for the STFC PRD scheme is currently underway, and the 'mini-MOPTOP' project commences in 2017.

Bibliography

Abdo, A. A., Ackermann, M., Ajello, M., et al. 2009a, ApJ, 700, 597

—. 2009b, ApJ, 707, 727

—. 2009c, ApJL, 707, L142

—. 2010a, *Nature*, 463, 919

Abdo, A. A., Ackermann, M., Agudo, I., et al. 2010b, ApJ, 716, 30

Abramowski, A., Acero, F., Aharonian, F., et al. 2012, ApJ, 746, 151

—. 2013, A&A, 554, A107

Abramowski, A., Aharonian, F., Ait Benkhali, F., et al. 2015a, ArXiv e-prints,
    arXiv:1501.05087

—. 2015b, ApJ, 802, 65

Acciari, V. A., Aliu, E., Beilicke, M., et al. 2008, ApJL, 684, L73

Acciari, V. A., Aliu, E., Arlen, T., et al. 2009a, ApJL, 693, L104

—. 2009b, ApJ, 695, 1370

Ackermann, M., Asano, K., Atwood, W. B., et al. 2010, ApJ, 716, 1178

Adelman-McCarthy, J. K., & et al. 2009, VizieR Online Data Catalog, 2294, 0

Agudo, I., Jorstad, S. G., Marscher, A. P., et al. 2011, ApJL, 726, L13

Aharonian, F., Akhperjanian, A. G., Bazer-Bachi, A. R., et al. 2006, A&A, 448, L19

Aharonian, F., Akhperjanian, A. G., Anton, G., et al. 2009, A&A, 502, 749

Aharonian, F. A. 2000, NewAstronomy, 5, 377

A'Hearn, M. F., Millis, R. C., Schleicher, D. O., Osip, D. J., & Birch, P. V. 1995, Icarus, 118, 223

Ahnen, M. L., Ansoldi, S., Antonelli, L. A., et al. 2016a, A&A, 590, A24

—. 2016b, MNRAS, 459, 2286

Albert, J., Aliu, E., Anderhub, H., et al. 2006a, ApJL, 642, L119

—. 2006b, ApJL, 648, L105

—. 2007a, ApJL, 654, L119

—. 2007b, ApJL, 666, L17

—. 2007c, ApJL, 667, L21

—. 2008, ApJ, 681, 944

Aleksić, J., Anderhub, H., Antonelli, L. A., et al. 2010, A&A, 515, A76

Aleksić, J., Antonelli, L. A., Antoranz, P., et al. 2011a, ApJL, 730, L8

—. 2011b, A&A, 530, A4

Aleksić, J., Alvarez, E. A., Antonelli, L. A., et al. 2012, ApJ, 748, 46

Aleksić, J., Ansoldi, S., Antonelli, L. A., et al. 2014a, Science, 346, 1080

—. 2014b, A&A, 569, A46

—. 2014c, A&A, 567, A41

—. 2015, MNRAS, 450, 4399

Aliu, E., Anderhub, H., Antonelli, L. A., et al. 2009, ApJL, 692, L29

Anderhub, H., Antonelli, L. A., Antoranz, P., et al. 2009, ApJL, 704, L129

Andruchow, I., Cellone, S. A., Romero, G. E., Dominici, T. P., & Abraham, Z. 2003, A&A, 409, 857

Andruchow, I., Combi, J. A., Muñoz-Arjonilla, A. J., et al. 2011, A&A, 531, A38

Angel, J. R. P., & Stockman, H. S. 1980, ARA&A, 18, 321

Angelakis, E., Hovatta, T., Blinov, D., et al. 2016, MNRAS, 463, 3365

Antón, S., Browne, I. W. A., & Marchã, M. J. 2008, A&A, 490, 583

Antonucci, R. 1993, ARA&A, 31, 473

Antonucci, R. R. J., & Miller, J. S. 1985, ApJ, 297, 621

Arlen, T., Aune, T., Beilicke, M., et al. 2013, ApJ, 762, 92

Arnold, D. M., Steele, I. A., Bates, S. D., Mottram, C. J., & Smith, R. J. 2012, in SPIE Conference Series, Vol. 8446, SPIE Conference Series

Atwood, W. B., Abdo, A. A., Ackermann, M., et al. 2009, ApJ, 697, 1071

Barker, B. M., & OConnell, R. F. 1975, Physical Reviews D, 12, 329

Barnsley, R. M., Jermak, H. E., Steele, I. A., et al. 2016, Journal of Astronomical Telescopes, Instruments, and Systems, 2, 015002

Barnsley, R. M., Steele, I. A., Bates, S. D., & Mottram, C. J. 2014, in Society of Photo-Optical Instrumentation Engineers (SPIE) Conference Series, Vol. 9147, Society of Photo-Optical Instrumentation Engineers (SPIE) Conference Series, 37

Barres de Almeida, U. 2011, International Cosmic Ray Conference, 8, 79

Barthelmy, S. D. 2000, in Society of Photo-Optical Instrumentation Engineers (SPIE) Conference Series, Vol. 4140, X-Ray and Gamma-Ray Instrumentation for Astronomy XI, ed. K. A. Flanagan & O. H. Siegmund, 50–63

Beall, J. H. 2003, Chinese Journal of Astronomy and Astrophysics Supplement, 3, 373

Berdyugin, A., Piirola, V., Sadegi, S., et al. 2016, A&A, 591, A92

Bertin, E., & Arnouts, S. 1996, A&AS, 117, 393

Bicknell, G. V. 1986, ApJ, 305, 109

Bjornsson, C.-I. 1982, ApJ, 260, 855

Blandford, R. D., & Levinson, A. 1995, ApJ, 441, 79

Blandford, R. D., & Payne, D. G. 1982, MNRAS, 199, 883

Blandford, R. D., & Rees, M. J. 1978, Physica Scripta, 17, 265

Blandford, R. D., & Znajek, R. L. 1977, MNRAS, 179, 433

Błażejowski, M., Sikora, M., Moderski, R., & Madejski, G. M. 2000, ApJ, 545, 107

Blinov, D., Pavlidou, V., Papadakis, I., et al. 2015, MNRAS, 453, 1669

Blinov, D., Pavlidou, V., Papadakis, I. E., et al. 2016, MNRAS, 457, 2252

Bloom, S. D., & Marscher, A. P. 1996, ApJ, 461, 657

Böttcher, M. 2012 (Wiley-VCH)

Böttcher, M., & Dermer, C. D. 2002, ApJ, 564, 86

—. 2010, ApJ, 711, 445

Böttcher, M., Reimer, A., Sweeney, K., & Prakash, A. 2013a, ApJ, 768, 54

Böttcher, M., Reimer, A., & Zhang, H. 2013b, in European Physical Journal Web of Conferences, Vol. 61, European Physical Journal Web of Conferences, 5003

Bradbury, S. M., Deckers, T., Petry, D., et al. 1997, A&A, 320, L5

Bradt, H. 2014, Astrophysics Processes (Cambridge University Press)

Bridle, A. H., & Perley, R. A. 1984, ARA&A, 22, 319

Browne, I. W. A. 1983, MNRAS, 204, 23P

Burbidge, E. M., & Kinman, T. D. 1966, ApJ, 145, 654

Burbidge, E. M., & Rosenberg, F. D. 1965, ApJ, 142, 1673

Burbidge, G., & Hewitt, A. 1992, in Variability of Blazars, ed. E. Valtaoja & M. Valtonen, 4

Cano, Z. 2012, PhD thesis, Liverpool John Moores University, arXiv:1208.0307

Cardamone, C., Schawinski, K., Sarzi, M., et al. 2009, MNRAS, 399, 1191

Casadio, C., Gómez, J. L., Jorstad, S. G., et al. 2015a, ApJ, 813, 51

Casadio, C., Gómez, J. L., Grandi, P., et al. 2015b, ApJ, 808, 162

Cavaliere, A., & D'Elia, V. 2002, ApJ, 571, 226

Chavero, C., Gómez, M., Whitney, B. A., & Saffe, C. 2006, A&A, 452, 921

Clarke, D., & Neumayer, D. 2002, A&A, 383, 360

Cohen, D. P., Romani, R. W., Filippenko, A. V., et al. 2014, ApJ, 797, 137

Collin, S., & Kawaguchi, T. 2004, A&A, 426, 797

Costamante, L., Ghisellini, G., Giommi, P., et al. 2001, A&A, 371, 512

Cucchiara, A., Cenko, S. B., Bloom, J. S., et al. 2011, ApJ, 743, 154

D'Ammando, F., & Orienti, M. 2014, The Astronomer's Telegram, 6731

D'Ammando, F., Orienti, M., Finke, J., Larsson, J., & Giroletti, M. 2013, in European Physical Journal Web of Conferences, Vol. 61, European Physical Journal Web of Conferences, 5006

Damour, T., & Schafer, G. 1988, Nuovo Cimento B Serie, 101, 127

Danforth, C. W., Keeney, B. A., Stocke, J. T., Shull, J. M., & Yao, Y. 2010, ApJ, 720, 976

Danforth, C. W., Nalewajko, K., France, K., & Keeney, B. A. 2013, ApJ, 764, 57

D'arcangelo, F. D., Marscher, A. P., Jorstad, S. G., et al. 2009, ApJ, 697, 985

de Almeida, U. B. 2012, International Journal of Modern Physics Conference Series, 8, 178

de Ugarte Postigo, A., Fatkhullin, T. A., Jóhannesson, G., et al. 2007, A&A, 462, L57

de Vaucouleurs, G., de Vaucouleurs, A., Corwin, Jr., H. G., et al. 1991, Third Reference Catalogue of Bright Galaxies. Volume I: Explanations and references. Volume II: Data for galaxies between 0^h and 12^h. Volume III: Data for galaxies between 12^h and 24^h.

De Young, D. S. 1991, Science, 252, 389

Dermer, C. D., & Schlickeiser, R. 1993, ApJ, 416, 458

Dermer, C. D., Schlickeiser, R., & Mastichiadis, A. 1992, A&A, 256, L27

Dermer, C. D., Sturner, S. J., & Schlickeiser, R. 1997, ApJS, 109, 103

Doi, A., Nagai, H., Asada, K., et al. 2006, PASJ, 58, 829

Draper, W., P., Gray, N., Berry, D. S., & Taylor, M. 2012, Starlink User Note, 214

Drenkhahn, G., & Spruit, H. C. 2002, A&A, 391, 1141

Drinkwater, M. J., Webster, R. L., Francis, P. J., et al. 1997, MNRAS, 284, 85

Eggen, J., Miller, H. R., & Maune, J. 2011, in Narrow-Line Seyfert 1 Galaxies and their Place in the Universe

Eggen, J. R., Miller, H. R., & Maune, J. D. 2013, ApJ, 773, 85

Eisenacher Glawion, D., Sitarek, J., Mannheim, K., et al. 2015, ArXiv e-prints, arXiv:1508.05031

Eldar, A., & Levinson, A. 2000, MNRAS, 314, 641

Elder, F. R., Gurewitsch, A. M., Langmuir, R. V., & Pollock, H. C. 1947, Physical Review, 71, 829

Falco, E. E., Kurtz, M. J., Geller, M. J., et al. 1999, PASP, 111, 438

Falcone, A. D., Barthelmy, S. D., Burrows, D. N., et al. 2006, GRB Coordinates Network, 4966, 1

Fan, Y. Z., Wei, D. M., & Wang, C. F. 2004, A&A, 424, 477

Fanaroff, B. L., & Riley, J. M. 1974, MNRAS, 167, 31P

Ferreira, J., Dougados, C., & Cabrit, S. 2006, A&A, 453, 785

Foschini, L. 2009, Advances in Space Research, 43, 1036

—. 2013a, Nuclei of Seyfert Galaxies and QSOs, arXiv:1301.5785

—. 2013b, International Journal of Modern Physics: Conference Series, arXiv:1310.5822

Foschini, L., Fermi/Lat Collaboration, Ghisellini, G., et al. 2010, in Astronomical Society of the Pacific Conference Series, Vol. 427, Accretion and Ejection in AGN: a Global View, ed. L. Maraschi, G. Ghisellini, R. Della Ceca, & F. Tavecchio, 243–248

Foschini, L., Maraschi, L., Tavecchio, F., et al. 2009, Advances in Space Research, 43, 889

Fossati, G., Maraschi, L., Celotti, A., Comastri, A., & Ghisellini, G. 1998, MNRAS, 299, 433

Fragile, P. C. 2008, in Microquasars and Beyond, 39

Frail, D. A., Kulkarni, S. R., Sari, R., et al. 2001, ApJL, 562, L55

Fruchter, A. S., Thorsett, S. E., Metzger, M. R., et al. 1999, ApJL, 519, L13

Furniss, A., Fumagalli, M., Danforth, C., Williams, D. A., & Prochaska, J. X. 2013, ApJ, 766, 35

Gabuzda, D. C., Cawthorne, T. V., Roberts, D. H., & Wardle, J. F. C. 1992, ApJ, 388, 40

Gaskell, C. M. 1982, PASP, 94, 891

Gaur, H., Gupta, A. C., Strigachev, A., et al. 2012, MNRAS, 425, 3002

Gehrels, N., Chincarini, G., Giommi, P., et al. 2004, ApJ, 611, 1005

Georganopoulos, M., & Kazanas, D. 2003, ApJL, 594, L27

Georganopoulos, M., & Marscher, A. P. 1998, ApJ, 506, 621

Ghisellini, G., & Lazzati, D. 1999, MNRAS, 309, L7

Ghisellini, G., & Madau, P. 1996, MNRAS, 280, 67

Ghisellini, G., & Tavecchio, F. 2008, MNRAS, 386, L28

Ghisellini, G., Tavecchio, F., Foschini, L., & Ghirlanda, G. 2011, MNRAS, 414, 2674

Glassmeier, K.-H., Boehnhardt, H., Koschny, D., Kührt, E., & Richter, I. 2007, School Science Review, 128, 1

Gómez, J.-L., Marscher, A. P., Alberdi, A., Jorstad, S. G., & Agudo, I. 2001, ApJL, 561, L161

Gómez, J.-L., Marscher, A. P., Alberdi, A., Jorstad, S. G., & García-Miró, C. 2000, Science, 289, 2317

Gómez, J. L., Roca-Sogorb, M., Agudo, I., Marscher, A. P., & Jorstad, S. G. 2011, ApJ, 733, 11

Goodrich, R. W. 1989, ApJ, 342, 224

Greiner, J., Klose, S., Reinsch, K., et al. 2003, *Nature*, 426, 157

Grupe, D., & Mathur, S. 2004, ApJL, 606, L41

Gruzinov, A., & Waxman, E. 1999, ApJ, 511, 852

Guidorzi, C., Monfardini, A., Gomboc, A., et al. 2006, PASP, 118, 288

Gupta, A. C., Agarwal, A., Bhagwan, J., et al. 2016, MNRAS, 458, 1127

Hagen-Thorn, V. A., Larionov, V. M., Jorstad, S. G., & Larionova, E. G. 2002a, AJ, 124, 3031

Hagen-Thorn, V. A., Larionova, E. G., Jorstad, S. G., Björnsson, C.-I., & Larionov, V. M. 2002b, A&A, 385, 55

Hagen-Torn, V. A., Marchenko, S. G., Smekhacheva, R. I., & Iakovleva, V. A. 1983, Astrofizika, 19, 199

Harrison, R., & Kobayashi, S. 2013, ApJ, 772, 101

Hartman, R. C., Bertsch, D. L., Fichtel, C. E., et al. 1992, ApJL, 385, L1

Hartman, R. C., Bertsch, D. L., Bloom, S. D., et al. 1999, ApJS, 123, 79

Hartman, R. C., Böttcher, M., Aldering, G., et al. 2001, ApJ, 553, 683

Heidt, J., & Nilsson, K. 2011, A&A, 529, A162

Ho, L. C., & Kim, M. 2009, ApJS, 184, 398

Hoffmeister, C. 1929, Astronomische Nachrichten, 236, 233

Holmes, P. A., Brand, P. W. J. L., Impey, C. D., et al. 1984, MNRAS, 211, 497

Holt, S. S., Neff, S. G., & Urry, C. M., eds. 1992, American Institute of Physics Conference Series, Vol. 254, Testing the AGN paradigm; Proceedings of the 2nd Annual Topical Astrophysics Conference, Univ. of Maryland, College Park, Oct. 14-16, 1991

Horan, D., Badran, H. M., Bond, I. H., et al. 2002, ApJ, 571, 753

Hovatta, T., Valtaoja, E., Tornikoski, M., & Lähteenmäki, A. 2009, A&A, 494, 527

Hovatta, T., Pavlidou, V., King, O. G., et al. 2014, MNRAS, 439, 690

Hudec, R. 2011, Journal of Astrophysics and Astronomy, 32, 91

Hudec, R., Bašta, M., Pihajoki, P., & Valtonen, M. 2013, A&A, 559, A20

Ikejiri, Y., Uemura, M., Sasada, M., et al. 2011, PASJ, 63, 639

Impey, C. D., Bychkov, V., Tapia, S., Gnedin, Y., & Pustilnik, S. 2000, AJ, 119, 1542

Impey, C. D., & Tapia, S. 1988, ApJ, 333, 666

—. 1990, ApJ, 354, 124

Itoh, R., Fukazawa, Y., Chiang, J., et al. 2013, PASJ, 65, 18

Itoh, R., Nalewajko, K., Fukazawa, Y., et al. 2016, ArXiv e-prints, arXiv:1610.04313

Jaffe, W., Meisenheimer, K., Röttgering, H. J. A., et al. 2004, *Nature*, 429, 47

Jannuzi, B. T., Smith, P. S., & Elston, R. 1994, ApJ, 428, 130

Jermak, H., Steele, I. A., & Smith, R. J. 2016, MOPTOP: a multi-colour optimised optical polarimeter, doi:10.1117/12.2232324

Jermak, H., Steele, I. A., Lindfors, E., et al. 2016, ArXiv e-prints, arXiv:1608.08860

Jones, T. W., O'dell, S. L., & Stein, W. A. 1974, ApJ, 188, 353

Jones, T. W., Rudnick, L., Aller, H. D., et al. 1985, ApJ, 290, 627

Jorstad, S. G., Marscher, A. P., Stevens, J. A., et al. 2007, AJ, 134, 799

Joshi, U. C., Baliyan, K. S., Ganesh, S., et al. 2000, Bulletin of the Astronomical Society of India, 28, 409

Kadler, M., Eisenacher, D., Ros, E., et al. 2012, A&A, 538, L1

Kellermann, K. I., Sramek, R., Schmidt, M., Shaffer, D. B., & Green, R. 1989, AJ, 98, 1195

Kennett, M., & Melrose, D. 1998, PASA, 15, 211

Kerr, R. P. 1963, Physical Review Letters, 11, 237

Khachikian, E. Y., & Weedman, D. W. 1974, ApJ, 192, 581

Kiehlmann, S., Savolainen, T., Jorstad, S. G., et al. 2013, in European Physical Journal Web of Conferences, Vol. 61, European Physical Journal Web of Conferences, 6003

Kikuchi, S., Mikami, Y., Inoue, M., Tabara, H., & Kato, T. 1988, A&A, 190, L8

Kobayashi, S. 2000, ApJ, 545, 807

Kobayashi, S., Piran, T., & Sari, R. 1999, ApJ, 513, 669

Komossa, S., Voges, W., Xu, D., et al. 2006, AJ, 132, 531

Kormendy, J., & Richstone, D. 1995, ARA&A, 33, 581

Kouveliotou, C., Meegan, C. A., Fishman, G. J., et al. 1993, ApJL, 413, L101

Lacy, M., Laurent-Muehleisen, S. A., Ridgway, S. E., Becker, R. H., & White, R. L. 2001, ApJL, 551, L17

Laing, R. A. 1980, MNRAS, 193, 439

Lamb, D. Q., Donaghy, T. Q., & Graziani, C. 2005, ApJ, 620, 355

Landi Degl'Innocenti, E., Bagnulo, S., & Fossati, L. 2007, in Astronomical Society of the Pacific Conference Series, Vol. 364, The Future of Photometric, Spectrophotometric and Polarimetric Standardization, ed. C. Sterken, 495

Landoni, M., Falomo, R., Treves, A., Scarpa, R., & Reverte Payá, D. 2015, AJ, 150, 181

Laor, A. 2000, ApJL, 543, L111

Larionov, V., Konstantinova, T., Kopatskaya, E., et al. 2008a, The Astronomer's Telegram, 1502, 1

Larionov, V. M., Jorstad, S. G., Marscher, A. P., et al. 2011, ArXiv e-prints, arXiv:1110.5861

—. 2008b, A&A, 492, 389

Lavaux, G., & Hudson, M. J. 2011, MNRAS, 416, 2840

Lawrence, C. R., Pearson, T. J., Readhead, A. C. S., & Unwin, S. C. 1986, AJ, 91, 494

Legg, M. P. C., & Westfold, K. C. 1968, ApJ, 154, 499

Lehto, H. J., & Valtonen, M. J. 1996, ApJ, 460, 207

Lister, M. L. 2008, in Astronomical Society of the Pacific Conference Series, Vol. 386, Extragalactic Jets: Theory and Observation from Radio to Gamma Ray, ed. T. A. Rector & D. S. De Young, 240

Liu, H., Wang, J., Mao, Y., & Wei, J. 2010, ApJL, 715, L113

Lorenz, E., & Martinez, M. 2005, Astronomy and Geophysics, 46, 6.21

Lott, B., Escande, L., Larsson, S., & Ballet, J. 2012, A&A, 544, A6

Lyutikov, M. 2006, New Journal of Physics, 8, 119

Lyutikov, M., Pariev, V. I., & Blandford, R. D. 2003, ApJ, 597, 998

MAGIC Collaboration, Albert, J., Aliu, E., et al. 2008, Science, 320, 1752

Magorrian, J., Tremaine, S., Richstone, D., et al. 1998, AJ, 115, 2285

Mannheim, K. 1993, A&A, 269, 67

Mannheim, K., & Biermann, P. L. 1992, A&A, 253, L21

Maraschi, L., Ghisellini, G., & Celotti, A. 1992, ApJL, 397, L5

Maraschi, L., & Tavecchio, F. 2003, ApJ, 593, 667

Marcha, M. J. M., Browne, I. W. A., Impey, C. D., & Smith, P. S. 1996, MNRAS, 281, 425

Marchant, J., Jermak, H., Steele, I., et al. 2015, in AAS/Division for Planetary Sciences Meeting Abstracts, Vol. 47, AAS/Division for Planetary Sciences Meeting Abstracts, 413.16

Mariotti, M. 2010, The Astronomer's Telegram, 2510

Marscher, A. P. 2014, ApJ, 780, 87

Marscher, A. P., & Gear, W. K. 1985, ApJ, 298, 114

Marscher, A. P., Jorstad, S. G., D'Arcangelo, F. D., et al. 2008, *Nature*, 452, 966

Marscher, A. P., Jorstad, S. G., Larionov, V. M., et al. 2010, ApJL, 710, L126

Mathur, S. 2000, MNRAS, 314, L17

Matthews, T. A., & Sandage, A. R. 1963, ApJ, 138, 30

Maune, J. D., Miller, H. R., & Eggen, J. R. 2011, in Narrow-Line Seyfert 1 Galaxies and their Place in the Universe

Maune, J. D., Miller, H. R., & Eggen, J. R. 2013, ApJ, 762, 124

Mawson, N. R., Steele, I. A., & Smith, R. J. 2013, Astronomische Nachrichten, 334, 729

Mead, A. R. G., Ballard, K. R., Brand, P. W. J. L., et al. 1990, A&AS, 83, 183

Meier, D. L. 2003, New Astronomy Reviews, 47, 667

Melandri, A., Mundell, C. G., Kobayashi, S., et al. 2008, ApJ, 686, 1209

Melrose, D. B. 1971, Ap&SS, 12, 172

Mészáros, P. 2006, Reports on Progress in Physics, 69, 2259

Mirabel, I. F., & Rodríguez, L. F. 1999, ARA&A, 37, 409

Monet, D. G., Levine, S. E., Canzian, B., et al. 2003, AJ, 125, 984

Morales-Rueda, L., Carter, D., Steele, I. A., Charles, P. A., & Worswick, S. 2004, Astronomische Nachrichten, 325, 215

Mücke, A., & Protheroe, R. J. 2001, Astroparticle Physics, 15, 121

Mücke, A., Protheroe, R. J., Engel, R., Rachen, J. P., & Stanev, T. 2003, Astroparticle Physics, 18, 593

Mukhopadhyay, B. 2013, Proceedings of 13th Marcel Grossman Meeting (MG13), arXiv:1302.3442

Mundell, C. G., Guidorzi, C., & Steele, I. A. 2010, Advances in Astronomy, 2010, arXiv:1003.3573

Mundell, C. G., Steele, I. A., Smith, R. J., et al. 2007, Science, 315, 1822

Mundell, C. G., Kopač, D., Arnold, D. M., et al. 2013, *Nature*, 504, 119

Mundt, R. 1985, in Protostars and Planets II, ed. D. C. Black & M. S. Matthews, 414–433

Naghizadeh-Khouei, J., & Clarke, D. 1993, A&A, 274, 968

Nalewajko, K. 2010, International Journal of Modern Physics D, 19, 701

—. 2013, MNRAS, 430, 1324

Nemmen, R. S., Georganopoulos, M., Guiriec, S., et al. 2012, Science, 338, 1445

Nilsson, K., Pasanen, M., Takalo, L. O., et al. 2007, A&A, 475, 199

Nilsson, K., Pursimo, T., Sillanpää, A., Takalo, L. O., & Lindfors, E. 2008, A&A, 487, L29

Nolan, P. L., Abdo, A. A., Ackermann, M., et al. 2012, ApJS, 199, 31

Ojha, R., & Dutka, M. 2013, The Astronomer's Telegram, 4858

Orienti, M., D'Ammando, F., Giroletti, M., & for the Fermi-LAT Collaboration. 2012, ArXiv e-prints, arXiv:1205.0402

Orr, M. J. L., & Browne, I. W. A. 1982, MNRAS, 200, 1067

Osterbrock, D. E. 1981, ApJ, 249, 462

—. 1984, Quarterly Journal of the RAS, 25, 1

Osterbrock, D. E., & Dahari, O. 1983, ApJ, 273, 478

Osterbrock, D. E., & Pogge, R. W. 1985, ApJ, 297, 166

Osterbrock, D. E., & Shuder, J. M. 1982, ApJS, 49, 149

Padovani, P., & Giommi, P. 1995, MNRAS, 277, 1477

Padovani, P., & Urry, C. M. 1990, ApJ, 356, 75

—. 1991, ApJ, 368, 373

Paliya, V. S., Stalin, C. S., Kumar, B., et al. 2013a, MNRAS, 428, 2450

Paliya, V. S., Stalin, C. S., Shukla, A., & Sahayanathan, S. 2013b, ApJ, 768, 52

Pavlidou, V., Angelakis, E., Myserlis, I., et al. 2014, MNRAS, 442, 1693

Peng, C. Y., Ho, L. C., Impey, C. D., & Rix, H.-W. 2002, AJ, 124, 266

Perlman, E. S., Padovani, P., Landt, H., et al. 2001, in Astronomical Society of the Pacific Conference Series, Vol. 227, Blazar Demographics and Physics, ed. P. Padovani & C. M. Urry, 200

Peterson, B. M. 1997, An Introduction to Active Galactic Nuceli (Cambridge University Press)

Petry, D., Böttcher, M., Connaughton, V., et al. 2000, ApJ, 536, 742

Piascik, A. S., Steele, I. A., Bates, S. D., et al. 2014, in SPIE, Vol. 9147, Ground-based and Airborne Instrumentation for Astronomy V, 91478H

Pihajoki, P. 2016, MNRAS, 457, 1145

Pihajoki, P., Valtonen, M., & Ciprini, S. 2013a, MNRAS, 434, 3122

Pihajoki, P., Valtonen, M., Zola, S., et al. 2013b, ApJ, 764, 5

Piirola, V., Berdyugin, A., & Berdyugina, S. 2014, in SPIE, Vol. 9147, Ground-based and Airborne Instrumentation for Astronomy V, 91478I

Piirola, V., Berdyugin, A., Coyne, G. V. ., Efimov, Y. S., & Shakhovskoy, N. M. 2006, A&A, 454, 277

Piirola, V., Berdyugin, A., Mikkola, S., & Coyne, G. V. 2005, ApJ, 632, 576

Piran, T. 1992, ApJL, 389, L45

—. 1999, Physics Reports, 314, 575

—. 2004, Reviews of Modern Physics, 76, 1143

Planck Collaboration, Ade, P. A. R., Aghanim, N., et al. 2014, A&A, 571, A16

Pogge, R. W. 2000, New Astronomy Reviews, 44, 381

Popović, L. Č. 2003, ApJ, 599, 140

Porth, O., Fendt, C., Meliani, Z., & Vaidya, B. 2011, ApJ, 737, 42

Poutanen, J., & Stern, B. 2010, ApJL, 717, L118

Prandini, E., Bonnoli, G., Maraschi, L., Mariotti, M., & Tavecchio, F. 2010, MNRAS, 405, L76

Puchnarewicz, E. M., Mason, K. O., Cordova, F. A., et al. 1992, MNRAS, 256, 589

Punch, M., Akerlof, C. W., Cawley, M. F., et al. 1992, *Nature*, 358, 477

Quinn, J., Akerlof, C. W., Biller, S., et al. 1996, ApJL, 456, L83

Raiteri, C. M., Villata, M., Tosti, G., et al. 1999, A&A, 352, 19

Raiteri, C. M., Villata, M., D'Ammando, F., et al. 2013, MNRAS, 436, 1530

Rieger, F. M., & Mannheim, K. 2005, Chinese Journal of Astronomy and Astrophysics Supplement, 5, 311

Riess, A. G., Macri, L. M., Hoffmann, S. L., et al. 2016, ApJ, 826, 56

Robbins, M., & Hadwen, B. 2003, Electron Devices, IEEE Transactions on, 50, 1227

Roche, P., & Szymanek, N. 2005, in In IAU Commission 55: Communicating Astronomy with the Public 2005, ed. I. Robson & L. L. Christensen, 384–386

Rowan-Robinson, M. 1977, ApJ, 213, 635

Rügamer, S., Angelakis, E., Bastieri, D., et al. 2011, ArXiv e-prints, arXiv:1109.6808

Ruszkowski, M., & Begelman, M. C. 2002, ApJ, 573, 485

Sambruna, R. M. 1997, ApJ, 487, 536

Sambruna, R. M., Chou, L. L., & Urry, C. M. 2000, ApJ, 533, 650

Sari, R. 1999, ApJL, 524, L43

Sari, R., Piran, T., & Halpern, J. P. 1999, ApJL, 519, L17

Sari, R., Piran, T., & Narayan, R. 1998, ApJL, 497, L17

Saunders, R., Baldwin, J. E., Pooley, G. G., & Warner, P. J. 1981, MNRAS, 197, 287

Scheuer, P. A. G. 1974, MNRAS, 166, 513

Schmidt, G. D., Elston, R., & Lupie, O. L. 1992, AJ, 104, 1563

Schmidt, M., & Matthews, T. A. 1964, ApJ, 139, 781

Schmitt, J. L. 1968, *Nature*, 218, 663

Schmitz, M., Baker, K., Chan, B., et al. 2011, in Bulletin of the American Astronomical Society, Vol. 43, American Astronomical Society Meeting Abstracts #217, 344.08

Schwinger, J. S. 1949, Phys.Rev., 75, 1912

Sciama, D. W., & Rees, M. J. 1967, *Nature*, 216, 147

Seta, H., Isobe, N., Tashiro, M. S., et al. 2009a, PASJ, 61, 1011

—. 2009b, PASJ, 61, 1011

Shaw, M. S., Romani, R. W., Healey, S. E., et al. 2009, ApJ, 704, 477

Sikora, M., Begelman, M. C., & Rees, M. J. 1994, ApJ, 421, 153

Sillanpaa, A., Haarala, S., Valtonen, M. J., Sundelius, B., & Byrd, G. G. 1988, ApJ, 325, 628

Sillanpää, A., Takalo, L. O., Nilsson, K., & Kikuchi, S. 1993, Ap&SS, 206, 55

Sillanpaa, A., Takalo, L. O., Pursimo, T., et al. 1996a, A&A, 305, L17

—. 1996b, A&A, 315, L13

Simmons, J. F. L., & Stewart, B. G. 1985, A&A, 142, 100

Singh, K. K., Yadav, K. K., Tickoo, A. K., et al. 2015, NewAstronomy, 36, 1

Skrutskie, M. F., Cutri, R. M., Stiening, R., et al. 2006, AJ, 131, 1163

Słowikowska, A., Krzeszowski, K., Żejmo, M., Reig, P., & Steele, I. 2016, MNRAS, 458, 759

Słowikowska, A., Stappers, B. W., Harding, A. K., et al. 2015, ApJ, 799, 70

Smith, J. E., Robinson, A., Alexander, D. M., et al. 2004, MNRAS, 350, 140

Smith, J. E., Young, S., Robinson, A., et al. 2002, MNRAS, 335, 773

Smith, P. S., Balonek, T. J., Elston, R., & Heckert, P. A. 1987, ApJS, 64, 459

Smith, P. S., Balonek, T. J., Heckert, P. A., Elston, R., & Schmidt, G. D. 1985, AJ, 90, 1184

Smith, P. S., Williams, G. G., Schmidt, G. D., Diamond-Stanic, A. M., & Means, D. L. 2007, ApJ, 663, 118

Sorcia, M., Benítez, E., Hiriart, D., et al. 2014, ApJ, 794, 54

Sparks, W. B., & Axon, D. J. 1999, PASP, 111, 1298

Steele, I. A., Bates, S. D., Gibson, N., et al. 2008, in Society of Photo-Optical Instrumentation Engineers (SPIE) Conference Series, Vol. 7014, Society of Photo-Optical Instrumentation Engineers (SPIE) Conference Series, 6

Steele, I. A., Bates, S. D., Guidorzi, C., et al. 2010, in Society of Photo-Optical Instrumentation Engineers (SPIE) Conference Series, Vol. 7735, Society of Photo-Optical Instrumentation Engineers (SPIE) Conference Series

Steele, I. A., & Carter, D. 1997, in SPIE, Vol. 3112, Telescope Control Systems II, ed. H. Lewis, 222–233

Steele, I. A., Mundell, C. G., Smith, R. J., Kobayashi, S., & Guidorzi, C. 2009, *Nature*, 462, 767

Steele, I. A., Smith, R. J., Rees, P. C., et al. 2004, in Society of Photo-Optical Instrumentation Engineers (SPIE) Conference Series, Vol. 5489, Ground-based Telescopes, ed. J. M. Oschmann, Jr., 679–692

Steele, I. A., Bates, S. D., Carter, D., et al. 2006, in Society of Photo-Optical Instrumentation Engineers (SPIE) Conference Series, Vol. 6269, Society of Photo-Optical Instrumentation Engineers (SPIE) Conference Series

Takalo, L. O., Nilsson, K., Lindfors, E., et al. 2008, in American Institute of Physics Conference Series, Vol. 1085, American Institute of Physics Conference Series, ed. F. A. Aharonian, W. Hofmann, & F. Rieger, 705–707

Takalo, L. O., & Sillanpaa, A. 1993, Ap&SS, 206, 191

Taniguchi, Y., Murayama, T., & Nagao, T. 1999, ArXiv Astrophysics e-prints, astro-ph/9910036

Tavani, M., Vittorini, V., & Cavaliere, A. 2015, ApJ, 814, 51

Tavecchio, F., Maraschi, L., & Ghisellini, G. 1998, ApJ, 509, 608

Taylor, M. G. G. T., Alexander, C., Altobelli, N., et al. 2015, Science, 347, 387

The MAGIC Collaboration, Aleksić, J., Ansoldi, S., et al. 2013, ArXiv e-prints, arXiv:1311.2833

Thompson, D. J., Bertsch, D. L., Fichtel, C. E., et al. 1993, ApJS, 86, 629

Tody, D. 1986, in Society of Photo-Optical Instrumentation Engineers (SPIE) Conference Series, Vol. 627, Instrumentation in astronomy VI, ed. D. L. Crawford, 733

Tommasi, L., Díaz, R., Palazzi, E., et al. 2001, ApJS, 132, 73

Tosti, G., Massaro, E., Takalo, L. O., Villata, M., & Efimov, Y. 1999, in Astronomical Society of the Pacific Conference Series, Vol. 159, BL Lac Phenomenon, ed. L. O. Takalo & A. Sillanpää, 149

Tosti, G., Fiorucci, M., Luciani, M., et al. 1998a, A&AS, 130, 109

—. 1998b, A&A, 339, 41

Turnshek, D. A., Bohlin, R. C., Williamson, II, R. L., et al. 1990, AJ, 99, 1243

Uehara, T., Toma, K., Kawabata, K. S., et al. 2012, ApJL, 752, L6

Uemura, M., Kawabata, K. S., Sasada, M., et al. 2010, PASJ, 62, 69

Ulrich, M.-H., Kinman, T. D., Lynds, C. R., Rieke, G. H., & Ekers, R. D. 1975, ApJ, 198, 261

Urry, C. 2004, in Astronomical Society of the Pacific Conference Series, Vol. 311, AGN Physics with the Sloan Digital Sky Survey, ed. G. T. Richards & P. B. Hall, 49

Urry, C. M. 2000, in American Institute of Physics Conference Series, Vol. 522, American Institute of Physics Conference Series, ed. S. S. Holt & W. W. Zhang, 299–306

Urry, C. M., & Padovani, P. 1995, PASP, 107, 803

Urry, C. M., Padovani, P., & Stickel, M. 1991, ApJ, 382, 501

Valtaoja, E. 1984, Ap&SS, 100, 227

Valtaoja, L., Karttunen, H., Valtaoja, E., Shakhovskoy, N. M., & Efimov, Y. S. 1993, A&A, 273, 393

Valtaoja, L., Sillanpaa, A., Valtaoja, E., Shakhovskoi, N. M., & Efimov, I. S. 1991, AJ, 101, 78

Valtonen, M., & Ciprini, S. 2012, memsai, 83, 219

Valtonen, M., & Pihajoki, P. 2013, A&A, 557, A28

Valtonen, M., & Sillanpää, A. 2011, Acta Polytechnica, 51, 76

Valtonen, M. J. 2007, ApJ, 659, 1074

Valtonen, M. J., Ciprini, S., & Lehto, H. J. 2012, MNRAS, 427, 77

Valtonen, M. J., Lehto, H. J., Takalo, L. O., & Sillanpää, A. 2011, ApJ, 729, 33

Valtonen, M. J., Lehto, H. J., Sillanpää, A., et al. 2006, ApJ, 646, 36

Valtonen, M. J., Lehto, H. J., Nilsson, K., et al. 2008, *Nature*, 452, 851

Valtonen, M. J., Nilsson, K., Villforth, C., et al. 2009, ApJ, 698, 781

Valtonen, M. J., Mikkola, S., Lehto, H. J., et al. 2010a, Celestial Mechanics and Dynamical Astronomy, 106, 235

Valtonen, M. J., Mikkola, S., Merritt, D., et al. 2010b, ApJ, 709, 725

Valtonen, M. J., Zola, S., Ciprini, S., et al. 2016, ApJL, 819, L37

Vermeulen, R. C., Ogle, P. M., Tran, H. D., et al. 1995, ApJL, 452, L5

Veron-Cetty, M.-P., & Veron, P. 2006, VizieR Online Data Catalog, 7248, 0

Villforth, C., Nilsson, K., Østensen, R., et al. 2009, MNRAS, 397, 1893

Villforth, C., Nilsson, K., Heidt, J., et al. 2010, MNRAS, 402, 2087

Wagner, S. J., Witzel, A., Krichbaum, T. P., et al. 1993, A&A, 271, 344

Wang, X. Y., Dai, Z. G., & Lu, T. 2003, ApJ, 592, 347

Wardle, J. F. C., Homan, D. C., Ojha, R., & Roberts, D. H. 1998, *Nature*, 395, 457

Waxman, E., Kulkarni, S. R., & Frail, D. A. 1998, ApJ, 497, 288

Weistrop, D., Shaffer, D. B., Hintzen, P., & Romanishin, W. 1985, ApJ, 292, 614

Wiersema, K., Curran, P. A., Krühler, T., et al. 2012, MNRAS, 426, 2

Wills, B. J., Wills, D., & Breger, M. 2011, ApJS, 194, 19

Wisniewski, J. P. 2005, PhD thesis, Ritter Observatory, University of Toledo

Xie, G. Z., Zhou, S. B., & Liang, E. W. 2004, AJ, 127, 53

Young, A. 2010, *Nature*, 463, 886

Yuan, W., Zhou, H. Y., Komossa, S., et al. 2008, ApJ, 685, 801

Zhang, B., & Kobayashi, S. 2005, ApJ, 628, 315

Zhang, B., Kobayashi, S., & Mészáros, P. 2003, ApJ, 595, 950

Zhang, B.-K., Zhou, X.-S., Zhao, X.-Y., & Dai, B.-Z. 2015a, Research in Astronomy and Astrophysics, 15, 1784

Zhang, H., & Böttcher, M. 2013, ApJ, 774, 18

Zhang, H., Chen, X., & Böttcher, M. 2014, ApJ, 789, 66

Zhang, H., Chen, X., Böttcher, M., Guo, F., & Li, H. 2015b, ApJ, 804, 58

Zhang, H., Deng, W., Li, H., & Böttcher, M. 2015c, ArXiv e-prints, arXiv:1512.01307

Zhang, S.-N. 2013, Frontiers of Physics, arXiv:1302.5485

Zhou, H., Wang, T., Yuan, W., et al. 2007, ApJL, 658, L13

Zhou, H.-Y., Wang, T.-G., Dong, X.-B., Zhou, Y.-Y., & Li, C. 2003, ApJ, 584, 147

Zola, S., Valtonen, M., Bhatta, G., et al. 2016, Galaxies, 4, 41